



A University of Sussex PhD thesis

Available online via Sussex Research Online:

<http://sro.sussex.ac.uk/>

This thesis is protected by copyright which belongs to the author.

This thesis cannot be reproduced or quoted extensively from without first obtaining permission in writing from the Author

The content must not be changed in any way or sold commercially in any format or medium without the formal permission of the Author

When referring to this work, full bibliographic details including the author, title, awarding institution and date of the thesis must be given

Please visit Sussex Research Online for more information and further details

**Development of a methodology for deriving
Plasmaspheric Electron Content from In-Situ electron
density measurements in highly eccentric equatorial
orbits**

**Development of a methodology for deriving
Plasmaspheric Electron Content from In-Situ electron
density measurements in highly eccentric equatorial
orbits**

Aliyuthuman Sadhique

School of Engineering and Informatics

University of Sussex

Submitted to the University of Sussex for the degree of PhD.

April 2017

DECLARATION

I hereby declare that this thesis has not been submitted, either in the same or different form, to this or any other University for a degree.

.....

Aliyuthuman Sadhique

DEDICATION

I dedicate the gains of this research to my mother and father.

ACKNOWLEDGEMENTS

I would like to express my sincere gratitude to my main supervisor Dr Andrew Buckley for his concern, advice and guidance on top of his supervision during all these years. I also would like to thank Prof. Paul Gaugh for his encouragement and resources. The inspiration I received from my supervisors is priceless and immense.

I would like express my special gratitude and appreciation towards Dr Camilla Briault and Dr Helen Prance for facilitating this. I also thank the University of Sheffield for providing the TC1 data for the research.

Last not the least, I would like to say a big “Thank you” to my wife and son, who sacrificed a lot for all these years and my family members who helped immensely towards this end.

ABSTRACT

Satellite communication and navigation applications suffer due to space weather phenomena. The effects are particularly pronounced in the equatorial regions, which are highly ionised and more easily susceptible to space weather effects than the mid latitude regions. Nevertheless, the bulk of the research on TEC profile and behaviour has been carried out with respect to mid-latitude regions.

The contribution of the Upper Plasmasphere (the altitudes above semi-synchronous orbit height up to the Plasmapause height) to the Total Electron Content at any given location has been and continues to be an un-quantified component.

The PEACE instrument in the Chinese – European Space Agency Double Star TC1 satellite and its highly eccentric equatorial orbit provides an excellent opportunity to build Upper Plasmaspheric Electron Content (UPEC) components in the Equatorial region from empirical in-situ measurements of electron density along the orbit in the 20000km to 40000km altitude range.

This work develops and presents a methodology for deriving Plasmaspheric Electron Content from In-Situ, empirical electron density measurements in highly eccentric, elongated equatorial orbits, using the data from the Double Star TC1 satellite. As such this thesis also generates a database of Upper Plasmaspheric Electron Content (UPEC) along the orbital path of the TC1.

This work also proposes a dedicated mission to be launched with highly eccentric orbits to generate a comprehensive equatorial TEC database based on this methodology. This work envisions that future mission to be preferably launched in the equatorial belt, thus providing the opportunity to develop an archive of data as well as a real time source for better understanding of the Appleton anomaly Effects on Plasmaspheric Electron Content.

CONTENTS

Chapter	Section	Page No.
Chapter 1:	Introduction	1
1.1	Motivation for the research and the original contribution of the research to knowledge	1
1.1.1	Motivation for the research	1
1.1.2	Original contribution to knowledge achieved by this research	3
1.2.	Total Electron Content	4
1.2.1	Why TEC is important? - Practical applications of TEC measurements	4
1.2.1.1	Application that require high precision electron content calculations	4
1.2.1.1.1	Satellite communications	4
1.2.1.1.2	Navigation Applications	5
1.2.2	Definition of Total Electron Content (TEC)	7
1.2.3	Equation for the Total Electron Content (TEC) and its unit	8
1.2.4	Vertical TEC and Slant TEC	9
1.2.5	Incident Angle α	9
1.2.6	Vertical TEC and Slant TEC relationship formula	10
1.2.7	Average electron density versus height profile	11
1.2.8	Global monthly average vertical TEC profile	13
1.2.9	Geographic regional variation patterns	14
1.2.10	Diurnal or Temporal variation pattern of TEC	15

Chapter	Section	Page No.
1.3	Plasmaspheric Electron Content (PEC or TEC _p)	19
1.4	Electron density and TEC measurement techniques	21
	1.4.1 Ionosonde	21
	1.4.2 Topside sounders	22
	1.4.3 GPS Dual Frequency Techniques	23
	1.4.3.1 GPS System Description	23
	1.4.3.2 GPS TEC Derivation	24
	a) Pseudorange Method	24
	b) Carrier Phase Method	26
1.5	GLONASS	27
1.6	Galileo GNSS	29
1.7	Descriptions of relevant orbit types	29
	1.7.1 Geo Synchronous Orbits	29
	1.7.2 Semi (Geo) Synchronous Orbits	30
	1.7.3 Molnya Orbit	31
	1.7.4 Geo Stationary Orbit	32
Chapter 2:	Ionospheric and Plasmaspheric effects	33
2.1	Introduction to Ionospheric and Plasmaspheric effects on radio waves	33
2.2.1	Amplitude and phase scintillation	33
	2.2.1 Amplitude scintillation indices	34
	2.2.2 Phase scintillation index	35

Chapter	Section	Page No.
	2.2.3 Classification of Scintillations	36
	2.2.4 Relationship between SI and S4 indices	36
	2.2.5 Frequency dependence of scintillations	36
2.3	Group Delay or Group Path Delay	36
2.4	RF carrier phase advance	38
	2.4.1 Differential carrier phase	38
	2.4.2 Second difference of carrier phase	39
2.5	Doppler Shift	39
2.6	Faraday Polarization Rotation	40
2.7	Angular Refraction	43
Chapter 3:		
	Mission Overviews – ATS-6, Cluster II, Double Star, and C-NOFS	44
3.1	Applications Technology Satellite-6 (ATS-6)	44
3.1.1	The methodology employed in determining the Plasmaspheric content	45
	a) Faraday Rotation Technique	45
	b) Dispersive Group Delay Technique	46
3.1.2	Results obtained	47
3.1.3	Observations	52
3.1.4	Conclusions	55
3.2	The Cluster Mission	56

Chapter	Section	Page No.
3.2.1	Orbital parameters	57
3.2.2	The experiments	58
3.3	Double Star Mission	58
3.3.1	Orbital parameters and significance of the mission	59
3.3.2.1	Plasma Electron and Current Experiment (PEACE)	62
3.3.2.1.1	The Instrument	62
3.3.2.1.2	Resolutions:	65
3.3.2.1.3	Operation	65
3.3.2.2	The Low Energy Electron Analyser (LEEAA):	65
3.3.2.3	The High Energy Electron Analyser (HEEA):	65
3.3.2.4	DWP Instrumentation	69
3.3.2.4.1	The processor module	69
3.3.2.4.2	Time resolution	70
3.3.2.4.3	Particle correlator	70
3.3.2.4.4	Operation of the Particle correlator	71
3.3.2.5	The Spatio-Temporal Analysis of Field	
	Fluctuations (STAFF)	7.2
3.3.2.5.1	Objectives and the instrument structure	72
Chapter 4 :	TEC modelling and Scintillation modelling	73
4.1	International Reference Ionosphere (IRI)	73
4.1.1	Brief Description	73
4.1.2	Parameters	74

Chapter	Section	Page No.
4.2	Global Ionospheric Scintillation Model (GISM)	74
	4.2.1 Scintillation fluctuations	75
4.3	NeQuick Model	77
4.4	Other models of interest	77
Chapter 5:	Data Extraction from TC1 DWP Correlator	78
5.1	Double Star Data dissemination structure	78
5.2	Double Star DWP Level 1 data acquisition	80
5.3	Double Star L1 data decommutation	80
5.4	Correlator DSD Header definition for DWP	82
5.5	Correlator science packet format	83
5.6	Extracting the Time Series and the ACFs – ACFTIMESBUILD	86
Chapter 6	Development of a methodology for deriving the Upper Plasmaspheric Electron Content (UPEC) along the orbital path of the TC1 from its empirical, in-situ electron density data	93
6.1	The case for this thesis	93
	6.1.1 Upper Plasmaspheric Electron Content (UPEC)	94
	6.1.2 TC1 orbit and the opportunity it provides	96
6.2	Data sources	97
	6.2.1 Electron Density Data -Double Star UK Data Centre	98
	6.2.2 Orbit Data - NASA Satellite Situation Centre	98

Chapter	Section	Page No.
6.3	Orbital elements and Coordinate Systems	
	-Primary background information	101
6.3.1	Orbital elements / Parameters	101
6.3.2	Geocentric Equatorial Inertial Coordinate Systems	105
a)	J2000 Frame Coordinate System (GEI /J2000)	106
b)	True of Date Frame Coordinate System (GEI /TOD)	106
6.4	The Methodology	107
6.4.1	Data acquisition and input	107
6.4.2	The Algorithm	111
6.4.3	Mechanism for the determination of the UPEC	118
6.4.4	Notes on automation of the algorithm	119
Chapter 7	Derivations, Theories and Calculations	121
7.1	Deriving the plane equation	121
7.1.1	Calculation of plane coefficients a, b, c	122
7.2.1	Calculation of the Inclination angle	125
7.3	Coordinate Transformation theories	125
7.3.1	Coordinate transformation of a two axes Cartesian plane by an angle of θ	125
7.3.2	Coordinate Transformation Matrix	126
7.4	Transformations to derive the orbital plane coordinates	126
7.4.1	Calculation of the Longitude of the Ascending Node	127
7.4.2	Transformations through the Argument of Periapsis (Ω^0)	128

Chapter	Section	Page No.
7.5	Calculation of an Orbital Arc Length	129
7.5.1	Ellipse equation of the orbit with its centre at the origin of x, y axes and Line of Apsides as the x axis	130
7.5.2	Calculation of the Arc Length of a function	130
7.5.3	Calculation of the Arc Length of the orbital ellipse with its centre at the origin and the Line of Apsides as the x axis	131
7.6	Calculation of the TEC Bar length	146
7.6.1	Tangent Line Construction and the determination of the Incident Angle	146
7.6.2	Calculation of the UPEC length	149
7.7	Summery of TEC Builder Calculations	152
7.8	Verifications	157
7.8.1	Verification 1: Line of Node intercept value close to zero	157
7.8.2	Verification 2: Z'' coordinate close to zero	158
7.8.3	Verification 3: Argument of Periapsis values are very close by vector analysis method and from the algorithm	162
7.8.4	Verification 4: The transformed coordinates produce perfect elliptical orbits.	164
7.8.5	Verification 5: Consistent inclination angle over the orbital period, which gradually changes in conformity with actual GEI/J2000 coordinate plots	169
7.9	Notes on vector analysis of this methodology	170

Chapter	Section	Page No.
Chapter 8	Analysis of Results, Conclusions, Further Research and Developments	172
8.1	Spatial variation of the Upper Plasmaspheric TEC component along the orbital path as a function of continuous time	173
8.2	Spatial variation of the Upper Plasmaspheric TEC component along the orbital path as a function of radial distance	183
8.3	Variation of Upper Plasmaspheric TEC component as a function of longitude	198
8.4	Observations from the results of Upper Plasmaspheric Electron Content (UPEC) generated by the TEC Builder methodology from TC1 data	208
8.5	Further Research and Developments	210
8.5.1	A dedicated mission to generate a comprehensive equatorial TEC research based on this methodology	211
8.5.2	Development of an International GNSS System for tracking, communications, ranging, search and rescue and disaster management applications	213
8.5.3	Development of a comprehensive TEC model and Scintillation model	213

Chapter	Section	Page No.
Appendices		215
Appendix 1	ACFTIMESBUILD.C	215
Appendix 2	tlmdecom process	227
Appendix 3	tlmdecom.c	228
Appendix 4	tlmproc.c	233
Appendix 5	tlmproc.h	244
Appendix 6	Least Square Fit	246
Appendix 7	Deriving solution to $ax + by + z + c = 0$ format	247
Appendix 8	Solving simultaneous equations with 3 unknowns	249
Appendix 9	Angle between two planes	251
Appendix 10	Coordinate transformation	253
Appendix 11	PEACE energy range (eV) and Correlator levels	256
Reference List		257
Bibliography		262

List of figures

No.	Figure	Page
1.1	Topside Ionosphere and Plasmasphere	008
1.2	Single Layer Model Ionosphere and the Incident Angle	010
1.3	Electron density profile with height for Jicamarca station	012
1.4	Global Vertical Monthly average TEC Contours in TEC Units For 2000UT March 1980 with Equatorial Anomaly Regions Prominently featuring in the western hemisphere and over Africa	013
1.5:	Monthly overplots of TEC for Ascension Island 1980 and 1981	017
1.6:	Monthly overplots of TEC for Hamilton MS for 1979	018
1.7	The Molniya orbit diagram illustrating orbital positions of the satellite with time	031
2.1	Variation of Time Delay with frequency for various values of TEC	037
2.2	Variation of Faraday Rotation with frequency for various values of TEC at a northern mid latitude station	042
3.1:	Variation of Total Electron Content up to geo-synchronous orbit height and Ionospheric electron content (TECG and TECI) at 15-minute intervals from 1600 EDT, 3 July 1974 to 0800 EDT 8 July 1974 at Fort Monmouth, NJ, USA	048
3.2:	Variation of Plasmaspheric electron content (TEC_P) plotted for each day.	049
3.3:	Variation of the ratio of Plasmaspheric to Ionospheric electron contents in percentage.	050
3.4:	Variation of the ratio of Plasmaspheric electron content to Total electron content to geo-stationary height in percentage	051
3.5	Orbital plots of Double Star TC-1 spacecraft in three different dates in 2004, 2005 and 2006	061
3.6	PEACE FM07 Instrument in MSSL Clean Room	062
3.7	A cross-section of the LEEA analyser showing the structure of the input collimator, the electrostatic analyser and the anode pattern	064
3.8	LEEA HEEA Sweep	066
3.9	LEEA HEEA sweeps and spin axis	066

3.10	LAR MAR HAR ENERGY TIME SPIN ANGLE	068
5.1:	Double Star Science Data System (DSDS) schematic diagram	078
5.2	Ground data segment of Double Star Project	079
6.1	The altitudes, period, radius and speed of relevant orbits	096
6.2	Orbital plane diagram showing Incident angle being equal to the angle the tangent to the orbit makes with the line connecting the centre of the earth with the spacecraft in the altitude range $3.5 R_e$ to $6.5 R_e$	097
6.3	Orbital Plane diagram	103
6.4	Orbital elements / Parameters Inclination Angle, Longitude of the Ascending Node and the Argument of Periapsis illustrated	104
6.5	Longitude of the Ascending Node (Ω) calculation for the orbit on 07.05.2005	110
6.6	Argument of Periapsis (ω) calculation for the orbit on 07.05.2005	110
6.7	Equatorial plane diagram showing Longitude of the Ascending Node (Ω) being equal to the Gradient angle of the Line of Nodes in GEI/J2000 system for a general case. The Z axis is perpendicular to the plane and is pointing out.	114
7.1	Angle between the Orbital plane and the Equatorial plane being equal to the angle between their Normal vectors n_o and n_e , which equals Inclination angle	125
7.2	Coordinate transformation of a two axes Cartesian plane by an angle θ	130
7.3	Transformations to derive the orbital plane coordinates with Line of apsides as the x axis	126
7.4	Transformations through the Argument of Periapsis with Line of apsides as the new y axis	128
7.5	Ellipse with centre at the origin of a 2D Cartesian plane	130
7.6	Arc length of a function $y = f(x)$ between two points $P_1(x_1, y_1)$ and $P_2(x_2, y_2)$ in a 2D Cartesian plane	130
7.7	Orbital ellipse with its centre at the origin of x, y axes and Line of Apsides as the x axis	131
7.8	Descriptive diagram for Tangent Line construction and the determination of the Incident Angle	146
7.9	Calculation of the TEC Bar length	150

7.10	Graph of GEI/J2000 Z coordinate values and z coordinates values after the coordinate transformations against Time starting at 00-00-00 on 10/06/2004	160
7.11	Graph of GEI/J2000 Z coordinate values and z coordinates values after the coordinate transformations against Time starting at 00-00-00 on 30/10/2004	160
7.12	Graph of GEI/J2000 Z coordinate values and z coordinates values after the coordinate transformations against Time starting at 00-00-00 on 08/08/2005	161
7.13	Graph of GEI/J2000 Z coordinate values and z coordinates values after the coordinate transformations against Time starting at 00-00-00 on 21/03/2006	161
7.14	Graph of GEI/J2000 Z coordinate values and z coordinates values after the coordinate transformations against Time starting at 00-00-00 on 11/02/2004	162
7.15	Vector diagram for the perigee and the Ascending Node	163
7.16	Orbital plot for 01/03/2004 to 20/03/2004	164
7.17	Orbital plot for 08/08/2005 to 27/08/2005	165
7.18	Orbital plot for 21/03/2006 to 09/04/2006	166
7.17	Orbital plot for 11/02/2004 to 29/02/2004	167
7.18	Orbital plot for 30/10/2004 to 19/11/2004	168
7.20	Orbital state vectors – the position vector and the velocity vector	170
8.1	Plasmaspheric TEC component generated for twenty day between 21.03.06 and 09.04.06. The X axis is calibrated with minutes from midnight 00:00:00 on 21.03.06	173
8.2	Plasmaspheric TEC component generated for twenty day between 21.05.06 and 07.06.06 The X axis is calibrated with minutes from midnight 00:00:00 on 21.05.06.	174
8.3	Plasmaspheric TEC component generated for twenty day between 16.08.06 and 08.09.06 The X axis is calibrated with minutes from midnight 00:00:00 on 16.08.06.	175
8.4	Plasmaspheric TEC component generated for twenty day between 16.08.06 and 08.09.06 The X axis is calibrated with minutes from midnight 00:00:00 on 08.08.05.	176

8.5	Plasmaspheric TEC component generated for twenty day between 09.06.05 and 28.06.05. The X axis is calibrated with minutes from midnight 00:00:00 on 09.06.05.	177
8.6	Plasmaspheric TEC component generated for twenty day between 01.03.04 and 22.03.04. The X axis is calibrated with minutes from midnight 00:00:00 on 01.03.04.	178
8.7	Plasmaspheric TEC component generated for twenty day between 10.04.04 and 29.04.04. The X axis is calibrated with minutes from midnight 00:00:00 on 10.04.04.	179
8.8	Plasmaspheric TEC component generated for twenty day between 30.04.04 and 20.05.04. The X axis is calibrated with minutes from midnight 00:00:00 on 30.04.04	180
8.9	Plasmaspheric TEC component generated for twenty day between 10.06.04 and 30.06.04. The X axis is calibrated with minutes from midnight 00:00:00 on 10.06.04	181
8.10	Plasmaspheric TEC component generated for twenty day between 30.10.04 and 19.11.04. The X axis is calibrated with minutes from midnight 00:00:00 on 30.10.04	182
8.11	Plasmaspheric TEC component generated for twenty day between 21.03.06 and 09.04.06 for minutes 0001 to 1650	183
8.12	Plasmaspheric TEC component generated for twenty day between 21.03.06 and 09.04.06 for minutes 4500 to 6200.	184
8.13	Plasmaspheric TEC component generated for twenty day between 21.03.06 and 09.04.06 for minutes 6200 to 7 800	185
8.14	Plasmaspheric TEC component generated for twenty day between 21.03.06 and 09.04.06 for minutes 8000-9600.	186
8.15	Plasmaspheric TEC component generated for twenty day between 21.03.06 and 09.04.06 for minutes 9600=11200.	187
8.16	Plasmaspheric TEC component generated for twenty day between 21.03.06 and 09.04.06 for minutes 11200-12300.	188
8.17	Plasmaspheric TEC component generated for twenty day between 21.03.06 and 09.04.06 for minutes 12800-14600	189
8.18	Plasmaspheric TEC component generated for twenty day between 21.03.06 and 09.04.06 for minutes 14950-16 7 00.	190

8.19	Plasmaspheric TEC component generated for twenty day between 21.03.06 and 09.04.06 for minutes 16 7 00-18400.	191
8.20	Plasmaspheric TEC component generated for twenty day between 21.03.06 and 09.04.06 for minutes 18600-20100.	192
8.21	Plasmaspheric TEC component generated for twenty day between 21.03.06 and 09.04.06 for minutes 20250-21900.	193
8.22	Plasmaspheric TEC component generated for twenty day between 21.03.06 and 09.04.06 for minutes 21900-23600.	194
8.23	Plasmaspheric TEC component generated for twenty day between 21.03.06 and 09.04.06 for minutes 23600-25300.	195
8.24	Plasmaspheric TEC component generated for twenty day between 21.03.06 and 09.04.06 for minutes 25300-26950.	196
8.25	Plasmaspheric TEC component generated for twenty day between 21.03.06 and 09.04.06 for minutes 14950-16 7 00	197
8.26	The Variation of Upper Plasmaspheric TEC component generated between 21.03.06 and 09.04.06 for minutes 0001 to 1650.	198
8.27	The Variation of Upper Plasmaspheric TEC component generated between 21.03.06 and 09.04.06 for minutes 1600-3200	199
8.28	The Variation of Upper Plasmaspheric TEC component generated between 21.03.06 and 09.04.06 for minutes 3400-5100	200
8.29	The Variation of Upper Plasmaspheric TEC component generated between 21.03.06 and 09.04.06 for minutes 5100-6 7 00.	201
8.30	The Variation of Upper Plasmaspheric TEC component generated between 21.03.06 and 09.04.06 for minutes 6 7 00-8400	202
8.31	The Variation of Upper Plasmaspheric TEC component generated between 21.03.06 and 09.04.06 for minutes 11000-11800	203
8.32	The Variation of Upper Plasmaspheric TEC component generated between 21.03.06 and 09.04.06 for minutes 15850 -1 7 500	204
8.33	The Variation of Upper Plasmaspheric TEC component generated between 21.03.06 and 09.04.06 for minutes 22 7 00-24300	205
8.34	The Variation of Upper Plasmaspheric TEC component generated between 21.03.06 and 09.04.06 for minutes 32200 -34500	206
8.35	The Variation of Upper Plasmaspheric TEC component generated between 21.03.06 and 09.04.06 for minutes 32200 -34500	207

8.36	The orbit arrangement for a dedicated mission to generate a comprehensive equatorial TEC research based on this methodology.	
	The two orbits for a pair of satellites with the same Line of Apsides	211
8.37	The orbit arrangement for a dedicated mission to generate a comprehensive equatorial TEC research based on this methodology.	
	Plane view from the North pole.	212
A9.1	Angle between the Orbital plane and the Equatorial plane being equal to the angle between their Normal vectors n_o and n_e , which equals Inclination angle	252
A9.2	Coordinate transformation of a two axes Cartesian plane by an angle of θ	253

List of Tables

No.	Table	Page
1.1	Civil Applications of Satellite Navigation	006
1.2	Non - civil Applications of Satellite Navigation	007
1.3	Comparison between the orbital and satellite communication parameters of the GPS and GLONASS systems	028
3.1:	List of Cluster II Experiments.	058
3.2:	List of Equatorial Double Star (TC-1) Experiments	056
3.3:	List of Polar Double Star (TC-2) Experiments	057
3.4	PEACE energy range (eV) and Correlator levels	065
5.1	TED header format	082
5.2	ACF + Time Series mode Science packet data structure	084
5.3	Time Series only mode Science packet data structure	085
5.4	DWP data Packet snippet for words 32 and 33	088
5.5	DWP data Packet snippet for the Fixed energy ACF Offset and Scale	089
5.6	DWP data Packet snippet for the first eight fixed energy time series in word 67	089
5.7	DWP data Packet snippet for the Fixed energy Zero lag ACF, Offset and Scale	091
5.8	Data Packet snippet for the first seven Fixed energy ACFs	092
6.1	NASA Satellite Situation Centre TC1 Spacecraft coordinates: Units and formatting options available for outputs and the selected options	099
6.2	NASA Satellite Situation Centre TC1 spacecraft coordinates: Available output options and the selected options	100
6.3	Geocentric Coordinate Systems, their abbreviations and the axes Definitions	105
6.4	Orbital data elements, their format and units	108
7.1	The coefficients of simultaneous equations, the summated equivalents and their TECbuilder positions	123
7.2	Components of the Arc Length calculation formula and corresponding TEC Builder Columns	144
7.3-a	Summery of TEC Builder Calculations - TEC Builder Sheet 1	152
7.3-b	Summery of TEC Builder Calculations - TEC Builder Sheet 1	153

7.3-c	Summery of TEC Builder Calculations - TEC Builder Sheet 1	154
7.3-d	Summery of TEC Builder Calculations - TEC Builder Sheet 1	155
7.4	Summery of TEC Builder Calculations - TEC Builder Sheet 2	156
7.5	Intercept values of the Line of Nodes equation for sampled dates	158
7.6	Inclination angle for sampled periods	169
A11	PEACE energy range (eV) and Correlator levels	256

Chapter 1: Introduction

1.2 Motivation for the research and the original contribution of the research to knowledge

1.1.1 Motivation for the research

Satellite communication and navigation applications suffer due to space weather phenomena. These effects are particularly pronounced in the equatorial regions, which are highly ionised and more easily susceptible to space weather effects than the mid latitude regions (Biktash, 2005)

As would be elaborated later, Total Electron Content (TEC) measurements, the primary measure that quantifies the number of thermal, free electrons intercepted by a traversing electromagnetic wave, yield very high values in the Near-Equatorial regions. This region extends approximately $\pm 20^{\circ} - 25^{\circ}$ on either sides of the magnetic equator (Basu et al. 1985)

Ironically, bulk of the research on the TEC profile and behaviour has been carried out with respect to mid-latitude regions. Recently, efforts have been undertaken by the scientific community in the equatorial belt as well as the international community to carry out research in this area, especially so after the advent of the GPS and its widespread usage. Nevertheless, much more studies need to be done.

The contribution of the Upper Plasmasphere (the altitudes above semi-synchronous orbit height up to the Plasmapause height) to the Total Electron Content at any given location has been and continues to be an unquantified component.

As Electron Content cannot be measured directly and needs to be derived from other parameters, it has not been possible to derive this component from traditional methods such as incoherent scattering radars, ground based ionosondes, satellite sounders and GPS. GPS dual frequency measurements cannot be employed as the Upper Plasmaspheric altitudes are above the GPS satellite orbit altitudes.

The PEACE instrument in the Chinese – European Space Agency Double Star TC1 satellite and its highly eccentric equatorial orbit provides an excellent opportunity to build Upper Plasmaspheric Electron Content (UPEC) components in the Equatorial region from empirical in-situ measurements of electron density along the orbit in the 20000km to 40000km altitude range.

The methodology developed and presented in this thesis generates a first time ever (comprehensive) database of UPEC components along the orbital path of the TC1. The resulting database provides the opportunity for a range of TEC analysis as elaborated later in the thesis.

1.1.2 Original contribution to knowledge achieved by this research

The following section lists what is new in this research and what are the main original contributions to knowledge it effects:

1. For the first time, a methodology has been developed from first principles to quantify the Upper Plasmaspheric Electron Content, from In-Situ electron density measurements.
2. As the last un-quantified component can now be quantified, the satellite to receiver Total Electron Content can be fully and precisely calculated, causing improvements in satellite communications, navigation and ranging applications.
3. As this is from In-Situ measurements, the errors are minimal, providing accurate measurements.
4. The equatorial Total Electron Content behaviour is very complex and not well understood. The development of this methodology opens up a way to analyse this in detail with precision.
5. The resulting Database of Total Electron Content is immensely useful in in satellite communications, navigation and ranging applications and in Space weather Total Electron Content modelling and forecasting.
6. This methodology can be applied on any highly eccentric orbit in equatorial and mid latitude regions, generating a global Total Electron Content database.

7. This methodology can be applied for the entire Plasmaspheric Electron Content (PEC)– complementing, supplementing and improving on the existing methods for PEC measurements.

1.2.1 Total Electron Content

1.2.2 Why TEC is important? - Practical applications of TEC measurements

As would be detailed in Chapter 2, Plasmaspheric and Ionospheric weather impacts on radio waves traversing through them by way of amplitude and phase scintillation, Group path delay, RF carrier phase advance, Doppler shift of the RF carrier, Faraday rotation of the plane of linearly polarised waves and angular refraction of the wave path and distortion of the waveform of the transmitted pulses. Of these effects, all the other effects except for the scintillation effect are proportional (at least to the first order) to the Total Electron Content (TEC).

1.2.1.1 Application that require high precision electron content calculations

TEC values are of critical importance in satellite communications, navigation, altimeter, remote sensing and military applications. The following sections elaborate on these impacts under respective headings.

1.2.2.1 Satellite communications:

For satellite communication applications, TEC measurements are crucial, as the communication signals are impaired in multiple ways as listed above. Hence, error corrections are programmed and implemented in communication algorithms to compensate for the errors encountered in the satellite communication link.

The correct quantification of electron content figure greatly improves quality and precision of the communication link.

1.2.2.2 Navigation applications:

Satellite navigation has critical dependency on the accuracy of positioning. A Global Navigation Satellite System (GNSS) is a constellation of satellites providing signals that contain positioning and timing data to GNSS receivers, which in turn use these data to determine their location by way of calculating the delay in receiving the signals.

The delay a satellite signal undergoes is severely affected by the space weather events and the TEC associated with the signal path, as elaborated in Chapter 2. GNSS systems and other dedicated satellite navigation systems are revolutionising existing industries and applications. At the meantime, entirely new technologies and applications are being developed and new industries are being formed based on these developments. Notable examples are drones, which are being extensively used in new applications such as search and rescue, surveying, autonomous transport, emergency services, security, defence and delivery services. All these applications require high precision guidance and navigation and they rely on satellites for these. Therefore, the maximum achievable precision in electron content quantification becomes critical in reducing the errors for these safety critical applications.

GNSS and other regional Satellite Navigation Systems or dedicated are widely used by a wide spectrum of industries and the applications can be categorised as follows:

Civil Applications	Road Applications <ul style="list-style-type: none"> • Road Navigation • Tolling • Emergency Services • Traffic Management • Fleet Management & • Vehicle Tracking 	Personal Applications <ul style="list-style-type: none"> • Pedestrian Navigation • Outdoor Navigation • Social Networking • Photography Geocoding • Location Based Services
	Aviation Applications <ul style="list-style-type: none"> • GNSS Augmentation Systems <ul style="list-style-type: none"> ○ Aircraft Based ○ Ground Based ○ Satellite Based • En Route Navigation • Approach • Attitude Determination • Air Traffic Control 	Maritime Applications <ul style="list-style-type: none"> • En Route Navigation • Observing the changes of sea level, • Dredging operations, • Wrecks location, • Laying pipe lines, • Search and Rescue of sinking vessels, • Dynamic positioning, • Positioning of oil rigs and • Fixing of satellite sea launch platforms • Maritime Products
	Industry Applications <ul style="list-style-type: none"> • Precision Agriculture • Package and Container Tracking • Mining 	Rail Applications <ul style="list-style-type: none"> • Traffic Management and Signalling

Table 1.1 Civil Applications of Satellite Navigation (ESA, 2011)

Surveying, Mapping and GIS	<ul style="list-style-type: none"> • Land Surveying • Mapping & GIS • Aerial Survey
GNSS-based Products	<ul style="list-style-type: none"> • Personal Products • Road Products • Aviation Products
Scientific Applications	<ul style="list-style-type: none"> • Earth Sciences • Space-time Metrology • Fundamental Physics
Space Applications	<ul style="list-style-type: none"> • Precise Orbit Determination • Satellite Realtime Navigation • Satellite Formation Flying
Autonomous Applications	<ul style="list-style-type: none"> • Autonomous Driving • Autonomous Flying
Military Applications	<ul style="list-style-type: none"> • Military Navigation • Target Acquisition
Emergency, security and humanitarian services	

Table 1.1 Non - civil Applications of Satellite Navigation (ESA, 2011)

1.2.2 Definition of Total Electron Content (TEC)

Total Electron Content is equal to the total number of free, thermal electrons in a unit area (1m^2) column from the ground to a height well above the peak of ionization. This height is nominally taken as the average height of the Plasmapause, above which the co-rotating plasma doesn't exist. But as would be indicated in the equation for TEC in the next paragraph, practically the whole ray path from the satellite to the receiver should be considered, as electron density along that path and its variation will affect the radio waves traversing the Ionosphere –Magnetosphere system (Breed and Goodwin, 2017; Klobuchar et al., 1973).

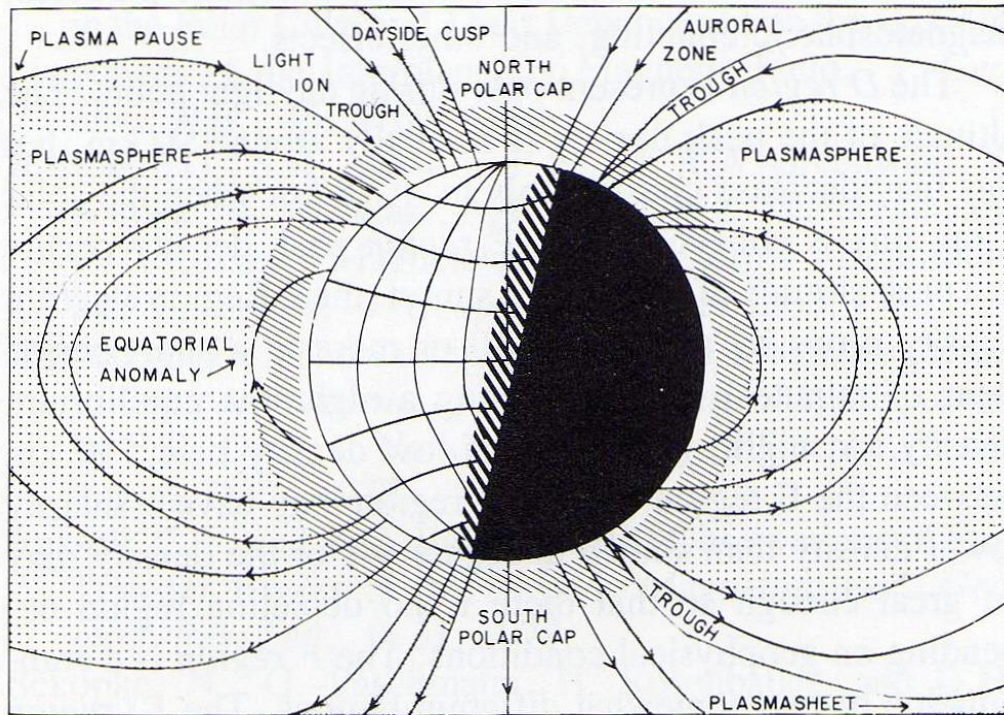


Figure 1.1 Topside Ionosphere and Plasmasphere (Rich and Basu 1985: p.9-2)

1.2.3 Equation for the Total Electron Content (TEC) and its unit

Total Electron Content (TEC) is defined as the total electron count in a unit area column and it is equal to the integral of the electron density over the length of the column

ie.

$$TEC = \int_s^r n_e(l) dl \quad 1.1$$

Here $n_e(l)$ is the electron density along the signal path from the satellite (s) to the receiver (r).

1 TEC Unit (TECU) is defined as 10^{16} el/m^2

Here, the upper limit of the integral is defined as the receiver height. Therefore, this measure of Total Electron Content is contextual, depending on the altitude of the receiver. As such, it will differ for a Low Earth Orbit, Medium Earth Orbit and a Geostationary Orbit satellite.

1.2.4 Vertical TEC and Slant TEC

Vertical TEC (abbreviated VTEC, vTEC or TEC_v) is the number of electrons in a column of one unit area vertically below the transmitting satellite.

Slant TEC (abbreviated STEC, sTEC or TEC_s) is the number of electrons in a column of one unit area along the true transmission path between the satellite and the receiver.

1.2.5 Incident Angle α

In a single layer model or thin layer model, the incident angle is defined as the angle the Line of Sight (LoS) between the satellite and the receiver in the ground makes with the line connecting the centre of the earth with the Ionospheric Penetration Point (Also the zenith angle at the Sub-Ionospheric Point C in figure 1.2).

The Ionospheric Penetration Point (IPP) is the point the Line of Sight between the satellite and the receiver intersects the Centre of Mass column (Centroid) of the Ionosphere, variously taken to be 300, 350, 400, 420 or 450 km. This height is sometimes considered as the mean Ionospheric height too (Gorman and Soicher, 1973).

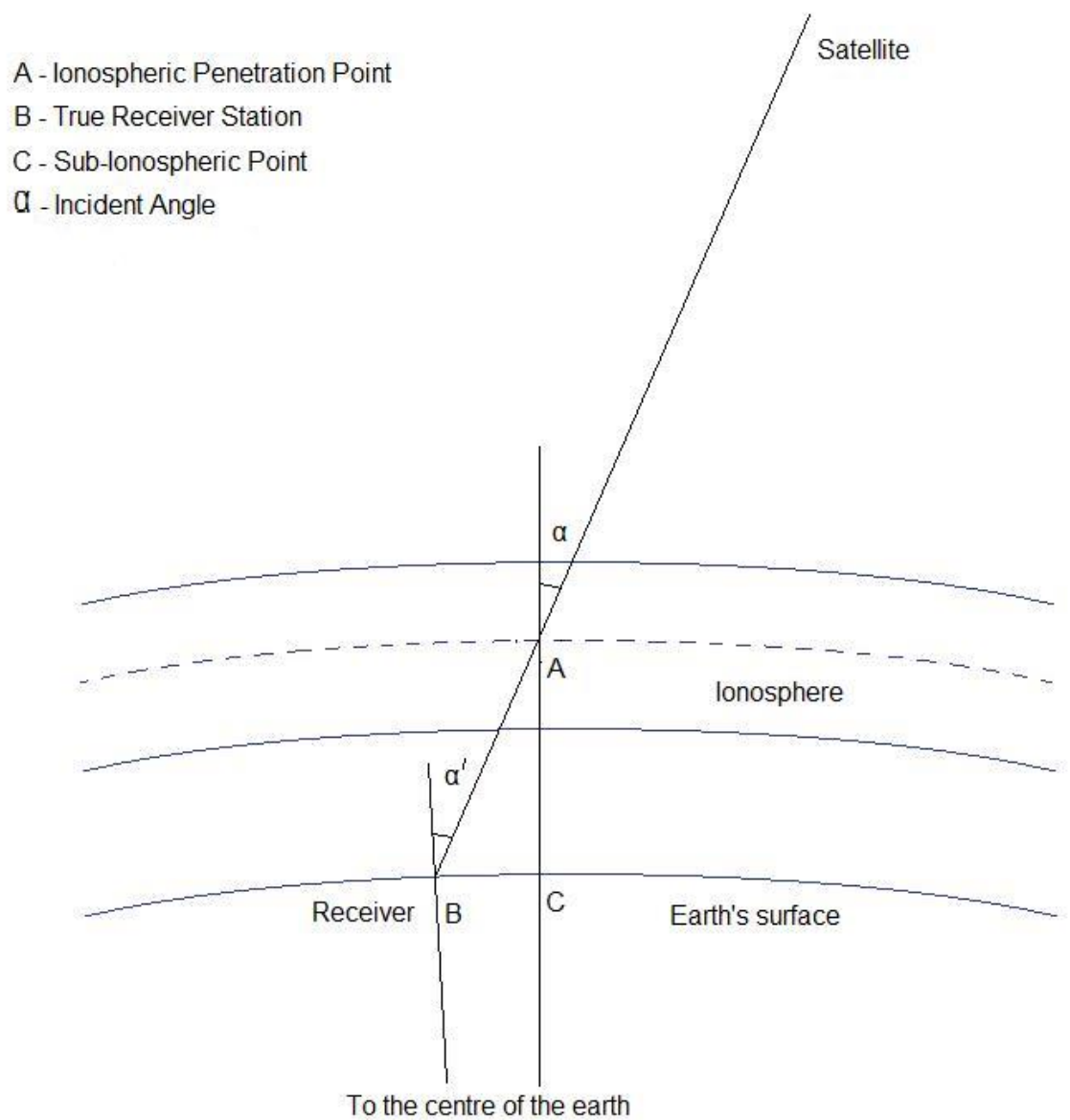


Figure 1.2 Single Layer Model Ionosphere and the Incident Angle

1.2.6 Vertical TEC and Slant TEC relationship formula

In Ionospheric Total Electron Content analysis, if the Ionosphere is considered to be a single layer or thin layer model, then from the geometry illustrated in Figure 1.3, the relationship between STEC and VTEC is as follows in the next page:

$$VTEC = STEC \times \frac{\sqrt{(R_e + h_m)^2 - R_e^2 \sin^2(\alpha)}}{R_e + h_m} \quad 1.2$$

Where R_e is the radius of the earth α is the incident angle and h_m is the height of the Ionospheric Penetration Point (Garner et al., 2008).

But for the purpose of TEC calculations, as the $R_e \gg h_m$, then $R_e + h_m \approx R_e$

Then, formula 1.2 can be approximated to

$$VTEC = STEC \times \cos(\alpha) \quad 1.3$$

This form of the relationship STEC and VTEC proves to be sufficient for TEC analysis (Ya'acob, Abdullah and Ismail, 2010).

1.2.7 Average electron density versus height profile

In any given geographic location, the greatest contribution to the Total Electron Content comes for the F2 region of the Ionosphere. The electron density increase drastically with height till the F2 layer and reduce exponentially thereafter. In mid latitude regions, under quite solar conditions, up to two thirds of the TEC is generated by the F2 layer (Basu et al. 1985; Wernik, Alfonsi and Materassi, 2004).

Electron density profile with height for Jicamarca station 19 Jul 1962

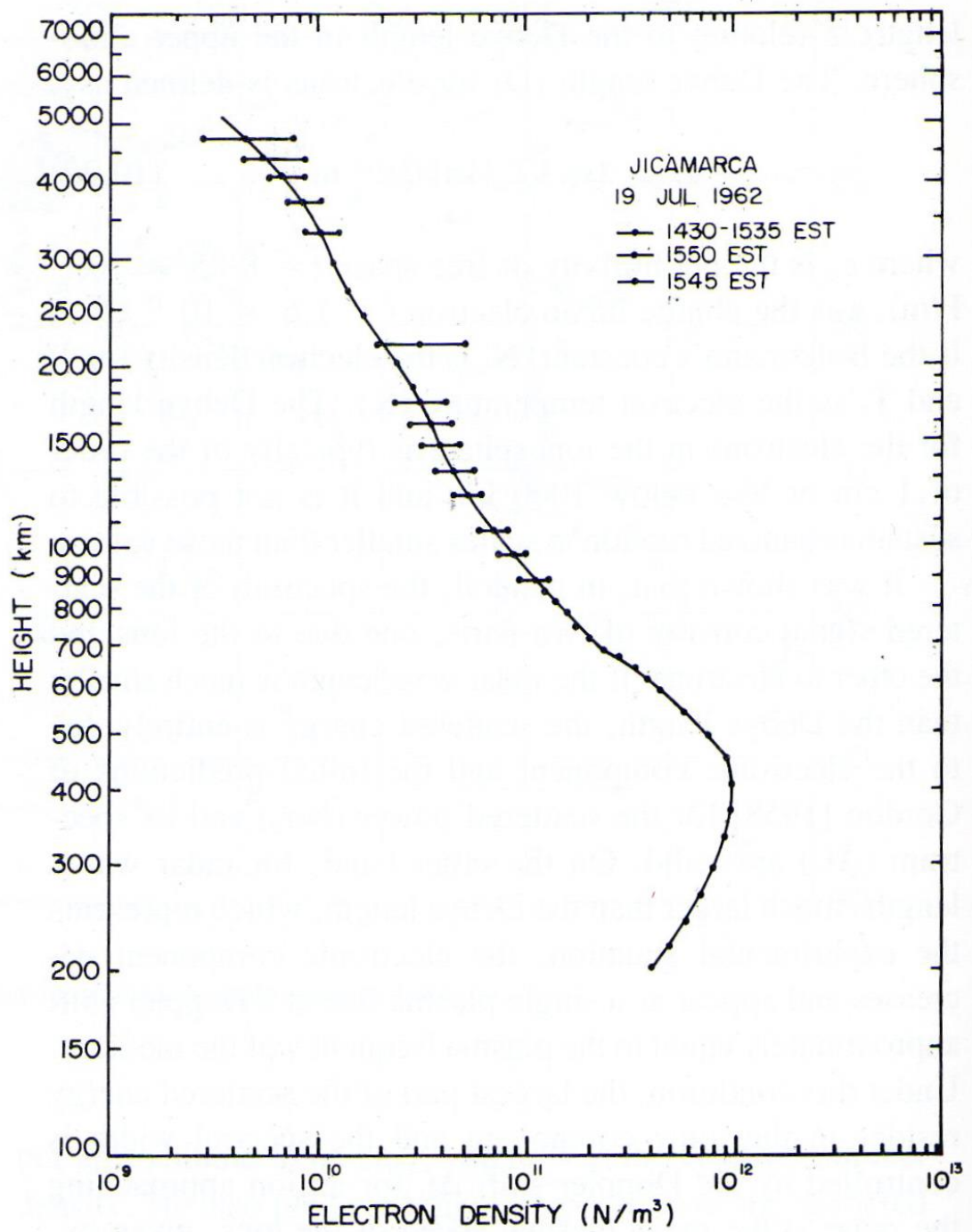


Figure 1.3 Electron density profile with height for Jicamarca station 19 Jul 1962

(Basu et al. 1985: p10-16)

1.2.8 Global monthly average vertical TEC profile

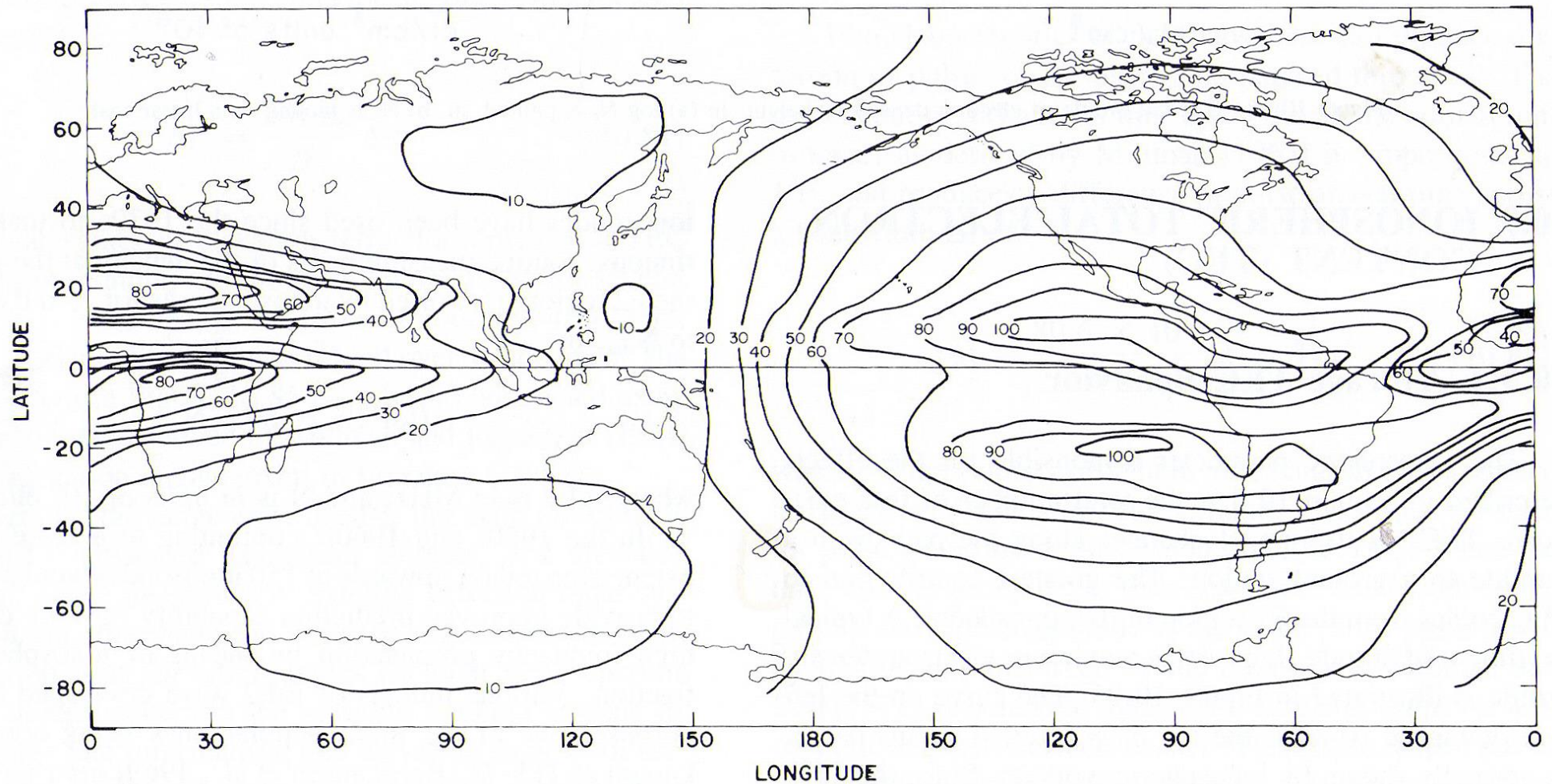


Figure 1.4 Global Vertical Monthly average TEC Contours in TEC Units for 2000UT March 1980

with Equatorial Anomaly Regions prominently featuring in the western hemisphere and over Africa (Basu et al. 1985: p10-90)

The electron density profile of the Ionosphere (and Plasmasphere by extension) has the following variation patterns:

1. Locational - Variations in relation to geographic and geomagnetic locations
2. Diurnal – Variations throughout the day (largely due to solar zenith angle)
3. Solar activity- Variation occurring due to changes in solar activity; both long term and disturbances.
4. Seasonal - Variations throughout the year disturbances
5. Height - Variation along the altitude in different layers (Basu et al. 1985)

1.2.9 Geographic regional variation patterns

Electron density has three distinctive patterns of variations geographically. The highest value for TEC is encountered in the Near-Equatorial regions. This region is approximately bounded by latitudes $\pm 20^\circ$ to $\pm 25^\circ$ on either sides of the magnetic equator. The highest value occurs in a region approximately ± 15 from the Magnetic Equator, rather than in the Equator itself. This region is called the “Equatorial Anomaly” region, due to the occurrence of the “Appleton Anomaly”.

Mid-latitudes yield moderate values for TEC and the variations are mostly predictable in quite solar conditions. The electron density profile and behaviour are well analysed and understood in this region than in the Near-Equatorial regions.

Polar Regions are easily perturbed by CME events and as such electron density variations and TEC values are unstable in those regions.

For a station in Northern mid-latitudes, the standard deviation from monthly mean diurnal TEC behaviour is 20% -25%.

For Near-Equatorial regions and the Polar/ Auroral regions, the standard deviation is very high. There are instances where the TEC value has been around 200 TEC units, near Ascension islands in the Equatorial Anomaly region (Basu et al. 1985).

1.2.10 Diurnal or Temporal variation patterns of TEC

In mid-latitudes, electron density starts to increase in the morning sunlight and reaches its peak in late evening. It falls steadily thorough out night hours through the Rayleigh-Taylor instability mechanism (Li, Ning and Yuan, 2007). This pattern holds for most of the seasons in quite solar conditions (Basu et al. 1985).

This pattern differs in the Near-Equatorial regions and the Polar/ Auroral regions. In the Near-Equatorial regions, the electron density starts to rise with sunlight and increases steadily throughout till sun set. After sunset, the electron density declination is either slow due to recombination of ions and electrons or shows an increase just before midnight, sometimes surpassing the maximum TEC attained during daytime. This anomaly is referred to as the “Appleton Anomaly” and is more pronounced in high TEC yielding geographical locations such Ascension Island (7°56'S, 14°22'W).

Appleton Anomaly is caused by the effect of Rayleigh-Taylor instabilities from the bottom side Ionosphere. During this process, the depleted electron density bubble rises into the region above the peak of the F2 layer. This is caused by the $E \times B$ drift of the post sunset F layer, in response to the pre reversal electric field.

Temporal variation of TEC in the equatorial anomaly region can be explained by the variability of equatorial electrojet strength during solar minimum periods, the dynamics are complex during solar maximum conditions.

In Auroral and Polar regions, the night time behaviour is highly varied and unpredictable. In these regions, TEC values occasionally surpass day time maximum values. The changes are rapid too. Specific large increases in TEC, unlike general auroral activity are not individually predictable. Statistically, they can be characterised as a function of magnetic activity (Basu et al. 1985; Ya'acob, Abdullah and Ismail, 2010)

The following plots indicate monthly diurnal variation for two locations in the Near Equatorial region and the Mid Latitude region.

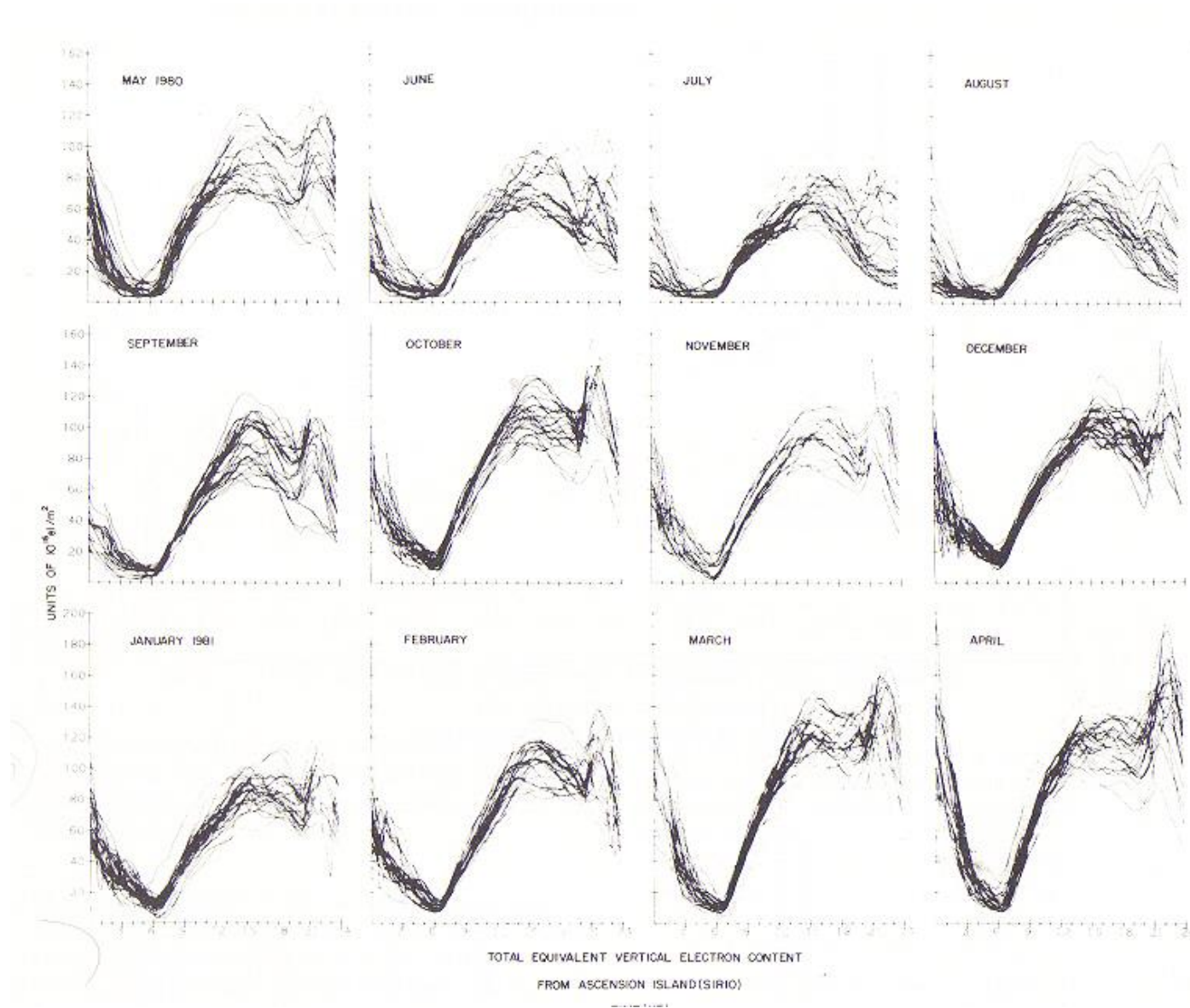


Figure 1.5: Monthly overplots of TEC for Ascension Island 1980 and 1981 (Basu et al. 1985: p10-91)

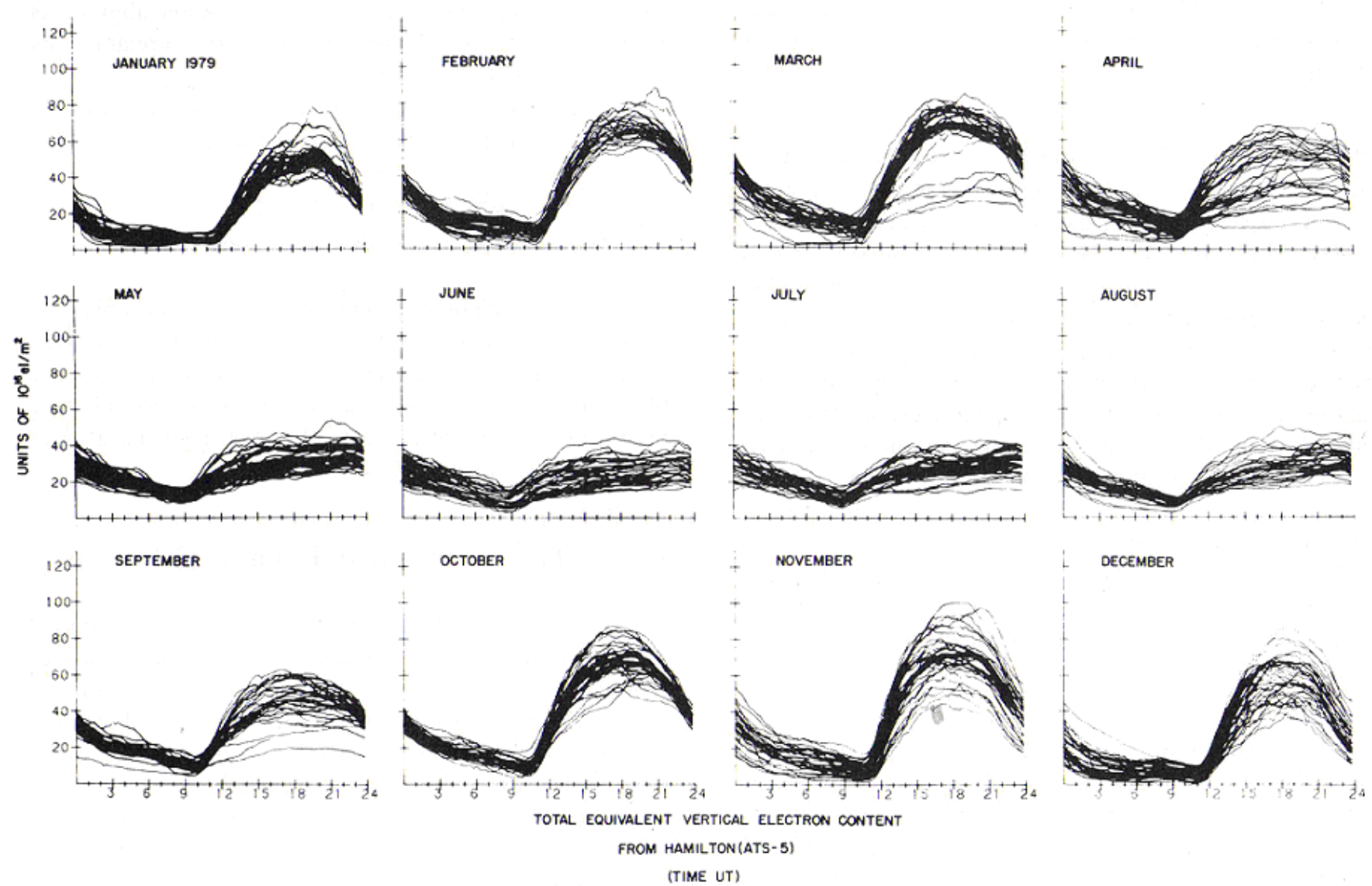


Figure 1.6: Monthly overplots of TEC for Hamilton MS for 1979 (Basu et al. 1985: p10-94)

1.3 Plasmaspheric Electron Content (PEC or TEC_p)

Plasmaspheric Electron Content can be defined as the total electron count in the Plasmasphere segment of a column of 1m^2 cross section, along the signal path from the satellite (s) to the receiver (r). Plasmaspheric Electron Content is abbreviated either as PEC (Mazzella 2012) or TEC_p (Gorman and Soicher, 1973).

Plasmaspheric Electron Content becomes of consequence only in trans-Ionospheric satellite communications and navigations applications. As such geo-stationary satellite communications systems, semi-synchronous orbital communications systems such as Molnya satellites, GPS, Russia's GLONASS, Europe's Galileo and the Chinese and Indian regional navigations systems have compelled towards the wide spread use of the trans-Ionospheric communication and navigation applications. With the proliferation of these satellite systems, the need to quantify the Plasmaspheric contribution to the TEC parameter is gaining importance. This scenario is particularly of important in the Near-Equatorial regions, where ionization is very high and where all the geo-stationary satellites are positioned.

The Plasmasphere occurs from 2000 km (the region above the O⁺/H⁺ transition height) to the height of the Plasmapause. The Plasmapause demarcates the boundary of co-rotating plasma and beyond which the electron density drastically depletes. Plasmapause height varies with all the space weather variables and the maximum occurs in the equatorial belt at about approximately about 7 R_e under quite solar conditions.

As Plasmapause reaches such heights, Plasmaspheric contribution to TEC also gains significance. Even though the altitudes are mildly ionised, the magnitude of the distances make the contribution from the Plasmasphere to be taken into account.

From the Faraday rotation and dispersive group delay observations conducted at Fort Monmouth Oceanport, NJ using the ATS-6, on the diurnal as well as day-to-day variations of Plasmaspheric content, its absolute magnitude was found to be varying from 1 to 8 TEC units and was nearly always above 50% of the Ionospheric content at night time and on occasions exceeded 100%. This ratio averaged 35% during day times (Gorman and Soicher, 1973).

At southern mid-latitudes, the Plasmaspheric contribution to the Ionosphere-Plasmasphere combined TEC is given at approximately 10% during day time (when electron density in the Ionosphere is high) and 40-50% during night time (when electron density in the Ionosphere is low). The understanding of the Plasmaspheric contribution to TEC at the near -e equatorial region is a still evolving study. This research strives to answer a part of that question by deriving the upper Plasmaspheric (above 22000km) contribution from in-situ electron density measurements from the Double Star TC 1 mission.

Plasmaspheric contribution to the Electron Content should be analysed in two parts, due to the fact that the most prevalent method (with the exception of some geo-stationary satellite missions such as ATS-6, which investigated the Plasmaspheric content up to orbit height) of calculating the Plasmaspheric contribution is GPS dual frequency method. The GPS system has an orbital altitude of 20000 km. Therefore the TEC derived from these calculations do not provide a measure for the electron population encountered above that altitude.

Earlier studies of the TEC in equatorial regions utilised Faraday rotation of the single frequency waves from geo stationary satellites. As would be explained later, Faraday rotation of the radio wave has the integral of the product of the electron density times the longitudinal component of the earth's magnetosphere as its main component.

This component is negligible in altitudes more than 2000 km, and the resulting Faraday rotation is insignificant for those altitudes. Therefore, the resulting TEC calculation only denoted Ionospheric TEC content.

Top side sounding technique has been applied to Magnetospheric plasma research with renewed interest during the last decade and fundamental new results had been obtained from Intercosmos-19, Cosmos-1809 and ISS-b missions (Beloff et al., 2004).

Geo-stationary satellites and semi-synchronous (such as Molniya) orbital systems have orbital altitudes up to 400000 km. Therefore, it becomes imperative that the upper Plasmaspheric contribution to Electron Content should be determined, specially in the near equatorial region where the Plasmapause occurs at up to 7 R_e height (Li, Ning and Yuan, 2007).

1.4 Electron density and TEC measurement techniques

1.4.1 Ionosonde

Sounding the Ionosphere with ionosondes is the oldest and one of most prevalent methods of Ionospheric investigations.

Ionosondes are variable frequency radars that measure the time it takes for the transmitted signal to be reflected from the various layers of the Ionosphere. By sweeping its frequency, an ionosonde generates ionograms, plotting Ionospheric reflection height as a function of frequency.

Electron density of the respective layer is deduced from the plasma frequency equation;

$$f_N = 0.009\sqrt{N_e}$$

$$N_e = 1.24 \times 10^{10} f_N^2 \text{ el} / m^3 \quad 1.4$$

1.4.2 Topside sounders

As the ground based sounders could only get information about the ionosphere up to the F2 layer peak density, the topside of ionosphere information was hard to come by. Therefore, with the onset of the space age, satellite based sounders were used to measure the ionosphere parameters from above. This technique is called topside sounding.

As with the ground based Ionosondes, topside sounders give information about the critical frequency of the highest ionised layer, which is the F2 layer normally, and hence its electron density.

In the event the topside sounding spacecraft height is very close to the maximum ionised layer height, the topside sounding techniques become complicated. Beloff et al (2004) studied the TEC determination methodology using the traces of the signals reflected from the earth from the ionosonde AI-840 in the MIR space station.

To determine the TEC below the orbital height (h_s) of 365 km, the plasma layer below the satellite was approximated by the equivalent parabolic distribution;

$$f_N^2(h) = f_m^2 \left[1 - \left(\frac{h_s - h}{H_p} \right)^2 \right] \quad 1.5$$

Where f_N is the electron plasma frequency; f_m is the critical frequency of the F region; h_s is the satellite height and H_p is a half thickness of the parabola. As the traces of the signals reflected from the topside of the ionosphere were recorded in a narrow band of frequencies and the records presented were of low quality due to strong deflective absorption, it was not possible to derive the electron density profile $N(h)$ above the F region maximum and determine $h_m F$. Therefore the methodology utilises measurement of group paths of signals reflected from the earth to derive TEC below orbital height.

The group paths reflected from the earth can be given by:

$$P'(f) = h_0 + \int_{h_s - H_p}^{h_s} \mu'(f, f_H, \theta) dh \quad 1.6$$

Where f is the sounding frequency; f_H is the gyrofrequency; θ is the angle between the vertical and vector of intensity of the geomagnetic field; h_0 is the height of the equivalent base layer and μ' denotes the group refractive indices for ordinary (o) and extra-ordinary(x) polarised waves.

The technique uses least squares method analysis to obtain the half-thickness of the parabola and hence the TEC (Beloff et al., 2004).

.

Integrating 1.4 with reference to 1.5 and 1.1 gives:

$$TEC = \int_0^{h_s} N_e(h) dh = \frac{2}{3} 1.24 \times 10^{10} f_m^2 H_p \quad 1.7$$

From this, the mean square error of TEC can be obtained as:

$$s(TEC) = TEC \left(\frac{2s(f_m)}{f_m} + \frac{s(H_p)}{H_p} \right) \quad 1.8$$

1.4.3 GPS Dual Frequency Techniques

The TEC encountered along a ray path introduces a time delay and changes to its phase. As GPS signals operate with two frequencies, the TEC can be deduced by differencing these two quantities from the two frequencies.

1.4.3.1 GPS System Description

The GPS system is a Global Navigational Satellite System operating in six geosynchronous medium earth orbits with an inclination of 55° . There are 30 satellites in

the constellation, with five satellites operating in each of the equally spaced six orbital planes and one or two auxiliary satellites in standby. Due to this set up, any geographic point on the surface of the earth will be in Line of Sight (LOS) to 8- 10 satellites or 1/3 of the constellation at any given time.

The orbits have period of 11 sidereal hours and 58 minutes and most importantly will remain within the ground receiver's field of view of 160° for 8 hours. The system has a typical data rate of 33.3 MHz corresponding to an angular difference of 0.167° between adjacent slant paths. Due to the orientation and the period of the constellation the GPS line of sight between the receiver and a particular satellite changes only 5° within 15 minutes and the system makes 30 measurements during that period. Even though the time frame of 15 minutes is a reasonable for large scale Ionospheric and Plasmaspheric dynamics, the spatial change of 5° is not substantial enough. Therefore the resulting TEC measurement can detect temporal variations within the Ionosphere and Plasmasphere system not good enough for horizontal variation.

The GPS system works on two L band frequencies, $L_1 = 1575.42$ MHz and $L_2 = 1227.60$ MHz (Garner et al., 2008; Basu, 2003).

1.4.3.2 GPS TEC Derivation:

The GPS dual frequency TEC Derivation technique makes use of the two components; the pseudorange ρ and the carrier phase Φ .

a) Pseudorange Method:

The pseudorange method is the most straight forward TEC measurement method of the two. The pseudorange equation is as follows:

$$\rho = D + c(b - B + e + E) + C(t + I + v_\rho) = c(t_r - t_s) \quad 1.9$$

Where D is the true range, c is the speed of light, B and b are the satellite and receiver clock biases, E and e are the electronics time delay within the satellite and receiver, T is the dispersionless Tropospheric time delay, I is the Ionospheric time delay, v_p is the signal and multipath noise, and t_s and t_r are the clock time at the satellite and the receiver.

The pseudorange can be calculated at both frequencies and thus the non-dispersive components can be removed. Thus we can write:

$$\Delta\rho = \rho_{L1} - \rho_{L2} \quad 1.10$$

$$\Delta\rho = c(e_{L2} - e_{L1} + E_{L2} - E_{L1} + v_{L2} - v_{L1} + I_{L2} - I_{L1}) \quad 1.11$$

This can be rearranged to:

$$\Delta I = \frac{\Delta\rho}{c} = \Delta e - \Delta E - \Delta v_p \quad 1.12$$

Δe and ΔE are referred to as the inter-frequency bias in the satellite and the receiver. They are difficult to quantify and are sensitive to local temperature and pressure variations. Hence they are treated as noise terms.

The Ionospheric time delay can be determined from the first order Ionospheric index of refraction:

$$\mu = \sqrt{1 - f_p^2 / f^2} \quad 1.12$$

This is given by:

$$\begin{aligned} I &= \int (1 - \mu) \frac{ds}{c} \\ &\approx \frac{e^2}{8\pi^2 c \epsilon_0 m_e} \frac{1}{f^2} \int n ds \\ &\approx \frac{1.345 \times 10^{-7}}{f^2} STEC \end{aligned} \quad 1.13$$

Where $f_P = \frac{e^2 n}{4\pi^2 \varepsilon_0 m_e}$ is the plasma frequency, f is the frequency of the radio signal, e is the charge of electron, n is the electron density, ε_0 is the permittivity of free space, m_e is the electron mass and ds is the incremental slant path.

Using the first term in the binomial series for $\sqrt{1 - f_P^2/f^2} = 1 - f_P^2/2f^2$ and combining 1.12 and 1.13, one gets:

$$STEC = \frac{8\pi^2 \varepsilon_0 m}{e^2} \frac{f_{L2}^2 \cdot f_{L1}^2}{f_{L1}^2 - f_{L2}^2} [\Delta\rho - c(\Delta e + \Delta E + \Delta v_\rho)]$$

$$STEC \approx 9.514 \times 10^{16} [m^{-3}] [\Delta\rho - c(\Delta e + \Delta E + \Delta v_\rho)] \quad 1.14$$

The drawback of deriving TEC from pseudorange method is that there is a quite large noise term v_ρ in the final expression and the inter-frequency biases cannot be ignored.

b) Carrier Phase Method:

The carrier phase change in both frequencies is used to determine TEC along the signal path. The relationship of carrier phase is given by:

$$\lambda\phi = D + c(b - B + e + E + T - I + v_\phi) + m\lambda \quad 1.15$$

Where λ is the wave length, v_ϕ is the noise in the phase and m is whole number, representing the phase ambiguity. Applying this equation in both frequencies the TEC can be derived from: $\Delta I = \lambda_{L1}\phi_{L1} - \lambda_{L2}\phi_{L2} + \Delta e + \Delta E + \Delta v_\phi + \Delta m\lambda$

$$= \frac{f_{L1}^2 - f_{L2}^2}{f_{L2}^2 \cdot f_{L1}^2} \frac{e^2}{8\pi^2 \varepsilon_0 m_e} STEC \quad 1.16$$

It is significant that the carrier phase noise v_ϕ much smaller than the pseudorange noise v_ρ typically by two orders of magnitude. However, the phase

ambiguity $\Delta m\lambda$ creates a significant offset and inter-frequency biases cause errors and cycle slips creates more problems in this method too. But there have been developments to remove these discrete discontinuities in the carrier phase before the TEC is computed. It should be noted that the TEC valued can be deduced from GPS measurements for only sub 22000 km altitudes (Garner et al., 2008).

1.5 GLONASS

With the need for a satellite based navigation system for military and civilian uses arising, the Russia developed a satellite navigation system based on one-way range measurements. This system, developed parallel to the United States GPS, is called GLONASS (Global Navigation Satellite System) and is continued by the Russian Federation. GLONASS has similar applications to those of GPS in precise navigation uses in land, sea, air and low orbiting spacecraft. Besides this, GLONASS signals can be used for the dissemination of highly precise global and local time scales and establishing global geodetic coordinate systems and local geodetic networks.

GLONASS provides a standard precision (SP) and a high precision (HP) navigation signal, similar to the Standard Positioning Service (SPS) and the Precise Positioning Service (PPS) of the GPS. These signals are also referred to as Channel of Standard Accuracy (CSA) and Channel of High Accuracy (CHA), respectively. The SP signal is available to all civil users globally on a continuous basis. GLONASS navigation systems are increasingly being incorporated into satellite navigation receivers, smart phones and other application either as stand-alone systems or as complementary systems along with GPS (Rossbach, 2001; Polischuk et al., 2002).

The GLONASS constellation orbits in three co-planar semi geo-synchronous, medium earth orbits with a 64.8 degree inclination and a period of 11 hours and 15

minutes. With eight satellites in each plane spaced 120° in longitude between the planes, the constellation achieves global coverage with 24 satellites. The constellation's orbital parameters makes it especially suited for usage in high latitudes (north or south), where getting a GPS signal can be problematic (Polischuk et al., 2002). The following table provides a comparison between the orbital and satellite communication parameters of the GPS and GLONASS systems:

Parameter	GLONASS	GPS
Semi-major axis	25510 km	26580 km
Orbital height	19130 km	20200 km
Orbital period	11 h 15.8 min	11 h 58 min
Inclination	64.8°	55°
Eccentricity	0.01	0.1
Distinguishing between satellites	FDMA (1 code, multiple frequencies)	CDMA (1 frequency, multiple codes)
Frequency L1	1602 - 1615.5 MHz	1575.42 MHz
Frequency L2	1246 - 1256.5 MHz	1227.60 MHz
Signal polarization	RHCP	RHCP

Table 1.3 Comparison between the orbital and satellite communication parameters of the GPS and GLONASS systems (Rossbach, 2001)

According to Sergei Ivanov, the Kremlin Chief of Staff (2014), the latest generation of GLONASS –K satellites have an accuracy of 2.9 metres (Bodner, 2014).

1.6 Galileo GNSS

The Galileo program is the GNSS program of The European Space Agency. It is still under development, with only two experimental GIOVE (Galileo In-Orbit Validation Element) satellites having been launched. Similar to GPS and GLONASS, the orbits will be Medium Earth Orbits at an altitude of 23222 km with a period of about 14 hours. There will be three orbit planes at an inclination of 56° to the equator. The constellation will consist of 30 satellites with 10 satellites orbiting in each plane. One satellite in each orbital plane will be a standby satellite.

The system is interoperable with GPS and the combined system will be of high reliability. GLONASS signals can also be utilised in receiver units and such units will have very high accuracy standards owing to the fact that they get input signal from three independent GNSS systems. Unlike GPS and GLONASS, the Galileo is purely a civilian project. Another major difference or upgrade from these two previous GNSS is the “Search and Rescue” capability, by which an orbiting satellite is able to pick up distress signals from a ground receiver and relay it to search and rescue personnel on earth. (Hapgood, 1992).

1.7 Descriptions of some relevant orbit types

1.7.1 Geo Synchronous Orbits

A Geo Synchronous orbit is an orbit around the Earth with an orbital period equal to one sidereal day, (Earth's sidereal rotation period which is approximately 23 hours 56 minutes and 4 seconds). As the name implies, the synchronization of the Earth's rotation and the orbital period means that an object in geosynchronous orbit returns to exactly the same position in the sky after a period of one sidereal day for an observer on the surface of the Earth. During the period of a

sidereal day the object traces out the shape of an analemma. The relationship between the semi-major axis and the period of an orbit is given by:

$$a = \sqrt[3]{\mu \left(\frac{P}{2\pi} \right)^2}$$

where a is the semi-major axis, P is the orbital period, and μ is the Geocentric Gravitational Constant, which is equal to $39.86 \times 10^{13} \text{ m}^3/\text{s}^2$.

As the orbital period is the only variable in the right hand side of the above equation, all orbits with the same orbital period have the same value for semi-major axis. Therefore, all Geo Synchronous orbits have the same semi-major axis, irrespective of whether they are circular or elliptical in shape, as they all have the same orbital period of one sidereal day.

1.7.2 Semi (Geo) Synchronous Orbits

A semi-synchronous orbit is defined as an orbit with half the period of the average rotational period of the body that is being orbited and rotating in the same direction of the main body's rotation. For Earth, a Semi (Geo) Synchronous Orbit is considered to be an orbit with a period of half a side real day, which is just below 12 hours and of an altitude about 20,000 kilometres above sea level (medium Earth orbit) (Bockstiegel, Benko and Hobe, 2005). The parentheses and the word “Geo” are being used to indicate that the orbit is an Earth orbit.

Practically, a Semi (Geo) Synchronous Orbit is nearly circular and has a radius of 26,560 kilometres from the centre of the Earth. As the Earth has a side real period of rotation of approximately 24-hours (23 hours 56 minutes and 4 seconds), a satellite in Semi (Geo) Synchronous Orbit, crosses over the same two spots on the equator every day. GPS satellites are deployed in this orbit. The orbital pattern is simple, less complex and highly predictable.

1.7.3 Molniya Orbit

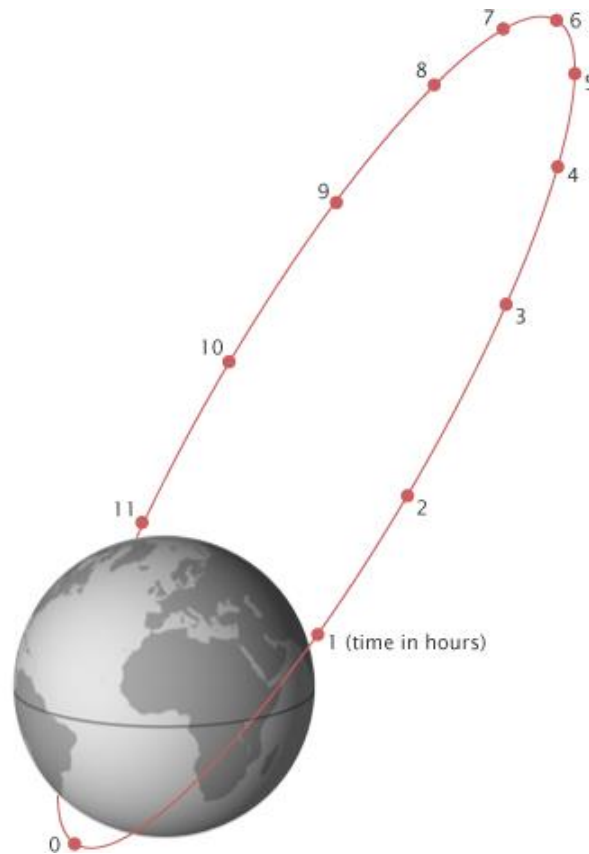


Figure 1.7 The Molniya orbit diagram illustrating orbital positions of the satellite with time (Nasa Earth Observatory, 2011)

As much of the former Soviet Union's territory was located at high latitudes, it was impractical to broadcast to those latitudes from a geostationary orbit due to the low elevation angles. Hence, the then Soviet space scientists devised the Molniya orbit, which was named after a series of communications satellites by the same name, which have been using this type of orbit since the mid-1960s

Molniya orbit is a highly elliptical orbit with an inclination of 63.4 degrees. Its argument of perigee is -90 degrees and its orbital period is one half of a sidereal day. As such, it is a special type of Semi (Geo) Synchronous Orbit.

As illustrated in Figure 1.7, a satellite in this highly eccentric orbit spends most of its time in the neighbourhood of apogee. The sub-satellite point at apogee for a

Molniya orbit satellite is at a latitude of 63.4 degrees North, therefore it spends most of its time in the high latitudes of the Northern hemisphere,.

Furthermore, as the apogee altitude is a very high 40,000 km, the orbit has an excellent visibility of the Northern hemisphere, including the former Soviet Union, Northern Europe, Greenland Canada and Alaska for a considerable period of time around the apogee. Nevertheless, at least three Molniya spacecraft are needed to get continuous high elevation coverage of the northern hemisphere.

In order to keep the argument of perigee at -90° , not perturbed by the J_2 term of the gravitational field of the Earth, the inclination is computed to have the value of 63.4° . (Nasa Earth Observatory, 2011; Pisacane, 2005)

1.7.4 Geo Stationary Orbit

A Geo Stationary Orbit is a unique geosynchronous orbit which has the Earth's equatorial plane as its orbital plane and is of a circular orbital profile. Therefore its eccentricity is zero and inclination is 0° . A Geo Stationary Orbit has a radius of approximately 42,164 km measured from the centre of the Earth and an altitude of approximately 35,786 km above mean sea level.

A satellite in Geo Stationary Orbit remains in the same position relative to the Earth's surface and hence it does not exhibit diurnal motion,

Arthur C Clarke is widely credited with proposing the concept of global telecommunications coverage with three satellites positioned at equidistance in the Geo Stationary Orbit, though the idea of Geo Stationary Orbit had been proposed earlier. The Geo Stationary Orbit is also called as “Clarke Orbit” in respect of the science fiction writer.

2.1 Introduction to Ionospheric and Plasmaspheric effects on radio waves

Electromagnetic waves traversing the Ionosphere and the Plasmasphere encounter free, thermal electrons. Changes in the electron density along the signal path and differing dielectric qualities of the ionised plasma impact radio waves in several ways and the resulting effects create many constraints and problems on the quality of communication, navigation, surveying and on ranging applications. The main effects Ionosphere and Plasmasphere impact on radio waves traversing through them are:

- 1) Amplitude and phase scintillation
- 2) Group path delay
- 3) RF carrier phase advance
- 4) Doppler shift of the RF carrier
- 5) Faraday rotation of the plane of linearly polarised waves
- 6) Angular refraction of the wave path
- 7) Distortion of the waveform of the transmitted pulses

Except for the scintillation effect, all the other effects are proportional (at least to the first order) to the Total Electron Content (Basu et al., 1985). The above effects are described briefly below:

2.2 Amplitude and phase scintillation

Distortions in phase and amplitude of radio wave such as fading, phase deviations and angle of arrival variations are called Scintillations. These effects vary with signal

frequency, magnetic and solar activity, time of day, season and latitude. Indices have been developed to quantify the amount of variations in amplitude and phase.

2.2.6 Amplitude scintillation indices

Two indices are being utilised to quantify the intensity of Ionospheric scintillations.

They are:

- 1 S4 Index and
- 2 SI (Scintillation Intensity) Index

The above two indices are generally used in two different scenarios.

The amplitude or the intensity variation is characterised by the variance in the received power and it is equal to the normalised second central moment of signal intensity fluctuations. This is denoted by the S_4 index:

$$S_4 = \sqrt{\frac{\langle I^2 \rangle - \langle I \rangle^2}{\langle I \rangle^2}} \quad 2.1$$

Here the quantity $\langle I^2 \rangle - \langle I \rangle^2$ denotes the variance of the received power and $\langle I \rangle$ denotes the mean value of the received power (Basu et al., 1985; Béniguel, 2011)

The SI (Scintillation Intensity) index is less complex and can be used for data deduced manually from chart records. The formula for the SI index is given by

$$SI = \frac{(P_{\max} - P_{\min})}{(P_{\max} + P_{\min})} \quad 2.2$$

Where P_{\max} is the power level of the third peak down from the maximum excursion of the scintillations and P_{\min} is the level of the third peak up from the minimum excursion, measured in dB.

The S4 index is used more often than the SI index as data can be deduced automatically with computer applications.

2.2.2 Phase scintillation index

The phase scintillation index or the standard deviation of phase fluctuations σ_ϕ can be obtained from:

$$\sigma_\phi = \frac{K}{f^2} \langle \delta N_e^2 \rangle GF(k_N, p_N) \quad 2.3$$

(Basu, 2003)

Where v_{eff} is the effective scan velocity of the propagation path through the irregularities and τ_c is the data interval that corresponds to $1/f_c$, where f_c is the low frequency cut off of the detrend filter.

S4 and σ_ϕ are statistical variables computed over a “reasonable” time period. Here “reasonable time” depends primarily on the effective velocity of the satellite ray path and it may vary from 10 to 100 seconds. Both these quantities are derived from detrended time series to analyze only the fluctuations of the intensity and phase. As mentioned earlier they depend on the density fluctuations in the medium. They can be related to physical parameters through phase screen theory (Rino, 1979).

In S4 calculations, for irregularity scale sizes less than the Fresnel scale F_r , F' has vanishing amplitude and F_r is given by:

$$F_r = \sqrt{2\lambda z} \quad 2.4$$

Where λ is the radio signal wavelength and z is the distance from the observer to the Ionospheric phase screen (~350 km or more). For L1 frequency F_r is typically 300-400

meters; density fluctuations larger than this scale size will not cause GPS amplitude scintillations.

2.2.3 Classification of Scintillations

Scintillations are generally classified into insignificant, weak and strong according to their S_4 values, by the following criteria:

Insignificant:	$S_4 < 0.3$
Weak:	$0.3 < S_4 < 0.6$
Strong:	$S_4 > 0.6$

Some radio astronomy applications may suffer from effects such as image degradation even during insignificant scintillations, ie $S_4 < 0.3$.

2.2.4 Relationship between SI and S_4 indices

$$SI = 27.3 S_4^{1.25} \quad 2.5$$

2.2.5 Frequency dependence of scintillations

The S_4 index shows a frequency dependence of $f^{-1.5}$ over the frequency range 100 MHz – 3000 MHz, where f is the frequency of the signal being transmitted.

2.3 Group Delay or Group Path Delay

The additional time delay, over the free space transit time of a signal transmitted from above the Ionosphere to earth's surface is given by

$$\Delta t = \frac{40.3}{cf^2} \times TEC(s) \quad 2.6$$

Where $TEC(s)$ is the slant total electron content, c is the speed of light and f^2 is the frequency of the signal (Basu et al., 1985; Klobuchar et al., 1973).

For a system operating at 1GHz, a TEC value of 10^{18} would make a time delay of 134ns and a range error of 40.2 m. For low frequency systems, the impact is very severe. A 100 MHz system would produce a time delay of 13.4 ms and a range error of more than 4 km, under the same TEC circumstances.

The following graph illustrates the variation of Time Delay with frequency for various values of TEC:

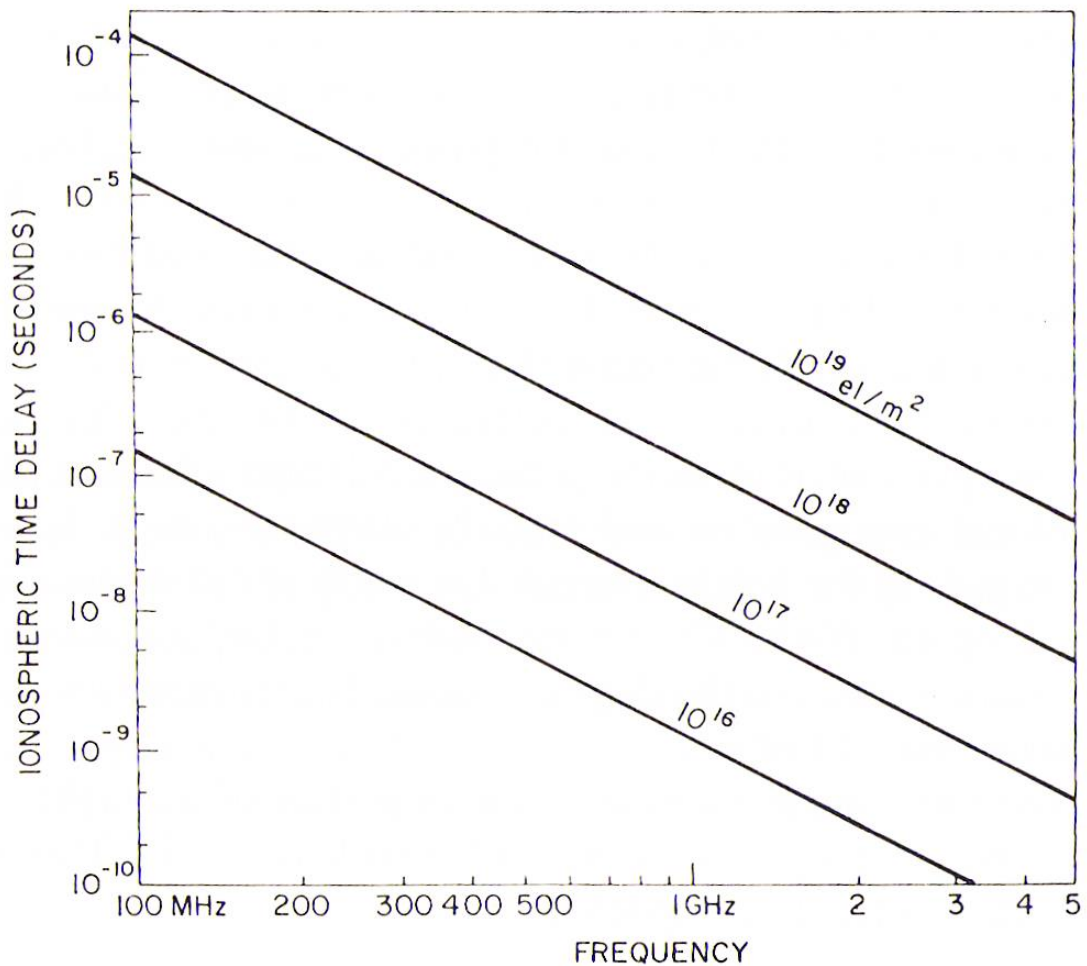


Figure 2.1 Variation of Time Delay with frequency for various values of TEC (Basu et al., 1985: p10-84)

2.4 RF Carrier Phase Advance

The phase of the carrier of the radio wave is advanced by the Ionosphere/Plasmasphere system when compared to a free space transmission. This effect is called the RF Carrier Phase Advance and is extremely critical in determining the velocity of the space objects by way of range rate measurements.

The phase increase is given by;

$$\Delta\phi = \frac{1.34 \times 10^{-7}}{f} \times TEC(\text{cycles}) \quad 2.7$$

Where TEC total electron content and f is the frequency of the signal (Basu et al., 1985)

2.4.1 Differential carrier phase

GNSS satellites transmit two coherently- derived carrier frequencies for differential carrier phase measurements. These are in addition to the dual frequency identical modulations transmitted.

For GPS frequencies L1 and L2, the differential carrier phase shift, referenced to the lower frequency is

$$\Delta\phi = \frac{1.34 \times 10^{-7}}{L_2} \times \frac{(m^2 - 1)}{m^2} TEC(\text{cycles}) \quad 2.8$$

Where $m = f_1 / f_2 = 1.2833$, $\Delta\phi = 4.31 \times 10^{-17} \times TEC$ or $2.32 \times 10^{16} \text{ el} / m^2$ per complete 2π cycles of differential carrier phase between L1 and L2, measured at L2.

2.4.2 Second difference of carrier phase

The second difference in phase between an RF carrier and that of its upper and lower sidebands can be used to measure absolute values of TEC.

For three coherently derived frequencies, $f - f_m$, f , $f + f_m$, the transmitted second difference of phase is:

$$\Delta_2\phi = (\phi_U - \phi_C) - (\phi_C - \phi_L) = (\phi_U - \phi_L) - 2 \times \phi_C \quad 2.9$$

From 2.7

$$\Delta_2\phi = \frac{2.68 \times 10^{-7}}{f(f^2 - f_m^2)} f_m^2 \times TEC(\text{cycles}) \quad 2.10$$

When

$$f^2 \gg f_m^2$$

$$\Delta_2\phi = \frac{2.68 \times 10^{-7}}{f^3} f_m^2 \times TEC(\text{cycles}) \quad 2.11$$

[1]

2.5 Doppler Shift

The changing TEC in the path of the wave propagation adds to geometric Doppler Shift.

This effect is caused as the frequency of any signal is the time derivative of its phase.

The Doppler shift component due to the changing TEC is given by:

$$\Delta f = \frac{d\phi}{dt} = \frac{1.34 \times 10^{-7}}{f} \frac{d}{dt} TEC \text{ (Hz)} \quad 2.12$$

Even though electron density variations along the signal path create Doppler shifts, the results are not significant. For high orbit satellites, where the diurnal changes in TEC are greater than geometric ones, the upper limit to the rate of change of TEC is approximately $0.1 \times 10^{16} \text{ el.m}^{-2}.\text{s}^{-1}$. This results in an additional frequency shift of less than 0.1 Hz for 1.6GHz and for 400MHz the figure will be 0.3 Hz.

2.6 Faraday Polarization Rotation

A linearly polarised radio wave that is traversing the ionosphere, undergoes rotation of the plane of polarization and it is called the Faraday polarization rotation. The TEC value can be deduced from the amount of Faraday polarization rotation undergoes while traversing the Ionosphere and the technique has long been used in measurement of TEC.

In high-frequency and quasi-longitudinal approximations, the two magneto-ionic modes are nearly circularly polarized in opposite senses. A plane polarized wave traversing an ionised dielectric media such as the Ionosphere can be regarded as the vector sum of its ordinary and extraordinary components. But these two components travel at different phase velocities and as a result the plane of polarization rotates continually along the signal's path. This rotation is called the Faraday Polarization Rotation.

The total rotation from the signal source to the observer is related to the total electron content by the expression:

$$\Omega = \frac{2.36 \times 10^{-5}}{f^2} \int B \cdot \cos \theta \cdot N_e dl \quad 2.13$$

Where B is the local magnetic field flux density in gammas, θ is the angle between the radio wave normal and the magnetic field direction. Thus $B.\cos\theta.N_e$ represents the product of electron density times the longitudinal component of the earth's magnetic field integrated along the signal path (Basu et al., 1985; Gorman and Soicher, 1973).

As the longitudinal magnetic field density changes much slower than the electron density of the Ionosphere, the equation can be approximated to:

$$\Omega = \frac{K}{f^2} B_L \times TEC \quad 2.14$$

Where $B_L = B.\cos\theta$ and is taken at the mean Ionospheric height, $K = 2.36 \times 10^{-5}$.

One very important note about the Faraday rotation technique in determining the TEC value is that the technique does not give out a value that is representative of the entire distance traversed by the radio wave. This is because, the term $B.\cos\theta.N_e$, which represents the product of electron density times the longitudinal component of the earth's magnetic field becomes insignificant in heights above the Ionosphere, becomes insignificant above Ionospheric altitudes, since B decreases inversely with the cube of the geocentric distance, and the electron density decreases exponentially with altitude above this region. Therefore, the integral is heavily weighted in near space altitudes and the Faraday rotation technique is considered to provide TEC values at altitudes below 1200 km only (Gorman and Soicher, 1973).

The following graph gives values of Faraday polarization rotation against frequency for Northern mid latitude station for different values of TEC.

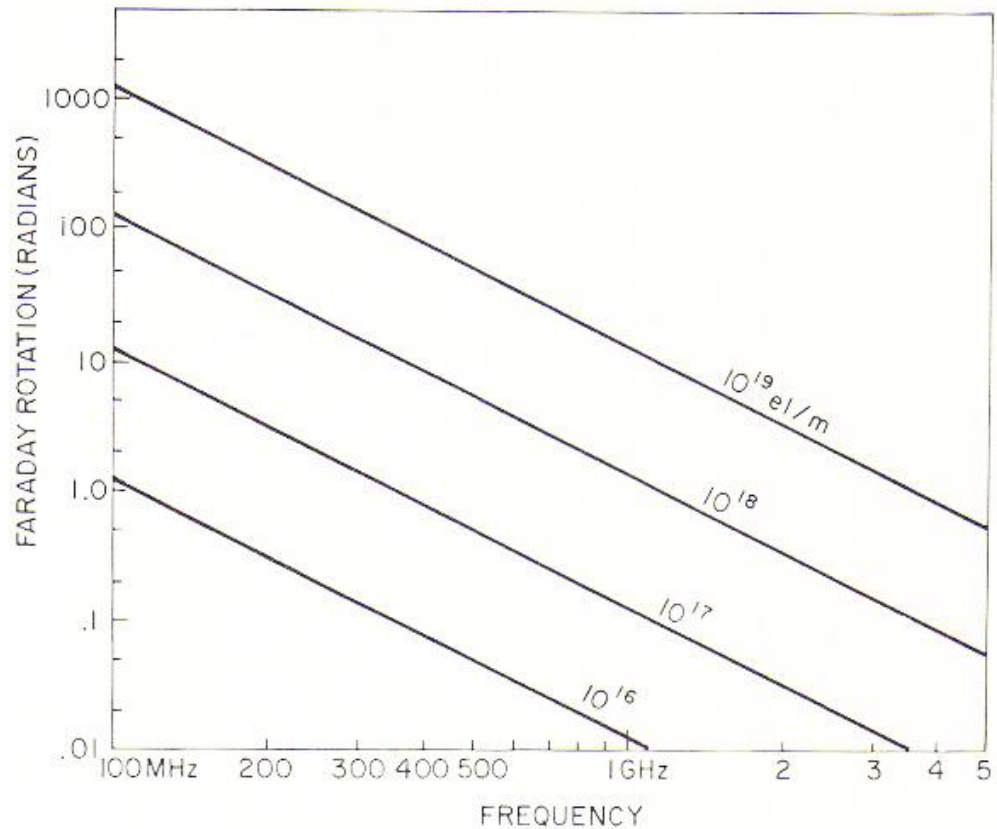


Figure 2.2 Variation of Faraday Rotation with frequency for various values of TEC at a northern mid latitude station: (Basu et al., 1985: p10-87)

From the figure 2.2 at a nominal commercial satellite transponder frequency band of 4GHz, the resulting Faraday rotation is around 0.1 rad and this figure is well above what is required for dual, linear orthogonal channel separation.

Faraday rotation is a major hindrance in satellite communication as the receiver gets a polarization rotation of nearly an odd integral multiple of 90° resulting in no signal received at the receiver's linearly polarised antenna. As a result, the receiver antenna needs to be realigned to obtain maximum received signal.

Circular polarization techniques are used to overcome Faraday rotation problem, but at the cost of received signal power.

2.8 Angular Refraction

Electromagnetic waves entering the Ionosphere get bent as in the optics. The refractive index of the ionosphere produces angular refraction increasing the path length the signal ray takes from the satellite to the receiver. The resulting range error is given by:

$$\Delta E = \frac{R + r_0 \sin E_0 (r_0 \cos E_0)}{h_i (2r_0 + h_i) + r_0^2 \sin E_0} \times \frac{\Delta R}{R} \quad 2.15$$

Where: E_0 is the apparent elevation angle, R is the apparent range, r_0 is the radius of the Earth and h_i is the Centroid of the TEC distribution, normally between 300 km and 400 km.

The ΔR quantity is calculated from $\Delta R = (40.3 / f^2) \times TEC$

Chapter 3 : Mission Overviews – ATS-6, Cluster II, Double Star, and C-NOFS

In this chapter, brief introduction is given to four missions; ATS-6 (1974), Cluster II (2000), Double Star (2004) and C-NOFS (2008), which have relevance to this research. They are presented in the chronological order of their launching and effort has been taken to briefly outline their experiments relating to electron density profiles and/or TEC.

3.1 Applications Technology Satellite-6 (ATS-6)

ATS-6 was a NASA experimental satellite launched in May, 1974 and decommissioned in July 1979. Along with scientific experiments, the mission also had other purposes including telecommunications, Air Traffic Control testing, satellite assisted search and rescue, pioneering direct TV broadcasting and broadcasting educational programmes. It was the most powerful telecommunication satellite in orbit at the time of its launch. It was also the first 3-axis stabilized spacecraft in geostationary orbit and was the first to use electric propulsion in geostationary orbit with success. The mission carried out 23 experiments, which included particle physics experiments. The first heavy ion detection in geostationary orbit was achieved by ATS-6. It also carried an experimental radiometer subsequently carried as a standard instrument aboard weather satellites.

The Radio Beacon Experiment (RBE) aboard the ATS-6 offered the first opportunity to the western scientific community to determine the TEC and/or the signal propagation delay to geostationary altitudes. More importantly, the beacon package provided the opportunity to conduct two relevant experiments. The first utilized the Faraday rotation

technique for determination of TEC. The second utilized the dispersive group delay technique which is independent of the magnetic field and determined the TEC to geostationary altitudes. The difference between the values of the integrated electron content obtained by the two techniques yields the content from 1200 km to geostationary altitudes, i.e., the Plasmaspheric electron content. This scenario becomes possible due to the fact that the Faraday rotation technique would yield the TEC value predominantly to the Ionospheric heights, as elaborated in section 2.6.

Gornan, Jr. and Soicher of Communications/Automatic Data Processing Laboratory, U. S. Army Electronics Command (1974) analysed the ATS-6 RBE data to determine the Plasmaspheric TEC and its variations using the difference of results between the above two methods (Gorman and Soicher, 1973). In general, the observed Plasmaspheric content exhibited diurnal as well as day-to-day variations, with its absolute magnitude varying from 1 to 8 TEC units (10^{16} el/m²). During night times, the Plasmaspheric content was nearly always above 50% of the Ionospheric content and on occasions exceeded 100%. During the day, this ratio averaged at 35%.

Gornan, Jr. and Soicher used the abbreviation TEC_p to denote the Plasmaspheric Electron Content in their work. Therefore, the same abbreviation has been in the following sections, which present the methodology used by them and the results obtained.

3.1.1 The methodology employed in determining the Plasmaspheric Electron Content

a) Faraday Rotation Technique

From 2.13, the total rotation from the signal source to the observer is related to the TEC by the expression

$$\Omega = \frac{2.36 \times 10^{-5}}{f^2} \int_0^s B \cdot \cos \theta \cdot N_e ds \quad 3.1$$

$$\Omega = \frac{2.36 \times 10^{-5}}{f^2} \int_0^s B \cdot \cos \theta \cdot \sec \chi N_e dh \quad 3.2$$

Where χ is the angle between the wave normal and the vertical, equal to incident angle.

Fort Monmouth (Monmouth County, New Jersey, US) from where the data were taken is a mid latitude location with coordinates 40.3140° N, 74.0450° W. Therefore the χ angle value will be very significant for a radio wave from a geo stationary satellite such as ATS-6.

As mentioned earlier, the relationship would yield the TEC value predominantly to the Ionospheric heights. The term $B \cdot \cos \theta \cdot \sec \chi$ in the equation 3.2 (denoted by \overline{M}) can be taken out of the integral sign and replaced by its value at a "mean" Ionospheric altitude, h (420 km). This will give:

$$\Omega = \frac{2.36 \times 10^{-5}}{f^2} \overline{M} \int_0^s N_e dh \quad 3.3$$

$$\Omega = \frac{2.36 \times 10^{-5}}{f^2} \overline{M} \times TEC_I \quad 3.4$$

Where TEC_I is the Ionospheric TEC measured by the Faraday rotation technique.

At Fort Monmouth, where the numerical value for was 56292, for 1 TEC unit and for $f = 140$ MHz, Gornan, and Soicher calculated Ω to be equal to 38.83^0 .

b) Dispersive Group Delay Technique

Using the dispersive-group-delay technique, the phase of the modulation envelope between a carrier and its sideband was compared at two frequencies

(nominally $f = 140$ and 360 MHz with sideband displacements of $\Delta f = +1$ MHz. As shown earlier, as the phase is insensitive to the earth's magnetic-field, this technique yields the TEC along the entire path from satellite to receiver.

From equation 2.6 for two signals at frequencies f_1 and f_2 , the differential time delay is:

$$\Delta t = \frac{40.3}{c} \left[\frac{1}{f_1^2} - \frac{1}{f_2^2} \right] \times TEC(s) \quad 3.5$$

If the two signals are modulated by a sideband separated by an equal Δf , then the modulation time delay Δt_m is equal to the differential group time delay, i.e.,

$$\Delta t = \Delta t_m = \frac{\Delta \phi}{360} \cdot \frac{1}{\Delta f} \quad 3.6$$

$$\Delta t_m = \frac{\Delta \phi}{360} \cdot \frac{1}{\Delta f} = \frac{40.3}{c} \left[\frac{1}{f_1^2} - \frac{1}{f_2^2} \right] \times TEC(s) \quad 3.7$$

Where $\Delta \phi$ is the differential modulation phase shift in degrees.

From this, it can be written:

$$TEC_G = \frac{\Delta \phi}{360} \cdot \frac{1}{\Delta f} \cdot \frac{c(\sec \chi)^{-1}}{40.3} \left(\frac{1}{f_1^2} - \frac{1}{f_2^2} \right)^{-1} \quad 3.8$$

Where TEC_G is the TEC up to geo-stationary orbit height. At Fort Monmouth for $TEC_G = 10^{16}$, a phase difference of 30.55° was measured.

3.1.2 Results obtained

The results of these measurements were studied by the researchers and plotted graphically. The following graphs presented in the forthcoming pages provide some of the observations:

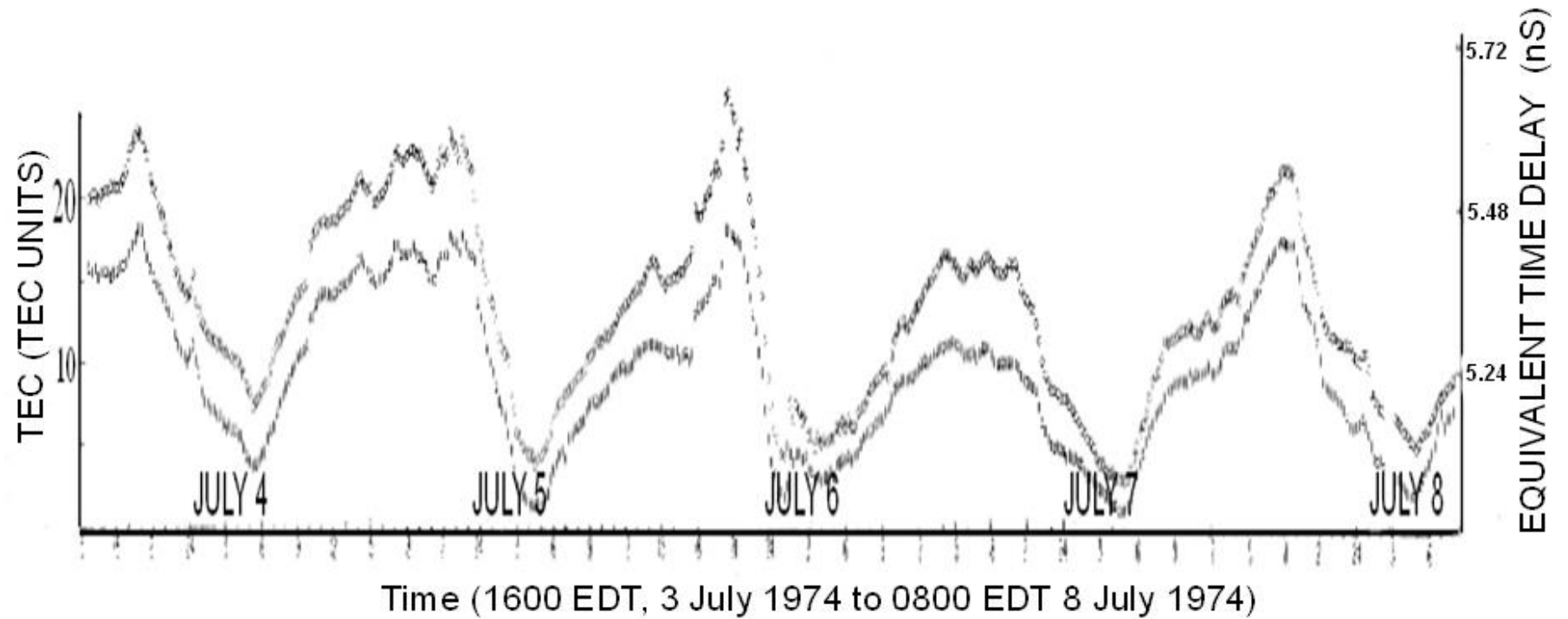


Figure 3.1: Variation of Total Electron Content up to geo-synchronous orbit height and Ionospheric electron content (TEC_G and TEC_I) at 15-minute intervals from 1600 EDT, 3 July 1974 to 0800 EDT 8 July 1974 at Fort Monmouth, NJ, USA. Equivalent time-delays for 1.6 GHz signals are also indicated (Gorman and Soicher, 1973: p448).

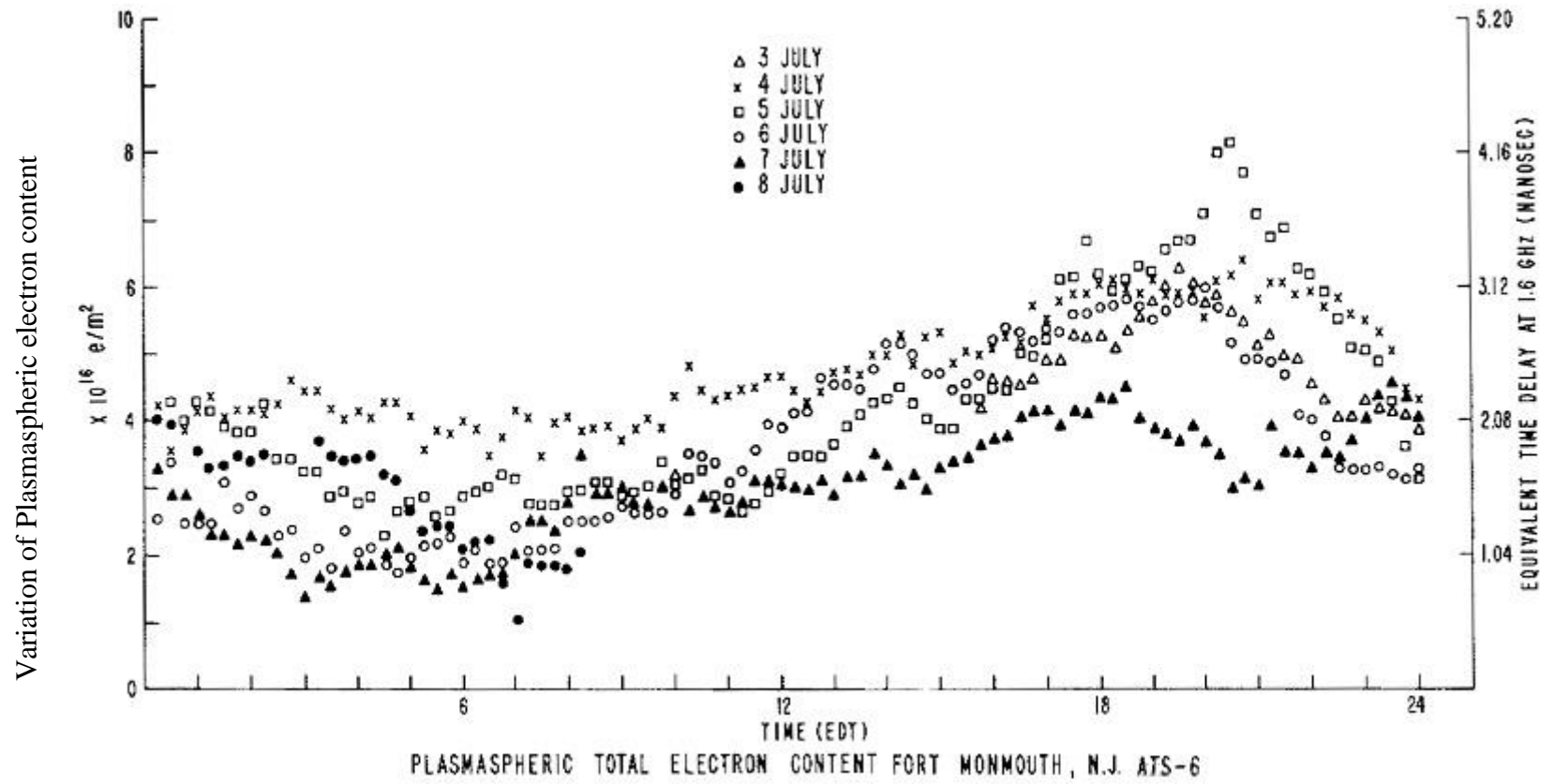


Figure 3.2: Variation of Plasmaspheric electron content (TEC_p) plotted for each day. The figures are from the same data of figure 3.1. The equivalent time delays are marked as well (Gorman and Soicher, 1973: p449).

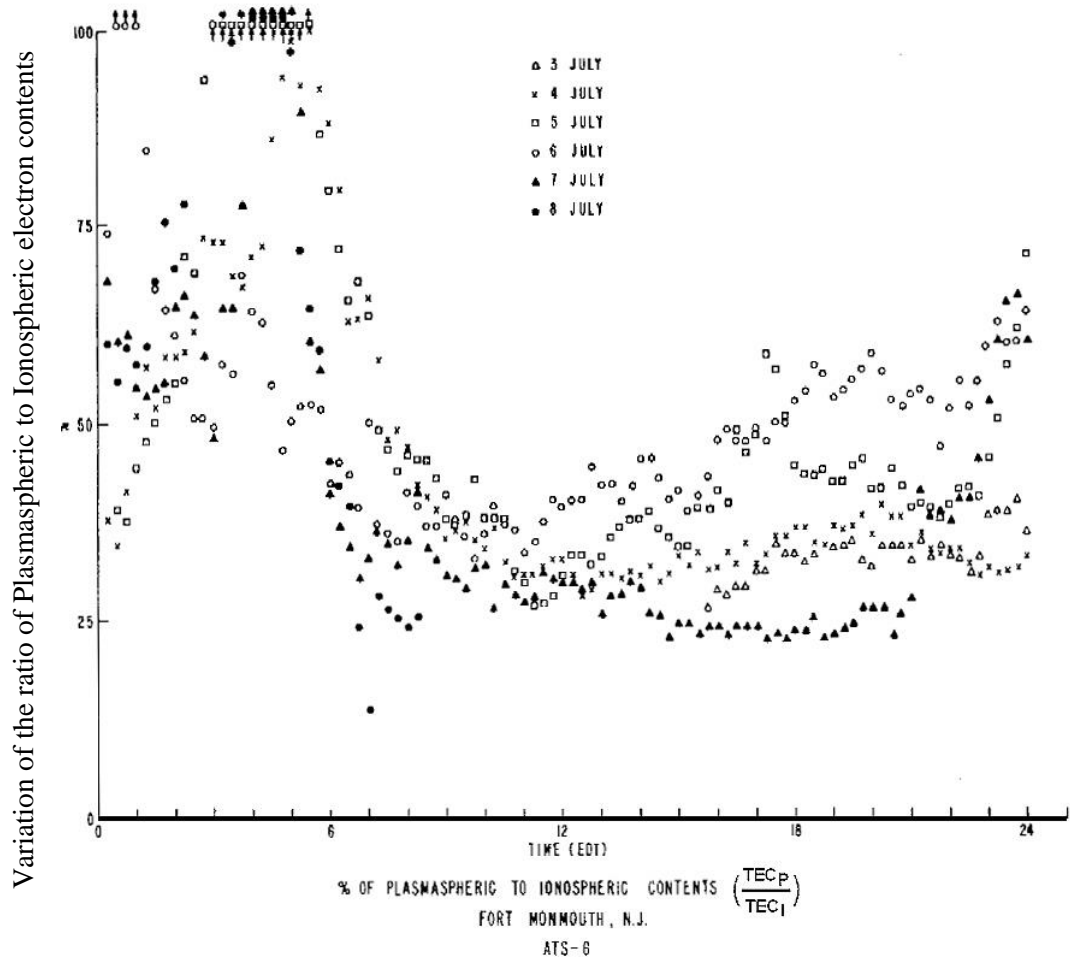


Figure 3.3: Variation of the ratio of Plasmaspheric to Ionospheric electron contents in percentage (Gorman and Soicher, 1973: p450).

$$\left[\frac{TEC_P}{TEC_I} \times 100\% \right]$$

The readings are from the same data as Figures 3.1 and 3.2 and taken in 15 minute intervals.

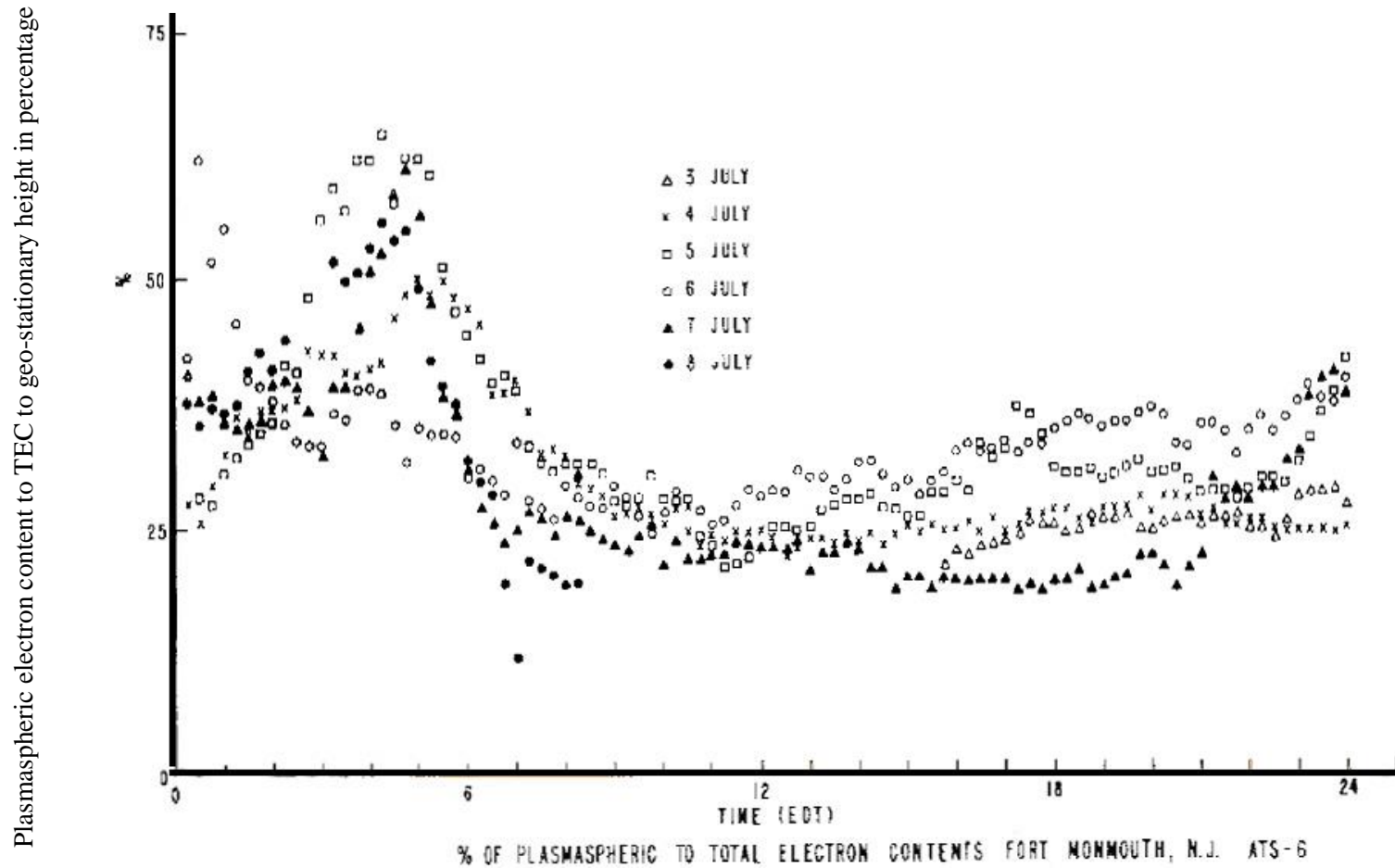


Figure 3.4: Variation of the ratio of Plasmaspheric electron content to Total electron content to geo-stationary height in percentage, ie. $[(TEC_p/TEC_G) \times 100\%]$. (Gorman and Soicher, 1973: p451). The readings are from the same data as Figures 3.1, 3.2 and 3.3 and taken in 15 minute intervals.

3.1.3 Observations

Figure 3.1 shows the variation of the total electron contents measured by the Faraday rotation and group delay techniques, at 15-minute intervals for the time period 1600 EDT on 3 July to 0800 EDT on 8 July. They provide the temporal variations of TEC_I and TEC_G respectively and were seen to be nearly parallel with most density variations observed on both curves.

It is very interesting to note the response to the two solar flares during the time period of observation. The two prominent increases in TEC between 0945 EDT and 1000 EDT on 4 July, were due to the solar flares (Figure 3.1). TEC_I can be seen to be increased by about 1.5 TEC Units, while TEC_G increased by about 2 TEC Units. As the frequency of readings is 15 minutes, the Figure 3.1 is not able to display the fluctuations in a better resolution. As a result, the full increase of TEC_I and TEC_G are not displayed. Starting at 0953 EDT, TEC_I can be seen to be increased by about 3.3 TEC Units in 3 minutes and then decaying to its previous value at 1000 EDT. TEC_G can also be seen to increase by approximately the same amount, at the same time.

On 5 July between 1730 EDT and 1745 EDT, TEC_I increased by about 1.9 TEC Units, while TEC_G increased by 2.3 TEC Units. The rapid increases can be seen starting at 1740 EDT with TEC_I increasing by 2.1 TEC Units in 6 minutes. TEC_G displays a similar increase.

It can be noticed that the equivalent signal-delay time corresponding to the VTEC distribution at 1.6 GHz (in the navigation frequency band) was always below 15 nanoseconds for the time period analysed. The following observations can also be made regarding the time delay:

- 1 On different days, the time delay varied by as much as 60% between the maximum and minimum on any one day and the largest was 12.
- 2 Superimposed on the normal diurnal variations of the content were quasi-sinusoidal variations which usually occur near the time period of maximum TEC in the daily cycle.
- 3 Mostly, these variations were caused by Ionospheric irregularities.

As illustrated earlier, the dispersive-group-delay technique measures the TEC from the receiver to the satellite (TEC_G), whereas the Faraday rotation technique yields the TEC only up to the Ionosphere (TEC_I). Therefore, the difference between the two yields the Plasmaspheric Electron Content (TEC_p).

Hence:

$$TEC_G - TEC_I = TEC_p \quad 3.9$$

The Figure 3.2 exhibits the variation of TEC_p for the same time intervals and for the same time period as that of Figure 3.1. It could be seen that the Plasmaspheric content (TEC_p) ranged from 1 to 8 TEC units, or equivalently from about 0.5 to over 4 nanoseconds for a 1.6 GHz signal.

It could be generalised for this Figure that the minimum of the Plasmaspheric content (TEC_p) occurred close to Ionospheric sunrise while its maximum occurred close Ionospheric sunset. It is also noticeable that during any single day, the diurnal variation was not as pronounced as the corresponding variation of the total or Ionospheric electron contents (TEC_G or TEC_I). The maximum variation, by a factor of

3.4, could be observed on 5 July. This is compared to a TEC_G variation by a factor of 12 for the same day. The day-to-day variability exhibited changes of up to 300% during comparable local time periods, for example on 4 and 7 July during night time hours.

Figure 3.3 displays the ratio of Plasmaspheric to the Ionospheric electron content, ie. $[(TEC_P/TEC_I) \times 100\%]$. The measure is of great importance to the applicability of global time delay models based on TEC data obtained by the Faraday rotation technique, as it is of the same magnitude as the variation of the ratio of Plasmaspheric to the Ionospheric time delays.

From the Figure 3.3 in could be seen that this ratio shows a diurnal as well as a day-to-day variability. Throughout the observation period, the ratio was nearly always above 50% and on occasions exceeded 100% between 0100 and 0700 EDT. After this time-period, the ratio decreased to its minimum at around 1100 EDT, after when it increased with the time of day. From 0700-0100 EDT, the average ratio increased from a round 30% to around 40 %.

A similar ratio analysis, with the ratio of the Plasmaspheric to the Total electron content up to the geo-stationary height, ie. $[(TEC_P/TEC_G) \times 100\%]$, is provided in Figure 3.4. This ratio would also give the same quantity in ratio between the time-delays due to free electrons along the signal's path along the two heights too. The diurnal and day-to-day variability of this ratio can be observed to be similar to that of (TEC_P/TEC_I) . During the night the ratio is seen to be high, reaching a value up to 70%. During the day, the ratio was much lower, averaging from about 25 % to 30%.

3.1.4 Conclusions

The researchers (F. J. Gornan, Jr. and H. Soicher) concluded that the group path delay of a navigation signal due to free electrons in the Plasmasphere cannot be neglected when it is compared to the delay due to the Ionosphere. They also concluded that the Group path delay prediction models based on Faraday rotation data alone would not adequately compensate for the total delay; at night, they may be differing by more than 50%, and during the day by an average of about 35%. This is in addition to other prediction errors, i.e., differences between observed and predicted values of the delay times. Furthermore, they opined that the Ionospheric Faraday rotation prediction models cannot be corrected by adding a constant offset to account for the Plasmaspheric delay, since the Plasmaspheric content exhibited a diurnal and day-to-day variation. Fortunately, the highest ratio of Plasmaspheric-to-Ionospheric delay time occurs at night, when the total delay time is relatively small.

As this research was carried out in 1974, the above conclusions can be termed as being in the early stages of understanding of the Plasmaspheric Electron Content analysis. The present state of knowledge in the sector has progressed substantially and the behaviour of Plasmaspheric Electron Content has been analysed in much more detail. Even then, the results obtained in the study are much more relevant and they provide absolute values for the TEC_P , its variation and the fractional values relative to TEC_I and TEC_G .

The researchers also commented on future developments with regard to ratios of Plasmaspheric-to-Ionospheric delays from future data at other geographic locations under condition different from the mid-latitude station (Fort Monmouth) and under different conditions unlike the quiet phase of the solar cycle this set of data was taken from. During such a phase and at such a location, it is obvious that the group delay

values are generally small. They noted that it remains to be seen if the observed ratios will be maintained when delay times will be large, such as during the maximum phase of the solar cycle and if such ratios are maintained during the maximum of the cycle, neglecting the Plasmaspheric content will cause errors exceeding the accuracy requirement of the system. They opined that the future modelling schemes should yield corrections within the accuracy requirements of the proposed navigation systems.

One very important drawback of this analysis is that the Fort Monmouth station is a mid-latitude station and a radio signal from a geo-stationary satellite makes a very large incident angle. The suitability of using a thin layer Ionospheric model in calculations and the resulting accuracy is debatable.

Moreover, the resulting TEC values cannot be treated as vertical TEC values for the mid latitude station as most of the Plasmaspheric regions the radio wave would be traversing would be above near equatorial regions, which exhibit very high electron density values than mid latitude regions.

Nevertheless, the resulting percentages and ratios are well in conformity with the prevailing knowledge about Plasmaspheric electron content behaviour and for that reason this premier research and its finding are imperative.

3.2 The Cluster Mission

Cluster is a constellation of four spacecraft flying in a tetrahedron formation around the Earth in closely formed synchronous polar orbits. The main objective of the European Space Agency program with NASA participation Cluster II programme is to study the small-scale spatial and temporal characteristics of the Magnetospheric and near-Earth solar wind plasma over the course of an entire solar cycle. .

The tetrahedron formation facilitates the three-dimensional data collection of how the solar wind interacts with the Magnetosphere and affects near-Earth space, including Aurorae. The four Cluster spacecraft have accumulated more than 17 years of data passing in and out of the Earth's Magnetosphere, since their launch in July-August 2000. Cluster II is one of the longest serving missions in the history of human space exploration.

Cluster mission was first proposed in November 1982 and approved in 1986 to study the 'cusp' and the 'Magnetotail' regions of the Earth's magnetosphere with a polar orbiting mission. Along with the Solar and Heliospheric Observatory (SOHO) program, the two missions were cornerstones of the ESA's Solar Terrestrial Physics Horizon 2000 missions programme.

The original Cluster spacecraft were destroyed in the explosion of the Ariane 5 rocket's first launch in 1996. The Cluster II is the follow up mission consisting of one spacecraft built from the spare parts of the initial program and three newly built spacecraft launched in two Soyuz rockets. The mission has now been extended until 2019.

3.2.1 Orbital parameters

The Cluster II spacecraft were launched in highly elliptical adjacent polar orbits with a Perigee of 19000 km and an apogee of 119000 km. The spacecraft had an orbital period of 57 hours. The spacecraft are now orbiting with much reduced perigee and apogee values.

3.2.2 The experiments

The table below lists the experiments of the Cluster mission, their acronyms and a brief description:

No.	Experiment	Description
1	FGM	Fluxgate Magnetometer
2	EDI	Electron Drift Instrument
3	ASPOC	Active Spacecraft Potential Control experiment
4	STAFF	Spatio-Temporal Analysis of Field Fluctuation experiment
5	EFW	Electric Field and Wave experiment
6	DWP	Digital Wave Processing experiment
7	WHISPER	Waves of High frequency and Sounder for Probing of Electron density by Relaxation experiment
8	WBD	Wide Band Data instrument
9	PEACE	Plasma Electron And Current Experiment
10	CIS	Cluster Ion Spectrometry experiment>
11	RAPID	Research with Adaptive Particle Imaging Detectors
12	WEC	Wave Experiment Consortium (DWP, EFW, STAFF, WBD, and WHISPER)

Table 3.1: List of Cluster II Experiments (ESA, 2014)

3.3 Double Star Mission

The Chinese National Space Administration – ESA joint program Double Star was a continuation of the Cluster II program and it consisted of two satellites, one in equatorial orbit (TC1) and another in polar orbit (TC2). Primary aim of the mission was to investigate the Sun's effects on the near space. The general region of interest was the

Magnetosphere with the Earth's Magnetotail region, where electrically charged particles (mainly ions and electrons) are accelerated towards the planet's magnetic poles by reconnection, being of special focus. The satellite had fifteen instruments, seven of which were identical to the instruments on the four Cluster II spacecraft. Another eight experiments were provided by Chinese institutes.

3.3.1 Orbital parameters and significance of the mission

TC-1 was launched on a highly elliptical orbit, with a very low perigee and a very high apogee. During its mission time, the orbital parameters had been changed continuously and varied significantly, enabling the scientific community to study various combinations of space weather parameters.

Just after the launch, the orbit of TC-1 had a perigee of 580 km and apogee of 78952 km, (corresponding to an apogee/perigee of $13.37 R_E/1.09 R_E$.) an inclination angle of 28.2° degrees to the equator and a orbital period of enabling TC1 to investigate the Earth's Magnetic tail and the sunward boundary between the Magnetosphere and the solar wind. The polar orbital satellite TC-2 had a perigee of 682 km, an apogee of 38279 km (corresponding to an apogee/perigee of $7.01 R_E/1.09 R_E$) and an orbital period of 11.7 hours.

This orbital arrangement enabled the sampling the polar cap and cusp regions, the primary regions where energy from the Sun flows into the Magnetosphere. Its instruments concentrated on the physical processes taking place over the magnetic poles and the development of auroras (ESA, 2013; Woolliscroft et al., 1997)

The Double Star mission was conceived to operate in conjunction with the Cluster II mission. Its orbits had been designed as such, so that their Magnetic Local Times (MLT) of apogee would be aligned with each other and with those of the four

Cluster II satellites during the summer of 2004, when all six spacecraft would have had their apogee in the Magnetotail.

The polar orbiting Cluster II and TC-2 spacecraft would maintain this coordinated phasing, but the MLT of apogee of TC-1 would drift apart from the other spacecraft. The NASA's Polar spacecraft's MLT of apogee was similar to these and as such could be phase locked with Cluster II.

This particular orbital coordination would provide a unique three point observation point opportunity involving a six spacecraft constellation (if the four Cluster II satellites are treated as a single observation point, albeit with special small-scale multi-point measurement capabilities), well suited to simultaneously examining Magnetotail processes both close to and far from the Earth.

Similarly it would also allow examining the dayside cusps at multi points while also making measurements at the low latitude Magnetopause. Thus, this unique constellation would be capable of making observations with which the drivers of global scale Magnetospheric processes could be examined.

The trough of data could be used in conjunction with the other active upstream monitors, Auroral and ring current imaging satellites, and sophisticated ground based Ionospheric monitors to provide detailed supporting observations of the global context.

A particular advantage of the Cluster II-Double Star combination is that, as mentioned above and would be detailed later, several Double Star instruments, including the PEACE instrument are identical or near identical copies of the Cluster II instrumentation, which helps in carrying out comparative data analysis studies.

The project had been rather cost-effective as significant parts of the infrastructure (operational and for science data dissemination and analysis) developed for Cluster II could be readily adapted for Double Star (Fazakerley et al., 2005).

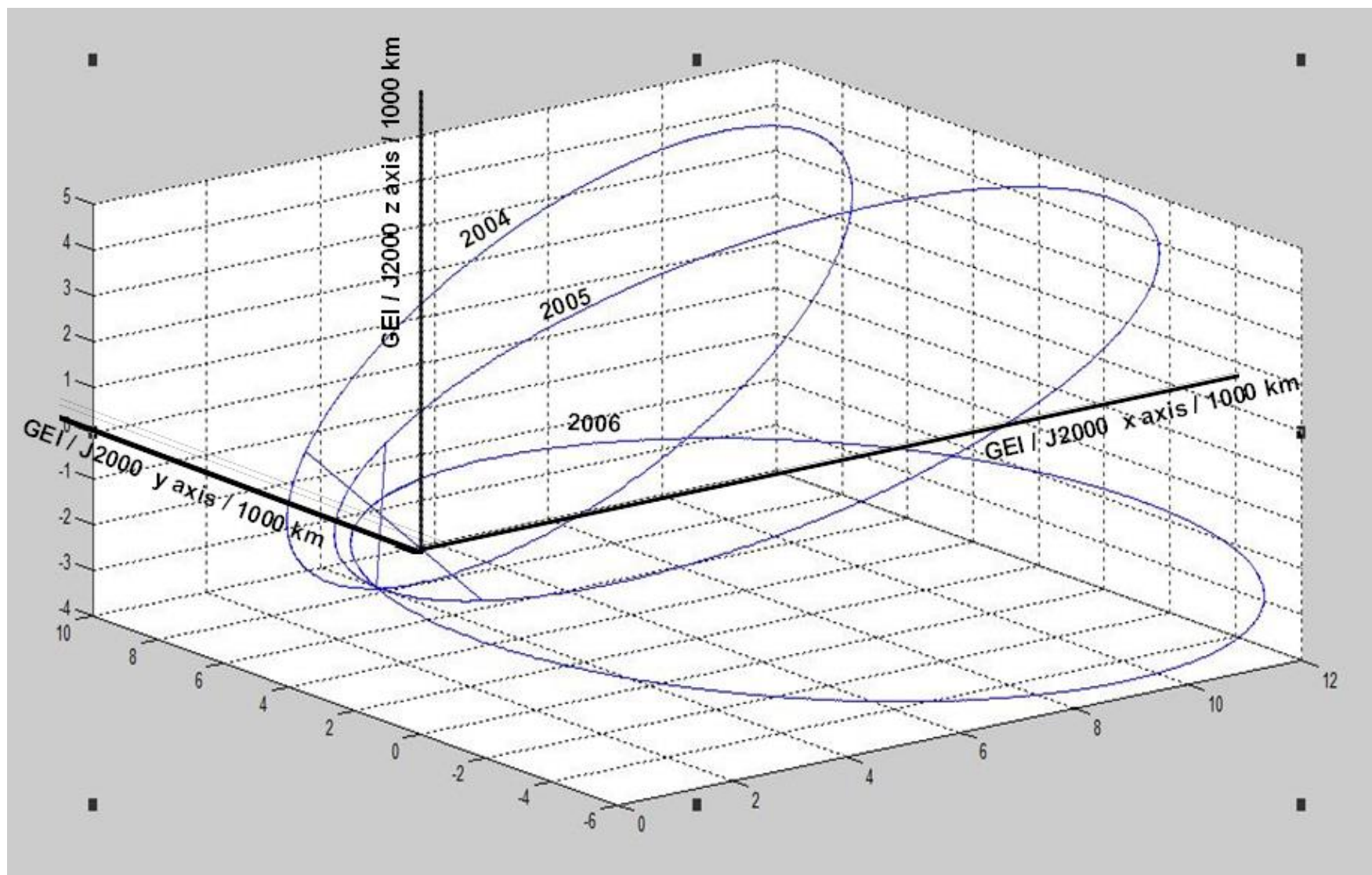


Figure 3.5 Orbital plots of Double Star TC-1 spacecraft in three different dates in 2004, 2005 and 2006

Out of the two spacecraft, the Equatorial space craft TC1 is of relevance to this research. Of the instruments, PEACE, STAFF and DWP of the Wave Experiment Consortium (WEC) deal with electron density in the space and as such the data analysed here are from those instruments. Therefore, it is of importance to analyse the instruments in details.

3.3.2.1 Plasma Electron and Current Experiment - PEACE

3.3.2.1.1 The Instrument

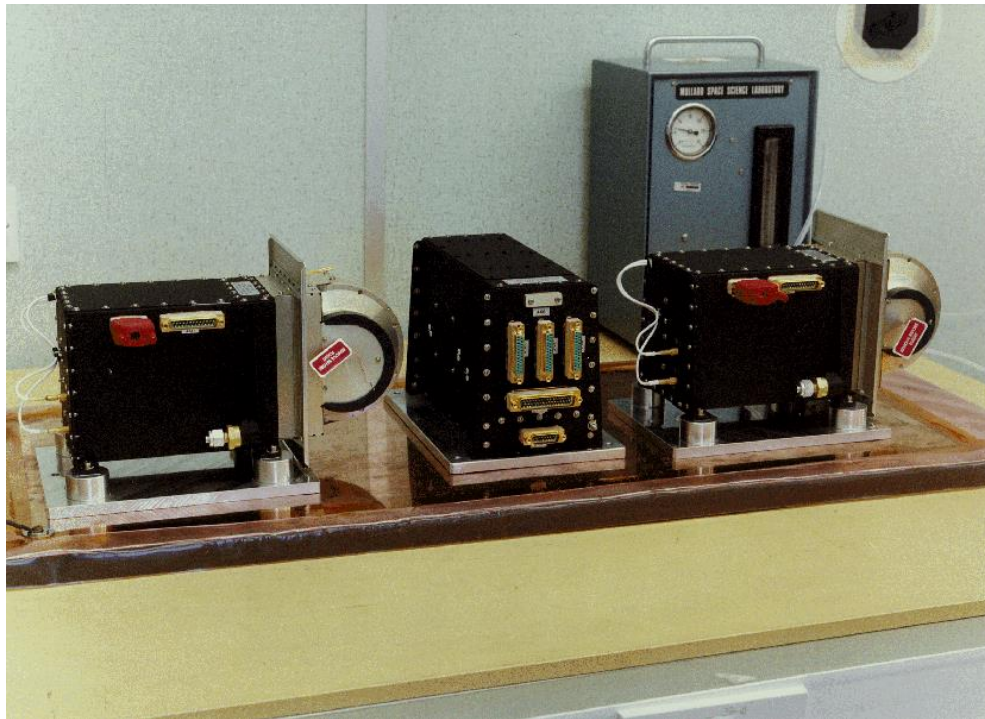


Figure 3.6: PEACE FM07 Instrument in MSSL Clean Room (MSSL, 2000)

The objective of the PEACE instrument is to measure the distribution function of the electrons as accurately and frequently as possible and to provide the data at the best resolution that the spacecraft telemetry will allow (Johnstone et al., 1997). The measurements are used to analyse the nature and causes of acceleration, scattering, and diffusion of electrons.

The PEACE instrument consists of two sensors with hemispherical electrostatic energy analysers. They contain position-sensitive microchannel plate detectors positioned to scan radially on opposite sides of the spacecraft (Figure 3.3). Together both sensors can cover the complete angular range in a half spin of the spacecraft. PEACE measures the three-dimensional velocity distribution of electrons in the energy range from 0.59 eV to 26.4 keV in 88 levels. The first 16 energy levels are equally spaced linearly. (Range from 0.59 eV to 9.45 eV). The rest of levels are equally spaced logarithmically. (Factor of 1.165 over the rest of the range).

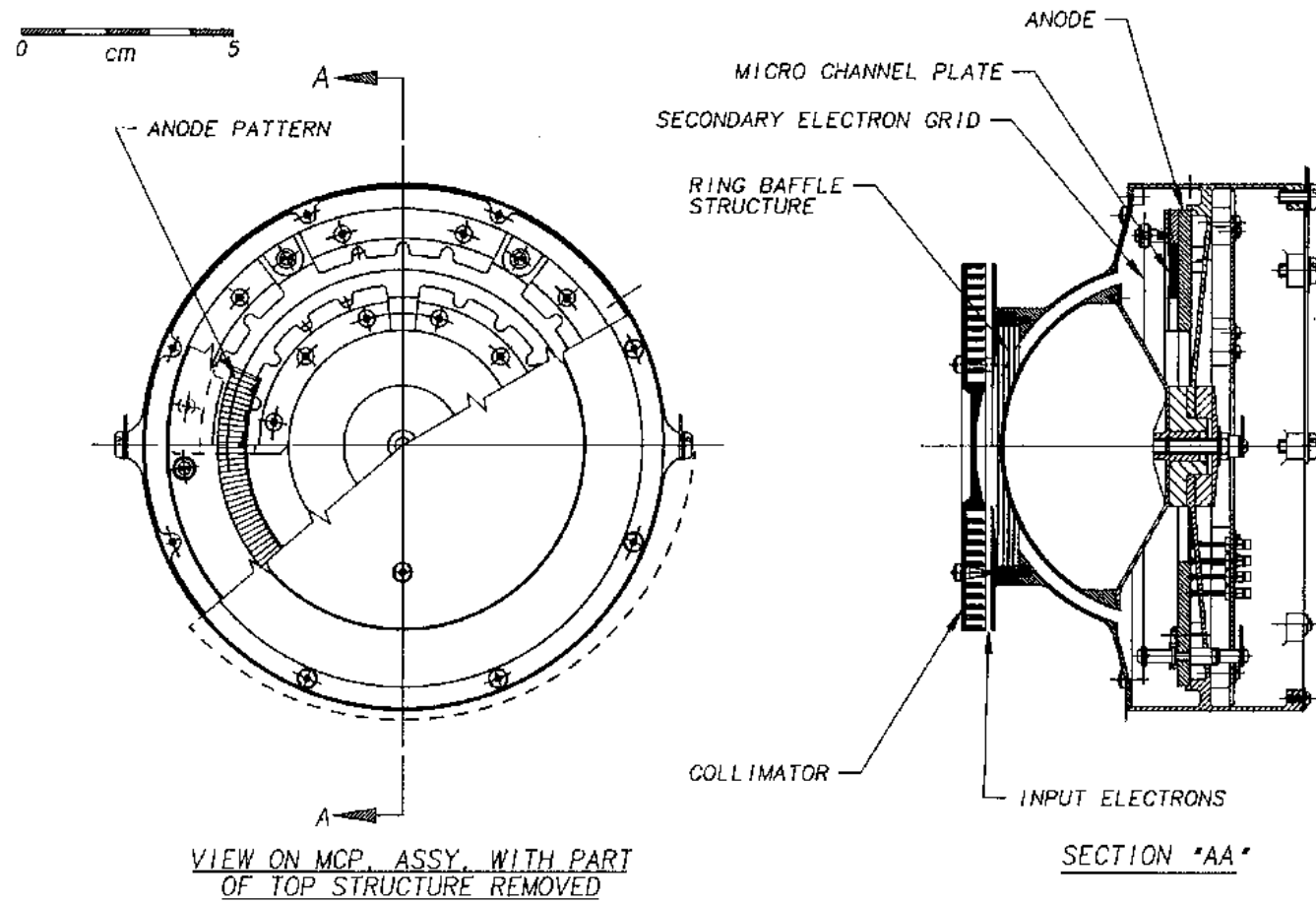


Figure 3.7. A cross-section of the LEEA analyser showing the structure of the input collimator, the electrostatic analyser and the anode pattern (Johnstone et al., 1997: p. 357)

3.3.2.1.2 Resolutions:

Intrinsic energy resolutions: 12.7% and 16.5% full width at half maximum.

Angular resolutions: 2.8° and 5.3 ° in an azimuthal direction

15 ° in a polar direction.

3.3.2.1.3 Operation

A voltage applied to the inner hemispherical plate sets the acceptance energy of the detector. The direction of arrival of the electron is determined from the position at which the electron strikes the detector. This is in relation to the meridian plane of the spacecraft. Both sensors can cover the full energy range from 0.59 eV to 26.4 keV but, the main difference between them is in their geometric factor.

3.3.2.2 The Low Energy Electron Analyser (LEEA):

The Low Energy Electron Analyser (LEEA) has been designed to specialise in coverage of the very lowest electron energies (0.59 eV–9.45 eV). It has the smaller (by a factor 4) geometric factor appropriate for the high fluxes to be found at low energy.

This is achieved by reducing the field of view at the entrance collimator, and reducing the size of the input aperture, which also help to improve the performance for the measurement of low energy electrons.

3.3.2.3 The High Energy Electron Analyser (HEEA):

The High Energy Electron Analyser (HEEA) measures the upper end of the electron energy spectrum. It has a larger geometric factor. This extends the dynamic range of the combination of sensors.

The pair of sensors are mounted opposite to each other on the spacecraft so that together they cover the complete angular range in a half rotation of the spacecraft (Johnstone et al., 1997)

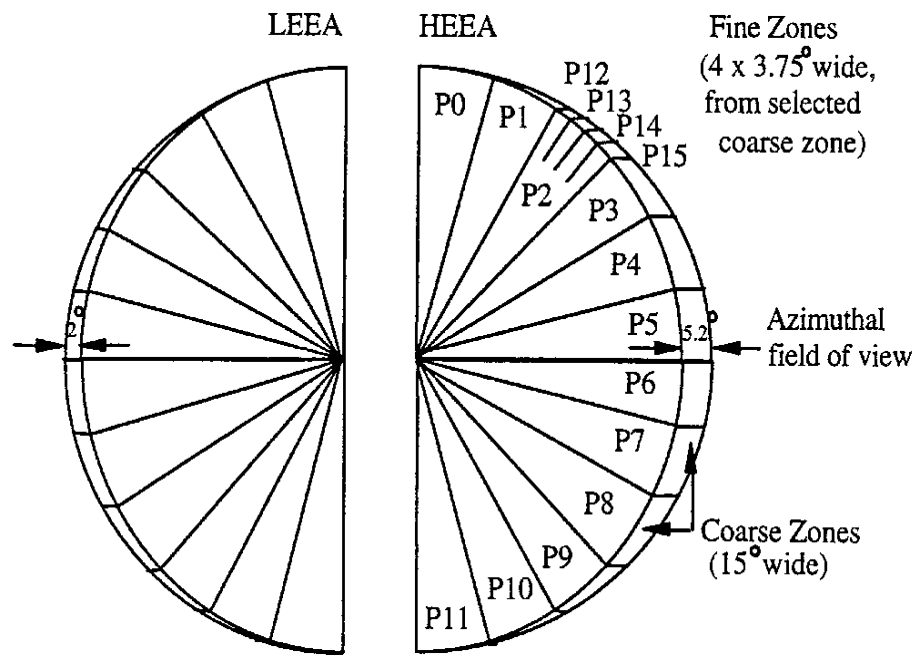
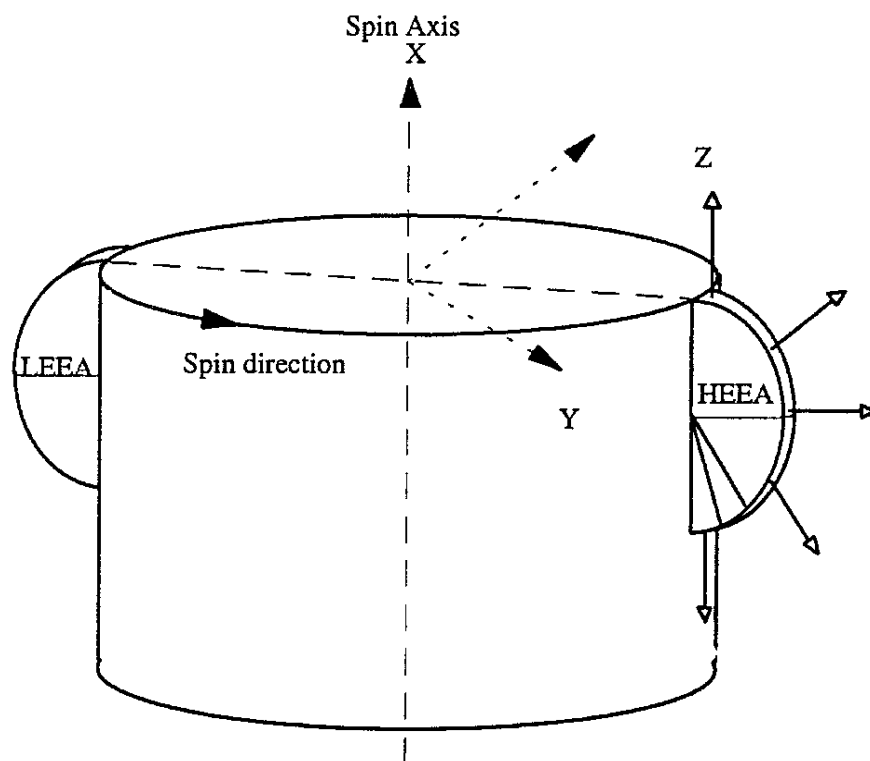


Figure 3.8 LEEA HEEA Sweep (Johnstone et al., 1997: p366)



Both HEEA and LEEA observe perpendicular to spacecraft spin axis with 180 degrees polar fans (Look direction range illustrated for HEEA)

Figure 3.9 LEEA HEEA sweeps and spin axis (Johnstone et al., 1997: p.374)

The sweep rate of the PEACE instrument is synchronized to the spin period of the space craft to ensure an integral number of sweeps during each spin. The starting point for the spin is controlled by varying the delay between the Sun pulse from the spacecraft and the initiation of the spin in the instrument.

The instrument can operate in four sweep modes. Their purpose is to vary the azimuthal angular resolution of the instrument:

- 1) Low Angular Resolution LAR; energy range 60 levels; 16 sweeps/spin; 22.5° resolution.
- 2) Medium Angular Resolution MAR; energy range 60 levels; 32 sweeps/spin; 11.25° resolution.
- 3) High Angular Resolution HAR: energy range 30 levels; 64 sweeps/spin; 5.625° resolution.
- 4) Fixed Energy FE; a constant energy for as long as required for energies up to 1800 eV.

Both sensors can use all four sweep modes and they can operate in different sweep modes, or start from different levels simultaneously.

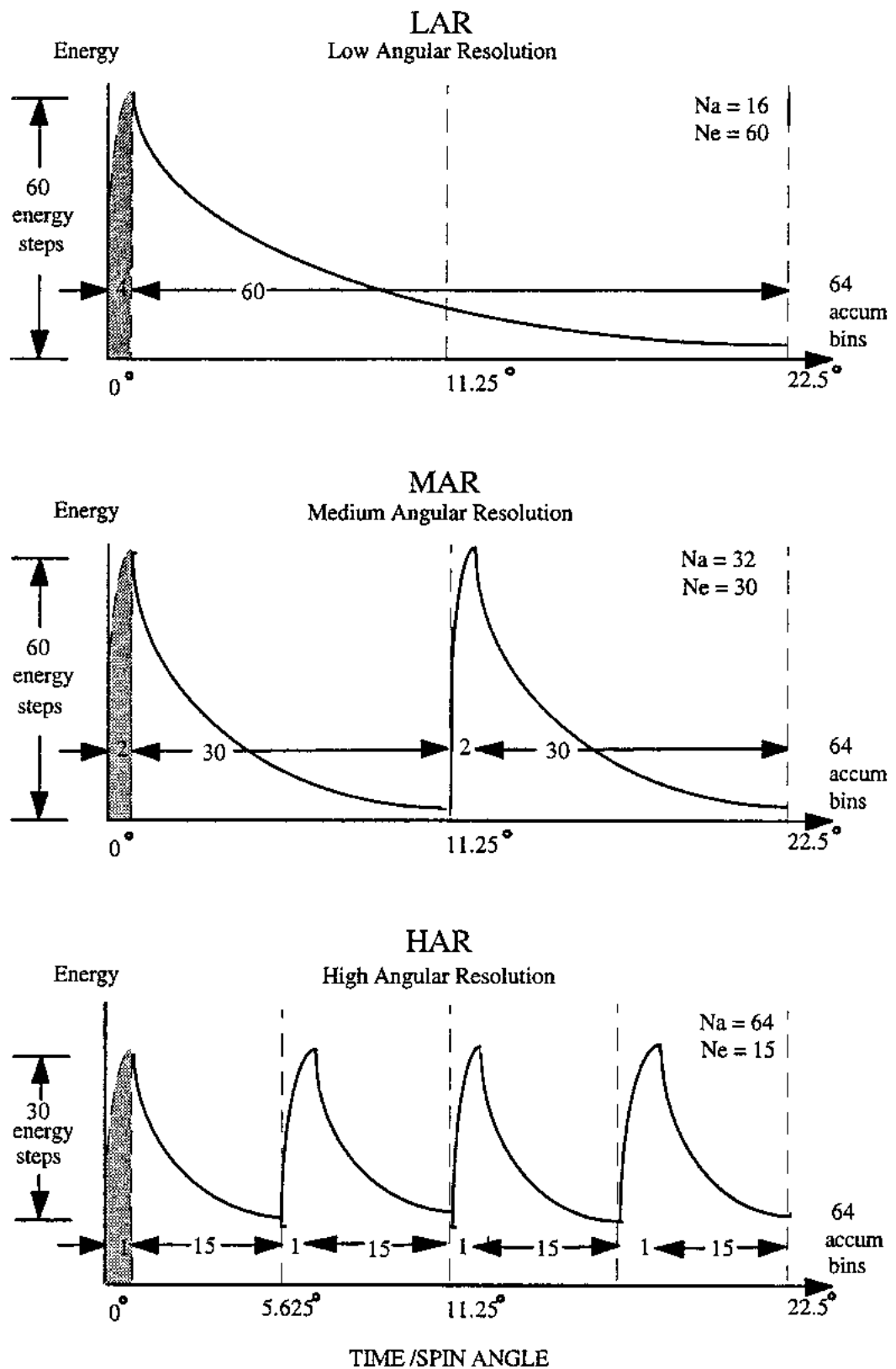


Figure 3.10 LAR MAR HAR ENERGY TIME SPIN ANGLE (Johnstone et al., 1997:

3.3.2.4 DWP Instrumentation

The Digital Wave Processing Experiment (DWP) is a component of the Wave Experiment Consortium (WEC). It is responsible for the coordination of WEC's operations, from providing electrical signals to synchronise instrument sampling to time tagging data in a consistent manner and facilitating complex WEC modes by means of macros.

As constraints on telemetry bandwidth are a major problem for most space instruments, data compression techniques are utilised. The DWP instrument employs the following data compression techniques:

- (a) Particle Correlator – Averaging
- (b) STAFF Search Coil (MWF) – Differential Encoding,
- (c) Wideband instrument – Digital Filtering with Re-sampling,
- (d) WHISPER – Data Selection followed by Pseudo-Logarithmic Compression,

(Woolliscroft et al., 1997)

3.3.2.4.1 The processor module of DWP instrument

The processor of the DWP instrument is a T225 transputer. It has 32 Kbytes of external RAM and the core of the each module is formed by 32 Kbytes of PROM. Each has a HS82C37A DMA controller, event multiplexer and instrument bus interface. In order to increase radiation tolerance, the internal memory is disabled (Woolliscroft et al., 1997).

The DWP instrument has been designed so as to allow the transputers to be operated at input clock frequencies of 2.5 or 5 MHz. This lower range enables less power consumption. The system architecture of the instrument utilises 16 bit microprocessor architecture, again to reduce power consumption. Higher order systems

such 32 bit architectures require more power. This is facilitated from the fact that fewer RAM and ROM chips are accessed in one cycle in a 16bit system, reducing power consumption. Most other instruments too use a 16-bit data length.

3.3.2.4.2 Time resolution

Accurate timing of data is of paramount importance in the study of polarizations and phases of wave information. On the other hand, the transducers (antennas) can measure wave field parameters over all frequencies of interest.

Data acquired by the on-board data-handling system are timed with an accuracy of ± 2 ms with respect to UTC for each spacecraft. The accuracy of comparing data from two spacecraft is of the order of ± 4 ms. The accuracy within the DWP more sharper as the time differences can be measured to a few microseconds. This is achieved by comparing the time stamp of the active edge of the DWP 900 Hz clock with the spacecraft reset pulse, using a transputer timer to a precision of 1 μ s. But the interrupt latency of the transputer plays a major part on the accuracy of individual measurements (Woolliscroft et al., 1997)

3.3.2.4.3 Particle correlator

The Particle Correlator processing system within the DWP instrument performs particle correlations, which facilitates the study of wave/particle interactions.

Particle correlation is based on forming autocorrelation functions of the time series of particle detector counts as a function of energy and pitch angle. The basic operations are carried out by the DWP resident software (Buckley et al., 2001)

The particle correlator operation facilitates the following two results:

- (i) The ability to detect bursts of particle flux on shorter time scales short compared to the energy and dwell time
- (ii) The ability to identify wave/particle interactions occurring regions of velocity space (Woolliscroft et al., 1997)

3.3.2.4.4 Operation of the Particle correlator

The DWP Particle Correlator takes raw electron detection pulses from the PEACE instrument and performs Auto-Correlation Functions (ACFs). The operation for the Particle Correlator is a three stage process:

Stage 1: The Particle Correlator gets a series of pulses as input from the PEACE HEEA electron sensor via the PEACE-to-DWP Inter Experiment Link (IEL), representing the number of individual electrons striking the sensor.

Stage 2: The number of pulses is calculated in 12 μs discrete time intervals by the algorithm, forming a time series of counts over a particular energy interval.

Stage 3: These time series are put through the ACF algorithm implemented by the DWP, producing the summed ACFs (Buckley et al., 2000; Buckley et al., 2001)

The ACF would reveal any probable modulations in the electron population over that particular energy range and short time particle bursts in the electron population as an indicator of wave-particle interactions. The ACFs are constructed in 1 of 15 Correlator electron contiguous energy bands which correspond to either two or four PEACE energy levels, irrespective of the PEACE energy sweeping rate. Thus structure holds the frequency information but the phase information is lost.

The data products from the Double Star Particle Correlator are different from the Cluster II structure. This will be analysed later in the Double Star section.

The ACFs are performed over 8 lags including the zero lag. The lag time of $45\ \mu\text{s}$ gives modulation frequencies up to 11.1 kHz. There are two data rates; High and normal. At normal rate the summation period is one spin (4s) and at high rate it is 1/32 spin. The data rate is constrained by the transmitting the summed ACF at two selected energy levels in a summation period and a third ACF that is stepped in energy once per summation period. This is repeated through the other 13 levels.

Therefore, the two selected energies are covered with a time resolution of 4 s in normal data rate mode, and the other energies have a time resolution of 52 s. In high data rate these periods are correspondingly 0.125 s and 1.625 s (Woolliscroft et al., 1997).

3.3.2.5 The Spatio-Temporal Analysis of Field Fluctuations (STAFF)

3.3.2.5.1 Objectives and the instrument structure

A part of the WEC, the main objective of the STAFF experiment is to characterise the waves and associated turbulence.

The STAFF instrument consists of a boom-mounted three-axis search coil magnetometer, a digital spectrum analyser and an on-board signal-processing unit. The three-axis search coil magnetometer can measure magnetic field fluctuations at frequencies up to 4 kHz and the latter permits the observation of the three magnetic waveforms up to either 10 Hz or 180 Hz, depending upon mode.

The STAFF instruments have a dynamic range of about 96 dB in both waveform and spectral power. This range allows the study of waves near plasma boundaries (Cornilleau-Wehrlin et al., 1997)

Chapter 4 : TEC modelling and Scintillation modelling

Several models have been developed for the Ionosphere and the Plasmasphere, for local electron density distribution and the resulting TEC and scintillation variations for diurnal, seasonal, locational and solar activity variations. As some of the earlier attempts become obsolete due to advances in scientific knowledge and due to the availability of modern tools, newer models using bigger empirical datasets and advanced algorithms have come into place. Still, the modelling efforts concerning TEC and scintillation behaviours in a global scale are far from being complete. In this section, the most important models are presented briefly.

4.1 International Reference Ionosphere (IRI)

4.1.1 Brief Description:

The International Reference Ionosphere (IRI) is an international project, sponsored by the Committee on Space Research (COSPAR) and the International Union of Radio Science (URSI). These organizations formed a Working Group in the late sixties to produce an empirical standard model for the ionosphere, based on all available data sources. Up to now, several enhanced versions of the model have been released. For a given location, time and date, IRI provides monthly averages of the electron density, electron temperature, ion temperature, and ion composition in the altitude range from 50 km to 2000 km. Additionally, parameters provided by the IRI include the TEC, (for which a user can select the starting and ending height of the integral), the occurrence probability for Spread-F and the equatorial vertical ion drift.

Worldwide network of ionosondes, powerful incoherent scatter radars (Jicamarca, Arecibo, Millstone Hill, Malvern, St. Santin), the ISIS and Alouette

topside sounders and the in-situ instruments on several satellites and rockets are the main data sources for the IRI (Kenpankho et al., 2011).

4.1.2 Parameters:

Electron density, electron temperature, ion temperature, ion composition (O^+ , H^+ , He^+ , NO^+ , O^+_{2}), ion drift, Ionospheric electron content (TEC), F1 and spread-F probability

4.2 Global Ionospheric Scintillation Model (GISM)

The Global Ionospheric Scintillation Model generates estimations for both the mean errors and scintillations due to propagation through ionosphere. This model has been accepted by the International Telecommunications Union (ITU) as a reference code for scintillations evaluations.

Amplitude and phase signal fluctuations are the result of propagation through ionosphere electron density irregularities. These signal fluctuations may occur specially during equinoxes, after sunset and last for a few hours. They are more intense during periods of high solar activity. These fluctuations result in signal degradation from VHF up to C band. They may affect several applications as navigation systems, communications, remote sensing and earth observation systems. Two global regions are impacted by such events: equatorial regions (-20° to $+20^\circ$ magnetic latitude) and polar regions ($> 60^\circ$). Scintillations are more intense at the equator and the resulting characteristics are different between these two regions.

GISM allows assessing both the mean effects and the scintillations for propagation through ionosphere for any locations of transmitter and receiver. Two sub models are involved. The first one provides the mean errors. It is based on a resolution

of Haselgrove equations. The second one provides the scintillation effects. It is based on the resolution of a parabolic equation.

The electron density in the ionosphere at any given time and location, which is a required input for both sub models, is provided by the NeQuick model. The NeQuick model has been developed by the Universities of Graz and Trieste. Inputs for the NeQuick model are the solar flux number, the year, the day of the year and the local time. NeQuick is used as a subroutine in the GISM model.

The line of sight is determined by resolution of Haselgrove equations. Mean errors are subsequently provided for Range error, Angular error and Faraday rotation. The scintillations are then calculated using a split step technique based on Fast Fourier Transform calculations (Béniguel, 2011; IEEE, 2011).

4.2.1 Scintillation fluctuations

The signal fluctuations, referred as scintillations, are created by random fluctuations of the medium's refractive index, which are caused by inhomogeneities inside the ionosphere. These inhomogeneities (or bubbles), or more generally the turbulences, develop under several deionization instability processes. These processes start after sunset when the sun ionization drops to zero, consequently at night time. To produce signal scintillation, the bubbles sizes should be below a typical dimension (typically one km) such that the diffracting pattern is inside the first Fresnel zone. The Fresnel zone dimension also depends on the distance from the Ionospheric Pierce Point (usually defined at about 350 km height) to the receiver and on the frequency.

The Global Ionospheric Propagation Model (GISM aims to calculate these effects, in particular:

1. The Line of sight errors

2. The Faraday rotation effect on polarization: being an anisotropic medium, ionosphere layers will impact a linear polarized wave by rotating its polarization plane.
3. The propagation Delay: the ranging error is proportional to the TEC and to the inverse square of the frequency.
4. The scintillation effects: phase and amplitude scintillations, shorter correlation distances with respect to space, time and frequency, cycle slips, loss of lock.

GISM model uses the Multiple Phase Screen technique (MPS). With this technique, the medium is divided into successive layers, each of them acting as a phase screen. The locations and altitudes of both the transmitter and the receiver are arbitrary. The link can consequently go through the entire ionosphere or through a small part of it. The whole calculation for one particular link is composed of two steps:

1. The calculation of the Line Of Sight (LOS)
2. The calculation of scintillations

The calculation of the Line of sight is done using a ray technique. GISM uses the NeQuick model to provide the value of the electron density inside ionosphere required at any time and location. At the end of this calculation the LOS errors, the Faraday rotation and the delays are calculated.

The LOS being determined, the scintillations are then calculated. To do this, at each screen location along the line of sight, the parabolic equation (PE) is solved. This calculation requires the knowledge of the medium statistical characteristics. They are defined with respect to the ionosphere electron density mean value at all points along the LOS.

GISM model estimates the scintillation parameters from the knowledge of the time series at receiver level using the signal intensity and phase and its correlation and structure functions. In case of strong scintillations (typically $S_4 > 0.7$), the phase may exhibit cycle slips with consequences on the receiver phase loop. It may also in that case lead to losses of lock for one or several satellites.

GISM model allows considering either a trajectory described by a list of successive points or a constellation (GPS, Galileo or GLONASS). An orbit generator has been introduced for this capability. The input in that case is the Yuma file. GISM allows considering either links, from a receiver to a satellite or a constellation, or maps (Be'niguel, 2011, Be'niguel and Hamel, 2011).

4.3 Nequick Model

The NeQuick Model gives electron density as a function of height, geographic latitude, geographic longitude, solar activity (specified by the sunspot number or by the 10.7 cm solar radio flux), season (month) and time. It also allows the calculation of electron density along arbitrarily chosen ray paths and the corresponding TEC (IEEE, 2011).

4.4 Other models of interest

Other models of interest include the ITS – 78 Model, the Bent Model, the Ionospheric Communication Analysis and Prediction Program (IONCAP), the Bradley Model and the WBMOD Model.

Chapter 5: Data Extraction from TC1 DWP Correlator

5.1 Double Star Data dissemination structure

The Double Star data products are distributed to the scientific community through the Double Star Science Data System (DSDS) among many other online and offline distribution arrangements. The following diagram illustrates the concept of DSDS.

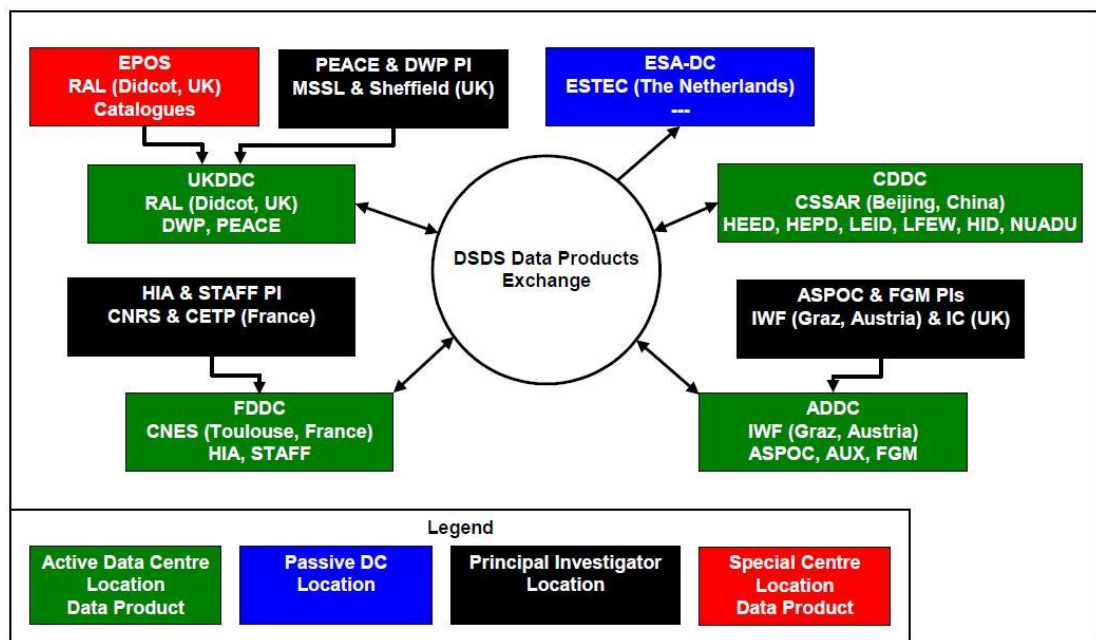


Figure 5.1: The Double Star Science Data System (DSDS) schematic diagram

(Torkar, 2007: p14)

The PEACE and DWP data are sent to and stored in the University of Sheffield and at the Mullard Space Science Laboratory, UCL. These institutions acted as the PI institutions for the PEACE & DWP projects.

Figure 5.2 shows the flow of Level 1 (L1) data from the European Double Star Data System to the European PIs.

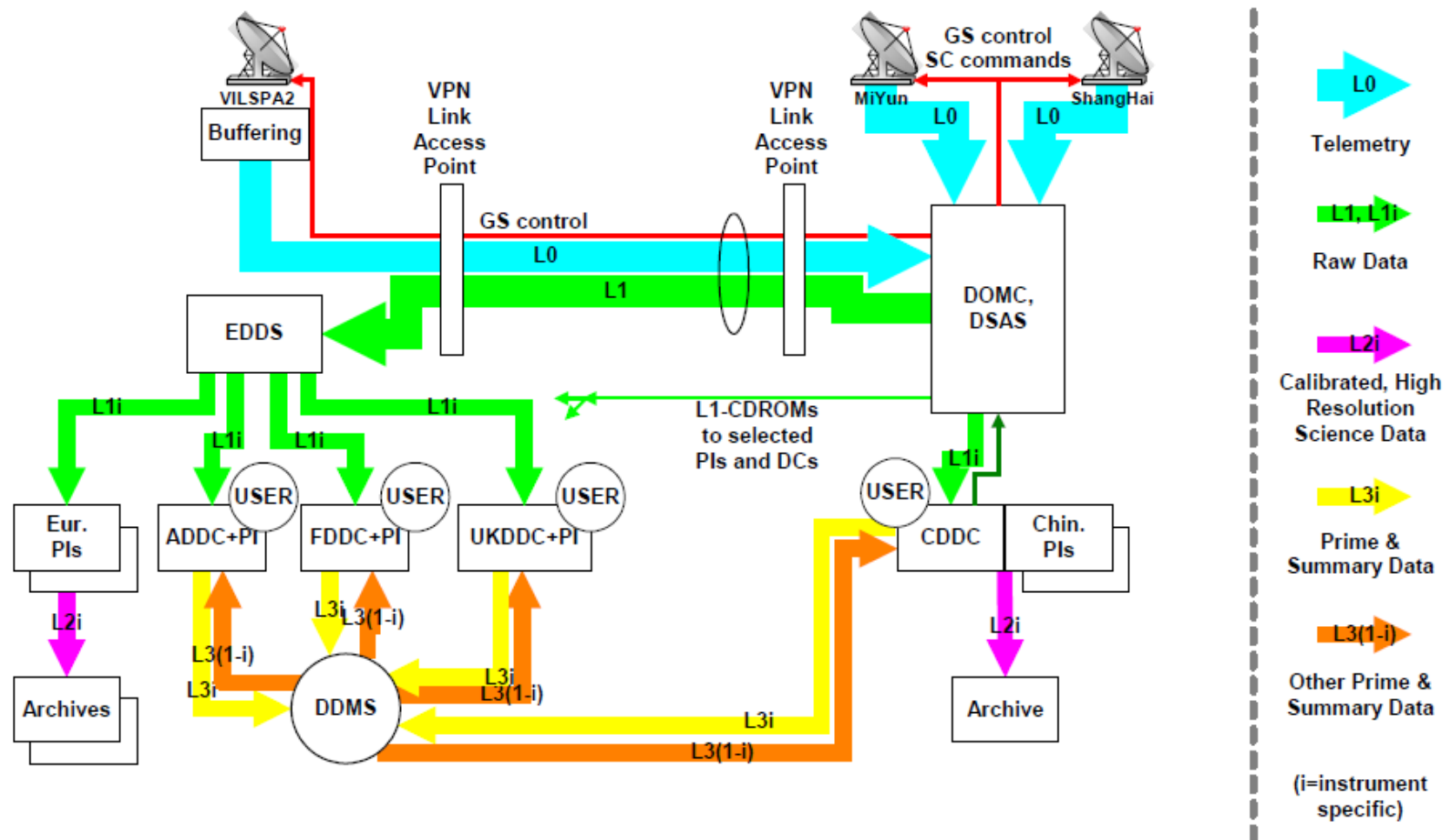


Figure 5.2 Ground data segment of Double Star Project (Torkar, 2007: p13)

5.2 Double Star DWP Level 1 data acquisition

The full level 1 data sets of the entire TC1 mission were downloaded via ftp from the University of Sheffield Double Star Data Archive at hoodie.shef.au.uk. The username, password, the relevant literature and relevant instructions were provided by Dr Andrew Buckley. The level 1 files had been stored under the L1 folder further organised into years, months and days. For each day there was a House Keeping file (hk_file) and a Science file (sci_file) named in the format YYMMDDWH.NA1 and YYMMDDWN.NA1 respectively. Here YY denotes the year, MM denotes the month and DD day of the month.

5.3 Double Star L1 data decommutation

The L1 data was needed to be decommutated in order to get Level 2 ASCII output files, which are readable and would provide useful data. As the PI institution for the project, the University of Sheffield had developed a decommutation program (Yearby et al., 2004) called TLMDECOM.

According to its author, the TLMDECOM is a simple program to decommutate the Double Star STAFF/DWP science telemetry like DECOM (a similar program for decommutating the Cluster II data) does for Cluster. TLMDECOM will also work on Cluster data. The output file may be in 'decom' or DSD format, but some of the fields of the DSD header may not be implemented. TLMDECOM is a C program with two source files `tlmdecom.c` and `tlmproc.c`. The executable `tlmdecom.exe` is compiled to run as a 'console application' (ie. in a DOS window) under Microsoft Windows 9x or XP.

In Linux environments, the program file is generated by:

```
gcc -lm -o <executable file> tlmdecom.c tlmproc.c
```

5.1

The resulting program is used to generate the Level 2 output from the house keeping file , science file combination.

The command syntax is:

```
Tlmdecom hk_file sci_file output_file /f=4 /h=1 /i=n 5.2
```

Where n is 1 for FFT, 2 for MWF normal mode, 3 for MWF burst mode, 5 for correlator.

The /h option controls the output header format. /h=0 outputs ‘decom’ format headers, whilst /h=1 outputs DSD format headers.

For Double Star correlator data only the values /h=2 or /h=3 may also be used for ‘decom’ or ‘DSD’ headers respectively. In that case the data packets are truncated to the Cluster size (the new summed counts and time series are removed) and the correlator mode word adjusted to Cluster format.

The output file is binary and has a header followed by science data as described in the format document and are provided in the following pages.

5.4 Correlator DSD Header definition for DWP

Words	Bytes	Comment
0	0	Software Version
0	1	Software Revision
1	2	Software Patch
1	3	Software User Patch
2	4-5	Spacecraft ID
3	6-7	Ground Station ID
4	8-9	Source Instrument
5	10-11	Diagnostics Word
6	12-13	Length of Science Data
7	14-15	SPRT Year
8	16-17	SPRT Month
9	18-19	SPRT Day of the Month
10	20-21	SPRT Hour
11	22-23	SPRT Minute
12	24-25	SPRT Second
13	26-27	SPRT Millisecond
14	28-29	SPRT Microsecond
15	30	DWP Master Clock Pulse Count
15	31	OBDH Reset Pulse Count (modulus 8)
16	32	UDEF 0
16	33	UDEF 1
17	34-35	DWP Model Tag
18	36-37	PEACE Flybacks per Spin
19	38-39	PEACE Sun Reference Pulse Offset
20	40-41	Correlator Disabled Flag
21	42-43	Correlation Processing Control
22-31	44-63	0

Table 5.1 – TED header format (Sussex Space Science Centre, 2010)

5.5 Correlator science packet format

Unlike the Cluster II DWP correlator, the Double Star correlator could operate in two modes:

Mode 1: The ACF mode which is similar to the Cluster correlator mode, plus the output of two unprocessed time series.

Mode II: The time series only mode where no ACF calculations are performed, but six unprocessed time series are output.

In the ACF mode, the packet descriptor and time tag are followed by two status words and two auto-correlation functions of 15 words each (packet length 34 words including packet descriptor and timetag). The status words contain a count of the number of ACFs that have been summed to make this packet along with mode bits and the PEACE energy level at which the ACF data was taken. Correct selection of the PEACE energy level depends on DWP being correctly informed by the telecommand of the PEACE sweep mode and offset. There is no on board link for this information.

One auto-correlation is calculated at a fixed energy level specified by the instrument processing word. This is referred to as the ‘fixed ACF’. The other is calculated at an energy level that steps through a number of levels, at one step per spin. This is called the ‘stepped ACF’. Each ACF is calculated over 32 lags, and the raw ACF lags are 24 bit integers. Only the zero lags are output directly. For the other 31 lags in each ACF, the minimum value is output as a 24 bit number, then the other lags are output as:

$$(Lag - Minimum) \gg Scale \quad 5.3$$

Where *scale* is the smallest number such that the resulting values are less than 63 and can be stored in 6 bits. The \gg symbol is the ‘shift right’ operator, and ‘ $\gg scale$ ’ means ‘divide by 2 to the power *scale*’. The largest possible value for *scale* is 18 so it can also

be stored as 6 bits. Therefore, there are 32 x 6 bit values which are packed into 12 words. The location of the correlator parameters within the science packet are given in the tables below.

Words	Bytes	Contents
0	0, 1	Packet descriptor (UDEF0 = 0, UDEF1 = 0)
1	2, 3	Time tag for summed ACF data (end of spin/sector)
2 (bits 15..8)	4	Fixed ACF count
2 (bits 7..4)	5 (bits 7..4)	Correlator mode bits (stepped energy limit for DSP)
2 (bits 3..0)	5 (bits 3..0)	Fixed energy level
3 (bits 15..8)	6	Stepped ACF count
3 (bits 5..4)	7 (bits 5..4)	PEACE mode bits (0 = fixed, 1 = LAR, 2 = MAR, 3
3 (bits 3..0)	7 (bits 3..0)	Stepped energy level
4, 5 (bits 7..0)	9, 8, 11	Fixed ACF zero lag, 24 bits
5 (bits 15..8), 6	10, 13, 12	Fixed ACF offset, 24 bits
7..18	14..37	Fixed ACF, scale + 31 lags, 6 bits each
19, 20 (bits	39, 38, 41	Stepped ACF zero lag, 24 bits
20 (bits 15..8),	40, 43, 42	Stepped ACF offset, 24 bits
22..33	44..67	Stepped ACF, scale + 31 lags, 6 bits each
34	68, 69	Fixed energy sum of counts
35	70, 71	Stepped energy sum of counts
36	72, 73	Time tag for time series data selected sweep (end of sweep)
37..53	74..107	1 fixed energy and 1 stepped time series data (compressed)

Table 5.2 ACF + Time Series mode Science packet data structure (Sussex Space Science Centre, 2010)

Words	Bytes	Contents
0	0, 1	Packet descriptor (UDEF0 = 1, UDEF1 = 0)
1	2, 3	Time tag for time series data selected sweep (end of sweep)
2 (bits 13..12)	4 (bits 5..4)	PEACE mode bits (0 = fixed, 1 = LAR, 2 = MAR, 3 = HAR)
2 (bits 11..8)	4 (bits 3..0)	Stepped energy level
2 (bits 7..4)	5 (bits 7..4)	Stepped energy limit
2 (bits 3..0)	5 (bits 3..0)	Fixed energy level
3..53	6..107	3 fixed energy and 3 stepped time series data (compressed)

Table 5.3 Time Series only mode Science packet data structure (Sussex Space Science Centre, 2010)

The compressed time series data has the same format in each case. Each time series contains 62 samples, and each is stored as:

$$(\text{Sample} - \text{Offset}) \gg \text{Scale} \quad 5.4$$

To extract the data it is first necessary to swap the bytes in each word, so for the ACF mode data the bytes should be assembled in the order 75, 74, 77, 76, 79, 78, and so on. Then divide the data into 17 byte blocks (2 in ACF mode, 6 in time series only mode). The first 15 bytes (numbered 0..14) contain the first 60 time series samples, 2 bits each, packed with the first sample in the least significant end of the byte. Byte 15 contains the last two samples in the least significant bits, plus the 4 bit offset. Byte 16 contains a 6 bit clock counter in the least significant part of the byte, plus the 2 bit scale.

The clock counter counts DWP master clock cycles from 0 to 35, and may be used to check whether time series are acquired on adjacent clock cycles. This counter is synchronised to the STAFF MWF sampling, with the NBR sample being taken on cycle 0 (TBC), and HBR samples (when active) taken on all odd numbered cycles. No correlator data is taken on clock cycles used for STAFF sampling.

5.6 Extracting the Time Series and the ACFs – ACFTIMESBUILD

(This section is my own work)

A bespoke extractor program was developed by the author of this thesis to extract the header information and the science data from the DWP correlator L2 output file from generated by running the decommutation program TLMDECOM. The program is called ACFTIMESBUILD and it has been developed in C. The code has been provided in annexure I.

The header and science combined data packet is essential in programming the extractor.

The structure of the combined data packet is annexed in annexure II.

The structure of the ACFTIMESBUILD program is detailed below;

- 1 As the input is going to be a level 1 file, a file pointer *fplv1 is declared
- 2 Two 84 word long arrays {p[84] and q[84]} are declared for storing the contents of the data packet.
- 3 As the time is given in hour, minute, second, millisecond and microsecond, it needs to be built in a suitable format. As millisecond resolution is sufficient, the time is built in milliseconds. A variable is declared for time in millisecond and initiated at timems = 0.

- 4 Six variables are declared for Fixed ACF count, Correlator mode bits, Fixed Energy level, Stepped ACF count, PEACE mode bits and Stepped energy level.
- 5 Variables are declared for the Offset, Scale and the 62 Fixed energy Time series.
- 6 Similarly variables are declared for the Offset, Scale and the 62 Stepped energy Time series.
- 7 Variables are also declared for Fixed energy Zero Lag ACF, Fixed energy ACF Offset, Fixed energy ACF Scale and 31 Fixed energy ACF Lags
- 8 Similarly, variables are also declared for Stepped energy Zero Lag ACF, Stepped Energy ACF Offset, Stepped energy ACF Scale and 31 Stepped energy ACF Lags
- 9 Array q[] is initiated from 0 and incremented.
- 10 Input file is opened and read. The contents stored in q[].
- 11 Array q[] is byte swapped in each word and result is saved in array p[].

```
int m=0;

for (m=0;m<84;m++){
p[m]=(((q[m] & 0xFF) << 8) + ((q[m] & 0xFFFFFFF0) >> 8));
```

Listing 5.1 – Code snippet for byte swapping

- 12 Time is calculated in milliseconds.

```
timems=(p[10]*3600000) + (p[11]*60000) + (p[12]*1000) +
p[13];
```

Listing 5.2 – Code snippet for time calculation in milliseconds

- 13 Fixed ACF count, Correlator mode bits, Fixed Energy level, Stepped ACF count, PEACE mode bits and Stepped energy level are calculated by manipulating bit-wise operators.

WORD	WORD NO. IN HEADER / SCIENCE	BYTE NO. IN HEADER / SCIENCE	CONTENT	BIT NO.	VARIABLE / ARRAY ELEMENT
32	2	5	Fixed Energy level	7 6 5 4 3 2 1 0	p323
			Correlator mode bits (Stepped energy limit for DSP)	7 6 5 4 3 2 1 0	p322
		4	Fixed ACF count	7 6 5 4 3 2 1 0	p321
33	3	7	Stepped energy level	7 6 5 4 3 2 1 0	p333
			PEACE mode bits (0 = fixed, 1 = LAR, 2 = MAR, 3 = HAR)	7 6 5 4 3 2 1 0	p332
		6	Stepped ACF count	7 6 5 4 3 2 1 0	p331

Table 5.4 DWP data Packet snippet for words 32 and 33

```

p321=((p[32] & 0xFF00) >> 8);
p322=(p[32] & 0xF0);
p323=(p[32] & 0xF);

p331=((p[33] & 0xFF00) >> 8);
p332=((p[33] & 0x30) >> 4);
p333=(p[33] & 0xF);

```

Listing 5.3 – Code snippet for the calculation of Fixed ACF count, Correlator mode bits, Fixed Energy level, Stepped ACF count, PEACE mode bits and Stepped energy level.

- 14 Fixed energy offset and scale are calculated by bit-wise operations

WORD	WORD NO. IN HEADER / SCIENCE	BYTE NO. IN HEADER / SCIENCE	CONTENT	BIT NO.	VARIABLE / ARRAY ELEMENT
74	45	88	Fixed energy Time series Sample 60	7 6	s160
			Fixed energy Time series Sample 61	1 0 7 6	s161
			Fixed energy Time series Sample 62	3 2 1 0 7 6	s162
			Fixed energy Time series Offset	5 4 3 2 1 0 7 6	offset1
75	45	91	Fixed energy 6 bit Clock Counter	5 4 3 2 1 0 7 6	
			Fixed energy Time series Scale	5 4 3 2 1 0 7 6	scale1
		90	Stepped energy Time series Sample 1	1 0 7 6	s201
			Stepped energy Time series Sample 2	3 2 1 0 7 6	s202

Table 5.5 DWP data Packet snippet for the Fixed energy ACF Offset and Scale.

```
offset1=((p[74] & 0xF0) >> 4);
scale1=((p[75] & 0xC000) >> 14);
```

Listing 5.4 – Code snippet for fixed energy offset and scale calculation.

- 15 The 62 fixed energy time series are calculated implementing (Sample - Offset) >> Scale and using offset and scale.

WORD	WORD NO. IN HEADER / SCIENCE	BYTE NO. IN HEADER / SCIENCE	CONTENT	BIT NO.	VARIABLE / ARRAY ELEMENT
67	37	75	Fixed energy Time series Sample 1	1 0	s101
			Fixed energy Time series Sample 2	3 2 1 0	s102
			Fixed energy Time series Sample 3	5 4 3 2 1 0	s103
			Fixed energy Time series Sample 4	7 6 5 4 3 2 1 0	s104
		74	Fixed energy Time series Sample 5	1 0	s105
			Fixed energy Time series Sample 6	3 2 1 0	s106
			Fixed energy Time series Sample 7	5 4 3 2 1 0	s107
			Fixed energy Time series Sample 8	6 5 4 3 2 1 0	s108

Table 5.6 DWP data Packet snippet for the first 8 fixed energy time series in word 67.

```

s101=(((p[67] & 0x300) >> 8) + offset1) << scale1);
s102=(((p[67] & 0xC00) >> 10) + offset1) << scale1);
s103=(((p[67] & 0x3000) >> 12) + offset1) << scale1);
s104=(((p[67] & 0xC000) >> 14) + offset1) << scale1);
s105=((p[67] & 0x3) + offset1) << scale1);
s106=(((p[67] & 0xC) >> 2) + offset1) << scale1);
s107=(((p[67] & 0x30) >> 4) + offset1) << scale1);
s108=(((p[67] & 0xC0) >> 6) + offset1) << scale1);

```

Listing 5.5 – Code snippet for the calculation of the first eight fixed energy time series

- 16 Stepped energy offset and scale are calculated by bit-wise operations
- 17 Stepped energy time series are calculated similarly as in Step 15 above.
- 18 Fixed energy Zero lag ACF, Fixed energy ACF Offset, and Fixed energy ACF Scale are calculated by bit-wise operations.

```

facflag0=((p[34] << 8) + ((p[35] & 0xFF00) >> 8));
facfoffset=((p[35] & 0xFF) << 16) + p[36]);
facfscale=((p[37] & 0xFC00) >> 10);

```

Listing 5.6 – Code snippet for the calculation of the Fixed energy Zero lag ACF, ACF Offset and Scale.

WORD	WORD NO. IN HEADER / SCIENCE	BYTE NO. IN HEADER / SCIENCE	CONTENT	BIT NO.	VARIABLE / ARRAY ELEMENT
34	4	9	Fixed ACF zero lag, 24 bits	0	facflag0
		8		1	
35	5	11	Fixed ACF offset, 24 bits	2	facflag0
		10		3	
36	6	13	Fixed ACF offset, 24 bits	4	facflag0
		12		5	
37	7	15	Fixed ACF Scale	6	facflag0

Table 5.7 DWP data Packet snippet for the Fixed energy Zero lag ACF, Offset and Scale

- 19 The 31 Fixed energy ACFs are built by implementing (Lag – Offset) >> Scale, the offset and the scale.

```

facflag1=(((p[37] & 0x3F0) >> 4) + facoffset) <<
facfscale);
facflag2=((((p[37] & 0xF) << 2) + ((p[38] & 0xC000) >>
14)) + facoffset) << facfscale);
facflag3=(((p[38] & 0x3F00) >> 8) + facoffset) <<
facfscale);
facflag4=(((p[38] & 0xFC) >> 2) + facoffset) <<
facfscale);
facflag5=((((p[38] & 0x3) << 4) + ((p[39] & 0xF000) >>
12)) + facoffset) << facfscale);
facflag6=(((p[39] & 0xFC0) >> 6) + facoffset) <<
facfscale);
facflag7=((p[39] & 0x3F) + facoffset) << facfscale);

```

Listing 5.7 – Code snippet for the calculation of the first seven Fixed energy ACFs

WORD	WORD NO. IN HEADER / SCIENCE	BYTE NO. IN HEADER / SCIENCE	CONTENT	BITS	VARIABLE / ARRAY ELEMENT
37	7	15	Fixed ACF Scale	7 6 5 4 3 2 1 0	facfscale
		14	Fixed ACF Lag 1	7 6 5 4 3 2 1 0	facflag1
			Fixed ACF Lag 2	7 6 5 4 3 2 1 0	facflag2
38	8	17	Fixed ACF Lag 3	7 6 5 4 3 2 1 0	facflag3
		16	Fixed ACF Lag 4	7 6 5 4 3 2 1 0	facflag4
			Fixed ACF Lag 5	7 6 5 4 3 2 1 0	facflag5
39	9	19	Fixed ACF Lag 6	7 6 5 4 3 2 1 0	facflag6
		18	Fixed ACF Lag 7	7 6 5 4 3 2 1 0	facflag7

Table 5.8 DWP data Packet snippet for the first seven Fixed energy ACFs

- 20 Stepped energy Zero lag ACF, Stepped energy ACF Offset, and Stepped energy ACF Scale are calculated by bit-wise operations.
- 21 The 31 Fixed energy ACFs are built by similarly as in Step 19 above.
- 22 The calculated variable values, the time series and the ACFs along with other most relevant header information are printed.

Chapter 6 Development of a methodology for deriving the Upper Plasmaspheric Electron Content component along the orbital path of the TC1 from its empirical, in-situ electron density data

A new methodology is developed and presented in this research, making use of the electron density data available from the TC1 mission to derive the Upper Plasmaspheric TEC component (above the semi-synchronous orbit height) along the orbital trace of the spacecraft.

6.1 The case for this thesis ((This section is my own work)

As mentioned earlier in this thesis, the absolute contribution of the Upper Plasmasphere to the Electron Content and its variations under locational, diurnal, seasonal and solar activity variations have been and continues to be unmeasured quantities.

The importance of the Plasmaspheric contribution to Electron Content in trans-Ionospheric satellite communications has been demonstrated in previous chapters. This thesis work classifies the Plasmasphere into two parts; the Upper Plasmasphere and the Lower Plasmasphere, demarcated by the semi synchronous orbit altitude at around 22,000 kms.

The Lower Plasmaspheric TEC contribution has been studied extensively by the scientific community using the GPS dual frequency techniques. As the GPS satellites have a global footprint, it has become possible to derive TEC figures (up to the Lower Plasmasphere altitude) throughout the year, building up a huge database of TEC figures. Comprehensive modelling of TEC variations (up to Lower Plasmaspheric altitude) has

become possible from these extensive sets of data, whereas the Upper Plasmaspheric contribution to the TEC remains unquantified.

6.1.1 Upper Plasmaspheric Electron Content (UPEC)

Upper Plasmaspheric Electron Content can be defined as the total electron count of the Upper Plasmasphere segment (the altitudes above semi-synchronous orbit height up to the up to geo-stationary orbit height) in a column of 1m^2 cross section, along the signal path from the satellite (s) to the receiver (r). Upper Plasmaspheric Electron Content can be abbreviated as UPEC.

The quantification of Upper Plasmaspheric Electron Content contribution to the Electron Content up to geo-stationary orbit heights becomes of practical significance in satellite communications, navigation, ranging, remote sensing and military applications. Chapter 2 lists the effects caused by the free electrons on radio waves traversing the space. Other than these effects, it is of prime academic interest to analyse this quantity, in order to thoroughly understand the phenomena.

In the satellite engineering applications listed above, the effects introduced by the Upper Plasmaspheric Electron Content are treated as errors and noise terms. In the absence of accurate quantification, larger tolerance allowances are used in overcoming the effects, thus affecting the link budgets significantly.

Geo- stationary orbits satellites and Molniya orbit satellites dwell in orbits higher than 35,000 kms and most of them have applications affected by the amount of TEC down to the ground receivers. In addition, many satellites in these orbits are used for the purpose of relaying satellite signals across the globe. The Chinese Navigation Satellite System (also known as COMPASS or BeiDou-2) and the Indian Regional Navigation Satellite System (IRNSS) use Geo- stationary orbits satellites as part of their constellation for satellite navigation. As mentioned before, there are severe ranging and

time delay implications for navigation applications due to the amount of TEC encountered by the reference signals.

Figure 6.1 illustrates the relative distances of the Upper Plasmaspheric content and Lower Plasmaspheric content as defined in this research. The upper limit of the Upper Plasmasphere is taken to be 40000 kms in order to accommodate the TEC component encountered by the Molniya orbit satellites. Therefore it is logical to assume that the Upper Plasmaspheric TEC component will be of the same order of the Lower Plasmaspheric content which can be calculated by the GPS Dual frequency method, as the distances concerned are 20, 000 kms and 18,000 kms respectively for the two components.

When comparing the extensive amount of research that has been under taken by the scientific community in relation to the Lower Plasmaspheric TEC content and its associated effects in recent years; the amount of research on the Upper Plasmaspheric TEC content is almost non-existent. The absence of a suitable technology is the main reason for the inability to quantify this component. This study firmly believes that the methodology developed in this research using electron density data for TC1 fills that lacuna, most probably for the first time.

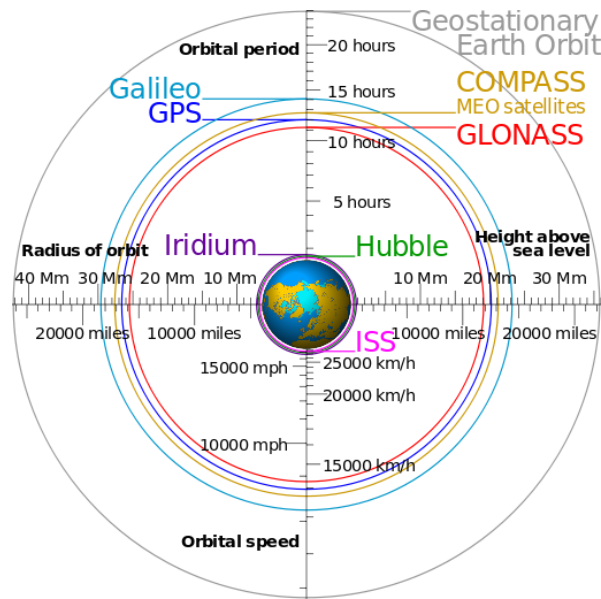


Figure 6.1 The altitudes, period, radius and speed of relevant orbits (Lee, 2014)

6.1.2 TC1 orbit and the opportunity it provides

The following points about the TC1 Mission make it appropriate for the development of this methodology:

- 1 TC1 mission consists of the PEACE experiment, which is equipped with a Langmuir Probe, enabling the in-situ measurements of electrons along the orbital path and the derivation of the electron density.
- 2 The orbit of TC1 is highly elliptical.
- 3 It has very low perigee and very high apogee.
- 4 The high eccentricity and the low perigee, high apogee of the TC1 orbit and the resulting smaller incident angle the orbital trace makes while in the 40000-20000 km altitude range resulting from it provide the ideal geometric opportunity to build the methodology and utilise the in-situ electron density measurements for the calculation of the Upper Plasmaspheric TEC component.
- 5 The inclination angle range of the TC1 mission makes it an equatorial mission that was confined to the Near-Equatorial region approximately $\pm 20^{\circ} - 25^{\circ}$ on either sides of the magnetic equator. As the most pronounced absolute TEC

values and variations are within this region, TC1 data offers an excellent opportunity to build a TEC database of this region.

It is note-worthy that the TC1 mission is unique among all the known space weather research missions, when one considers the above characteristics that facilitate the development of this methodology.

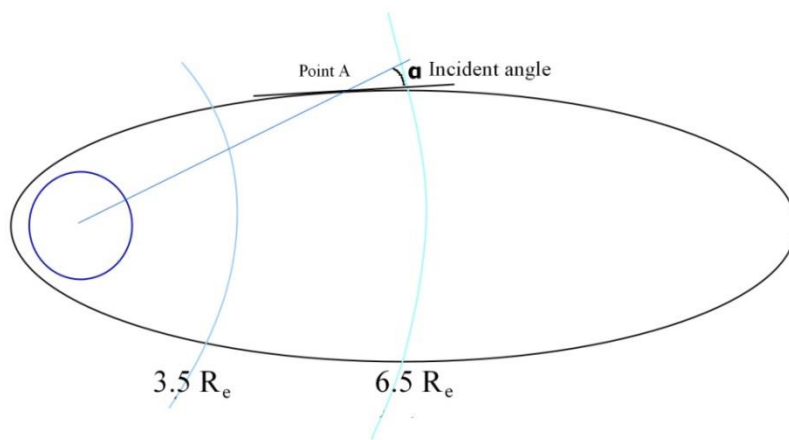


Figure 6.2 Orbital plane diagram showing Incident angle being equal to the angle the tangent to the orbit makes with the line connecting the centre of the earth with the spacecraft in the altitude range $3.5 R_e$ to $6.5 R_e$ (Diagram not to scale)

6.2 Data sources

Electron density and spacecraft time data from the Double Star UK Data centre and the orbital position and spacecraft time and date data from the NASA's Satellite Situation Centre needs to be combined to form the input data file for the methodology. These two sets of data were downloaded separately and combined as would be explained later.

6.2.1 Electron Density Data -Double Star UK Data Centre

Electron density data is sourced from the Double Star Science Data System, UK Data Centre, hosted at <http://www.cluster.rl.ac.uk/ddms/>.

On the selection of TC1, PEACE the date range, output format (CDF/CEF/ASCII/Plot) and the data parameter (electron density), the listing is generated. The listing tabulates interval centred time tag rounded to nearest millisecond with electron density. The date is given in DD-MM-YYYY format and the time is given in HH:MM:SS.MS format. The electron density is given in N_e/cm^3 . If the electron density was outside the tolerance level of the instrument or if the instrument had been turned off, a figure of -1.00000E+31 is output.

Density data was downloaded for 20 days at a time and saved as a spreadsheet, arranged under year of operation.

6.2.2 Orbit Data - NASA Satellite Situation Centre

The NASA Satellite Situation Centre, run under the Space Physics Data Facility of the Goddard Space Flight Centre provides spacecraft coordinate information for a range of missions. The coordinate datasets for TC1 and TC2 are included in the databases. The data is available at <http://sscweb.gsfc.nasa.gov/cgi-bin/Locator.cgi>. In order to download the coordinates one needs to select the spacecraft, the date and time range, output units / formatting and the output options.

The table 6.1 on the next page gives the formatting and units options available for outputs and the selected options.

Date	Time
<input checked="" type="radio"/> yyyy ddd <input type="radio"/> yy/mm/dd <input type="radio"/> yy-Mmm-dd <input type="radio"/> yy-MMM-dd	<input type="radio"/> hh.hhhh <input checked="" type="radio"/> hh:mm:ss <input type="radio"/> hh:mm
Distance	Degrees Format
<input type="radio"/> R _E - Earth Radii <input checked="" type="radio"/> km - Kilometers <input type="radio"/> km - Integers <input type="radio"/> km - Scientific Notation with <input type="text" value="2"/> decimal places	<input checked="" type="radio"/> -dd.ddd... with <input type="text" value="2"/> decimal places <input type="radio"/> -ddd dd' <input type="radio"/> -ddd dd ' dd"
Direction/Range	
<input type="radio"/> Lat (-90,+90), Long(0,360) <input checked="" type="radio"/> Lat (-90,+90), Long (-180,+180) <input type="radio"/> Lat (90S,90N), Long (180W,180E)	
Output Format Options	
<input type="radio"/> CDF <input checked="" type="radio"/> Text <input type="text" value="1"/> line(s) per page	

Table 6.1 NASA Satellite Situation Centre TC1 Spacecraft coordinates: Units and formatting options available for outputs and the selected options.

The table 3.2 on the next page gives the output options available and the selected options.

	X Y Z	LAT LON	X	Y	Z	LAT	LON	LOCAL TIME
GEI/TOD	<input type="checkbox"/>	<input type="checkbox"/>	<input type="checkbox"/>	<input type="checkbox"/>	<input type="checkbox"/>	<input type="checkbox"/>		
GEI/J2000	<input type="checkbox"/>	<input checked="" type="checkbox"/>	<input checked="" type="checkbox"/>	<input checked="" type="checkbox"/>	<input checked="" type="checkbox"/>	<input checked="" type="checkbox"/>		
GEO	<input type="checkbox"/>	<input type="checkbox"/>	<input type="checkbox"/>	<input type="checkbox"/>	<input type="checkbox"/>	<input type="checkbox"/>	<input type="checkbox"/>	<input type="checkbox"/>
GM	<input type="checkbox"/>	<input type="checkbox"/>	<input type="checkbox"/>	<input type="checkbox"/>	<input type="checkbox"/>	<input type="checkbox"/>	<input type="checkbox"/>	<input type="checkbox"/>
GSE	<input type="checkbox"/>	<input type="checkbox"/>	<input type="checkbox"/>	<input type="checkbox"/>	<input type="checkbox"/>	<input type="checkbox"/>	<input type="checkbox"/>	<input type="checkbox"/>
GSM	<input type="checkbox"/>	<input type="checkbox"/>	<input type="checkbox"/>	<input type="checkbox"/>	<input type="checkbox"/>	<input type="checkbox"/>		
SM	<input type="checkbox"/>	<input type="checkbox"/>	<input type="checkbox"/>	<input type="checkbox"/>	<input type="checkbox"/>	<input type="checkbox"/>	<input type="checkbox"/>	<input type="checkbox"/>

Additional Options		
Regions	Values	Distance From
<input type="checkbox"/> Spacecraft Regions	<input checked="" type="checkbox"/> Radial Distance	<input type="checkbox"/> T95 Neutral Sheet
<input type="checkbox"/> Radial Traced Footpoint Regions	<input type="checkbox"/> B Field Strength	<input type="checkbox"/> P93 Bow Shock
<input type="checkbox"/> North B Traced Footpoint Regions	<input type="checkbox"/> Dipole L Value	<input type="checkbox"/> RS93 MPause
<input type="checkbox"/> South B Traced Footpoint Regions	<input type="checkbox"/> Dipole Inv Lat	<input type="checkbox"/> B GSE X-Y-Z

B Field Trace Output Options			
	Footpoint Latitude	Footpoint Longitude	Field Line Length
GEO NORTH	<input type="checkbox"/>	<input type="checkbox"/>	<input type="checkbox"/>
GEO SOUTH	<input type="checkbox"/>	<input type="checkbox"/>	<input type="checkbox"/>
GM NORTH	<input type="checkbox"/>	<input type="checkbox"/>	<input type="checkbox"/>
GM SOUTH	<input type="checkbox"/>	<input type="checkbox"/>	<input type="checkbox"/>

Table 6.2 NASA Satellite Situation Centre TC1 spacecraft coordinates: Available output options and the selected options

20 days of data was downloaded in GEI/J2000 coordinates in ASCII format. As would be elaborated later in section 6.3.2, GEI/J2000 are inertial coordinates, therefore are not affected by the rotation of the earth. It is important that the coordinate system selected should be able to provide the elliptic shape in order to carry out the geometric constructions. The radial distance is also downloaded along with the coordinates, facilitating the calculation of apogee and perigee values.

6.3 Orbital elements and Coordinate Systems -Primary background information

This section gives the primary background information about the Orbital elements and Coordinate Systems used in the analysis

6.3.1 Orbital elements / Parameters

Primarily five parameters uniquely define an orbit. They are:

- 1 Semimajor axis (a)
- 2 Eccentricity (e)
- 3 Inclination angle (i)
- 4 Longitude of the Ascending Node (Ω)
- 5 Argument of Periapsis (ω)

The definitions for the orbital elements are given below:

- 1 Semimajor axis (a)** – Half the sum of the Periapsis and Apoapsis distances.

From Figure 6.3

$$a = \frac{1}{2}(r_a + r_p) \quad 6.1$$

2 Eccentricity (e) – The eccentricity of an ellipse is the measure of its elongation compared to a perfect circle.

From Figure 6.3

$$e = \frac{r_a - r_p}{r_a + r_p} \quad 6.2$$

The following two elements define the orientation of the orbital plane with respect to the reference (equatorial) plane and the reference direction:

3 Inclination angle (i) - Angle of the Ascending node, countered positively (counter clockwise) in the forward direction between 0^0 and 180^0 between the normal (directed towards the east) to the line of nodes in the equatorial plane and the normal (in the direction of the velocity) to the line of nodes in the orbital plane.

4 Longitude of the Ascending Node (Ω) – The angle between the reference direction (Vernal Equinox) and that of the Ascending Node in the Line of Nodes (the intersection of the orbital plane and the equatorial plane) measured positively (counter clockwise) from 0^0 to 180^0 in the forward direction.

5 Argument of Periapsis (ω) - The orientation of the orbital ellipse in the orbital plane is determined by this angle, which is defined as the angle measured positively from 00 to 3600 in the direction of the motion of the satellite between the Line of Nodes from direction of the Ascending Node to the direction of the Periapsis.[59]

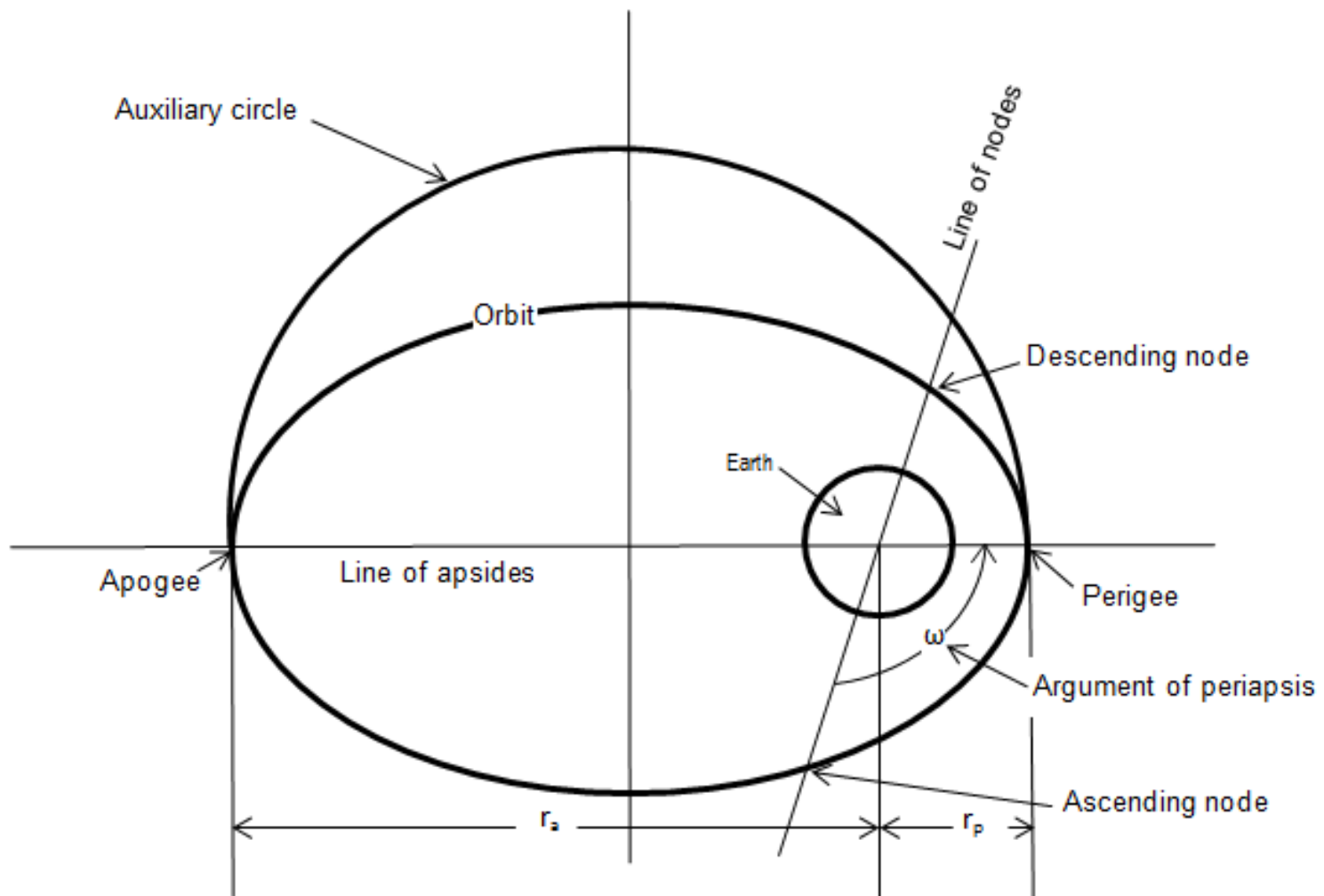


Figure 6.3

Orbital Plane diagram

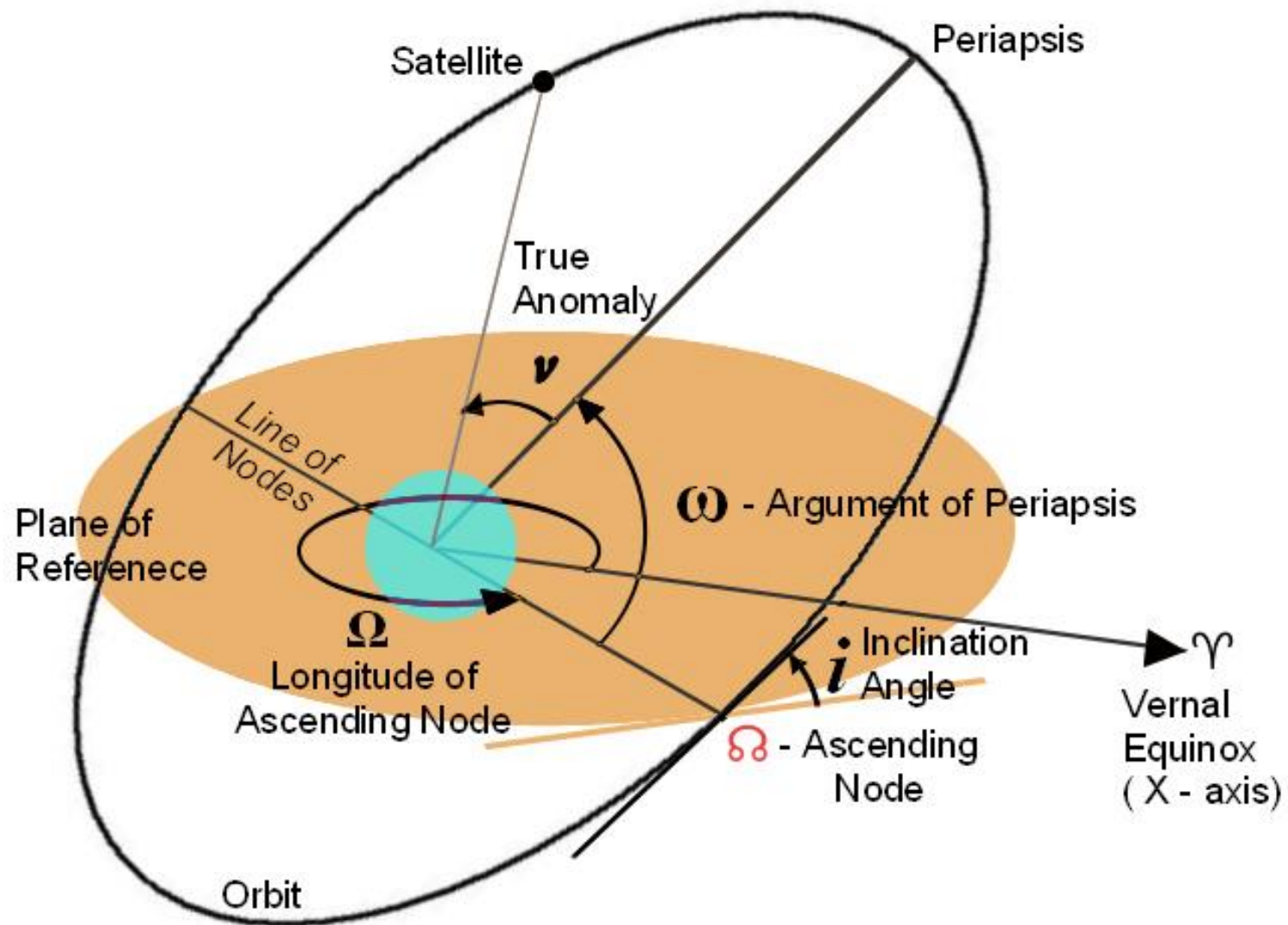


Figure 6.4 Orbital elements / Parameters Inclination Angle, Longitude of the Ascending Node and the Argument of Periaapsis illustrated

6.3.2 Geocentric Equatorial Inertial Coordinate Systems

The following table lists the main Geocentric Coordinate Systems, their abbreviations and the axes definitions:

System		Definition of Axes
Geocentric Equatorial Inertial	GEI	X = First Point of Aries
		Z = Geographic North Pole
Geographic	GEO	X = Intersection of Greenwich meridian and geographic equator
		Z = Geographic North Pole
Geocentric Solar Ecliptic	GSE	X = Earth-Sun line
		Z = Ecliptic North Pole
Geocentric Solar Magnetospheric	GSM	X = Earth-Sun line
		Z = Projection of dipole axis on GSE YZ plane
Solar Magnetic	SM	Y = Perpendicular to plane containing Earth-Sun line and dipole axis. Positive sense is opposite to Earth's orbital motion.
		Z = Dipole axis
Geomagnetic	MAG	Y = Intersection between geographic equator and the geographic meridian 90 ⁰ East of the meridian containing the dipole axis
		Z = Dipole axis

Table 6.3 Geocentric Coordinate Systems, their abbreviations and the axes definitions
(Hapgood, 1992: p712)

In the table above, the undefined third axis completes the right handed Cartesian Triad system.

In order to execute the methodology, it is essential to construct the true elliptic shape of the orbit. Of these Geocentric Coordinate Systems, only GEI systems are suitable for this analysis, as that system does not change with the rotation of the earth and therefore, the ellipse of the orbit can be constructed.

In the GEI system, the X axis points towards the First Point of Aries and the Z axis points to the Geographic North Pole with the earth's centre as the origin. This direction is also the intersection of the Earth's equatorial plane and the ecliptic plane. It points towards the Sun in Vernal Equinox. The Z axis, which is the rotation axis pointing towards the North Pole of the Earth and Y axis completes the right-handed orthogonal set. The normal GEI coordinate system changes slowly in time owing to the effects of astronomical precession and the nutation of the Earth's rotation axis. Therefore it is important to standardise the epoch date and time, in order to have a unique reference point (Hapgood, 1992).

Multiple GEI coordinates systems have been established and utilised by researchers. The NASA Satellite Situation Centre for spacecraft coordinate data is available in the J2000 Frame Coordinate System (GEI /J2000) and the True of Date Frame Coordinate System (GEI /TOD), which are two of the GEI coordinates systems utilised (Table 6.2).

a) J2000 Frame Coordinate System (GEI /J2000)

The most commonly used Geocentric Equatorial Inertial Coordinate Systems frame is the J2000 frame. It is defined with the x-axis being aligned with the mean equinox at 12:00 Terrestrial Time on 1 January 2000 and the earth's Mean Equator on that date. The system is also referred to as the EME2000.

b) True of Date Frame Coordinate System (GEI /TOD)

The True of Date (TOD) frame is defined using the true equator and equinox on the date, when the coordinates are generated.

Out of the two, the GEI /J2000 is selected for this research, as coordinates from more than one dates are involved in the analysis.

6.4 The Methodology ((This section is my own work)

As demonstrated in previous chapters, the orbit of TC1 has been constantly changed over the mission lifetime. The declared inclination, apogee and perigee information at the beginning of the mission are not factually holding. Therefore, each orbit needs to be analysed on its own merit and the orbital parameters and the other relevant figures should be derived for each individual orbit.

6.4.1 Data acquisition and input

- 1 From the NASA Satellite Situation Centre TC1 data set, the orbital coordinates and the associated data are downloaded in 20 days of data sets blocks. This data is called the “Spacecraft Position Data Set” and is provided in one minute intervals. The data elements, their format and units are given in table 6.4 in the next page.

Data element	Format	Unit
Year	YYYY	-
Day of year	DDD	-
Time	HH:MM::SS	-
X	GEI/J2000	Kilometres
Y	GEI/J2000	Kilometres
Z	GEI/J2000	Kilometres
Latitude	Lat (-90,+90)	dd.dd
Longitude	Long (-180,+180)	dd.dd
Radial Distance	-	Kilometres

Table 6.4 Orbital data elements, their format and units

- 2 From the Double Star UK Data Centre Spacecraft date and time and the one minute averaged electron density data is obtained either in CDF/CEF format or in ASCII format for the same 20 days period. The date is in DD/MM/YYYY and the time is in HH.MM.SS.MS format. The unit of electron density is N_e/cm^3 .
- 3 From the Spacecraft Position Data Set, one orbit long sets of data (usually around 1630 sets of data) are selected and loaded into the sheet 1 of the programmed spreadsheet “TEC Builder” in columns B to J.
- 4 The corresponding electron density data set is selected for the same time range and loaded into the sheet 2 of the “TEC Builder” spreadsheet. The date

data is loaded in column B, the time data is loaded in column D and the density data is loaded in column G.

- 5 On loading these sets of data, the program automatically carries out all of the calculations except the Line of Nodes and the Argument of Periapsis calculations.
- 6 The Ascending Node and the Descending Node coordinates should be manually loaded in the “TEC Builder”. For that the values of the Z axis should be analysed and the two points where the sign change occurs should be marked and the respective X, Y coordinate along with the Z coordinate should be copied and loaded. The “TEC Builder” calculates the Gradient and the Intercept values of the line equation of the Line of Nodes in the Equatorial plane and thus the Longitude of the Ascending Node (Ω).
- 7 The Argument of Periapsis should be calculated from the X and Y coordinate values of the Periapsis and Apoapsis points in the orbital plane. These values are calculated in the W and Z columns in the “TEC Builder”. The Periapsis and Apoapsis points in the original coordinates are marked their respective transformed axis coordinates in the orbital plane are used for the calculation of the Argument of the Periapsis.

		LINE OF NODES				
		x	y	z		
A	1	-6141.53	4789.66	232.89		
	2	-6294.85	4283.25	-15.36		
B	1	32640.38	-22565.16	-32.76		
	2	32836.55	-22582.92	14.8		
					x0A	-6285.36
					y0A	4314.58
					x0B	32775.50
					y0B	-22577.39
					m	-0.688463357
					c	-12.65937091
					Ω	-34.5459869

Figure 6.5 Longitude of the Ascending Node (Ω) calculation for the orbit on
07.05.2005

	ARGUMENT OF PERIAPSIS				
Xp	70798.36	Xa	2488.589948		
Yp	44211.72946	Ya	22450.86993		16.5375663
Yp/Xp	0.62447396	Xa/Ya	0.296926818	w	31.98370447

Figure 6.6 Argument of Periapsis (ω) calculation for the orbit on 07.05.2005

8 With these calculations, the “TEC Builder” completes the whole procedure.

6.4.2 The Algorithm

- 1 After the data entry, the “TEC Builder” spreadsheet has the spacecraft position data and the density data in two different sheets, Sheet 1 and Sheet 2 respectively.
- 2 As both data sets need to be merged, each data line needs to be given unique time stamp. To achieve this, in Sheet 1 the day of the year in column C is multiplied by 24 and added with the time data in column D. The result is stored in column A and formatted to decimal numbers. The formula is:

$$A1 = (C1*24) + D1 \quad 6.3$$

- 3 In density data in Sheet 2, column B contains date in DD/MM/YYYY format. It is converted to day of the year format and stored in column C by the formula below:

$$C1 = B1-DATE(YEAR(B1),1,0) \quad 6.4$$

- 4 In density data, the electron density is averaged for one minute and the averaged figure is given against the average time. Therefore the time information is 30 seconds past the minute. As the spacecraft position data is time stamped at the beginning of the minute, the 30 seconds need to be deducted, in order to synchronise the time stamp. This is achieved by entering 00:00:30 seconds in column E and deducting E from D and storing the result in F. The formula is:

$$F1 = D1 - E1 \quad 6.5$$

As the density data is averaged for the minute, it does not have any effect if the time stamp denoted at the beginning of the minute.

- 5 The unique time stamp is achieved by multiplying day of the year in column C by 24 and adding it with the new time data in column F. The result is stored in column A and formatted to decimal numbers. The formula is:

$$A1 = (C1*24) + F1 \quad 6.6$$

- 6 From point 7 till point 35, the algorithm determines the ellipse equation of the orbit in the format:

$$\frac{x^2}{a^2} + \frac{y^2}{b^2} = 1 \quad 6.7$$

For that, it is necessary to carry out axis rotations to bring the GEI/J2000 based coordinates to the orbital axis, then rotate the X axis to the semi major axis of the ellipse and then move the origin to the centre of the ellipse from the centre of the earth which is a focus of the ellipse.

- 7 For these manipulations, it is necessary to calculate the orbital elements from the available coordinate set.
- 8 As the first step, the equation of the orbital plane needs to be determined. As there is a big set of X, Y and Z coordinates, the best fitting plane equation has to be determined. This is achieved by way of applying the Least Squares Fit method. The theory used, the calculations made and the programming are described in Appendix 6. The constants of the orbital plane equation are determined by “TEC Builder” spreadsheet.

- 9 As the orbital plane equation is determined, the angle between this plane and the reference (which is the equatorial plane) can be determined. As the equatorial plane consists of the X and Y axes and the Z axis coordinates are zero in that plane, the equation of the equatorial plane is:

$$Z = 0 \quad 6.8$$

- 10 The angle between the two planes above is equal to the Inclination angle (i). The theory and calculations are given in section 6.6.2. The resulting Inclination angle (i) is tabulated in Column Y of the “TEC Builder”

- 11 The Ascending Node and the Descending Node coordinates are determined by locating the $Z = 0$ points. As the coordinates are downloaded in kilometres, it is extremely unlikely to get 0 value. Therefore, the coordinate values where the Z axis undergoes sign changes are located. As explained in Section 6.4.1 previously, the corresponding X, Y coordinates are loaded to the “TEC Builder” spreadsheet and the program calculates the coordinates for the Ascending Node and the Descending Node by interpolating for the zero values of Z coordinates. The corresponding ratio interpolated X, Y coordinates are calculated and they yield the coordinates for the Ascending Node and the Descending Node.

- 12 The Ascending Node and the Descending Node are differentiated by the sign change of the Z coordinates. A Plus to Minus sign change denotes the Descending Node and a Minus to Plus sign change denotes the Ascending Node.

- 13 The Line of Nodes is the intersection line of the orbital plane and the reference plane. By definition the Longitude of the Ascending Node (Ω) is the angle

between the reference direction (Vernal Equinox) and that of the Ascending Node in the Line of Nodes measured positively from 0^0 to 180^0 in the forward direction. If the line equation of the Line of Nodes is determined from the GEI/J2000 coordinates of the Ascending Node and the Descending Node, the Gradient of that line will be equal to the Longitude of the Ascending Node (Ω) as the reference X axis direction is the direction of Vernal Equinox. Z coordinates in that line equation will be equal to (or very close to) zero.

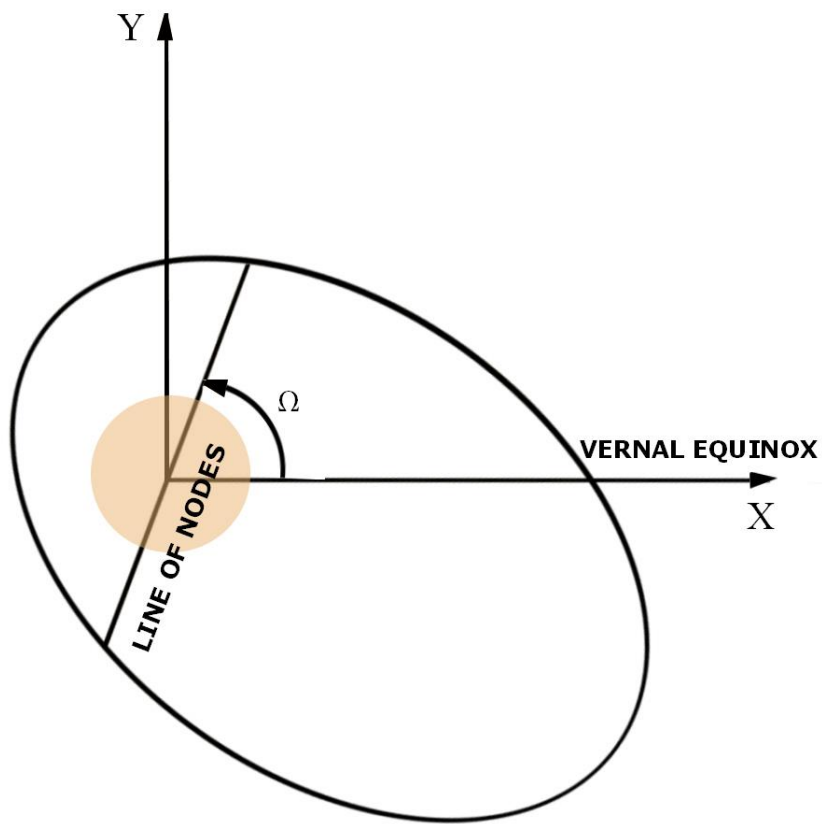


Figure 6.7 Equatorial plane diagram showing Longitude of the Ascending Node (Ω) being equal to the Gradient angle of the Line of Nodes in GEI/J2000 system for a general case. The Z axis is perpendicular to the plane and is pointing out.

- 14 The calculation of the Longitude of the Ascending Node (Ω) is shown in Figure 6.6 and detailed in the following sections.

The formula for the calculation is:

$$\Omega = (\text{ATAN}(P1703)) * 180 / \text{PI}() \quad 6.9$$

Where P1703 denotes m – the gradient of the Line of Nodes.

The value of the Longitude of the Ascending Node (Ω) is tabulated in Column V.

15 The first axis transformation is carried out by rotating the reference plane by the Longitude of the Ascending Node (Ω) angle in the clockwise direction. The Z axis values remain the same as the reference plane consists of X and Y axes and only those axes are rotated.

16 The Longitude of the Ascending Node (Ω) value is tabulated in the Column V of “TEC Builder”. The calculations for the rotation of the new X and Y axes are as follows:

$$X' = ((E1 * (\text{COS}(V1 * \text{PI}() / 180))) + (F1 * (\text{SIN}(V1 * \text{PI}() / 180)))) \quad 6.10$$

$$Y' = ((F1 * (\text{COS}(V1 * \text{PI}() / 180))) - (E1 * (\text{SIN}(V1 * \text{PI}() / 180)))) \quad 6.11$$

The theory of axis rotation is detailed in the following sections.

17 The new X axis is Line of Nodes, towards the Ascending Node. The Z axis is the previous Z axis, which is the earth’s axis of rotation that goes through the Geographic North pole. The origin is the centre of the earth and the Y axis completes the right hand triad.

18 Now the second coordinate transformation would take place. In this transformation, the coordinates Y' and Z are rotated positively (counter clockwise) through the Inclination angle (i). Therefore the X axis remains the same from the previous transformation and the Y and Z axes are rotated. The coordinates are named Y'' and Z'' and are tabulated in Columns Z and AA . The Inclination angle (i) is tabulated in Column Y .

19 The calculations for the rotation of the new X and Y axes are as follows:

$$Y'' = ((X1 * (\cos(Y1 * \pi / 180))) + (G1 * (\sin(Y1 * \pi / 180)))) \quad 6.12$$

$$Z'' = ((G1 * (\cos(Y1 * \pi / 180))) - (X1 * (\sin(Y1 * \pi / 180)))) \quad 6.13$$

20 Now the new coordinates system has its X and Y axes in the orbital plane and the X axis points towards the Vernal Equinox. As elaborated in section 6.3.1, the with these two axis transformations through the Longitude of the Ascending Node (Ω) and the Inclination angle (i), the orbital plane is defined and fixed.

21 As the new X and Y axes as are in the orbital plane now, the Z coordinates should be zero. This is verified by Z values in Column AA , which are either zero or negligible values.

22 Next, the Argument of Periapsis (ω) needs to be calculated. The data input procedure was detailed in section 6.4.1 and the Figure 6.6.

23 The new coordinates of the orbit are derived from the Input Dataset. All the z values should be equal to zero in the new, transitory coordinates.

- 24 Now, the distance between a starting point and the origin is calculated.
- 25 The procedure is repeated for all points in the orbit.
- 26 The maximum and the minimum distances are marked.
- 27 The corresponding coordinates are marked. They are the Apoapsis and Periapsis points.
- 28 The line connecting these points is the semi major axis.
- 29 The semi major axis line equation is determined using these points.
- 30 The Argument of Periapsis is determined by the angle between this line equation and the Line of Nodes line equation.
- 31 Now the coordinate system is turned anti clockwise through this angle about the new Z axis.
- 32 The new coordinates of the orbit are determined.
- 33 The Apoapsis and Periapsis points' new coordinates are determined.
- 34 Now the semi major axis is the new X axis and the centre of the earth is the focus.

- 35 The 2D Cartesian ellipse equation of the orbit can now be determined by the Periapsis and Apoapsis information.
- 36 From this new and final coordinate system transformation, the true anomaly of any satellite position can be determined.
- 37 From here onwards the, the mechanism for the determination of the UPEC values can be implemented, as detailed in the following methodology.

6.4.3 Mechanism for the determination of the UPEC

The methodology is devised as below:

- 1 The orbital trace through the altitude 20000km to 40000km is considered (about 3.5 Re to 6.5 Re).
- 2 The spacecraft passes this region in 1 hour and 7 minutes (4020 seconds)
- 3 Mean electron densities are calculated every 60 seconds, equalling 15 spins.
- 4 The distance covered in every 60 second is called a UPEC Bar
- 6 If the electron density variation turns out to be more than 10% within that bar, halved sub bars are considered.

- 7 The orbital arc distance covered by the UPEC bar in 60 seconds is calculated.
- 8 The mean point along that path is calculated. The tangent line at this meant point is determined.
- 9 The angle the tangent line to the orbit at this point makes with the line to the centre of the earth is called the incident angle.
- 10 Numerical integration is performed on electron density along the UPEC bar orbital distance.
- 11 The resulting value is taken as the STEC at the tangent point, the incident angle being calculated in point 9 above.
- 12 The VTEC for that arc is derived from the STECs and the incident angles.
- 13 This value is proportionately multiplied by the ratio of the $2.5 R_e$ divided by the arc distance calculated in point 7 above and the UPEC bar is derived.

6.4.4 Notes on automation of the algorithm.

The 37 point algorithm elaborated above is automated except for one step. The coordinates of the Ascending Node and the Descending Node need to be manually loaded in TEC Builder for the rest of the calculations to be automatically executed. This is done in Step 11 of the algorithms above.

Even this step can be automated by way of locating the sign change in the Z coordinate.

If there is a sign change, the following logic will apply:

For a positive to negative change:

$$|Z_n - Z_{(n+1)}| > |Z_n| \quad 6.14$$

Where Z_n is the n^{th} reading and $Z_{(n+1)}$ is the $(n+1)^{\text{th}}$ reading

For a negative to positive change:

$$|Z_n - Z_{(n+1)}| > |Z_n| \quad 6.15$$

Where Z_n is the n^{th} reading and $Z_{(n+1)}$ is the $(n+1)^{\text{th}}$ reading

Therefore, commonly for a sign change in Z coordinates:

$$|Z_n - Z_{(n+1)}| > |Z_n| \quad 6.16$$

Where Z_n is the n^{th} reading and $Z_{(n+1)}$ is the $(n+1)^{\text{th}}$ reading

By implementing this in the program, the Z coordinate sign change can be located and consequently the coordinates of the Ascending Node and the Descending Node can be found automatically.

Chapter 7 Derivations, Theories and Calculations

((This Chapter is completely my own work))

During the course of the research, further analysis of the TEC calculation methodology has resulted in a few changes to the initial procedure. The most significant being the correction introduced to calculate the hypotenuse length in the imaginary right angled triangle along the orbital path from the orbital arc length. As there is a way to calculate the incident angle directly from the ellipse equation in the orbital plane, the need to construct the imaginary triangle does not arise.

7.1 Deriving the plane equation

The general 3d equation 7.01 below needs to be solved and the coefficients determined to derive the plane equation.

$$ax + by + z + c = 0 \quad 7.01$$

The Appendices 6 and 7 demonstrates the mathematical derivations utilised and the resulting plane coefficient relationships are as follows:

$$2x^2a + 2xyb + 2xc + 2xz = 0$$

$$2xya + 2y^2b + 2yc + 2yz = 0$$

$$2xa + 2yb + 2c + 2z = 0$$

7.1.1 Calculation of plane coefficients a, b, c

From the Spacecraft Position Data Set, one orbit long sets of data (usually around 1630 sets of data) are selected and loaded into the sheet 1 of the programmed spreadsheet “TECbuilder” in columns B to J. The summated versions of the plane coefficient relationships 7.02, 7.03 and 7.4 are used to generate the three simultaneous equations needed for the determination of the plane equation.

The corresponding summated formats respectively are:

$$2\sum_{i=1}^n x_i^2 a + 2\sum_{i=1}^n x_i y_i b + 2\sum_{i=1}^n x_i c + 2\sum_{i=1}^n x_i z_i = 0 \quad 7.02$$

$$2\sum_{i=1}^n x_i y_i a + 2\sum_{i=1}^n y_i^2 b + 2\sum_{i=1}^n y_i c + 2\sum_{i=1}^n y_i z_i = 0 \quad 7.03$$

$$2\sum_{i=1}^n x_i a + 2\sum_{i=1}^n y_i b + 2c + 2\sum_{i=1}^n z_i = 0 \quad 7.04$$

The corresponding three simultaneous equations with coefficients $m_1, n_1, o_1, m_2, n_2, o_2, m_3, n_3, o_3$ and constants d_1, d_2, d_3 as shown in Appendix 8 are:

$$m_1 a + n_1 b + o_1 c + d_1 = 0$$

$$m_2 a + n_2 b + o_2 c + d_2 = 0$$

$$m_3 a + n_3 b + o_3 c + d_3 = 0$$

The following Table 7.1 on the next page gives the coefficients of simultaneous equations, the summated equivalents and their TecBuilder Positions.

	Coefficient/Constant	Summated quantity	TEC Builder Position
1	m_1	$2\sum_{i=1}^n x_i^2$	L1654
2	m_2	$2\sum_{i=1}^n x_i y_i$	P1656
3	m_3	$2\sum_{i=1}^n x_i$	S1658
4	n_1	$2\sum_{i=1}^n x_i y_i$	P1656
5	n_2	$2\sum_{i=1}^n y_i^2$	M1656
6	n_3	$2\sum_{i=1}^n y_i$	T1658
7	o_1	$2\sum_{i=1}^n x_i$	S1654
8	o_2	$2\sum_{i=1}^n y_i$	T1656
9	o_3	2	O1658
10	d_1	$2\sum_{i=1}^n x_i z_i$	R1654
11	d_2	$2\sum_{i=1}^n y_i z_i$	Q1656
12	d_3	$2\sum_{i=1}^n z_i$	U1658

Table 7.1 - The coefficients of simultaneous equations, the summated equivalents and their TECbuilder positions

The plane coefficients a, b and c are calculated using these summated values, as per the equations in Appendix 8.

$$c = (-1) \frac{[(d_1 m_2 - d_2 m_1)(n_1 m_3 - n_3 m_1) - (d_1 m_3 - d_3 m_1)(n_1 m_2 - n_2 m_1)]}{[(o_1 m_2 - o_2 m_1)(n_1 m_3 - n_3 m_1) - (o_1 m_3 - o_3 m_1)(n_1 m_2 - n_2 m_1)]}$$

$$b = \left[\frac{(o_1 m_2 - o_2 m_1)c + (d_1 m_2 - d_2 m_1)}{(n_2 m_1 - n_1 m_2)} \right]$$

$$a = \left[\frac{-1}{m_1} \right] (n_1 b + o_1 c + d_1)$$

The corresponding TecBuilder calculations are:

$$\begin{aligned} c = & (((L1664*M1662) - (L1662*M1664))*((L1666*P1662) - (L1662*P1666))) - \\ & (((L1666*M1662) - (L1662*M1666))*((L1664*P1662) - \\ & (L1662*P1664))))/(((L1666*M1662) - (L1662*M1666))*((L1664*N1662) - \\ & (L1662*N1664))) - (((L1664*M1662) - (L1662*M1664))*((L1666*N1662) - \\ & (L1662*N1666)))) \end{aligned}$$

7.05

$$\begin{aligned} b = & ((N1664*L1662*Q1670) + (P1664*L1662) - (N1662*L1664*Q1670) - \\ & (P1662*L1664))/((M1662*L1664) - (M1664*L1662)) \end{aligned}$$

7.06

$$a = (-1)*((M1662*Q1673)+(N1662*Q1670)+(P1662))/(L1662)$$

7.07

The values of the plane coefficients a , b and c are calculated at the TecBuilder positions Q 1676, Q1673 and Q1670 respectively.

7.2.1 Calculation of the Inclination angle

The Inclination angle is derived as described in Appendix 8. Therefore:

$$\cos(i) = \left\{ \frac{|a \times 0 + b \times 0 + 1 \times 1|}{\left(\sqrt{a^2 + b^2 + 1 \times 1} \right) \left(0^2 + 0^2 + 1^2 \right)} \right\} \quad 7.08$$

$$i = \cos^{-1} \left\{ \frac{1}{\left(\sqrt{a^2 + b^2 + 1} \right)} \right\} \quad 7.09$$

In the TEC Builder, $\cos(i)$ is calculated in the cell Q1679 by the following equation:

$$\cos(i) = 1 / (\text{SQRT}((Q1673) * (Q1673) + (Q1676) * (Q1676) + 1)) \quad 7.10$$

Consequently, Inclination angle i is calculated in the cell Q1681 by the following equation:

$$i = (\text{ACOS}(Q1679)) * 180 / \text{PI}() \quad 7.11$$

7.3 Coordinate Transformation theories

7.3.1 Coordinate transformation of a two axes Cartesian plane by an angle of θ

New coordinates of a two dimensional coordinate system, after a rotation by θ^0 are given by:

$$x' = (x \cos \theta + y \sin \theta) \quad 7.12$$

$$y' = (y \cos \theta - x \sin \theta) \quad 7.13$$

7.3.2 Coordinate Transformation Matrix

The transformed coordinates can be represented by the following matrix equation:

$$\begin{bmatrix} x' \\ y' \end{bmatrix} = \begin{pmatrix} x \cos \theta + y \sin \theta \\ y \cos \theta - x \sin \theta \end{pmatrix} \quad 7.14$$

$$\therefore \begin{bmatrix} x' \\ y' \end{bmatrix} = \begin{bmatrix} x \\ y \end{bmatrix} \begin{bmatrix} \cos \theta & \sin \theta \\ -\sin \theta & \cos \theta \end{bmatrix} \quad 7.15$$

Therefore, the rotation matrix is given by:

$$R(\theta) = \begin{bmatrix} \cos \theta & \sin \theta \\ -\sin \theta & \cos \theta \end{bmatrix} \quad 7.16$$

7.4 Transformations to derive the orbital plane coordinates

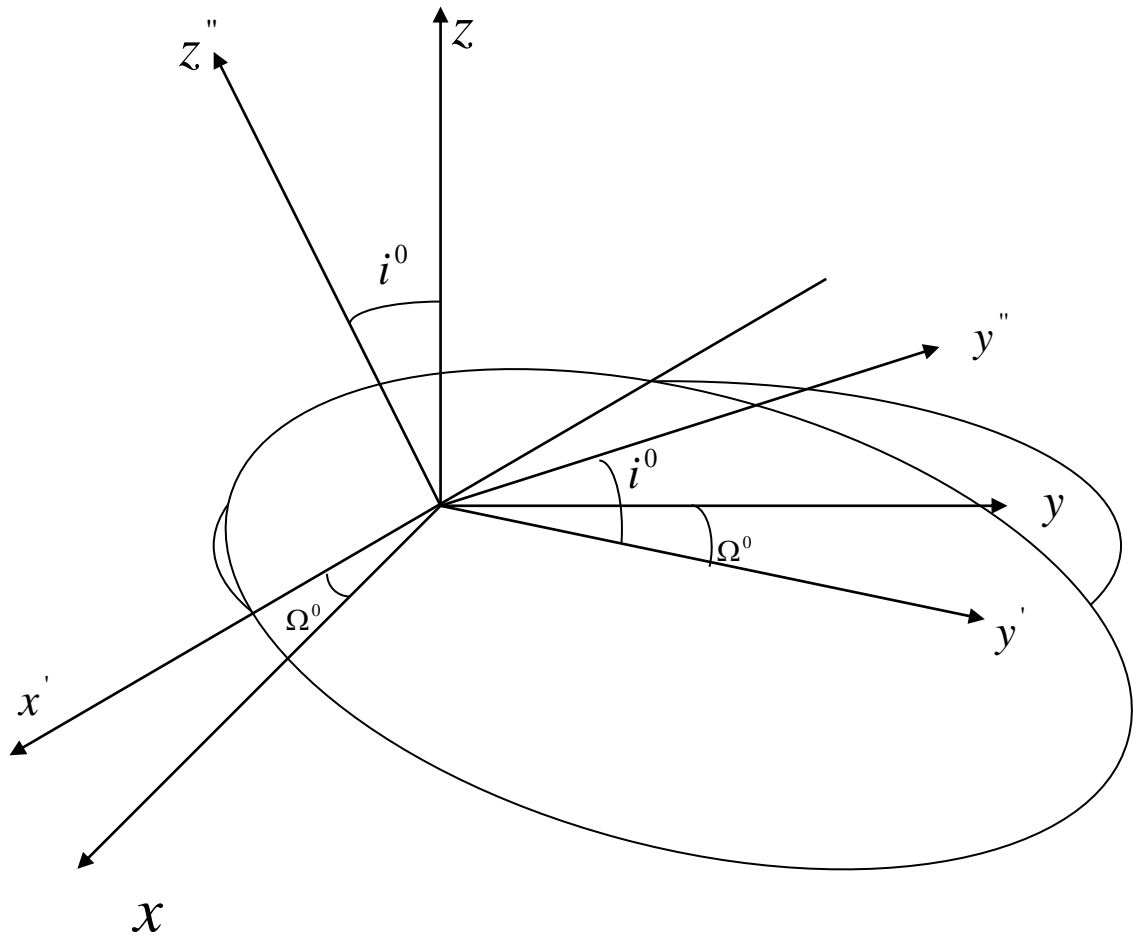


Figure 7.3 Transformations to derive the orbital plane coordinates with Line of apsides as the x axis

Transformations to derive the orbital plane coordinates with Line of apsides as the x axis are carried out in two stages:

Transformation 1: Transformation through the Longitude of the Ascending Node (Ω^0)

Transformation 2: Transformation through the Inclination angle (i^0)

Transformation 1: Transformation through the Longitude of the Ascending Node. (Ω^0)

This transformation generates x' from x and y' from y . In this transformation take place in the orbital plane, the z coordinates don't change. The resulting coordinates system will have the Line of Nodes as its x axis.

7.4.1 Calculation of the Longitude of the Ascending Node (Ω^0)

$$7.12, 7.13 \quad \Rightarrow \quad x' = (x \cos \Omega^0 + y \sin \Omega^0) \quad 7.17$$

$$y' = (y \cos \Omega^0 - x \sin \Omega^0) \quad 7.18$$

In the TEC Builder, $\cos(i)$ is calculated in the cell Q1679 by the following equation:

$$\cos(i) = 1 / (\text{SQRT}((Q1673)^2 + (Q1676)^2 + 1)) \quad 7.19$$

Transformation 2: Transformation through the Inclination angle (i^0) about the Line of Nodes - This transformation generates y'' from y' and z'' from z . As the transformation is about the new x axis, which is the Line of Nodes, the x axis coordinates, (which are x') do not change, during this transformation. The resulting coordinates are:

$$7.12, 7.13 \quad \Rightarrow \quad y'' = (y' \cos(i^0) + z' \sin(i^0)) \quad 7.20$$

$$z'' = (z' \cos(i^0) - y' \sin(i^0)) \quad 7.21$$

7.5.5 Transformations through the Argument of Periapsis

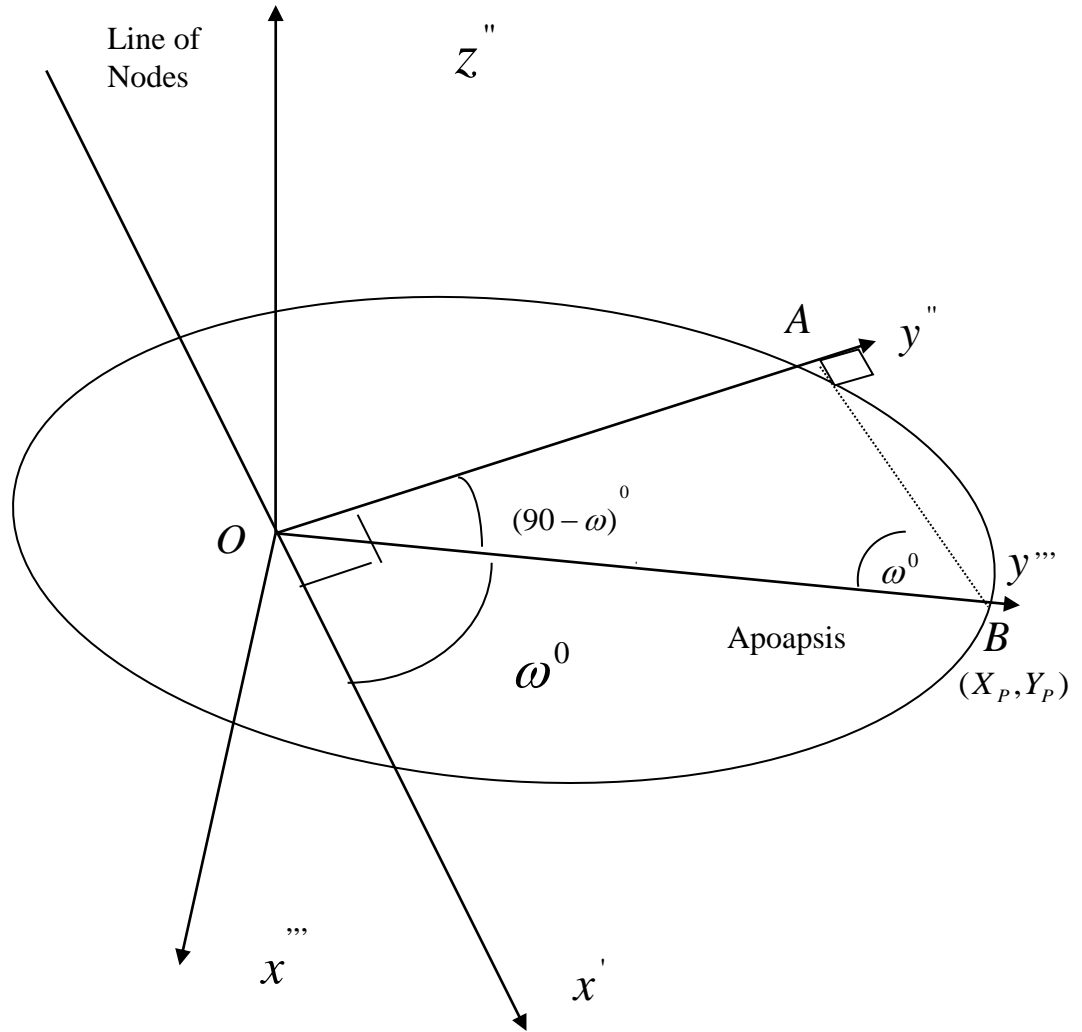


Figure 7.4 Transformations through the Argument of Periapsis with Line of apsides as the new y axis

The transformation is carried out by rotating the x' and y'' axes by $(270 + \omega)^0$ in the clockwise direction.

In Figure 7.4, considering the triangle ΔABO :

$$AO = y'' \quad 7.22$$

$$AB = x' \quad 7.23$$

$$\tan(\omega^0) = \frac{AO}{AB} \quad 7.24$$

$$7.22, 7.23, 7.24 \Rightarrow \tan(\omega^0) = \frac{y''}{x'}$$

$$\omega^0 = \tan^{-1}\left(\frac{y''}{x'}\right) \quad 7.25$$

The transformed coordinates will be given by:

$$x''' = x' \cos(270 + \omega)^o + y'' \sin(270 + \omega)^o \quad 7.26$$

$$y''' = y'' \cos(270 + \omega)^o + x' \sin(270 + \omega)^o \quad 7.27$$

7.6 Calculation of an Orbital Arc Length

In the Section 6.4.3, “Mechanism for the determination of the TEC” in the Methodology, the point 7 stipulates that “the orbital arc distance covered by the TEC bar in 60 seconds is calculated”. This is achieved by determining the ellipse equation of the orbit with its centre at the origins of the x, y axes and applying the Arc Length formula derived from the following section 7.5.1.

7.5.1 Ellipse equation of the orbit with its centre at the origin of x, y axes and

Line of Apsides as the x axis

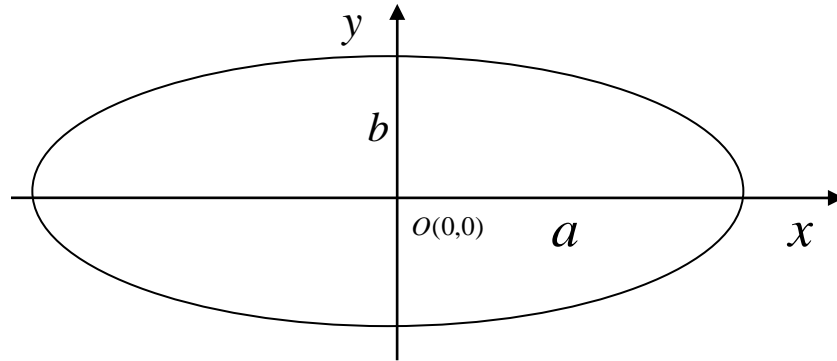


Figure 7.5 Ellipse with centre at the origin of a 2D Cartesian plane

Considering an ellipse with its centre at the origin of a 2D Cartesian plane (Figure 7.5),

if it's Semi Major Axis is a and Semi Minor Axis is b , then the ellipse equation gives:

$$\frac{x^2}{a^2} + \frac{y^2}{b^2} = 1 \quad 7.28$$

$$\therefore y = b \sqrt{\left(1 - \frac{x^2}{a^2}\right)} \quad 7.29$$

7.6.2 Calculation of the Arc Length of a function

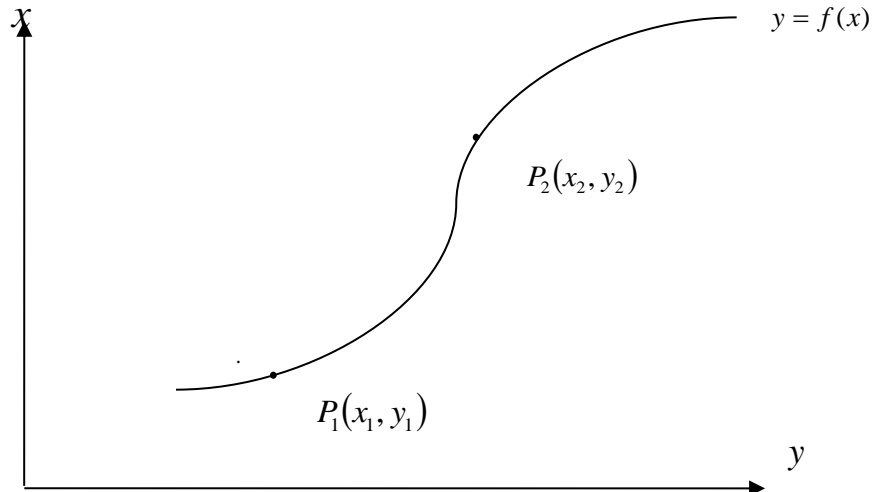


Figure 7.6 Arc length of a function $y = f(x)$ between two points $P_1(x_1, y_1)$ and

$P_2(x_2, y_2)$ in a 2D Cartesian plane

The Arc Length of any given function in a 2D Cartesian plane, of the form $y = f(x)$ is given by:

$$P_1P_2 = \int_{x_1}^{x_2} \sqrt{1 + \left(\frac{dy}{dx}\right)^2} dx \quad 7.30$$

7.5.3 Calculation of the Arc Length of the orbital ellipse with its centre at the origin and the Line of Apsides as the x axis

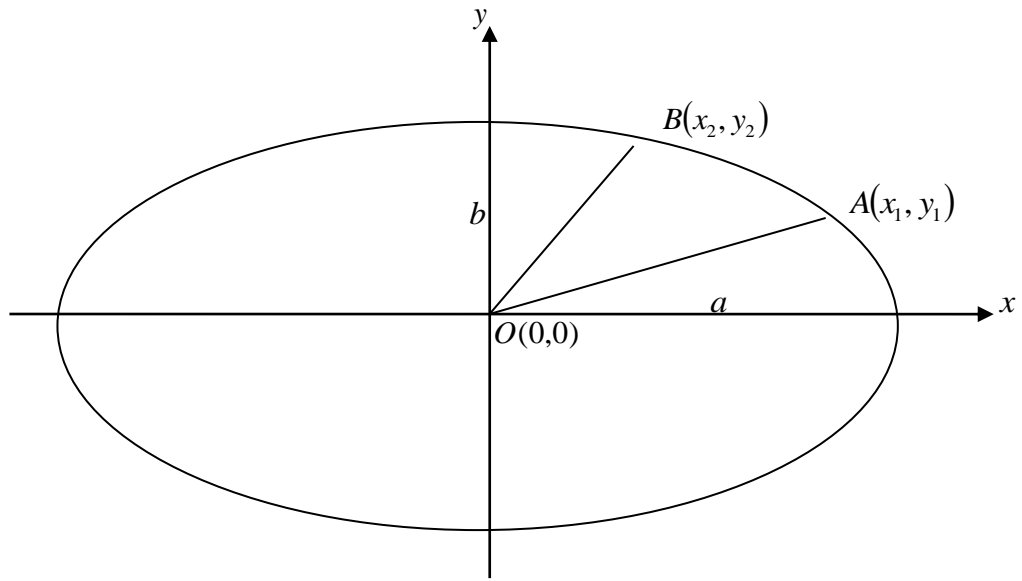


Figure 7.7 Orbital ellipse with its centre at the origin of x, y axes and Line of Apsides as the x axis

$A(x_1, y_1)$ and $B(x_2, y_2)$ are two points along its Perimeter, then the Arc Length of the arc AB is given by:

$$7.30 \Rightarrow \text{Arc Length } AB = \int_{x_1}^{x_2} \sqrt{1 + \left(\frac{dy}{dx}\right)^2} dx \quad 7.31$$

$$7.31 \quad \Rightarrow \quad y = b \sqrt{\left(1 - \frac{x^2}{a^2}\right)}$$

$$y = \frac{b}{a} \sqrt{(a^2 - x^2)} \quad 7.32$$

$$7.28 \quad \Rightarrow \quad \frac{x^2}{a^2} + \frac{y^2}{b^2} = 1$$

Differentiating both sides with respect to x , we get:

$$\frac{d}{dx} \left[\frac{x^2}{a^2} + \frac{y^2}{b^2} \right] = \frac{d(1)}{dx}$$

$$\frac{2x}{a^2} + \frac{2y}{b^2} \frac{dy}{dx} = 0$$

$$\frac{2y}{b^2} \frac{dy}{dx} = -\frac{2x}{a^2}$$

$$\frac{dy}{dx} = -\frac{x}{y} \frac{b^2}{a^2}$$

$$7.32 \quad \Rightarrow \quad \frac{dy}{dx} = -\frac{x}{\frac{b}{a} \sqrt{(a^2 - x^2)}} \frac{b^2}{a^2}$$

$$\frac{dy}{dx} = -\frac{b}{a} \frac{x}{\sqrt{(a^2 - x^2)}} \quad 7.33$$

$$\left(\frac{dy}{dx} \right)^2 = \left(-\frac{b}{a} \frac{x}{\sqrt{(a^2 - x^2)}} \right)^2$$

$$\left(\frac{dy}{dx} \right)^2 = \left(\frac{b^2}{a^2} \frac{x^2}{(a^2 - x^2)} \right)$$

$$\left(\frac{dy}{dx} \right)^2 = \left(\frac{b^2 x^2}{(a^4 - a^2 x^2)} \right) \quad 7.34$$

$$7.31 \Rightarrow \quad \text{Arc Length} \quad AB = \int_{x_1}^{x_2} \sqrt{1 + \left(\frac{dy}{dx}\right)^2} dx$$

$$7.34 \Rightarrow \quad \begin{aligned} AB &= \int_{x_1}^{x_2} \sqrt{1 + \frac{b^2 x^2}{(a^4 - a^2 x^2)}} dx \\ AB &= \int_{x_1}^{x_2} \sqrt{\frac{a^4 - a^2 x^2 + b^2 x^2}{(a^4 - a^2 x^2)}} dx \\ AB &= \int_{x_1}^{x_2} \sqrt{\frac{a^4 - (a^2 - b^2)x^2}{(a^4 - a^2 x^2)}} dx \\ AB &= \int_{x_1}^{x_2} \sqrt{\frac{a^4 - (a^2 - b^2)x^2}{a^2(a^2 - x^2)}} dx \\ AB &= \frac{1}{a} \int_{x_1}^{x_2} \sqrt{\frac{a^4 - (a^2 - b^2)x^2}{(a^2 - x^2)}} dx \end{aligned} \quad 7.35$$

$$\text{Substitute} \quad x = a \sin \theta \quad 7.36$$

$$\therefore \quad dx = a \cos \theta . d\theta \quad 7.37$$

$$\text{Also} \quad \sin^2 \theta = \frac{x^2}{a^2}$$

$$\cos^2 \theta = 1 - \frac{x^2}{a^2}$$

$$\cos^2 \theta = \frac{(a^2 - x^2)}{a^2}$$

$$(a^2 - x^2) = a^2 \cos^2 \theta \quad 7.38$$

The limits of the integral are x_1 and x_2 , which are the x coordinates of the points A and B . For the above substitution, the new limits need to be calculated.

Let θ_1 and θ_2 be the new limits. Then;

7.36 \Rightarrow

$$x_1 = a \sin \theta_1$$

$$\theta_1 = \sin^{-1} \left(\frac{x_1}{a} \right) \quad 7.39$$

Similarly

$$x_2 = a \sin \theta_2 \quad 7.40$$

$$\theta_2 = \sin^{-1} \left(\frac{x_2}{a} \right)$$

Substituting 7.55, 7.56 and 7.57 in 7.58, we get, Arc length;

$$AB = \frac{1}{a} \int_{\theta_1}^{\theta_2} \sqrt{\left(\frac{a^4 - (a^2 - b^2)(a \sin \theta)^2}{a^2 \cos^2 \theta} \right)} a \cos \theta d\theta$$

$$AB = \frac{1}{a} \int_{\theta_1}^{\theta_2} \sqrt{\left(\frac{a^4 - (a^2 - b^2)(a \sin \theta)^2}{a^2 \cos^2 \theta} \right)} d\theta$$

$$AB = \frac{1}{a} \int_{\theta_1}^{\theta_2} \sqrt{a^4 - (a^2 - b^2)(a \sin \theta)^2} d\theta$$

$$AB = \frac{1}{a} \int_{\theta_1}^{\theta_2} a^2 \sqrt{\frac{a^4 - (a^2 - b^2)(a^2 \sin^2 \theta)}{a^4}} d\theta$$

$$AB = a \int_{\theta_1}^{\theta_2} \sqrt{1 - \frac{(a^2 - b^2)}{a^2} \sin^2 \theta} d\theta \quad 7.41$$

But, from the properties of ellipse

$$\text{Eccentricity} \quad e = \sqrt{1 - \frac{b^2}{a^2}} \quad 7.42$$

$$e^2 = \left(\frac{a^2 - b^2}{a^2} \right) \quad 7.43$$

$$7.41, 7.43 \quad \Rightarrow \quad \text{Arc length} \quad AB = a \int_{\theta_1}^{\theta_2} \sqrt{1 - e^2 \sin^2 \theta} . d\theta \quad 7.44$$

This function cannot be integrated directly. Therefore it needs to be converted into a series using the binomial theorem and then can be integrated.

The binomial theorem gives:

$$(p + q)^n = \sum_{k=0}^n \binom{n}{k} p^{n-k} q^k \quad 7.45$$

$$7.44, 7.45 \quad \Rightarrow \quad \text{Arc length} \quad AB = a \int_{\theta_1}^{\theta_2} \left(1 - e^2 \sin^2 \theta \right)^{\frac{1}{2}} . d\theta$$

Evaluating this integral can be easier if it's evaluated as an Indefinite Integral and the limits applied after the final solution is derived.

Therefore, the length AB can be expressed in terms of the Constant of Integration C .

$$AB = a \int \left(1 - e^2 \sin^2 \theta \right)^{\frac{1}{2}} . d\theta + C$$

Applying Binomial theorem;

$$AB = a \int \left(1 + \left(\frac{1}{2} \right) (-e^2 \sin^2 \theta) + \left(\frac{1}{2} \right) \left(-\frac{1}{4} \right) (-e^2 \sin^2 \theta)^2 \right. \\ \left. + \left(\frac{1}{2} \right) \left(-\frac{1}{4} \right) \left(-\frac{3}{6} \right) (-e^2 \sin^2 \theta)^3 + \left(\frac{1}{2} \right) \left(-\frac{1}{4} \right) \left(-\frac{3}{6} \right) \left(-\frac{5}{8} \right) (-e^2 \sin^2 \theta)^4 + \dots \right) d\theta + C$$

$$AB = a \int \left(1 - \left(\frac{1}{2} \right) (e^2 \sin^2 \theta) - \left(\frac{1}{2} \right) \left(\frac{1}{4} \right) (e^4 \sin^4 \theta) \right. \\ \left. - \left(\frac{1}{2} \right) \left(\frac{1}{4} \right) \left(\frac{3}{6} \right) (e^6 \sin^6 \theta) - \left(\frac{1}{2} \right) \left(\frac{1}{4} \right) \left(\frac{3}{6} \right) \left(\frac{5}{8} \right) (e^8 \sin^8 \theta) + \dots \right) d\theta + C$$

$$AB = a \left[\int \left(1 - \left(\frac{1}{2} \right) (e^2 \sin^2 \theta) - \left(\frac{1}{2} \right) \left(\frac{1}{4} \right) (e^4 \sin^4 \theta) \right. \right. \\ \left. \left. - \left(\frac{1}{2} \right) \left(\frac{1}{4} \right) \left(\frac{3}{6} \right) (e^6 \sin^6 \theta) - \left(\frac{1}{2} \right) \left(\frac{1}{4} \right) \left(\frac{3}{6} \right) \left(\frac{5}{8} \right) (e^8 \sin^8 \theta) + \dots \right) d\theta \right] + C$$

$$AB = a \left[\int d\theta - \int \left(\frac{1}{2} \right) (e^2 \sin^2 \theta) d\theta - \int \left(\frac{1}{2} \right) \left(\frac{1}{4} \right) (e^4 \sin^4 \theta) d\theta \right. \\ \left. - \int \left(\frac{1}{2} \right) \left(\frac{1}{4} \right) \left(\frac{3}{6} \right) (e^6 \sin^6 \theta) d\theta - \int \left(\frac{1}{2} \right) \left(\frac{1}{4} \right) \left(\frac{3}{6} \right) \left(\frac{5}{8} \right) (e^8 \sin^8 \theta) d\theta - \dots \right] + C$$

$$AB = a \left[\int d\theta - \left(\frac{1}{2} \right) (e^2) \int (\sin^2 \theta) d\theta - \left(\frac{1}{2} \right) \left(\frac{1}{4} \right) e^4 \int (\sin^4 \theta) d\theta \right. \\ \left. - \left(\frac{1}{2} \right) \left(\frac{1}{4} \right) \left(\frac{3}{6} \right) e^6 \int (\sin^6 \theta) d\theta - \left(\frac{1}{2} \right) \left(\frac{1}{4} \right) \left(\frac{3}{6} \right) \left(\frac{5}{8} \right) e^8 \int (\sin^8 \theta) d\theta - \dots \right] + C$$

7.46

As these integrals are of the form $\int \sin^n \theta d\theta$, they can be integrated using the following Reduction Formula.

Reduction Formula gives:

If
$$I_n = \int \sin^n \theta d\theta,$$

Then,
$$nI_n = -\sin^{n-1} \theta \cos \theta + (n-1)I_{n-2} \quad 7.47$$

$$I_n = \frac{1}{n} \left[-\sin^{n-1} \theta \cos \theta + (n-1)I_{n-2} \right] \quad 7.48$$

$$I_0 = \int \sin^0 \theta d\theta$$

$$I_0 = \int 1 d\theta$$

$$I_0 = \theta + C_1 \quad 7.49$$

$$7.48 \Rightarrow n=2 \quad \int (\sin^2 \theta) d\theta = \frac{1}{2} \left[(-\sin^{(2-1)} \theta \cos \theta) + (2-1)I_{2-2} \right] + C_2$$

$$\int (\sin^2 \theta) d\theta = \frac{1}{2} \left[(-\sin \theta \cos \theta) + I_0 \right] + C_2$$

$$\int (\sin^2 \theta) d\theta = \frac{1}{2} \left[(-\sin \theta \cos \theta) + \theta \right] + C_3 \quad 7.50$$

$$7.48 \Rightarrow n=4 \quad \int (\sin^4 \theta) d\theta = \frac{1}{4} \left[(-\sin^{(4-1)} \theta \cos \theta) + (4-1)I_{4-2} \right] + C_4$$

$$\int (\sin^4 \theta) d\theta = \frac{1}{4} \left[(-\sin^3 \theta \cos \theta) + (3)I_2 \right] + C_4$$

$$\int (\sin^4 \theta) d\theta = \frac{1}{4} \left[(-\sin^3 \theta \cos \theta) + (3) \int (\sin^2 \theta) d\theta \right] + C_4$$

7.51

$$7.48 \quad \Rightarrow \quad n=6 \quad \int (\sin^6 \theta) d\theta = \frac{1}{6} \left[(-\sin^{(6-1)} \theta \cos \theta) + (6-1)I_{6-2} \right] + C_5$$

$$\int (\sin^6 \theta) d\theta = \frac{1}{6} \left[(-\sin^5 \theta \cos \theta) + (5)I_4 \right] + C_5$$

$$\int (\sin^6 \theta) d\theta = \frac{1}{6} \left[(-\sin^5 \theta \cos \theta) + (5) \int (\sin^4 \theta) d\theta \right] + C_5 \quad 7.52$$

$$7.48 \quad \Rightarrow \quad n=8 \quad \int (\sin^8 \theta) d\theta = \frac{1}{8} \left[(-\sin^{(8-1)} \theta \cos \theta) + (8-1)I_{8-2} \right] + C_6$$

$$\int (\sin^8 \theta) d\theta = \frac{1}{8} \left[(-\sin^7 \theta \cos \theta) + (7)I_6 \right] + C_6$$

$$\int (\sin^8 \theta) d\theta = \frac{1}{8} \left[(-\sin^7 \theta \cos \theta) + (7) \int (\sin^6 \theta) d\theta \right] + C_6 \quad 7.53$$

Substituting 7.59, 7.60, 7.61, 7.62 and 7.63 in 7.56 gives us the solution for the length AB .

7.49, 7.50, 7.51, 7.52 and 7.53 in 7.46 \Rightarrow

$$\begin{aligned} AB = a & \left[\theta - \left(\frac{1}{2} \right) (e^2) \frac{1}{2} \left[(-\sin \theta \cos \theta) + \theta \right] \right. \\ & - \left(\frac{1}{2} \right) \left(\frac{1}{4} \right) e^4 \frac{1}{4} \left[(-\sin^3 \theta \cos \theta) + (3) \int (\sin^2 \theta) d\theta \right] \\ & - \left(\frac{1}{2} \right) \left(\frac{1}{4} \right) \left(\frac{3}{6} \right) e^6 \frac{1}{6} \left[(-\sin^5 \theta \cos \theta) + (5) \int (\sin^4 \theta) d\theta \right] \\ & \left. - \left(\frac{1}{2} \right) \left(\frac{1}{4} \right) \left(\frac{3}{6} \right) \left(\frac{5}{8} \right) e^8 \frac{1}{8} \left[(-\sin^7 \theta \cos \theta) + (7) \int (\sin^6 \theta) d\theta \right] - \dots \right] + C_7 \end{aligned}$$

$$\begin{aligned}
AB = a & \left[\theta - \left(\frac{1}{2} \right) \left(\frac{1}{2} \right) (e^2) [(-\sin \theta \cos \theta) + \theta] \right. \\
& - \left(\frac{1}{2} \right) \left(\frac{1}{4} \right) \left(\frac{1}{4} \right) e^4 \left[(-\sin^3 \theta \cos \theta) + (3) \int (\sin^2 \theta) d\theta \right] \\
& - \left(\frac{1}{2} \right) \left(\frac{1}{4} \right) \left(\frac{3}{6} \right) \left(\frac{1}{6} \right) e^6 \left[(-\sin^5 \theta \cos \theta) + (5) \int (\sin^4 \theta) d\theta \right] \\
& \left. - \left(\frac{1}{2} \right) \left(\frac{1}{4} \right) \left(\frac{3}{6} \right) \left(\frac{5}{8} \right) \left(\frac{1}{8} \right) e^8 \left[(-\sin^7 \theta \cos \theta) + (7) \int (\sin^6 \theta) d\theta \right] - \dots \right] + C_7
\end{aligned}$$

7.54

The value of the integral can be determined in terms of x by back-substituting the values of $\theta, \sin \theta, \cos \theta$ and e .

7.46 \Rightarrow

$$x = a \sin \theta$$

$$\therefore \sin^2 \theta = \frac{x^2}{a^2}$$

$$\sin \theta = \sqrt{\frac{x^2}{a^2}}$$

$$\theta = \sin^{-1} \left(\frac{x}{a} \right)$$

$$\cos^2 \theta = 1 - \frac{x^2}{a^2}$$

$$\cos \theta = \sqrt{\frac{(a^2 - x^2)}{a^2}} \quad 7.55$$

7.43 \Rightarrow

$$e^2 = \left(\frac{a^2 - b^2}{a^2} \right)$$

7.36, 7.54 & 7.55 \Rightarrow

$$\begin{aligned}
 AB = a & \left[\left(\sin^{-1} \left(\sqrt{\frac{x^2}{a^2}} \right) \right) - \left(\frac{1}{2} \right) \left(\frac{1}{2} \right) (e^2) \left[\left(- \left(\sqrt{\frac{x^2}{a^2}} \right) \left(\sqrt{\frac{(a^2 - x^2)}{a^2}} \right) \right) + \left(\sin^{-1} \left(\sqrt{\frac{x^2}{a^2}} \right) \right) \right] \right. \\
 & - \left(\frac{1}{2} \right) \left(\frac{1}{4} \right) \left(\frac{1}{4} \right) e^4 \left[\left(- \left(\sqrt{\frac{x^2}{a^2}} \right) \cdot \left(\sqrt{\frac{(a^2 - x^2)}{a^2}} \right) \right) + (3) \left[\left(- \left(\sqrt{\frac{x^2}{a^2}} \right) \left(\sqrt{\frac{(a^2 - x^2)}{a^2}} \right) \right) + \left(\sin^{-1} \left(\sqrt{\frac{x^2}{a^2}} \right) \right) \right] \right] \\
 & - \left(\frac{1}{2} \right) \left(\frac{1}{4} \right) \left(\frac{3}{6} \right) \left(\frac{1}{6} \right) e^6 \left[\left(- \left(\sqrt{\frac{x^2}{a^2}} \right) \cdot \left(\sqrt{\frac{(a^2 - x^2)}{a^2}} \right) \right) + (5) \left[\left(- \left(\sqrt{\frac{x^2}{a^2}} \right) \cdot \left(\sqrt{\frac{(a^2 - x^2)}{a^2}} \right) \right) + (3) \left[\left(- \left(\sqrt{\frac{x^2}{a^2}} \right) \left(\sqrt{\frac{(a^2 - x^2)}{a^2}} \right) \right) + \left(\sin^{-1} \left(\sqrt{\frac{x^2}{a^2}} \right) \right) \right] \right] \right] \\
 & - \left(\frac{1}{2} \right) \left(\frac{1}{4} \right) \left(\frac{3}{6} \right) \left(\frac{5}{8} \right) \left(\frac{1}{8} \right) e^8 \left[\left(- \left(\sqrt{\frac{x^2}{a^2}} \right) \cdot \left(\sqrt{\frac{(a^2 - x^2)}{a^2}} \right) \right) + (7) \left[\left(- \left(\sqrt{\frac{x^2}{a^2}} \right) \cdot \left(\sqrt{\frac{(a^2 - x^2)}{a^2}} \right) \right) + (5) \left[\left(- \left(\sqrt{\frac{x^2}{a^2}} \right) \cdot \left(\sqrt{\frac{(a^2 - x^2)}{a^2}} \right) \right) + (3) \left[\left(- \left(\sqrt{\frac{x^2}{a^2}} \right) \left(\sqrt{\frac{(a^2 - x^2)}{a^2}} \right) \right) + \left(\sin^{-1} \left(\sqrt{\frac{x^2}{a^2}} \right) \right) \right] \right] \right] - \dots \right] + C_7
 \end{aligned}$$

7.56

The terms succeeding the third term in the above integral are insignificant due to the larger denominators and very high powers of e .

Therefore they can be neglected and the length AB can be equated to the first three terms for all realistic calculations with a high degree of confidence.

$$AB \cong a \left[\left(\sin^{-1} \left(\sqrt{\frac{x^2}{a^2}} \right) \right) - \left(\frac{1}{2} \right) \left(\frac{1}{2} \right) (e^2) \left[\left(- \left(\sqrt{\frac{x^2}{a^2}} \right) \left(\sqrt{\frac{(a^2 - x^2)}{a^2}} \right) \right) + \left(\sin^{-1} \left(\sqrt{\frac{x^2}{a^2}} \right) \right) \right] \right. \\ \left. - \left(\frac{1}{2} \right) \left(\frac{1}{4} \right) \left(\frac{1}{4} \right) e^4 \left[\left(- \left(\sqrt{\frac{x^2}{a^2}} \right)^3 \left(\sqrt{\frac{(a^2 - x^2)}{a^2}} \right) \right) + (3) \left[\left(- \left(\sqrt{\frac{x^2}{a^2}} \right) \left(\sqrt{\frac{(a^2 - x^2)}{a^2}} \right) \right) + \left(\sin^{-1} \left(\sqrt{\frac{x^2}{a^2}} \right) \right) \right] \right] \right] + C_8$$

7.57

The above integral provides the Arc Length of the orbital ellipse as an Indeterminate Integral. The Determinate Integral can have the limits x_1 and x_2 , respective to θ_1 and θ_2 .

Therefore the arc length between the x coordinates x_1 and x_2 can be given as:

$$AB = a \left[\left(\sin^{-1} \left(\frac{x}{a} \right) \right) - \left(\frac{1}{2} \right) \left(\frac{1}{2} \right) (e^2) \left[\left(- \left(\frac{x}{a} \right) \left(\sqrt{\frac{(a^2 - x^2)}{a^2}} \right) \right) + \left(\sin^{-1} \left(\frac{x}{a} \right) \right) \right] \right. \\ \left. - \left(\frac{1}{2} \right) \left(\frac{1}{4} \right) \left(\frac{1}{4} \right) e^4 \left[\left(- \left(\left(\frac{x}{a} \right) \right)^3 \left(\sqrt{\frac{(a^2 - x^2)}{a^2}} \right) \right) + (3) \left[\left(- \left(\frac{x}{a} \right) \left(\sqrt{\frac{(a^2 - x^2)}{a^2}} \right) \right) + \left(\sin^{-1} \left(\frac{x}{a} \right) \right) \right] \right] \right]_{x_1}^{x_2}$$

7.58

The technique used in TEC Builder calculates the length of the arc from the origin to the position of the satellite on every row. Therefore the upper limit of the integral is the x coordinate x''' in the new transformed coordinate system and the lower limit is 0.

Therefore the arc length from $x=0$ or the y axis can be calculated by substituting $x_2 = 0$ and $x_1 = x'''$.

7.58 \Rightarrow

$$\begin{aligned}
 AB = & a \left[\left(\sin^{-1} \left(\frac{x_2}{a} \right) \right) - \left(\frac{1}{2} \right) \left(\frac{1}{2} \right) (e^2) \left[\left(- \left(\frac{x_2}{a} \right) \left(\sqrt{\frac{(a^2 - x_2^2)}{a^2}} \right) \right) + \left(\sin^{-1} \left(\frac{x_2}{a} \right) \right) \right] \right. \\
 & - \left(\frac{1}{2} \right) \left(\frac{1}{4} \right) \left(\frac{1}{4} \right) e^4 \left[\left(- \left(\frac{x_2}{a} \right)^3 \left(\sqrt{\frac{(a^2 - x_2^2)}{a^2}} \right) \right) + (3) \left[\left(- \left(\frac{x_2}{a} \right) \left(\sqrt{\frac{(a^2 - x_2^2)}{a^2}} \right) \right) + \left(\sin^{-1} \left(\frac{x_2}{a} \right) \right) \right] \right] \\
 & - a \left[\left(\sin^{-1} \left(\frac{x_1}{a} \right) \right) - \left(\frac{1}{2} \right) \left(\frac{1}{2} \right) (e^2) \left[\left(- \left(\frac{x_1}{a} \right) \left(\sqrt{\frac{(a^2 - x_1^2)}{a^2}} \right) \right) + \left(\sin^{-1} \left(\frac{x_1}{a} \right) \right) \right] \right. \\
 & \left. \left. - \left(\frac{1}{2} \right) \left(\frac{1}{4} \right) \left(\frac{1}{4} \right) e^4 \left[\left(- \left(\frac{x_1}{a} \right)^3 \left(\sqrt{\frac{(a^2 - x_1^2)}{a^2}} \right) \right) + (3) \left[\left(- \left(\frac{x_1}{a} \right) \left(\sqrt{\frac{(a^2 - x_1^2)}{a^2}} \right) \right) + \left(\sin^{-1} \left(\frac{x_1}{a} \right) \right) \right] \right] \right] \right]
 \end{aligned}$$

7.59

Substituting $x_2 = 0$ and $x_1 = x''' \Rightarrow$

$$\begin{aligned}
 AB = & a \left[\left(\sin^{-1} \left(\frac{x'''}{a} \right) \right) - \left(\frac{1}{2} \right) \left(\frac{1}{2} \right) (e^2) \left[\left(- \left(\frac{x'''}{a} \right) \left(\sqrt{\frac{(a^2 - x'''^2)}{a^2}} \right) \right) + \left(\sin^{-1} \left(\frac{x'''}{a} \right) \right) \right] \right. \\
 & - \left(\frac{1}{2} \right) \left(\frac{1}{4} \right) \left(\frac{1}{4} \right) e^4 \left[\left(- \left(\frac{x'''}{a} \right)^3 \left(\sqrt{\frac{(a^2 - x'''^2)}{a^2}} \right) \right) + (3) \left[\left(- \left(\frac{x'''}{a} \right) \left(\sqrt{\frac{(a^2 - x'''^2)}{a^2}} \right) \right) + \left(\sin^{-1} \left(\frac{x'''}{a} \right) \right) \right] \right] \\
 & - a \left[\left(\sin^{-1} \left(\frac{0}{a} \right) \right) - \left(\frac{1}{2} \right) \left(\frac{1}{2} \right) (e^2) \left[\left(- \left(\frac{0}{a} \right) \left(\sqrt{\frac{(a^2 - 0^2)}{a^2}} \right) \right) + \left(\sin^{-1} \left(\frac{0}{a} \right) \right) \right] \right. \\
 & \left. \left. - \left(\frac{1}{2} \right) \left(\frac{1}{4} \right) \left(\frac{1}{4} \right) e^4 \left[\left(- \left(\frac{0}{a} \right)^3 \left(\sqrt{\frac{(a^2 - 0^2)}{a^2}} \right) \right) + (3) \left[\left(- \left(\frac{0}{a} \right) \left(\sqrt{\frac{(a^2 - 0^2)}{a^2}} \right) \right) + \left(\sin^{-1} \left(\frac{0}{a} \right) \right) \right] \right] \right] \right]
 \end{aligned}$$

$$\begin{aligned}
AB &= a \left[\left(\sin^{-1} \left(\frac{x''''}{a} \right) \right) - \left(\frac{1}{2} \right) \left(\frac{1}{2} \right) (e^2) \left[\left(- \left(\frac{x''''}{a} \right) \left(\sqrt{\frac{(a^2 - x''''^2)}{a^2}} \right) \right) + \left(\sin^{-1} \left(\frac{x''''}{a} \right) \right) \right] \right. \\
&\quad \left. - \left(\frac{1}{2} \right) \left(\frac{1}{4} \right) \left(\frac{1}{4} \right) e^4 \left[\left(- \left(\frac{x''''}{a} \right)^3 \left(\sqrt{\frac{(a^2 - x''''^2)}{a^2}} \right) \right) + (3) \left[\left(- \left(\frac{x''''}{a} \right) \left(\sqrt{\frac{(a^2 - x''''^2)}{a^2}} \right) \right) + \left(\sin^{-1} \left(\frac{x''''}{a} \right) \right) \right] \right] \right. \\
&\quad \left. - a \left[\left(\sin^{-1}(0) \right) - \left(\frac{1}{2} \right) \left(\frac{1}{2} \right) (e^2) \left[\left(- (0) \left(\sqrt{\frac{(a^2 - 0^2)}{a^2}} \right) \right) + \left(\sin^{-1}(0) \right) \right] \right] \right. \\
&\quad \left. - \left(\frac{1}{2} \right) \left(\frac{1}{4} \right) \left(\frac{1}{4} \right) e^4 \left[\left(- (0)^3 \left(\sqrt{\frac{(a^2 - 0^2)}{a^2}} \right) \right) + (3) \left[\left(- (0) \left(\sqrt{\frac{(a^2 - 0^2)}{a^2}} \right) \right) + \left(\sin^{-1}(0) \right) \right] \right] \right]
\end{aligned}$$

Therefore:

$$\begin{aligned}
AB &= a \left[\left(\sin^{-1} \left(\frac{x''''}{a} \right) \right) - \left(\frac{1}{2} \right) \left(\frac{1}{2} \right) (e^2) \left[\left(- \left(\frac{x''''}{a} \right) \left(\sqrt{\frac{(a^2 - x''''^2)}{a^2}} \right) \right) + \left(\sin^{-1} \left(\frac{x''''}{a} \right) \right) \right] \right. \\
&\quad \left. - \left(\frac{1}{2} \right) \left(\frac{1}{4} \right) \left(\frac{1}{4} \right) e^4 \left[\left(- \left(\frac{x''''}{a} \right)^3 \left(\sqrt{\frac{(a^2 - x''''^2)}{a^2}} \right) \right) + (3) \left[\left(- \left(\frac{x''''}{a} \right) \left(\sqrt{\frac{(a^2 - x''''^2)}{a^2}} \right) \right) + \left(\sin^{-1} \left(\frac{x''''}{a} \right) \right) \right] \right] \right. \\
&\quad \left. - a \left[(0) - \left(\frac{1}{2} \right) \left(\frac{1}{2} \right) (e^2) [0] - \left(\frac{1}{2} \right) \left(\frac{1}{4} \right) \left(\frac{1}{4} \right) e^4 [(0) + (3)][(0) + (0)] \right] \right]
\end{aligned}$$

$$\begin{aligned}
AB &= a \left[\left(\sin^{-1} \left(\frac{x''''}{a} \right) \right) - \left(\frac{1}{2} \right) \left(\frac{1}{2} \right) (e^2) \left[\left(- \left(\frac{x''''}{a} \right) \left(\sqrt{\frac{(a^2 - x''''^2)}{a^2}} \right) \right) + \left(\sin^{-1} \left(\frac{x''''}{a} \right) \right) \right] \right. \\
&\quad \left. - \left(\frac{1}{2} \right) \left(\frac{1}{4} \right) \left(\frac{1}{4} \right) e^4 \left[\left(- \left(\frac{x''''}{a} \right)^3 \left(\sqrt{\frac{(a^2 - x''''^2)}{a^2}} \right) \right) + (3) \left[\left(- \left(\frac{x''''}{a} \right) \left(\sqrt{\frac{(a^2 - x''''^2)}{a^2}} \right) \right) + \left(\sin^{-1} \left(\frac{x''''}{a} \right) \right) \right] \right] \right] - 0
\end{aligned}$$

$$AB = a \left[\left(\sin^{-1} \left(\frac{x''''}{a} \right) \right) - \left(\frac{1}{2} \right) \left(\frac{1}{2} \right) (e^2) \left[\left(- \left(\frac{x''''}{a} \right) \left(\sqrt{\frac{(a^2 - x'''^2)}{a^2}} \right) \right) + \left(\sin^{-1} \left(\frac{x''''}{a} \right) \right) \right] \right. \\ \left. - \left(\frac{1}{2} \right) \left(\frac{1}{4} \right) \left(\frac{1}{4} \right) e^4 \left[\left(- \left(\frac{x''''}{a} \right) \left(\sqrt{\frac{(a^2 - x'''^2)}{a^2}} \right) \right) + (3) \left[\left(- \left(\frac{x''''}{a} \right) \left(\sqrt{\frac{(a^2 - x'''^2)}{a^2}} \right) \right) + \left(\sin^{-1} \left(\frac{x''''}{a} \right) \right) \right] \right] \right]$$

7.60

The above expression has been used in calculating the arc length from the $x = 0$ or the y axis in column AP in TEC Builder.

The TEC Builder calculates the above expression in parts. The parts calculated and their corresponding TEC Builder Columns are given below:

	Calculation part	TEC Builder Column
1	a	AK
2	x''''	AG
3	$\sin^{-1} \left(\frac{x''''}{a} \right)$	AN
4	$\left[\left(- \left(\frac{x''''}{a} \right) \left(\sqrt{\frac{(a^2 - x'''^2)}{a^2}} \right) \right) + \left(\sin^{-1} \left(\frac{x''''}{a} \right) \right) \right]$	AO
5	e^2	AM

Table 7.2 Components of the Arc Length calculation formula and corresponding
TEC Builder Columns

As the integral component $\left(-\left(\frac{x'''}{a} \right) \left(\sqrt{\frac{(a^2 - x''^2)}{a^2}} \right) + \left(\sin^{-1} \left(\frac{x'''}{a} \right) \right) \right)$ is repeated twice in

the formula 7.110. Therefore, it is separately calculated in column AO and used in the final calculation of the formula. The following Excel formula is used for it's calculation:

$$AO=(AN1 -(AG1*(SQRT((AK1*AK1) - (AG1*AG1)))/(AK1*AK1))) \quad 7.61$$

The Arc length from the from $x=0$ or the y axis in column AP using the following Excel formula:

$$AP1=(AK1)*((AN1) - (((AM1)/4)*(AO1)) - (((AM1*AM1)/32)*((3*(AO1)) - ((AG1*AG1*AG1)*(SQRT((AK1*AK1) - (AG1*AG1)))/(AK1*AK1*AK1*AK1)))))) \quad 7.62$$

The final Arc length the satellite traces between two subsequent readings (ie. between two x coordinates) is determined by calculating the difference between the successive Arc lengths from y axis calculated in column AP.

The following Excel formula gives the Arc Length between two subsequent readings:

$$AQ1=ABS(AP1-AP2) \quad 7.63$$

7.6 Calculation of the UPEC Bar length

7.6.1 Tangent Line Construction and the determination of the Incident Angle

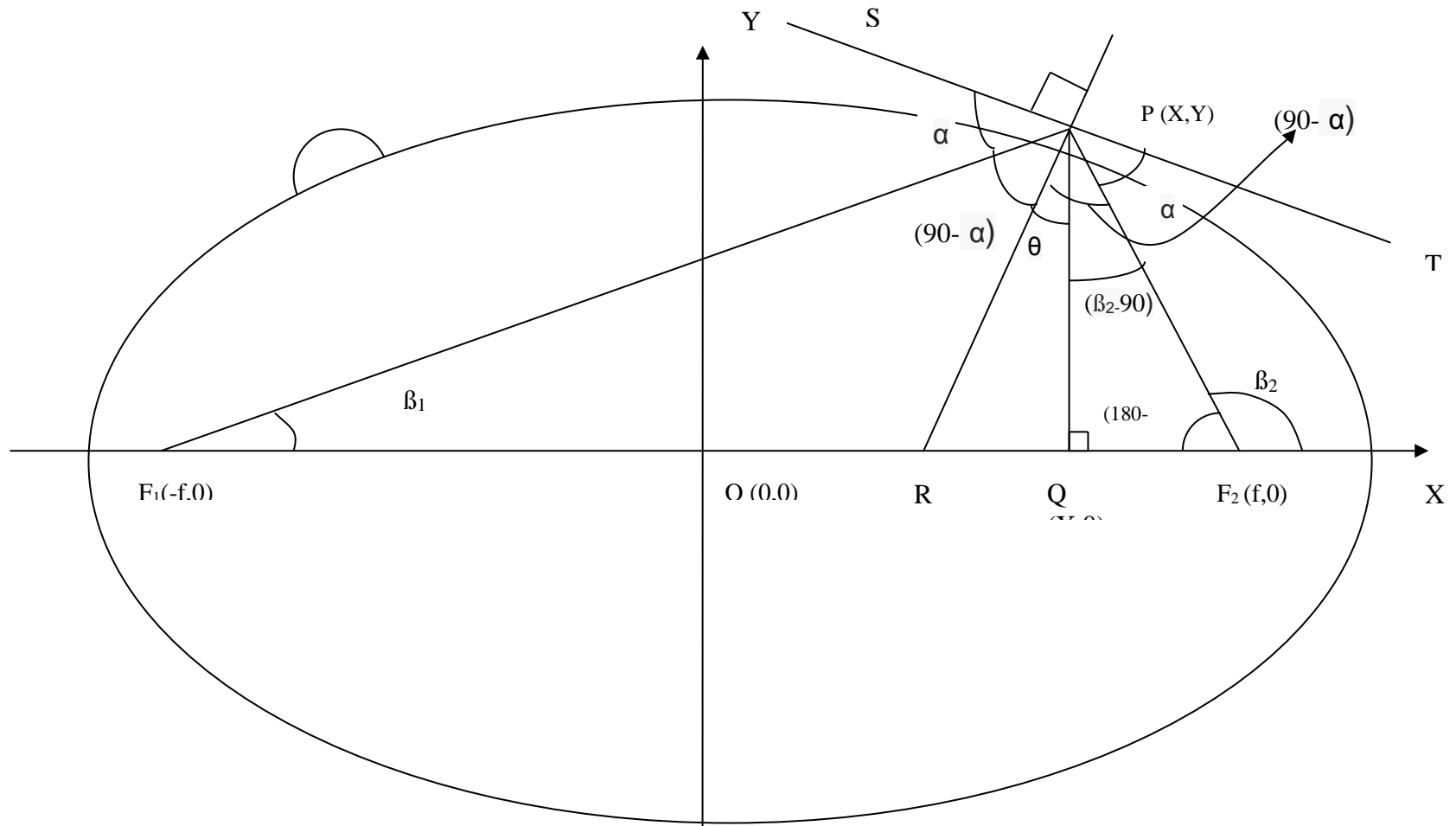


Figure 7.8 Descriptive diagram for Tangent Line construction and the determination of the Incident Angle

Considering the figure 7.8:

Let $P(x, y)$ be any point in the orbital ellipse and the line SPT be the Tangent at that point;

Let $F_1(-f, 0)$ and $F_2(f, 0)$ be the foci of the ellipse. Either one of them could be the centre of the earth.

By the definition of ellipse,

$$\angle SPF_1 = \angle TPF_2$$

7.64

This angle is equal to the Incident angle α .

If the lines connecting the satellite and the foci make angles β_1 and β_2 respectively with the x axis, the perpendicular line to the x axis from the satellite meets the x axis at Q, the perpendicular line to the tangent line meets the x axis at R and the angle between PR and PQ ($\angle QPR$) is θ , then:

$$\angle PF_2Q = 180 - \beta_2$$

7.65

$$\angle QPF_2 = 180 - 90 - (180 - \beta_2)$$

$$\angle QPF_2 = (\beta_2 - 90)$$

7.66

$$SPT \perp RP$$

7.64

$$\angle SPF_1 = \angle TPF_2 = \alpha$$

$$\angle RPF_1 = \angle RPF_2 = 90 - \alpha \quad 7.67$$

$$\angle QPF_1 = 90 - \beta_1 \quad 7.68$$

$$\angle RPQ = \theta \quad 7.69$$

$$\angle QPF_1 = \angle QPR + \angle RPF_1$$

$$\angle RPQ = \angle QPF_1 - \angle RPF_1$$

7.67, 7.68 & 7.69

$$\theta = (90 - \beta_1) - (90 - \alpha)$$

$$\theta = (\alpha - \beta_1) \quad 7.68$$

$$\angle RPF_2 = \angle RPQ + \angle QPF_2$$

$$\angle RPQ = \angle RPF_2 - \angle QPF_2$$

7.67, 7.68 & 7.69

$$\theta = (90 - \alpha) - (\beta_2 - 90)$$

$$\theta = (180 - \alpha - \beta_2) \quad 7.69$$

7.68 & 7.69

$$\theta = (\alpha - \beta_1) = (180 - \alpha - \beta_2)$$

$$2\alpha = (\beta_1 - \beta_2 + 180)$$

$$\alpha = \frac{(\beta_1 - \beta_2 + 180)}{2} \quad 7.70$$

In ΔPQF_1 ,

$$\tan \beta_1 = \frac{PQ}{F_1Q}$$

$$\tan \beta_1 = \frac{y}{|f| + x}$$

$$\beta_1 = \tan^{-1} \left[\frac{y}{|f| + x} \right] \quad 7.73$$

In ΔPQF_2 ,

$$\tan(180 - \beta_2) = \frac{PQ}{F_2Q}$$

$$\tan \beta_2 = \frac{y}{|f| - x}$$

$$180 - \beta_2 = \tan^{-1} \left[\frac{y}{|f| - x} \right]$$

$$\beta_2 = 180 - \tan^{-1} \left[\frac{y}{|f| - x} \right] \quad 7.74$$

β_1, β_2 & α are calculate in columns AH, AI & AJ in the TEC Builder. The formulae used are:

$$AH1 = \text{ATAN}(AE1/(AF1+AG1))*180/\text{PI}() \quad 7.75$$

$$AI1 = (180 - \text{ATAN}(AE1/(AF1-AG1))*180/\text{PI}()) \quad 7.76$$

$$AJ1 = (AH1 - AI1 + 180)/2 \quad 7.77$$

7.6.2 Calculation of the UPEC Bar length

If the equation for an ellipse is given as

$$\frac{x^2}{a^2} + \frac{y^2}{b^2} = 1$$

Then, the equation of the Tangent line to that ellipse at a point $P(x_0, y_0)$ in the ellipse is given by:

$$\frac{xx_0}{a^2} + \frac{yy_0}{b^2} = 1 \quad 7.78$$

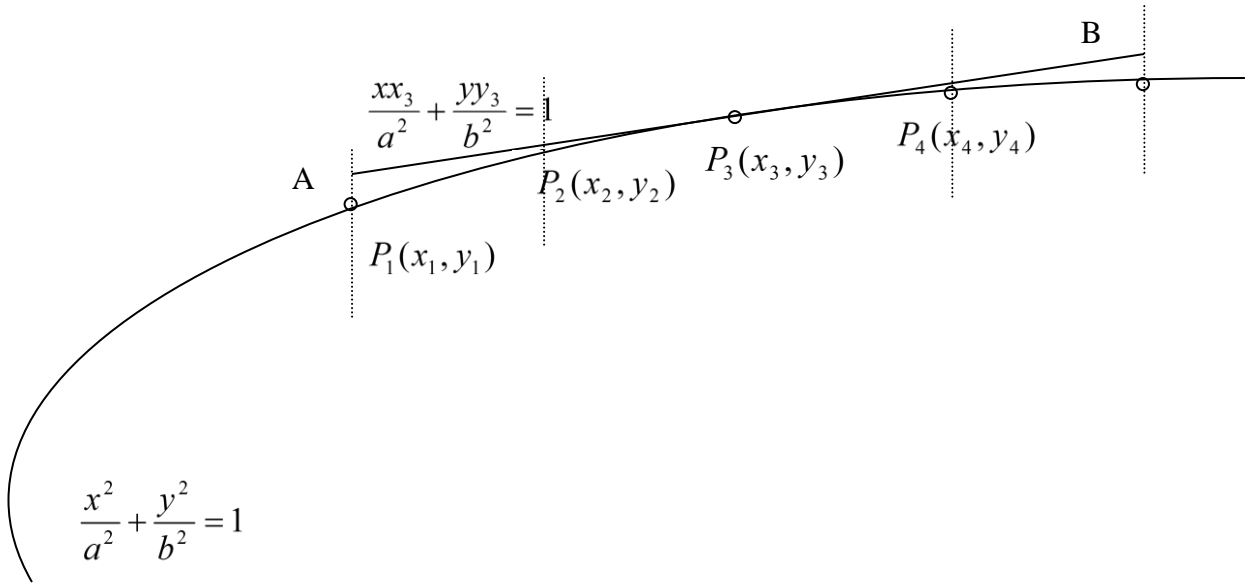


Figure 7.9 – Calculation of the UPEC Bar length

Considering the Figure 7.9 above:

The orbital position data and the electron density data are provided in per minute basis.

The distance between two points in straight line is given by:

$$d = \sqrt{[(x_a - x_b)^2 + (y_a - y_b)^2]} \quad 7.79$$

The line equation of a tangent line at point $P_3(x_3, y_3)$ is given by:

$$\frac{xx_3}{a^2} + \frac{yy_3}{b^2} = 1 \quad 7.80$$

$$xx_3b^2 + yy_3a^2 = a^2b^2$$

$$y = \frac{a^2b^2 - xx_3b^2}{y_3a^2}$$

$$y = \frac{b^2}{a^2} \frac{(a^2 - x x_3)}{y_3} \quad 7.81$$

Any point on the tangent line can be given by 7.81

$$y_1^* = \frac{b^2}{a^2} \frac{(a^2 - x_1 x_3)}{y_3}$$

$$y_5^* = \frac{b^2}{a^2} \frac{(a^2 - x_5 x_3)}{y_3}$$

$$7.79 \quad d = \sqrt{[(x_5 - x_1)^2 + (y_5^* - y_1^*)^2]}$$

$$d = \sqrt{\left[(x_5 - x_1)^2 + \left(\frac{b^2}{a^2} \frac{(a^2 - x_5 x_3)}{y_3} - \frac{b^2}{a^2} \frac{(a^2 - x_1 x_3)}{y_3} \right)^2 \right]}$$

$$d = \sqrt{\left[(x_5 - x_1)^2 + \left(\frac{b^2}{a^2} \frac{(a^2 - x_5 x_3)}{y_3} - \frac{b^2}{a^2} \frac{(a^2 - x_1 x_3)}{y_3} \right)^2 \right]}$$

$$d = \sqrt{\left[(x_5 - x_1)^2 + \frac{b^4}{a^4 y_3^2} \left((a^2 - x_5 x_3) - (a^2 - x_1 x_3) \right)^2 \right]}$$

$$d = \sqrt{\left[(x_5 - x_1)^2 + \frac{b^4}{a^4 y_3^2} (x_1 x_3 - x_5 x_3)^2 \right]}$$

$$d = \sqrt{\left[(x_5 - x_1)^2 + \frac{b^4 x_3^2}{a^4 y_3^2} (x_1 - x_5)^2 \right]}$$

$$d = \sqrt{\left[(x_5 - x_1)^2 \left(1 + \frac{b^4 x_3^2}{a^4 y_3^2} \right) \right]}$$

$$d = \sqrt{\left[\frac{(x_5 - x_1)^2}{a^2 y_3^2} (a^4 y_3^2 + b^4 x_3^2) \right]}$$

$$d = \frac{(x_5 - x_1)}{a y_3} \sqrt{[(x_3 b^2)^2 + (y_3 a^2)^2]} \quad 7.82$$

Here $x = x'''$ and $y = y'''$

7.7 Summery of TEC Builder Calculations

TEC Builder Sheet 1

No.	TEC Builder Column	Excel Formula
1.	A.	$A1=(C1*24) + D1$
2.	B.	Direct Input
3.	C.	Direct Input
4.	D.	Direct Input
5.	E.	Direct Input
6.	F.	Direct Input
7.	G.	Direct Input
8.	H.	Direct Input
9.	I.	Direct Input
10.	J.	Direct Input
11.	K.	Empty
12.	L.	$L1=E1*E1$

Table 7.3-a Summery of TEC Builder Calculations - TEC Builder Sheet 1

No.	TEC Builder Column	Excel Formula
13.	M.	$M1 = F1 * F1$
14.	N.	$N1 = G1 * G1$
15.	O.	1
16.	P.	$P1 = 2 * E1 * F1$
17.	Q.	$Q1 = (2) * F1 * G1$
18.	R.	$R1 = (2) * E1 * G1$
19.	S.	$S1 = 2 * E1$
20.	T.	$T1 = 2 * F1$
21.	U.	$U1 = (2) * G1$
22.	V.	$V1 = P1709$
23.	W.	$W1 = ((E1 * (\cos(V1 * \pi() / 180))) + (F1 * (\sin(V1 * \pi() / 180))))$
24.	X.	$X1 = ((F1 * (\cos(V1 * \pi() / 180))) - (E1 * (\sin(V1 * \pi() / 180))))$
25.	Y.	$Y1 = Q1681$
26.	Z.	$Z1 = ((X1 * (\cos(Y1 * \pi() / 180))) + (G1 * (\sin(Y1 * \pi() / 180))))$

Table 7.3-b Summery of TEC Builder Calculations - TEC Builder Sheet 1

No.	TEC Builder Column	Excel Formula
27.	AA.	$AA1 = ((G1 * (\cos(Y1 * \pi / 180))) - (X1 * (\sin(Y1 * \pi / 180))))$
28.	AB.	$AB1 = \sqrt{(W1 * W1) + (Z1 * Z1)}$
29.	AC.	$AC1 = P1718$
30.	AD.	$AD1 = ((W1 * (\cos(AC1 * \pi / 180))) + (Z1 * (\sin(AC1 * \pi / 180))))$
31.	AE.	$AE1 = ((Z1 * (\cos(AC1 * \pi / 180))) - (W1 * (\sin(AC1 * \pi / 180))))$
32.	AF.	$AF1 = P1738$
33.	AG.	$AG1 = ((AD1) - (AF1))$
34.	AH.	$AH1 = \text{ATAN}(AE1 / (AF1 + AG1)) * 180 / \pi$
35.	AI.	$AI1 = (180 - \text{ATAN}(AE1 / (AF1 - AG1)) * 180 / \pi)$
36.	AJ.	$AJ1 = (AH1 - AI1 + 180) / 2$
37.	AK.	$AK1 = P1741$
38.	AL.	$AL1 = P1743$
39.	AM.	$AM1 = ((AK1 * AK1) - (AL1 * AL1)) / (AK1 * AK1)$
40.	AN.	$AN1 = \text{ASIN}(AG1 / AK1)$

Table 7.3-c Summery of TEC Builder Calculations - TEC Builder Sheet 1

No.	TEC Builder Column	Excel Formula
41.	AO.	$AO1=(AN1-(AG1*(SQRT((AK1*AK1)-(AG1*AG1)))/(AK1*AK1)))$
42.	AP.	$AP1=(AK1)*((AN1)-(((AM1)/4)*(AO1))-(((AM1*AM1)/32)*((3*(AO1))-((AG1*AG1*AG1)*(SQRT((AK1*AK1)-(AG1*AG1)))/(AK1*AK1*AK1*AK1))))))$
43.	AQ.	$AQ1=ABS(AP1-AP2)$
44.	AR.	$AR1=VLOOKUP(A1,Sheet2!A:G,7,FALSE)$
45.	AS.	$AS1=(AQ1*AR1)*1000000000$
46.	AT.	$AT1=(AS1+AS2+AS3+AS4)$
47.	AU.	$AU1=AQ1+AQ2+AQ3+AQ4$
48.	AV.	$AV1=(AT1/AU1)/1000$
49.	AW.	$AW1=P30412$
50.	AX.	$AX1=P30414$
51.	AY.	$AY1=((AG1-AG5)/(((AW1)^2)*AE3))*(SQRT(((AG3*((AX1)^2))^2)+((AE3*((AW1)^2))^2)))$
52.	AZ.	$AZ1=AV1*AY1/(10^{13})$
53.	BA.	$BA1=((AZ1/AY1)*20000)$
54.	BB.	$BB1=IF(BA1>0.00001,BA1*100\%,0\%)$

Table 7.3-d Summery of TEC Builder Calculations - TEC Builder Sheet 1

TEC Builder Sheet 2

No.	TEC Builder Column	Calculation	Excel Formula
1.	A.		$A1 = (C1 * 24) + F1$
2.	B.	Value Only	Direct Input
3.	C.		$C1 = B1 - \text{DATE}(\text{YEAR}(B1), 1, 0)$
4.	D.	Value Only	Direct Input
5.	E.	Value Only	Direct Input
6.	F.		$F1 = D1 - E1$
7.	G.	Value Only	Direct Input

Table 7.4 Summery of TEC Builder Calculations - TEC Builder Sheet 2

7.8 Verifications

Verification of the multitude of calculations carried out in TEC Builder can be carried out by means of the following evidences:

- Verification 1: Line of Node intercept value close to zero
- Verification 2: Z'' coordinate close to zero
- Verification 3: Argument of Periapsis values are very close by both methods
- Verification 4: The transformed coordinates produce perfect elliptical orbits.
- Verification 5: Consistent inclination angle over the orbital period, which gradually changes in conformity with actual GEI/J2000 coordinate plots

The principles behind the above verifications and evidences for them are provided in the following sections:

7.8.1 Verification 1: Line of Node intercept value close to zero

In the algorithm, the Step 13 states “the Line of Nodes is the intersection line of the orbital plane and the reference plane. By definition the Longitude of the Ascending Node (Ω) is the angle between the reference direction (Vernal Equinox) and that of the Ascending Node in the Line of Nodes measured positively from 0^0 to 180^0 in the forward direction. If the line equation of the Line of Nodes is determined from the GEI/J2000 coordinates of the Ascending Node and the Descending Node, the Gradient of that line will be equal to the Longitude of the Ascending Node (Ω) as the reference X axis direction is the direction of Vernal Equinox. Z coordinates in that line equation will be equal to (or very close to) zero.” This can be illustrated by Figure 6.7.

Also, the intercept of that line should be going through the origin, which is the centre of the earth, if all the calculations, transformations and programming worked correctly.

When the algorithm is implemented, this verification is attained as the intercept values are very close to zero.

The intercept values of the Line of Nodes equation are given below in Table 7.5 for sampled dates:

No	Date	Intercept values of the Line of Nodes equation (as a percentage of periapsis)
1	01/03/2004	0.00013
2	11/02/2004	0.00012
3	12/05/2004	0.00014
4	06/07/2004	0.00021
5	17/01/2005	0.00019
6	24/04/2005	0.00020
7	17/05/2005	0.00018
8	18/07/2005	0.00014
9	08/08/2005	0.00019
10	02/03/2006	0.00068

Table 7.5 Intercept values of the Line of Nodes equation for sampled dates

7.8.2 Verification 2: Z'' coordinate close to zero

The algorithm converts GEI/J2000, which have varying x, y, z coordinates to a coordinate system with x and y axes on the orbital plane and the z axis perpendicular to that plane.

The step 6 of the algorithm states that “from point 7 till point 35, the algorithm determines the ellipse equation of the orbit in the format:

$$\frac{x^2}{a^2} + \frac{y^2}{b^2} = 1 \quad 6.7$$

For that, it is necessary to carry out axis rotations to bring the GEI/J2000 based coordinates to the orbital axis, then rotate the X axis to the semi major axis of the ellipse and then move the origin to the centre of the ellipse from the centre of the earth which is a focus of the ellipse”.

Therefore, if the algorithm is working without errors, all the z coordinates obtained after the last coordinates transformation should be zero (or very small values). It can be seen that the equation 6.7 is a 2D equation and there are no z values. This is verified by the following graphs of original z coordinates in GEI/J2000 coordinates values and z coordinates values after the coordinate transformations against Time.

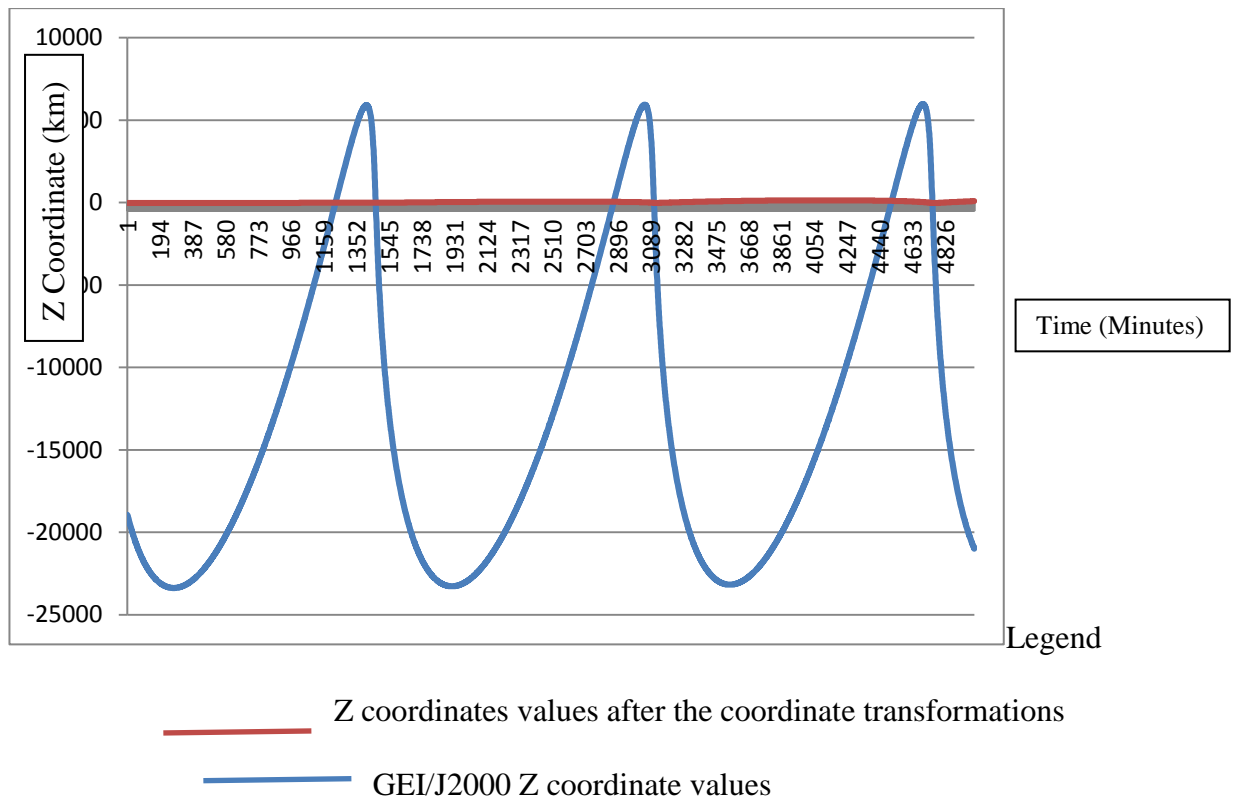


Figure 7.10 Graph of GEI/J2000 Z coordinate values and z coordinates values after the coordinate transformations against Time starting at 00-00-00 on 10/06/2004

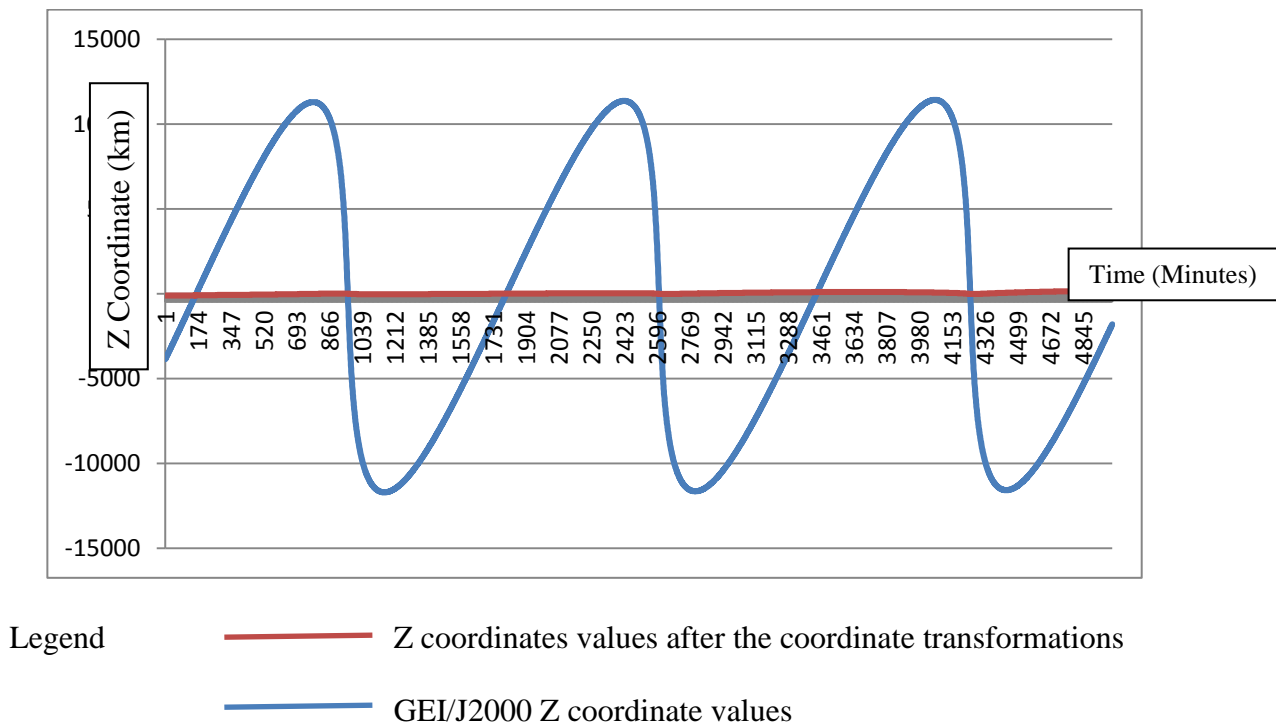


Figure 7.11 Graph of GEI/J2000 Z coordinate values and z coordinates values after the coordinate transformations against Time starting at 00-00-00 on 30/10/2004

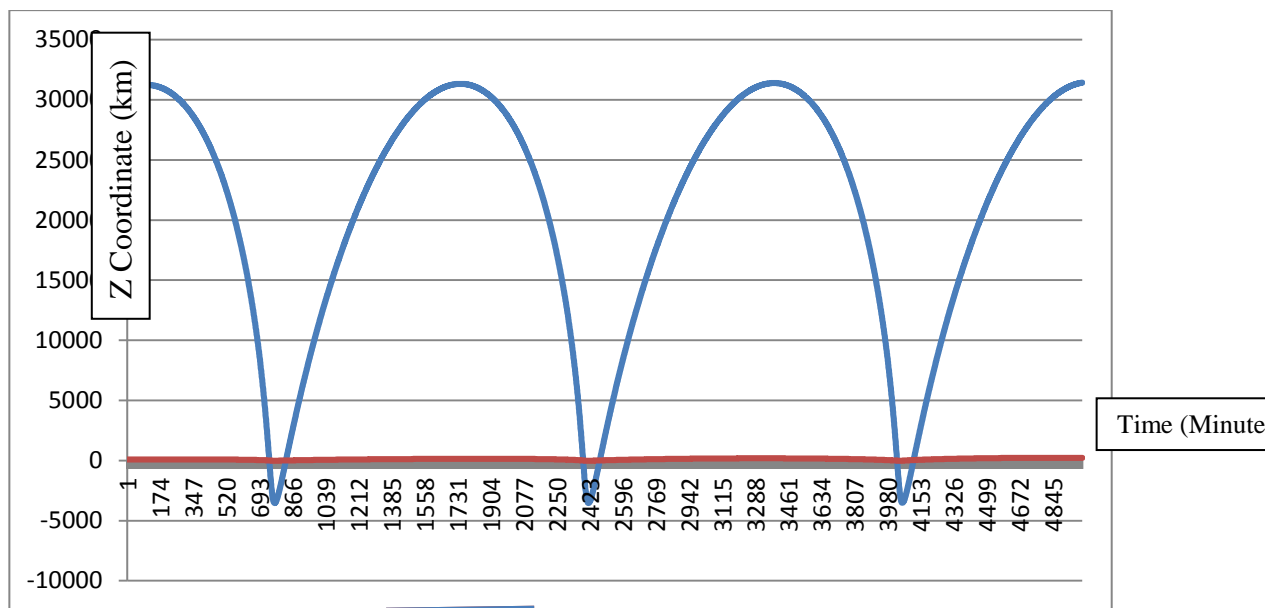


Figure 7.12 Graph of GEI/J2000 Z coordinate values and z coordinates values after the coordinate transformations against Time starting at 00-00-00 on 08/08/2005

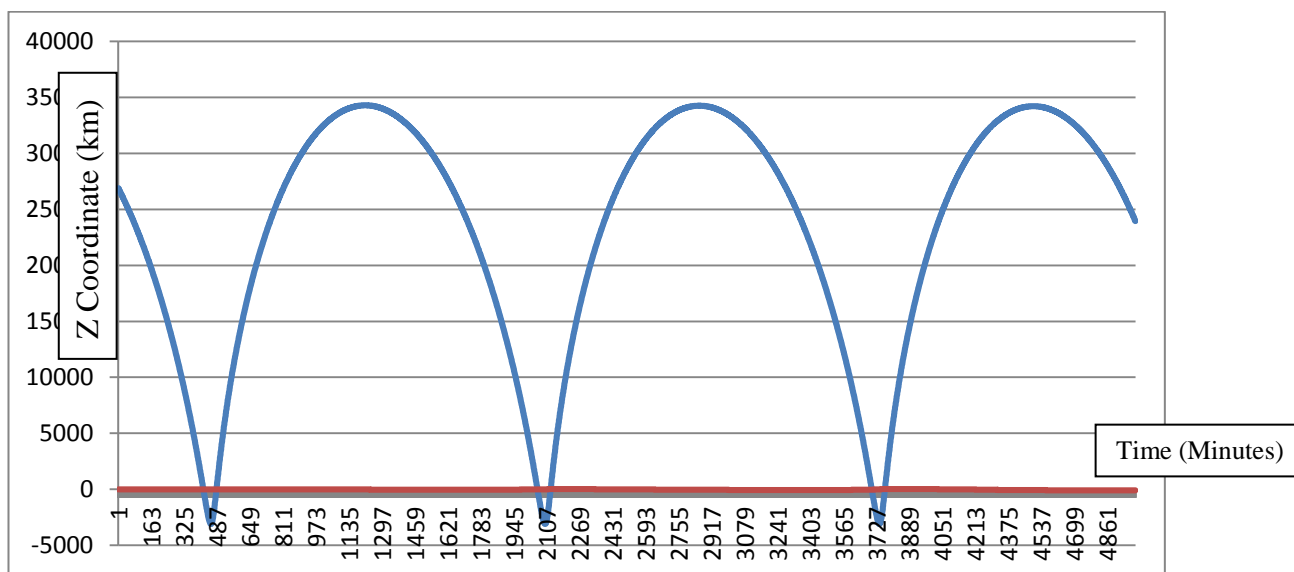
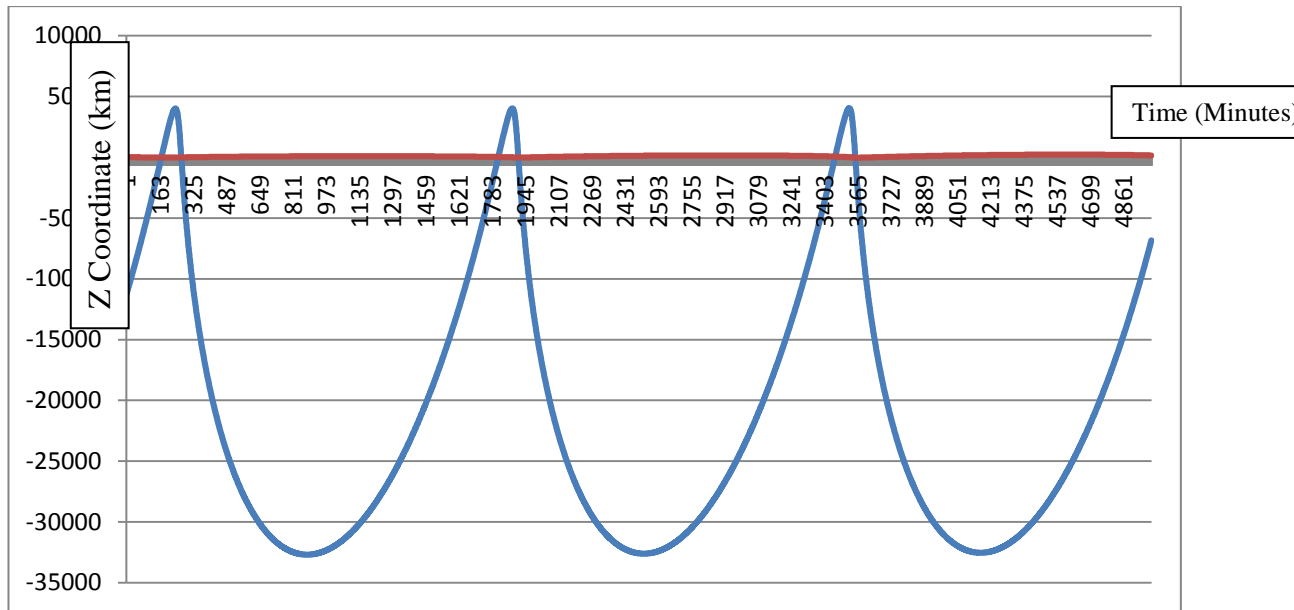


Figure 7.13 Graph of GEI/J2000 Z coordinate values and z coordinates values after the coordinate transformations against Time starting at 00-00-00 on 21/03/2006



Legend

- Z coordinates values after the coordinate transformations
- GEI/J2000 Z coordinate values

Figure 7.14 Graph of GEI/J2000 Z coordinate values and z coordinates values after the coordinate transformations against Time starting at 00-00-00 on 11/02/2004

7.8.3 Verification 2: Argument of Periapsis values are very close by vector analysis method and from the algorithm

The algorithm calculates the Argument of Periapsis (ω) at Step 22. The procedure was detailed in section 6.4.1 and detailed in Figure 6.6. The point 7 of the section 6.4.1 states that “ The Argument of Periapsis should be calculated from the X and Y coordinate values of the Periapsis and Apoapsis points in the orbital plane. These values are calculated in the W and Z columns in the “TEC Builder”. The Periapsis and Apoapsis points in the original coordinates are marked their respective transformed axis coordinates in the orbital plane are used for the calculation of the Argument of the Periapsis”.

For verification, the Argument of Periapsis (ω) can also be calculated from the GEI/J2000 coordinates of the apogee / perigee points and the Line of Nodes equation, in vector analysis.

The verification is demonstrated for the orbit on 01/03/2004 below:

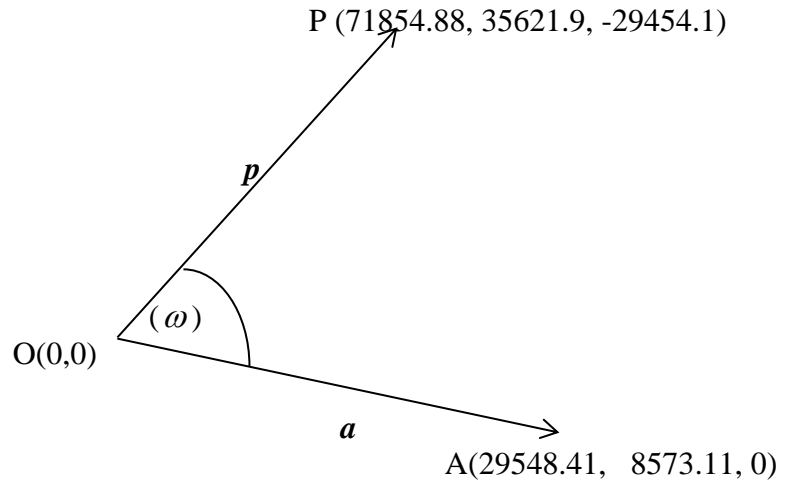


Figure 7.15 Vector diagram for the perigee and the Ascending Node

Perigee coordinates in GEI/J2000 P(71854.88, 35621.9, -29454.1)

Therefore the vector $\mathbf{p} = 71854.88 \mathbf{i} + 35621.9 \mathbf{j} - 29454.1 \mathbf{k}$

Ascending Node coordinates in GEI/J2000 A(29548.41, 8573.11, 0)

Therefore the vector $\mathbf{a} = 29548.41\mathbf{i} + 8573.11\mathbf{j} + 0 \mathbf{k}$

Therefore the angle between them $\omega = \text{Cos}^{-1}(\mathbf{a} \cdot \mathbf{p} / (|\mathbf{a}| \cdot |\mathbf{p}|))$

Argument of Periapsis (ω) = 46.29°

From the TEC Builder the Argument of Periapsis (ω) = 46.23°

The values are very close.

7.8.4 Verification 4: The transformed coordinates produce perfect elliptical orbits.

The algorithm produces perfect elliptical orbits as illustrated by the plots obtained for sampled dates below (Multiple orbits have been plotted consequently for continuous verification):

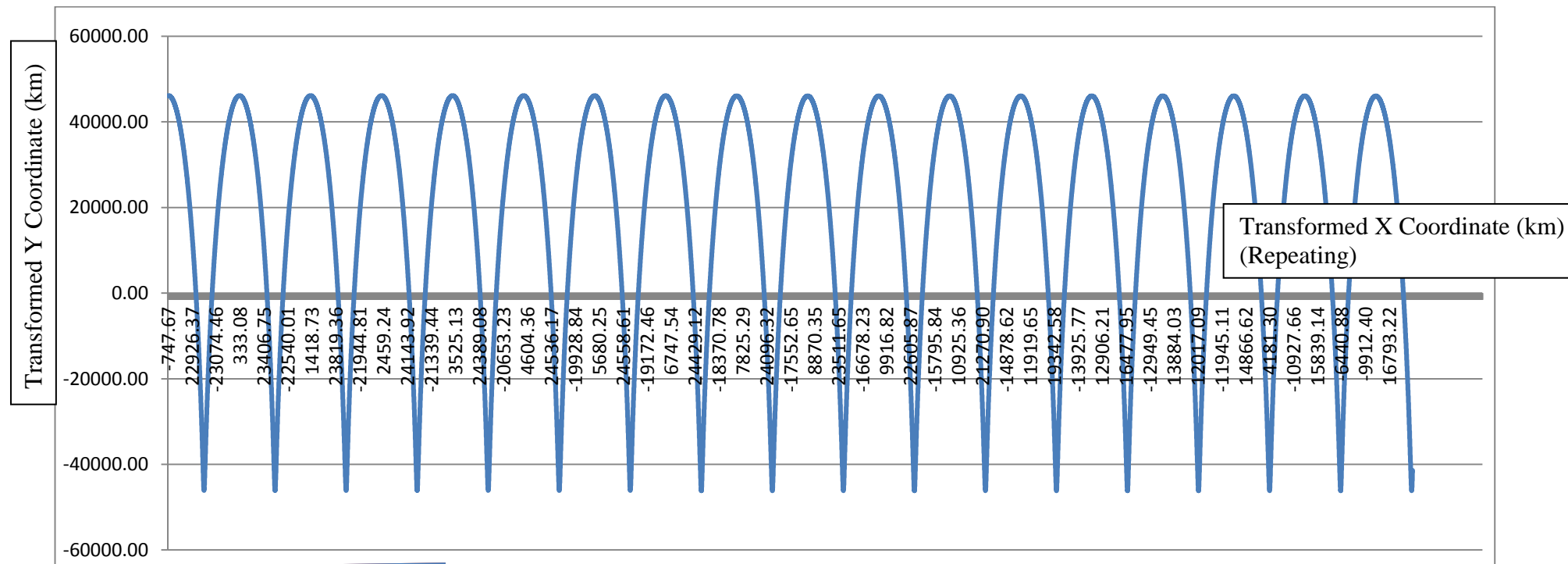


Figure 7.16 Orbital plot for 01/03/2004 to 20/03/2004

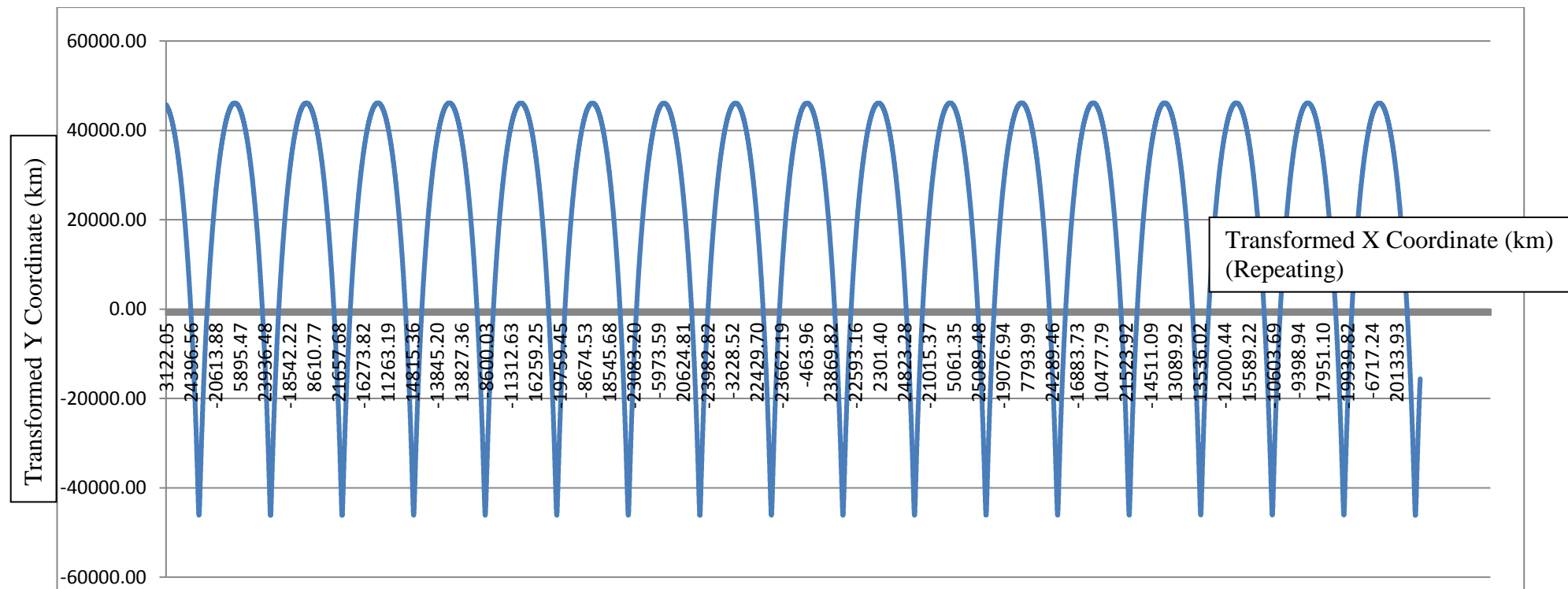


Figure 7.17 Orbital plot for 08/08/2005 to 27/08/2005

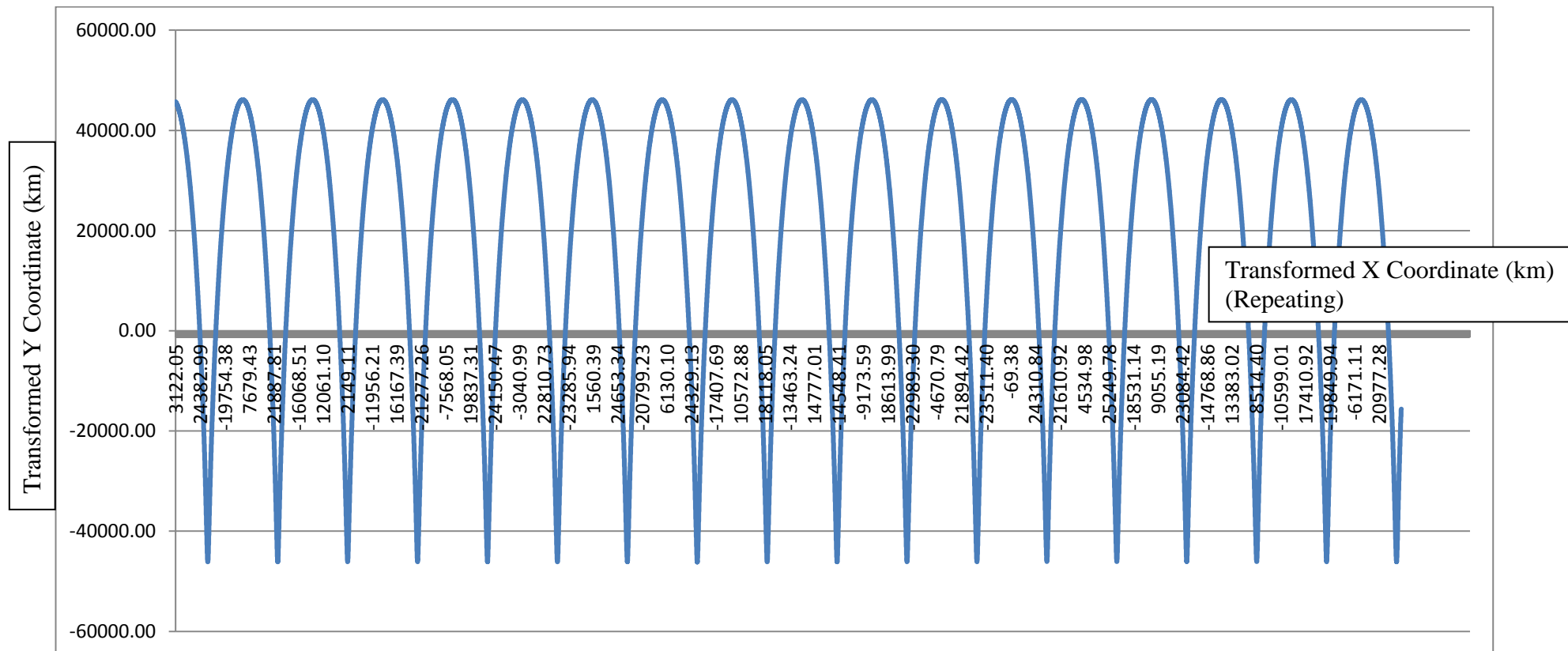


Figure 7.18 Orbital plot for 21/03/2006 to 09/04/2006

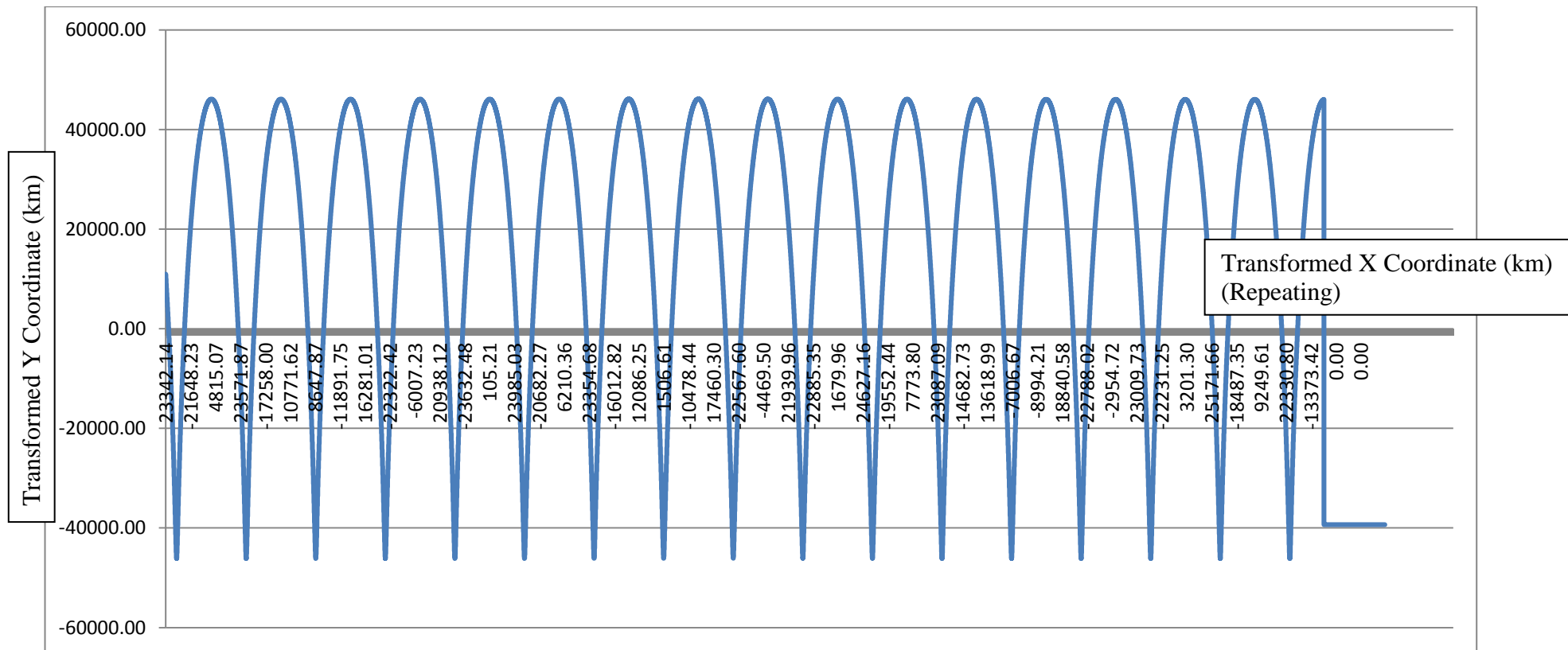


Figure 7.17 Orbital plot for 11/02/2004 to 29/02/2004

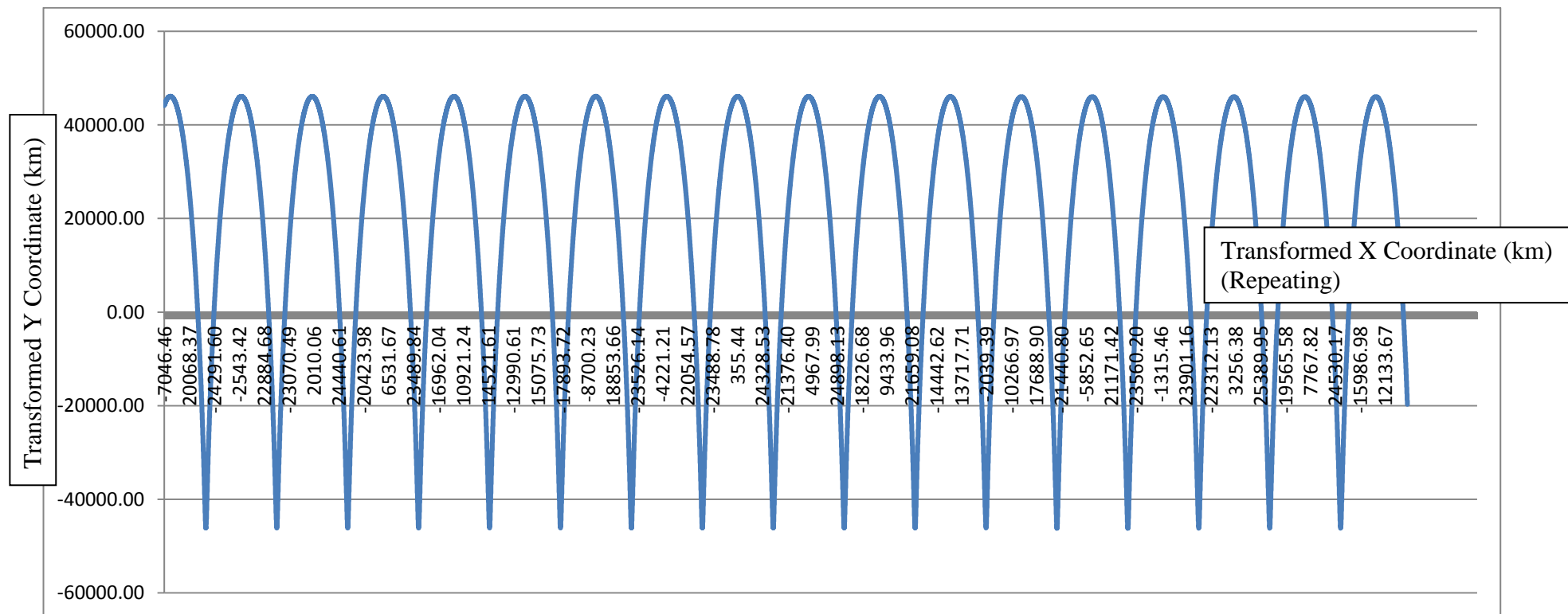


Figure 7.18 Orbital plot for 30/10/2004 to 19/11/2004

7.8.5 Verification 5: Consistent inclination angle over the orbital period, which gradually changes in conformity with actual GEI/J2000 coordinate plots

The inclination angle calculated by the algorithm is consistent throughout the orbital period and it gradually changes over time as the satellite has been manoeuvred over the years. This is in consistent with the orbital plots in Figure 3.5, which demonstrates the changing orbital elements over the years 2004, 2005 & 2006.

The inclination angle values are given below in Table 7.6 for sampled period:

No	Period	The inclination angle values
1	11/02/2004 to 29/02/2004	28.41
2	01/03/2004 to 20/03/2004	28.58
3	10/06/2004 to 30/06/2004	28.68
4	30/10/2004 to 19/11/2004	28.18
5	08/08/2005 to 28/08/2005	25.35
6	21/03/2006 to 09/04/2006	24.53

Table 7.19 Inclination angle for sampled periods

7.9 Notes on vector analysis of this methodology

The above analysis could be implemented using orbital state vectors of the satellite too.

Comparing Figures 7.8 and 7.10, it is seen that the Incident angle α will be equal to the angle between the position vector r and velocity vector v . Therefore, if the two orbital state vectors – the position vector and the velocity vector could be worked out from the

available data, the Incident angle α could be worked out. Furthermore, the orbital elements can be worked out using standard conversion formulae.

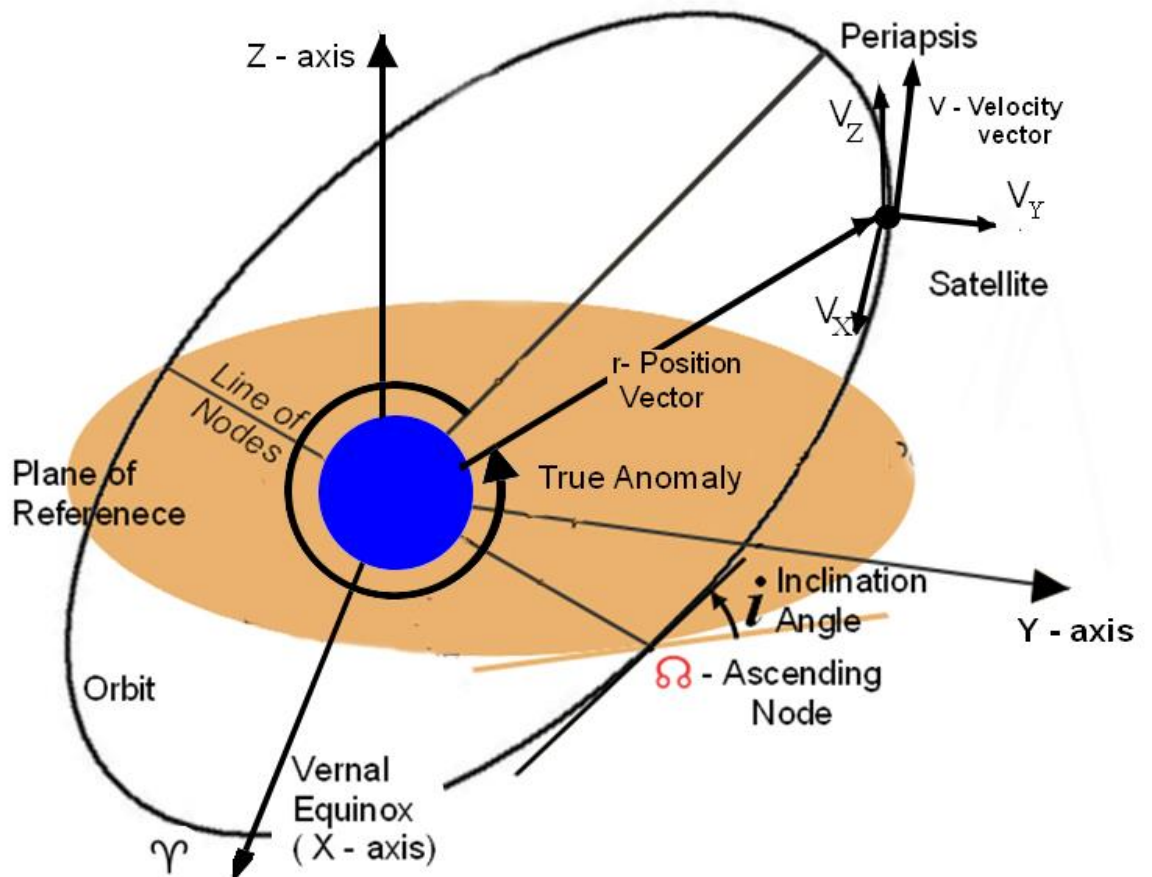


Figure 7.20 Orbital state vectors – the position vector and the velocity vector

From the NASA Satellite Situation Centre data, the position vector r can be directly determined using the GEI/J2000 coordinates. Nevertheless, the velocity vector cannot be directly determined as the satellite velocity data is not available.

Therefore, the velocity vector needs to be worked out from the GEI/J2000 coordinates data and the available time stamp data. That process will involve interpolating and approximating satellite displacement over two or three consecutive datasets, as the exact direction of the velocity vector cannot be known from a single set

of x , y , z coordinates. This interpolation and approximation have the potential to introduce an additional layer of errors into the subsequent calculations.

This additional layer of error is avoided in the geometrical analysis method utilised in this research. Nevertheless, even if the vector analysis method is used in spite of this, the arc length calculation needs to be done utilising the same calculus as used in this research. Therefore this research opts to utilise geometrical analysis method for UPEC determination.

Chapter 8 Analysis of Results, Conclusions, Further Research and Developments

The TEC Builder methodology was applied to data from TC1 as explained in the previous chapters. The results are presented in this chapter.

The results are analysed under the following headings:

- 1) Spatial variation of the Upper Plasmaspheric Electron Content (UPEC) along the orbital path as a function of time
- 2) Spatial variation of the Upper Plasmaspheric Electron Content (UPEC) along the orbital path as a function of radial distance
- 3) Variation of Upper Plasmaspheric Electron Content (UPEC) as a function of longitude

The observations and contributions are provided later in the chapter.

8.1 Spatial variation of Upper Plasmaspheric Electron Content (UPEC) along the orbital path as a function of time

8.1.1 Upper Plasmaspheric Electron Content (UPEC) generated between 21.03.06 and 09.04.06

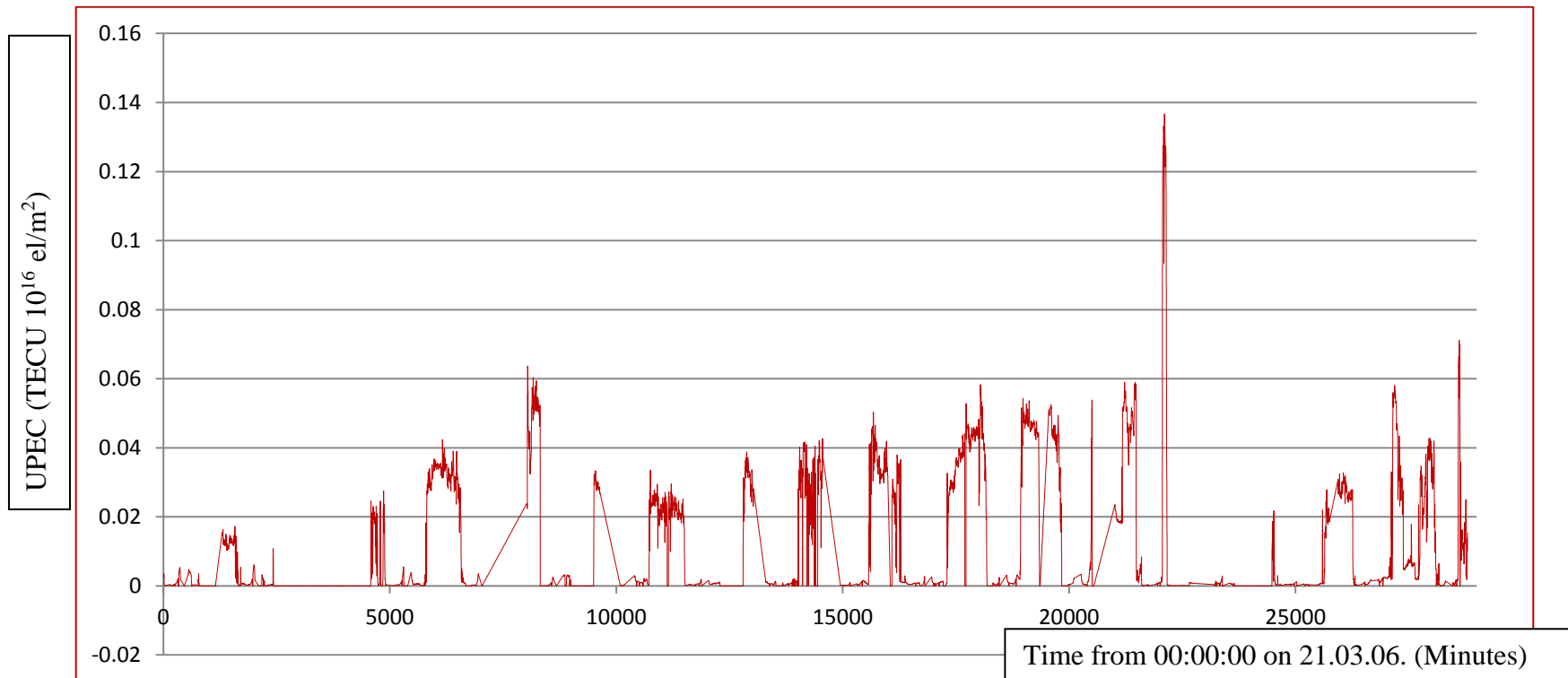


Figure 8.1 Upper Plasmaspheric Electron Content (UPEC) generated for twenty day between 21.03.06 and 09.04.06. The X axis is calibrated with minutes from midnight 00:00:00 on 21.03.06. Straight lines connect gaps between the series. Y axis denotes UPEC in TECU(10^{16} el/m²).

8.1.2 Upper Plasmaspheric Electron Content (UPEC) generated between 21.05.06 and 08.06.06

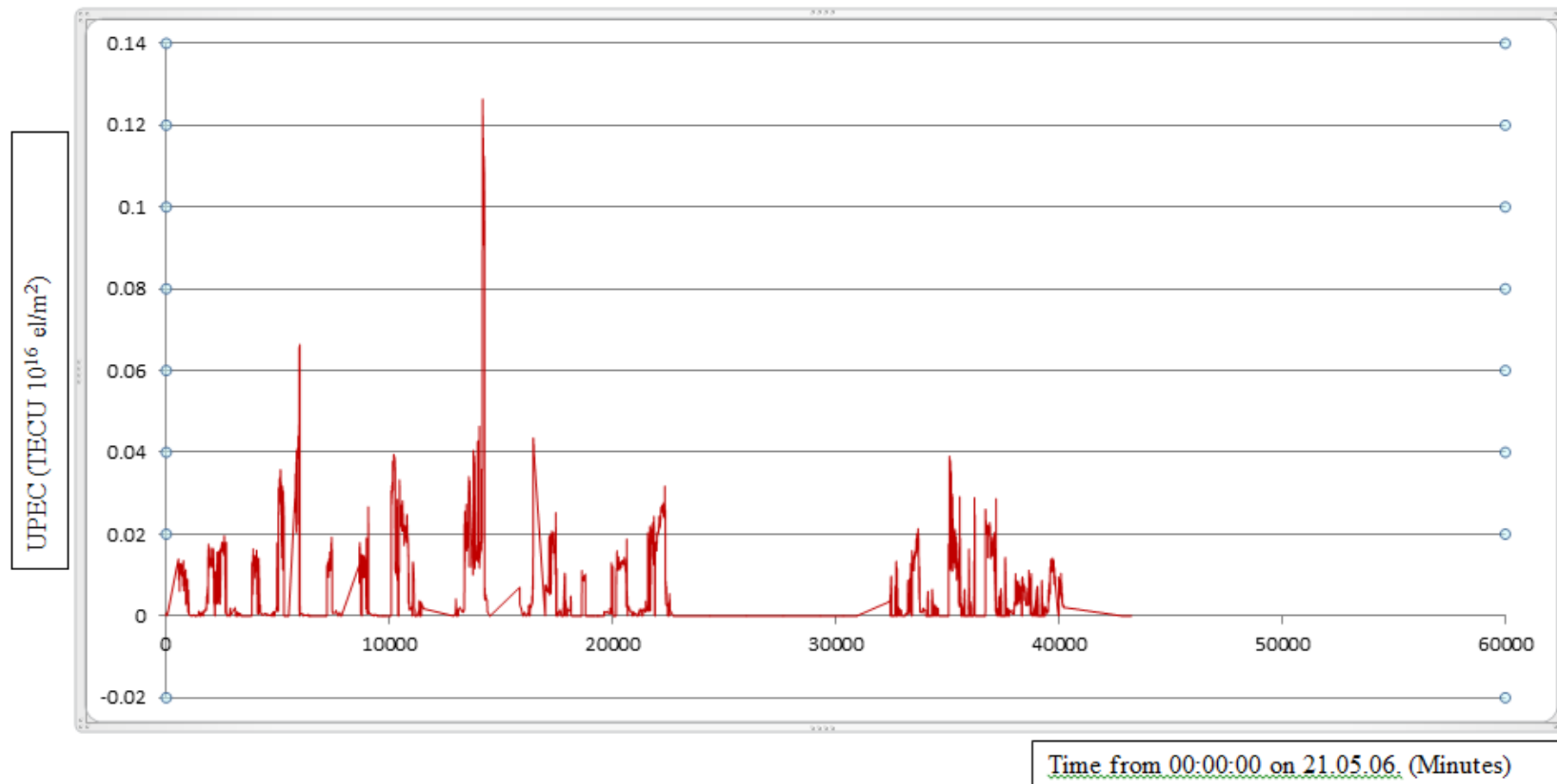


Figure 8.2 Upper Plasmaspheric Electron Content (UPEC) generated for twenty day between 21.05.06 and 08.06.06 The X axis is calibrated with minutes from midnight 00:00:00 on 21.05.06. Straight lines connect gaps between the series. Y axis denotes UPEC in $\text{TECU}(10^{16} \text{ el/m}^2)$. The instrument has been turned off for a few days in between.

8.1.3 Upper Plasmaspheric Electron Content (UPEC) generated between 16.08.06 and 08.09.06

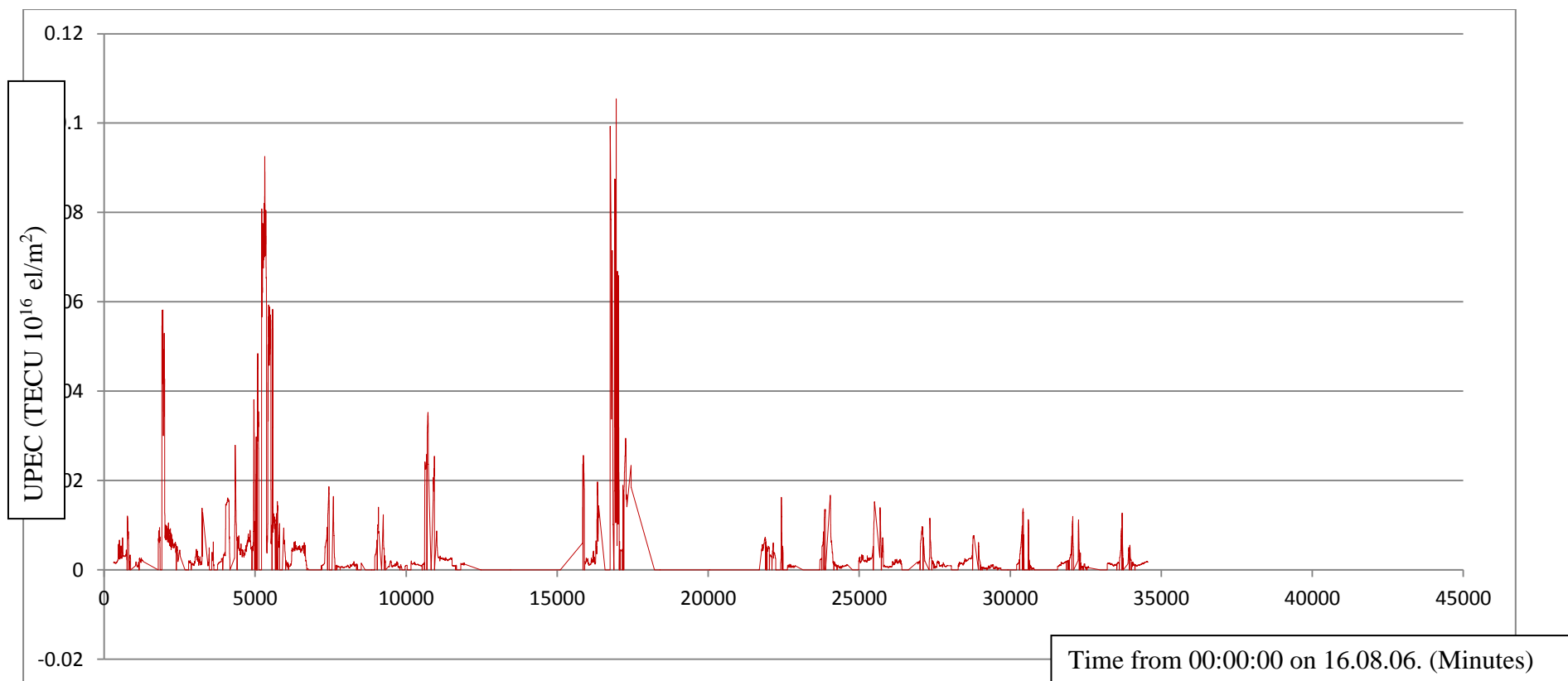


Figure 8.3 Upper Plasmaspheric Electron Content (UPEC) generated for twenty day between 16.08.06 and 08.09.06 The X axis is calibrated with minutes from midnight 00:00:00 on 16.08.06. Straight lines connect gaps between the series. Y axis denotes UPEC in TECU(10^{16} el/m²). The instrument has been turned off for a few days in between.

8.1.4 Upper Plasmaspheric Electron Content (UPEC) generated between 08.08.05 and 28.08.05

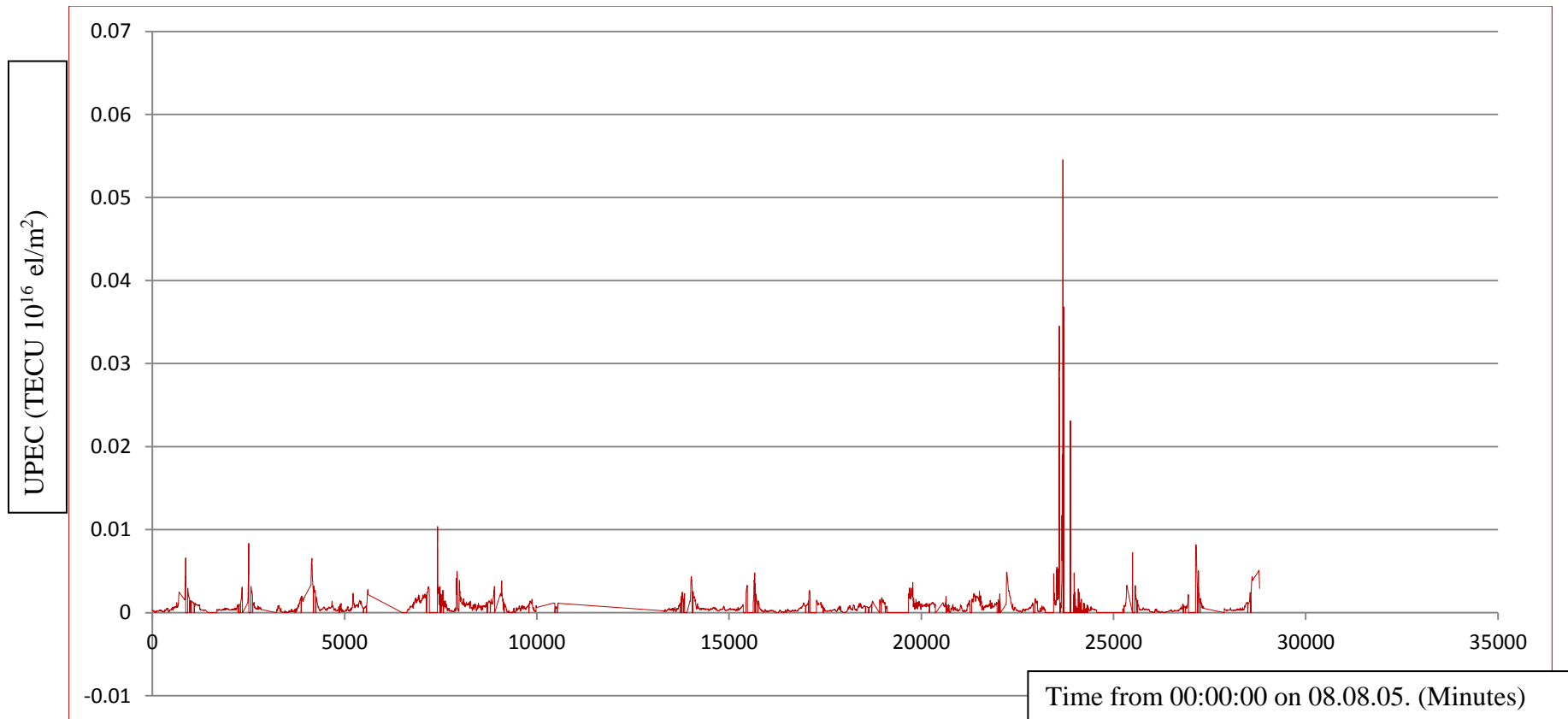


Figure 8.4 Upper Plasmaspheric Electron Content (UPEC) generated for twenty day between 16.08.06 and 08.09.06 The X axis is calibrated with minutes from midnight 00:00:00 on 08.08.05. Straight lines connect gaps between the series. Y axis denotes UPEC in TECU(10^{16} el/m²).

8.1.5 Upper Plasmaspheric Electron Content (UPEC) generated between 09.06.05 and 28.06.05

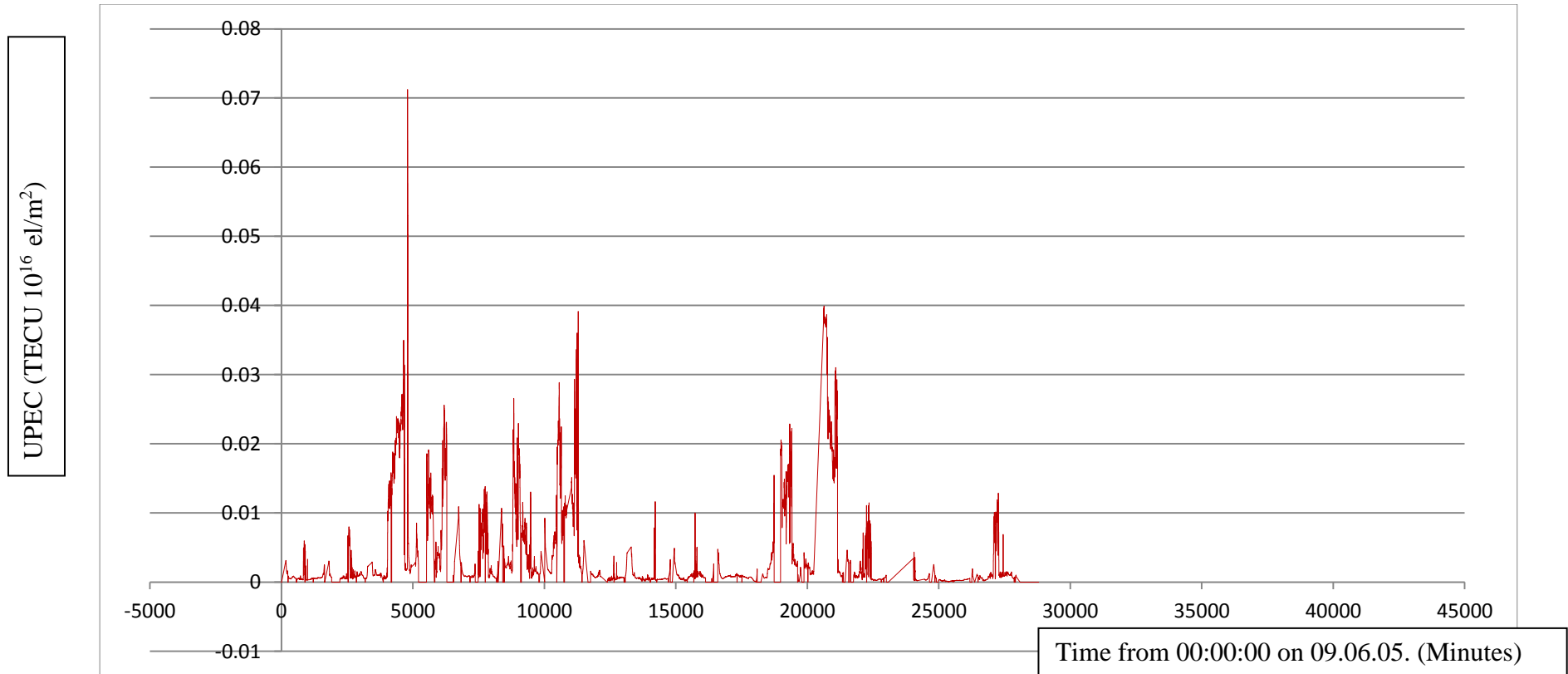


Figure 8.5 Upper Plasmaspheric Electron Content (UPEC) generated for twenty day between 09.06.05 and 28.06.05. The X axis is calibrated with minutes from midnight 00:00:00 on 09.06.05. Straight lines connect gaps between the series. Y axis denotes UPEC in TECU(10^{16} e/m²).

8.1.6 Upper Plasmaspheric Electron Content (UPEC) generated between 01.03.04 and 22.03.04

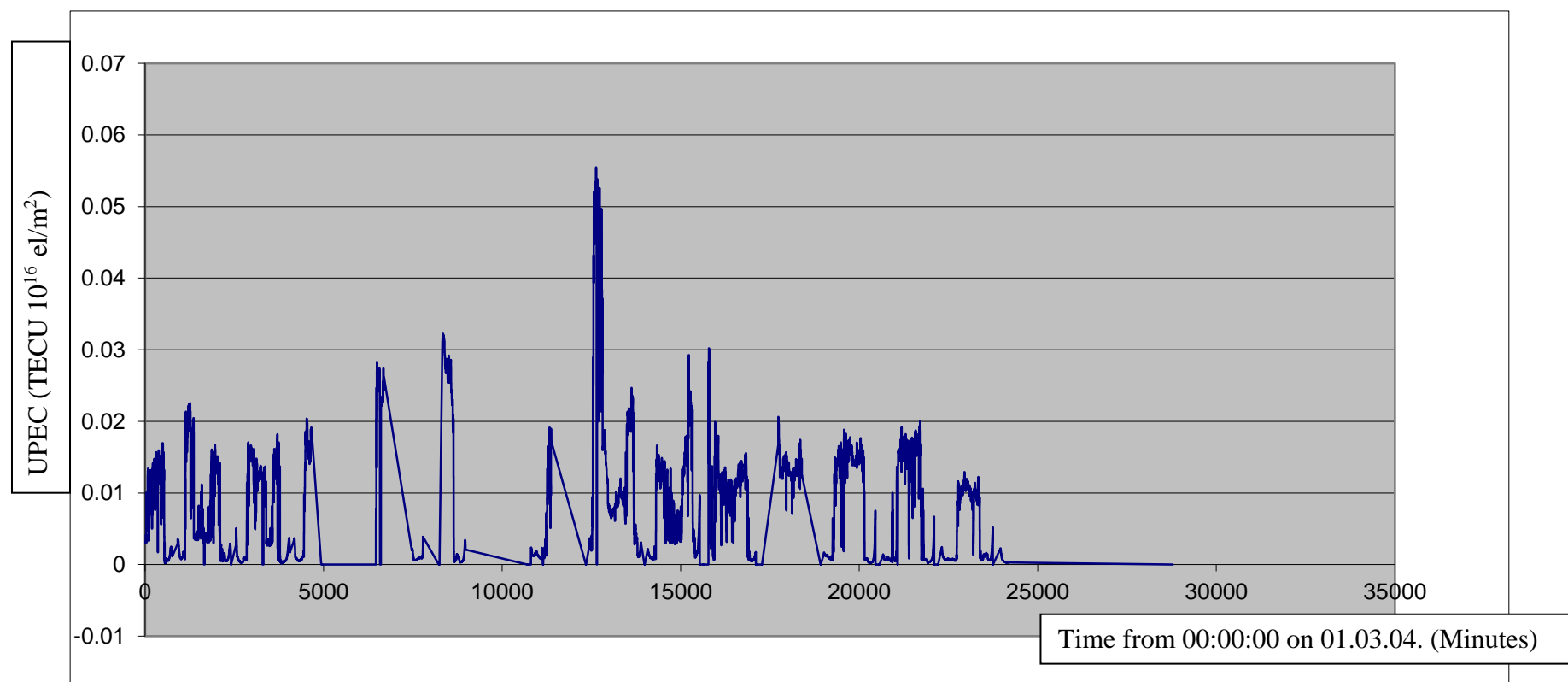


Figure 8.6 Upper Plasmaspheric Electron Content (UPEC) generated for twenty day between 01.03.04 and 22.03.04. The X axis is calibrated with minutes from midnight 00:00:00 on 01.03.04. Straight lines connect gaps between the series. Y axis denotes UPEC in TECU(10^{16} e/m²).

8.1.7 Upper Plasmaspheric Electron Content (UPEC) generated between 10.04.04 and 29.04.04

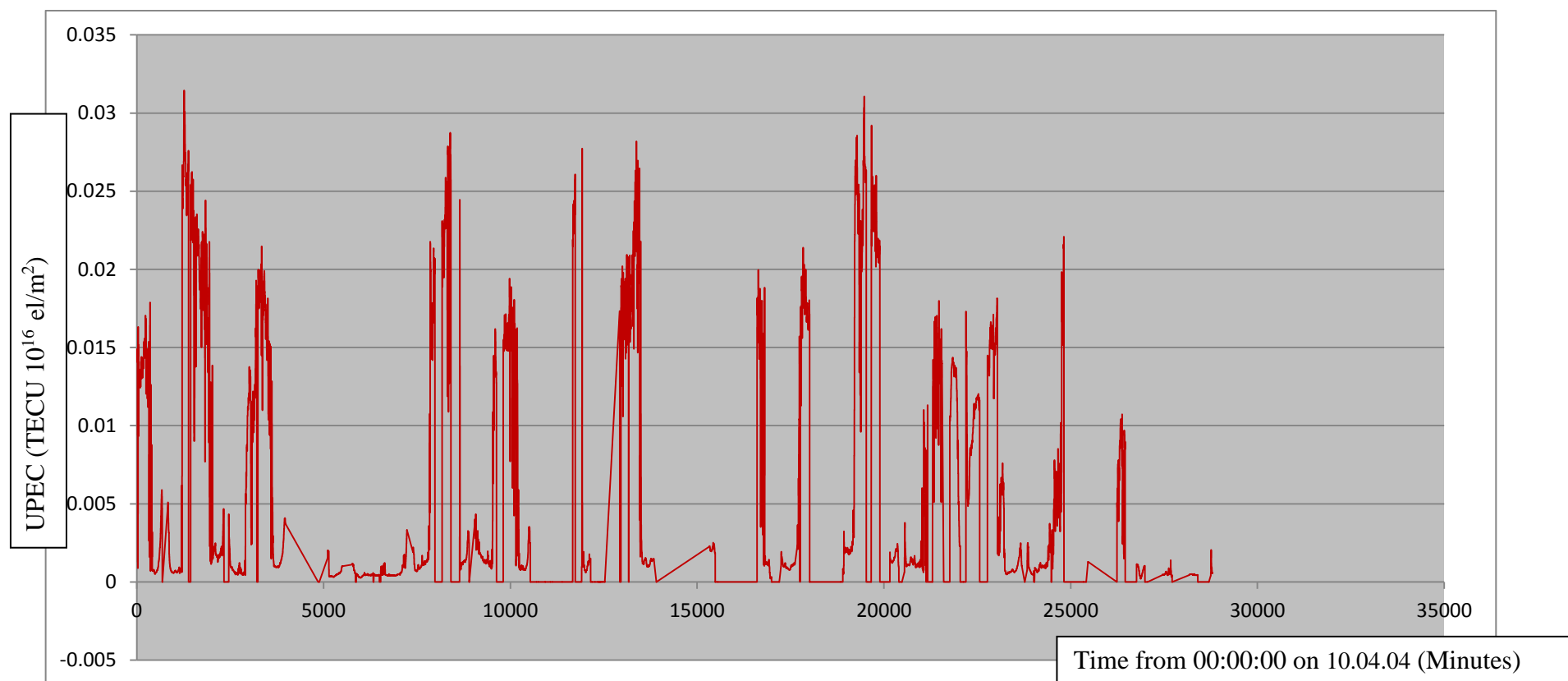


Figure 8.7 Upper Plasmaspheric Electron Content (UPEC) generated for twenty day between 10.04.04 and 29.04.04. The X axis is calibrated with minutes from midnight 00:00:00 on 10.04.04. Straight lines connect gaps between the series. Y axis denotes UPEC in TECU(10^{16} el/m²).

8.1.8 Upper Plasmaspheric Electron Content (UPEC) generated between 30.04.04 and 20.05.04

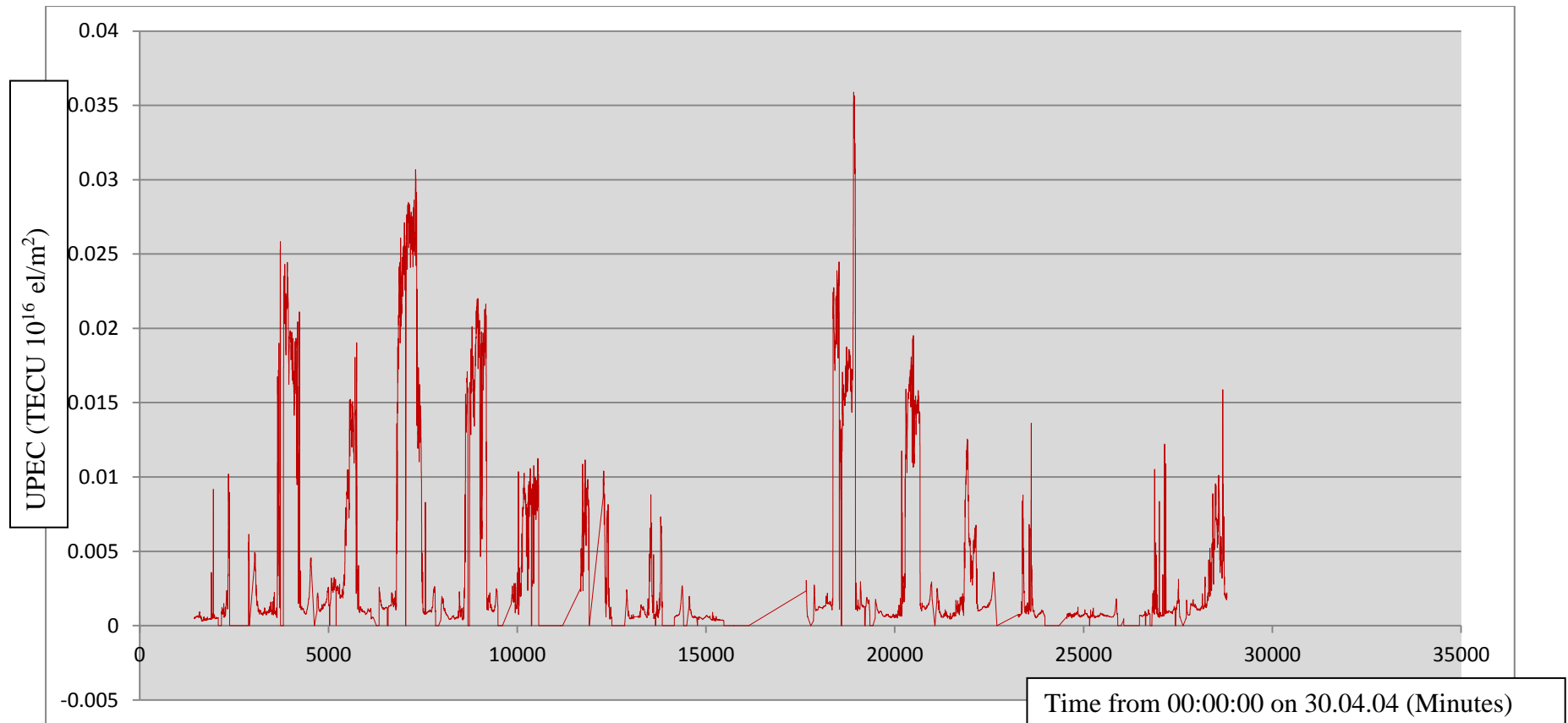


Figure 8.8 Upper Plasmaspheric Electron Content (UPEC) generated for twenty day between 30.04.04 and 20.05.04. The X axis is calibrated with minutes from midnight 00:00:00 on 30.04.04. Straight lines connect gaps between the series. Y axis denotes UPEC in TECU(10^{16} el/m²).

8.1.9 Upper Plasmaspheric Electron Content (UPEC) generated between 10.06.04 and 30.06.04

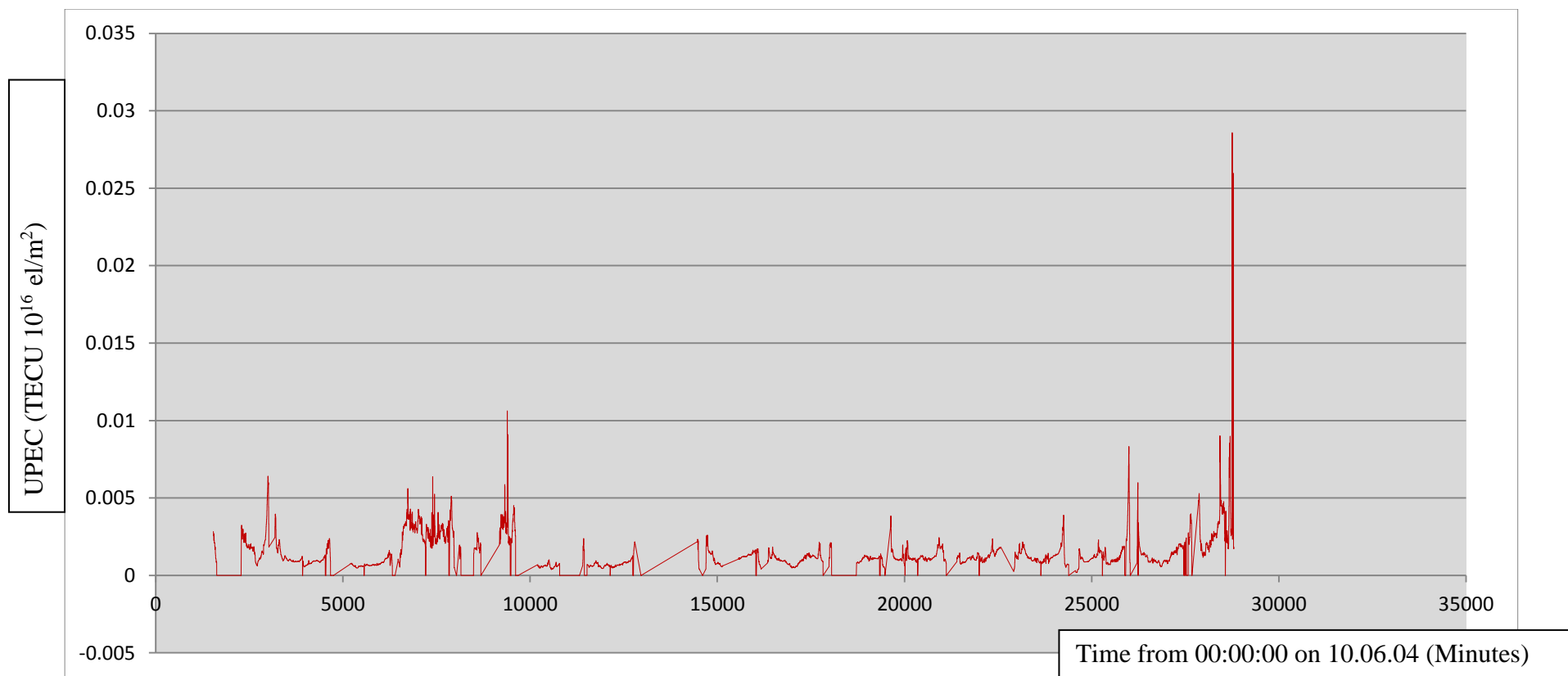


Figure 8.9 Upper Plasmaspheric Electron Content (UPEC) generated for twenty day between 10.06.04 and 30.06.04. The X axis is calibrated with minutes from midnight 00:00:00 on 10.06.04. Straight lines connect gaps between the series. Y axis denotes UPEC in TECU(10^{16} el/m²).

8.1.10 Upper Plasmaspheric Electron Content (UPEC) generated between 30.10.04 and 19.11.04

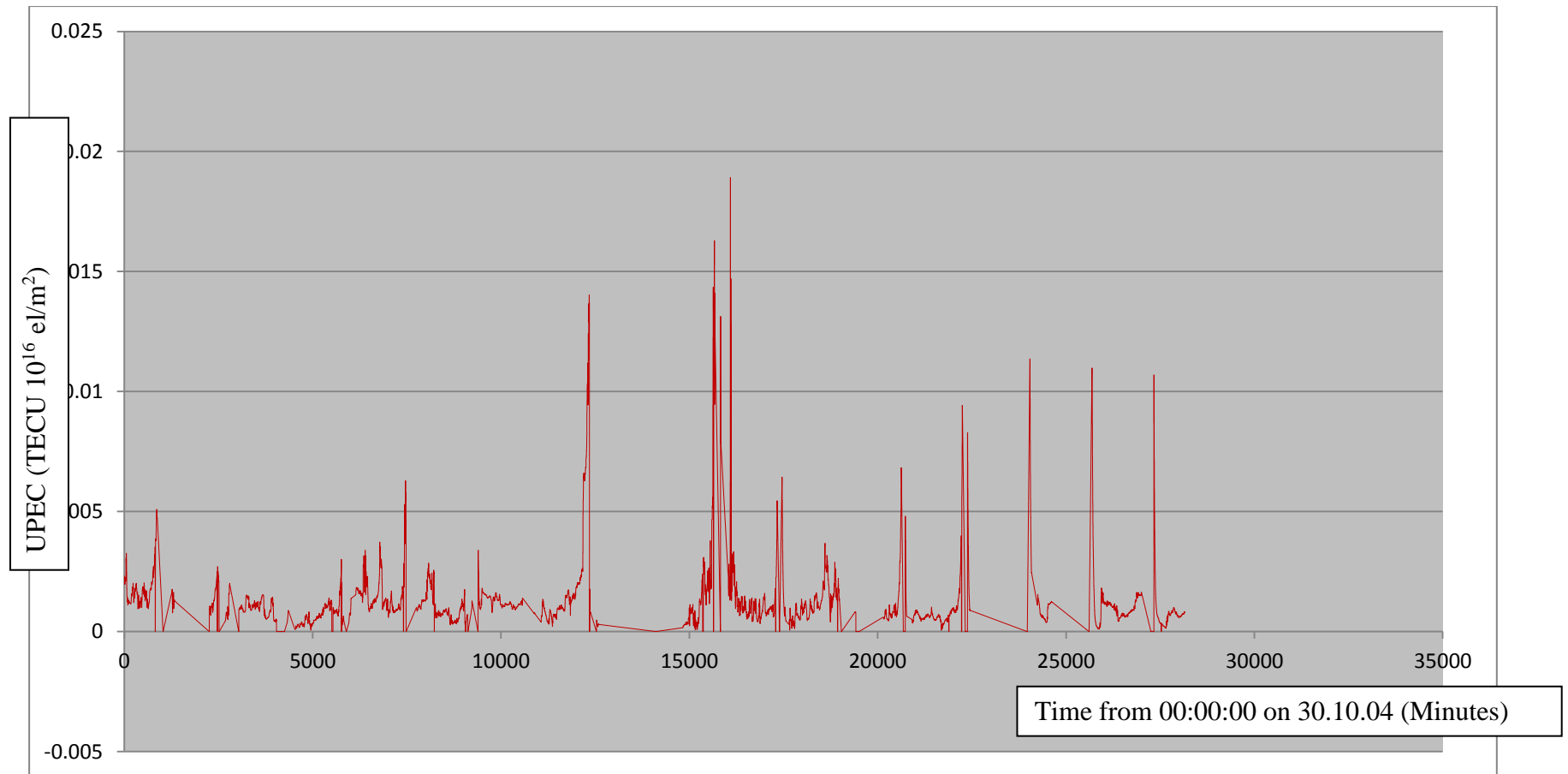


Figure 8.10 Upper Plasmaspheric Electron Content (UPEC) generated for twenty day between 30.10.04 and 19.11.04. The X axis is calibrated with minutes from midnight 00:00:00 on 30.10.04. Straight lines connect gaps between the series. Y axis denotes UPEC in TECU(10^{16} el/m²).

8.2 Spatial variation of the Upper Plasmaspheric Electron Content (UPEC) along the orbital path as a function of radial distance

8.2.1 Upper Plasmaspheric Electron Content (UPEC) generated between 21.03.06 and 09.04.06 – Minutes 0001 to 1650

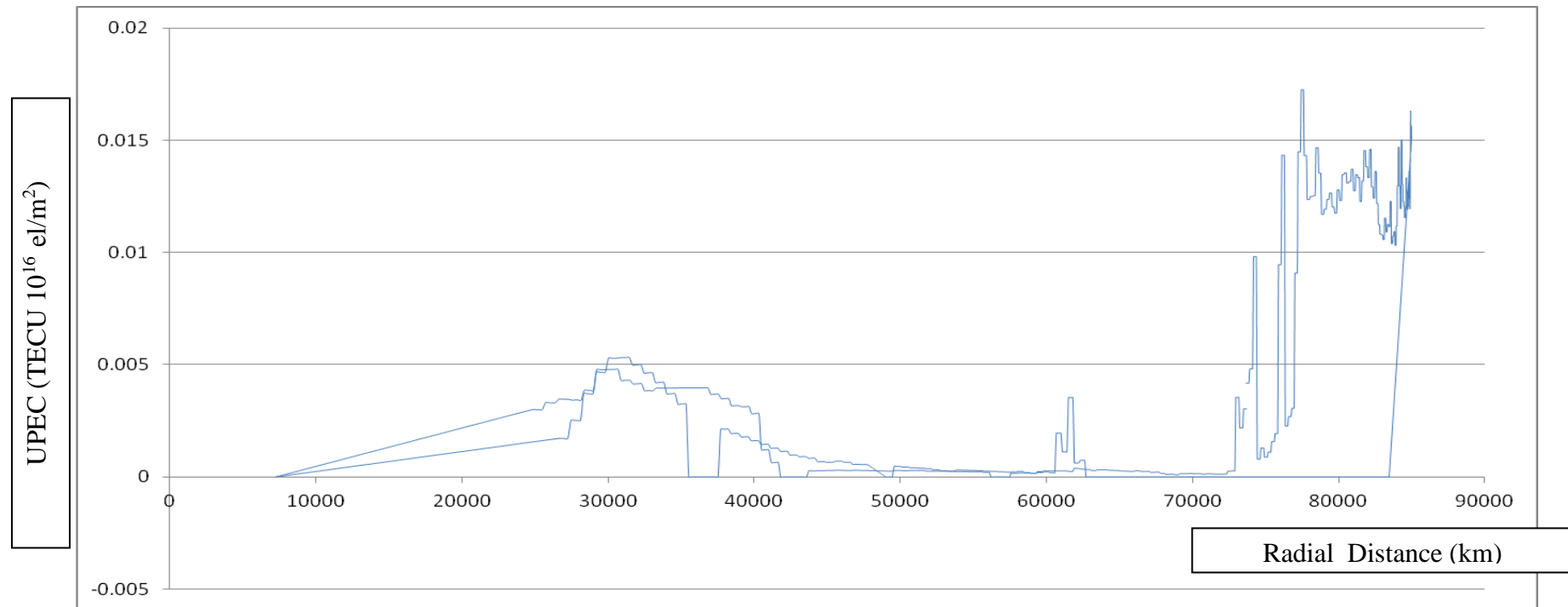


Figure 8.11 Upper Plasmaspheric Electron Content (UPEC) generated for twenty day between 21.03.06 and 09.04.06 for minutes 0001 to 1650. The X axis is calibrated with the Radial Distance in km. Straight lines connect gaps between the series. Y axis denotes UPEC in TECU(10^{16} el/m²).

8.2.2 Upper Plasmaspheric Electron Content (UPEC) generated between 21.03.06 and 09.04.06 – Minutes 4500 – 6200

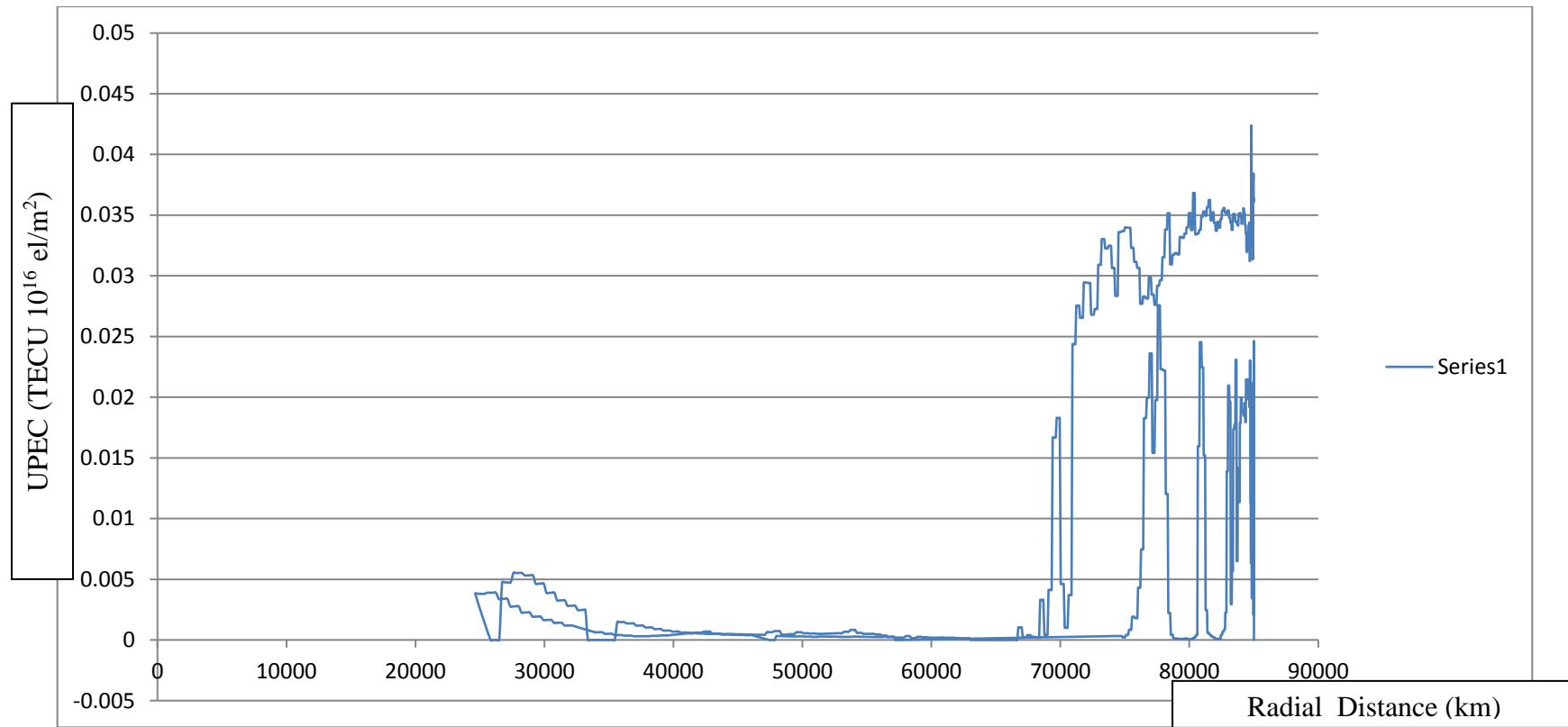


Figure 8.12 Upper Plasmaspheric Electron Content (UPEC) generated for a twenty day period between 21.03.06 and 09.04.06 for minutes 4500 to 6200. The X axis is calibrated with the Radial Distance in km. Straight lines connect gaps between the series. Y axis denotes UPEC in TECU(10^{16} el/m²).

8.2.3 Upper Plasmaspheric Electron Content (UPEC) generated between 21.03.06 and 09.04.06 – Minutes 6200-6X00

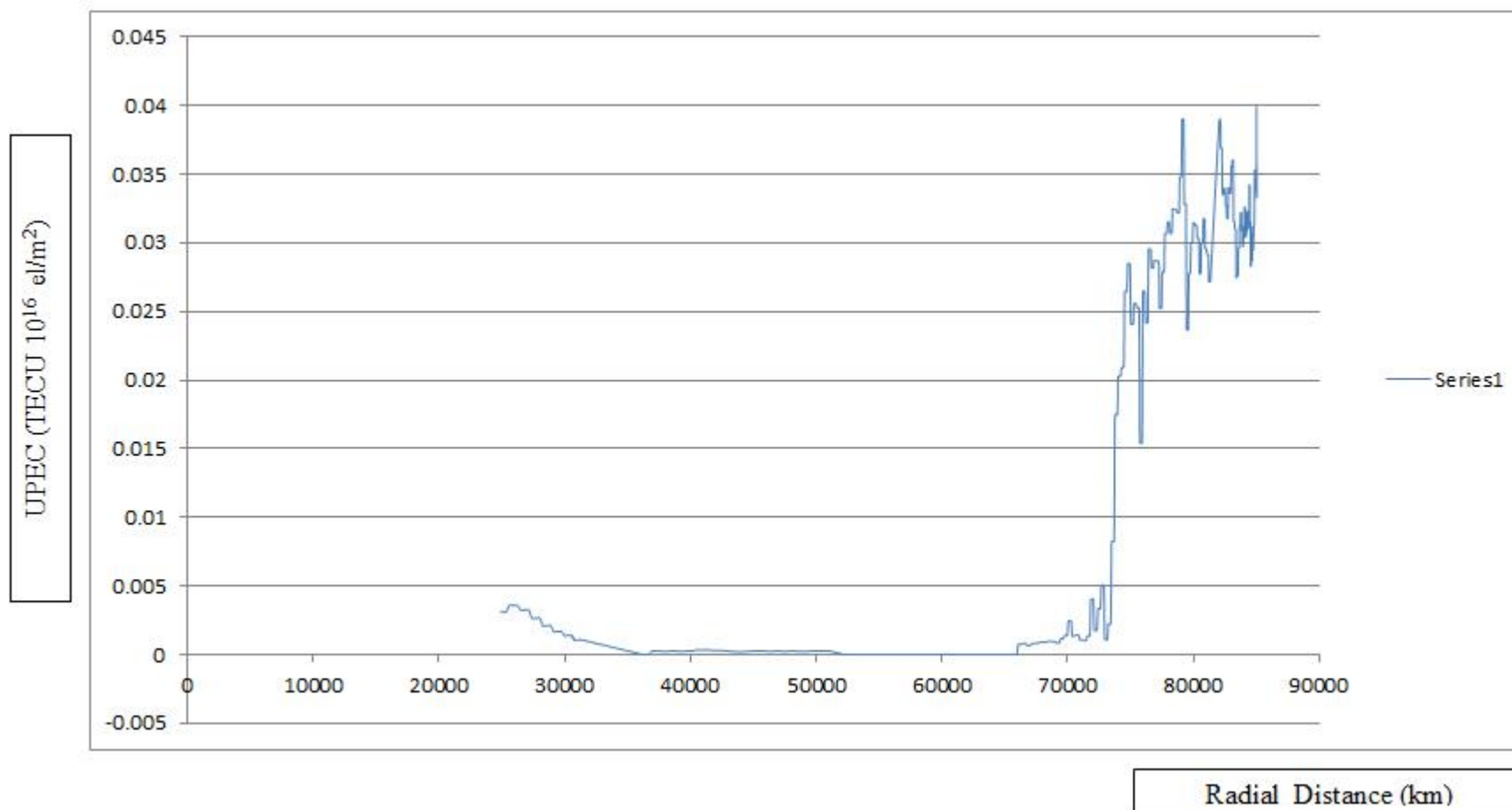


Figure 8.13 Upper Plasmaspheric Electron Content (UPEC) generated for twenty day between 21.03.06 and 09.04.06 for minutes 6200 to 6X00. The X axis is calibrated with the Radial Distance in km.. Straight lines connect gaps between the series. UPEC in TECU(10^{16} el/m²).

8.2.4 Upper Plasmaspheric Electron Content (UPEC) generated between 21.03.06 and 09.04.06 – Minutes 8000-9600

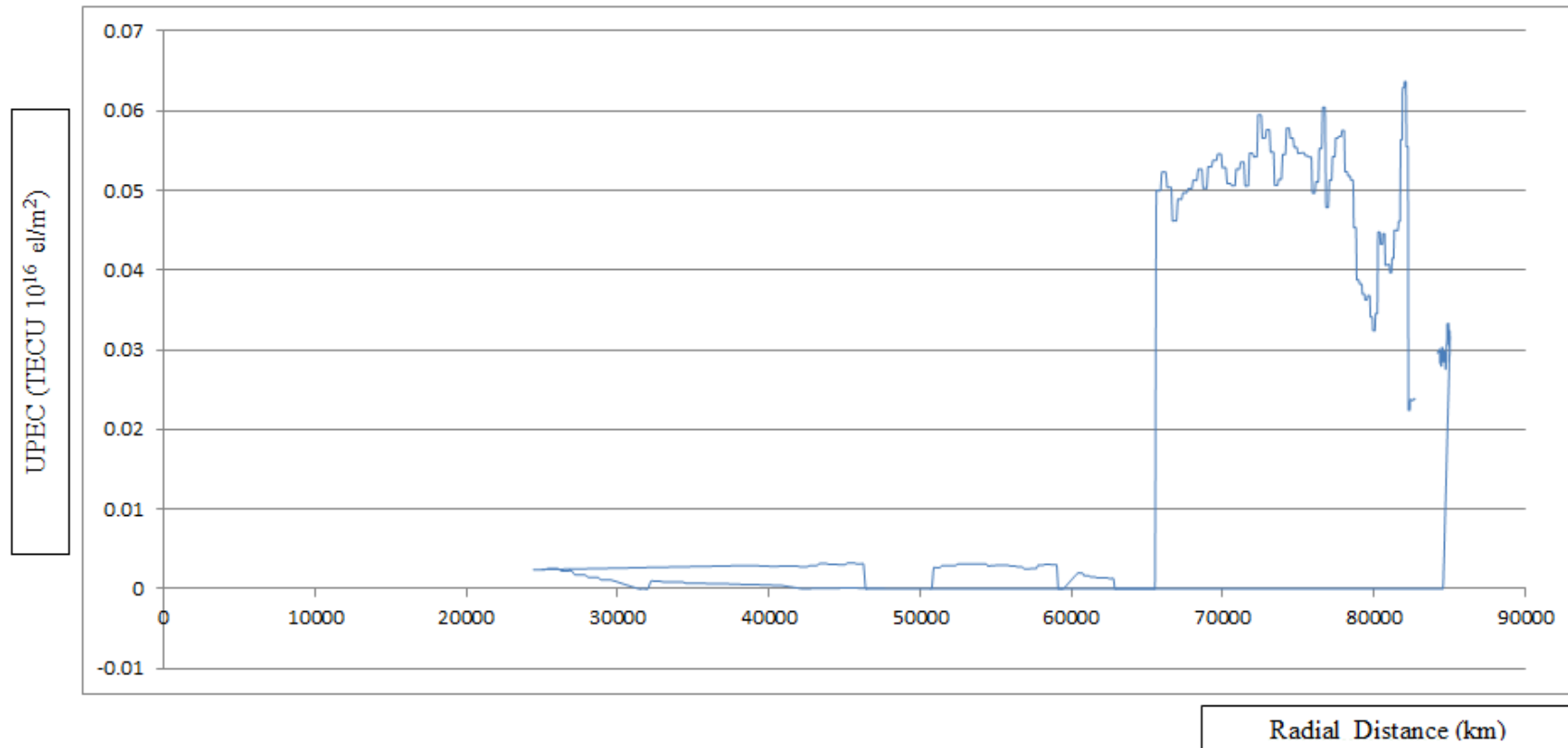


Figure 8.14 Upper Plasmaspheric Electron Content (UPEC) generated for twenty day between 21.03.06 and 09.04.06 for minutes 8000-9600. The X axis is calibrated with the Radial Distance in km.. Straight lines connect gaps between the series. Y axis denotes UPEC in TECU(10^{16} el/m²).

8.2.5 Upper Plasmaspheric Electron Content (UPEC) generated between 21.03.06 and 09.04.06 – Minutes 9600-11200

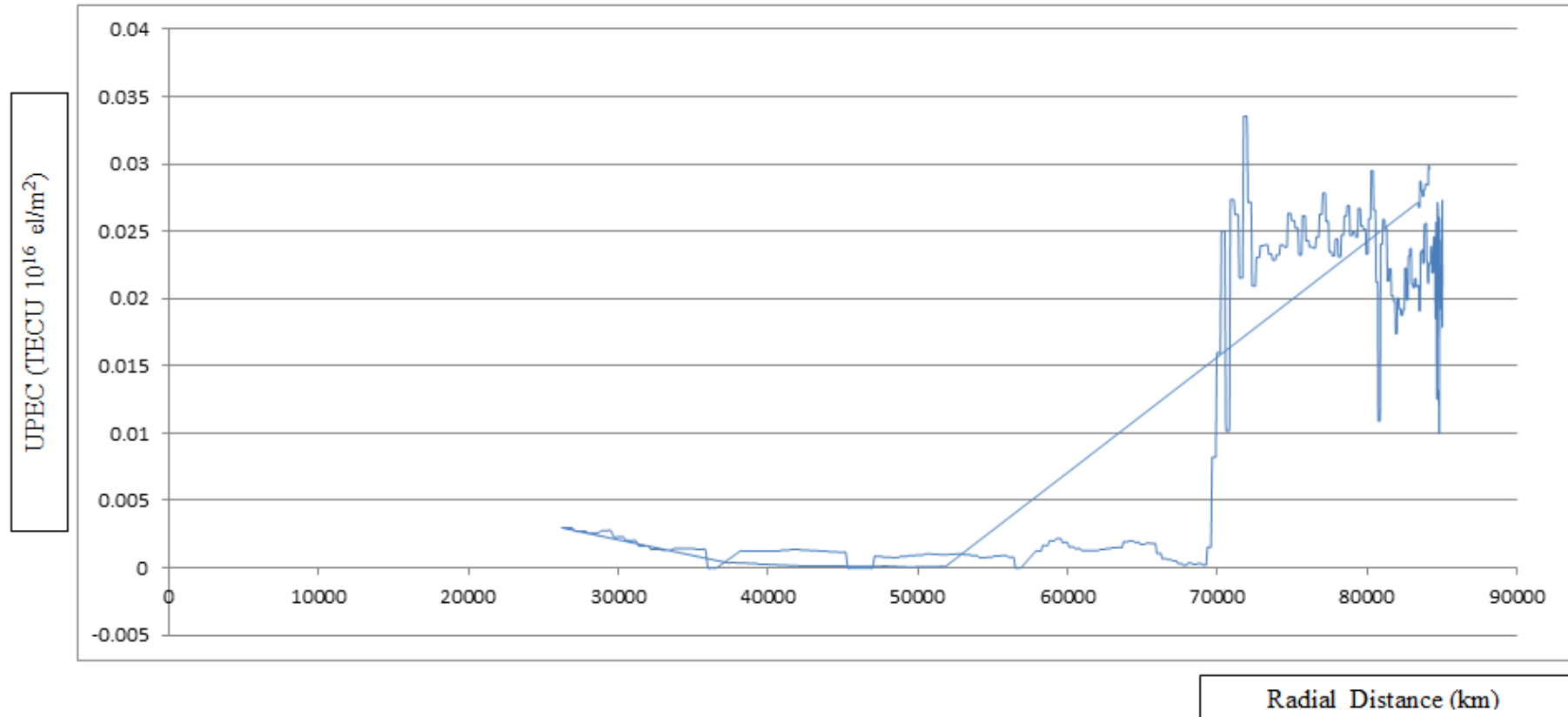


Figure 8.15 Upper Plasmaspheric Electron Content (UPEC) generated for twenty day between 21.03.06 and 09.04.06 for minutes 9600=11200. The X axis is calibrated with the Radial Distance in km.. Straight lines connect gaps between the series. UPEC TEC component in TECU(10^{16} el/m²)

8.2.6 Upper Plasmaspheric Electron Content (UPEC) generated between 21.03.06 and 09.04.06 – Minutes 11200-12300

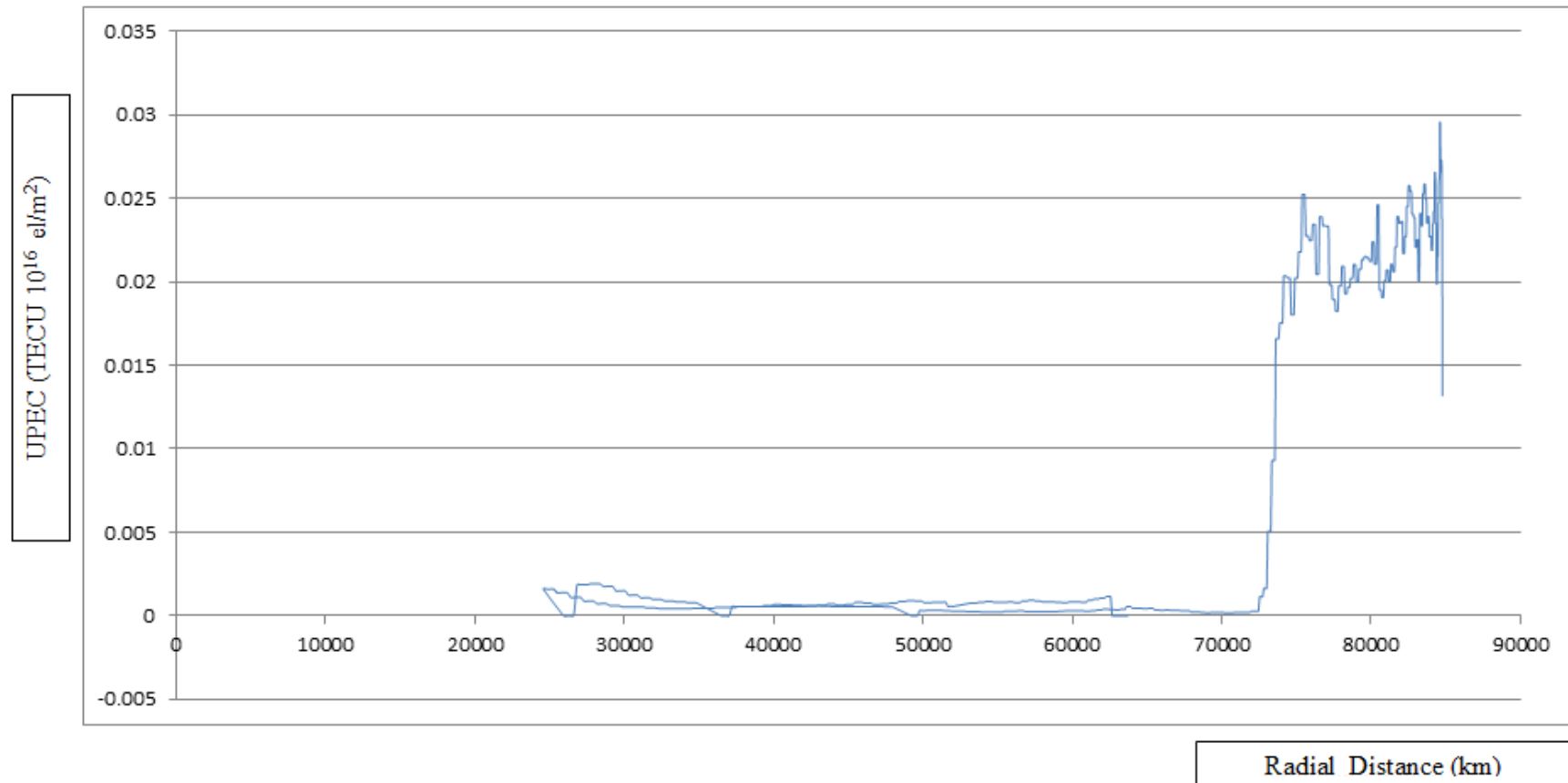


Figure 8.16 Upper Plasmaspheric Electron Content (UPEC) generated for twenty day between 21.03.06 and 09.04.06 for minutes 11200-12300. The X axis is calibrated with the Radial Distance in km.. Straight lines connect gaps between the series. Y axis denotes UPEC in TECU(10^{16} el/m²).

8.2.7 Upper Plasmaspheric Electron Content (UPEC) generated between 21.03.06 and 09.04.06 – Minutes 12800-14600

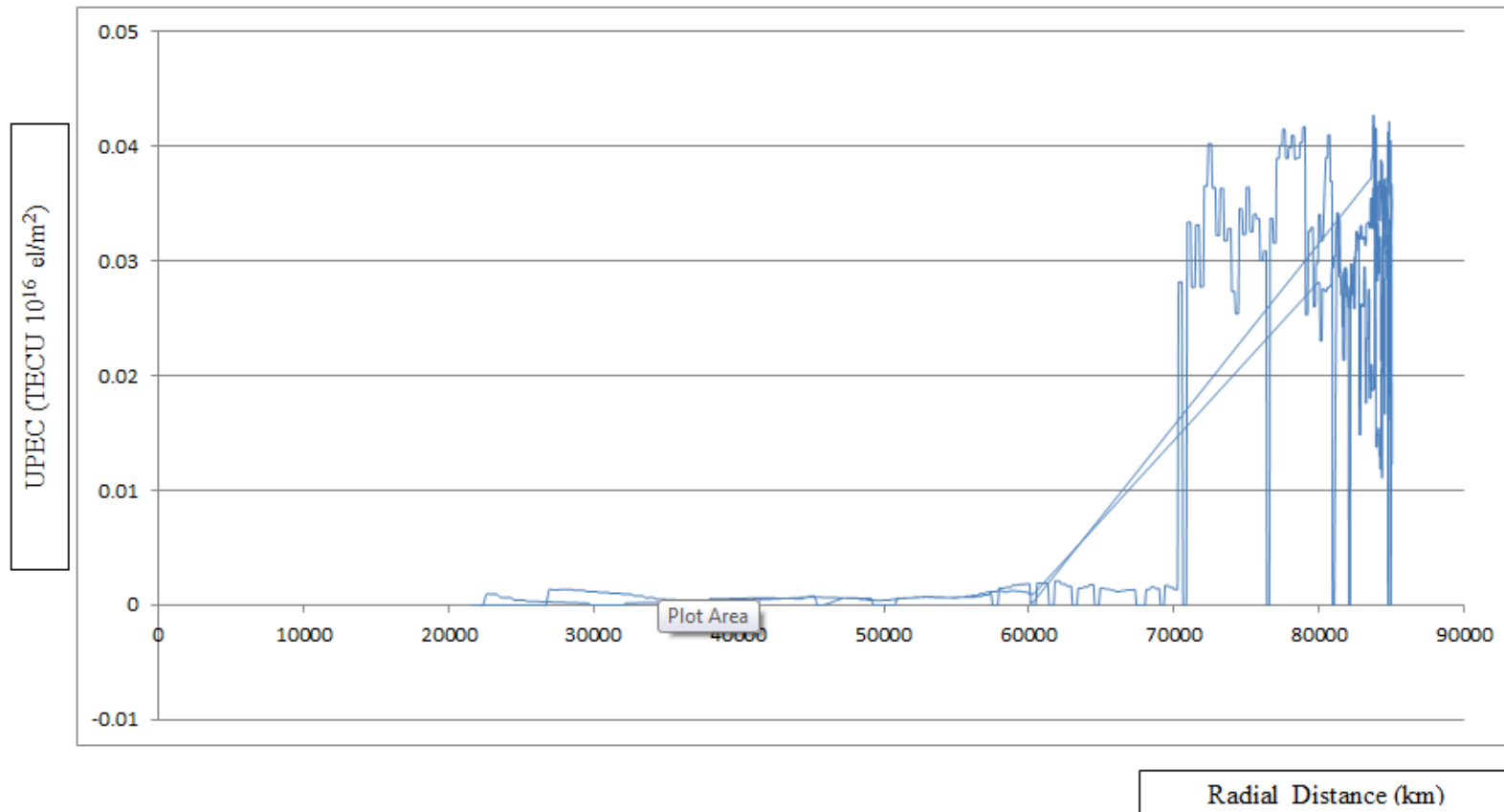


Figure 8.17 Upper Plasmaspheric Electron Content (UPEC) generated for twenty day between 21.03.06 and 09.04.06 for minutes 12800-14600. The X axis is calibrated with the Radial Distance in km.. Straight lines connect gaps between the series. Y axis denotes UPEC in TECU(10^{16} el/m²).

8.2.8 Upper Plasmaspheric Electron Content (UPEC) generated between 21.03.06 and 09.04.06 – Minutes 14950-16700

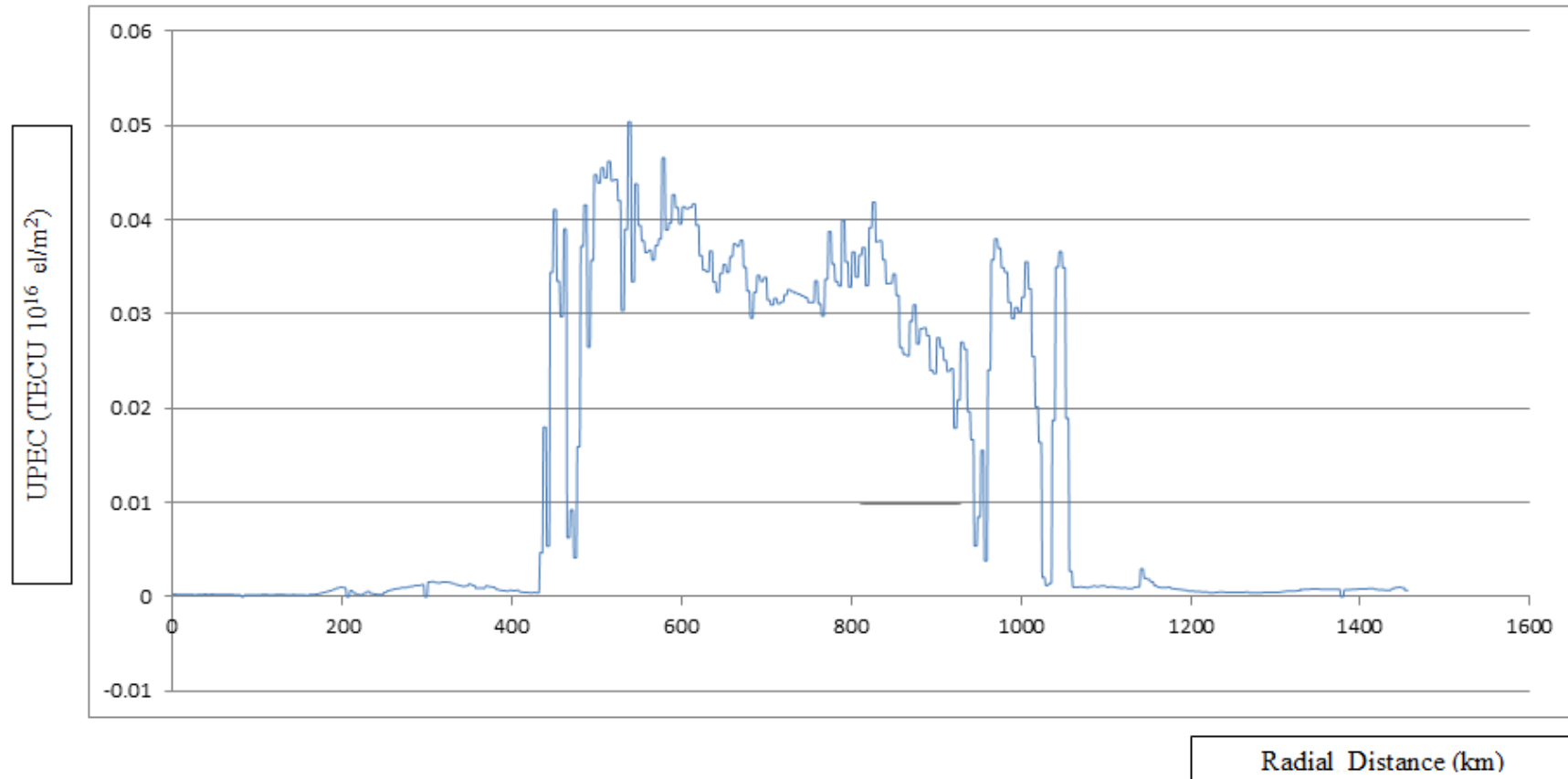


Figure 8.18 Upper Plasmaspheric Electron Content (UPEC) generated for twenty day between 21.03.06 and 09.04.06 for minutes 14950-16700. The X axis is calibrated with the Radial Distance in km.. Straight lines connect gaps between the series. Y axis denotes UPEC in TECU(10^{16} el/m²).

8.2.9 Upper Plasmaspheric Electron Content (UPEC) generated between 21.03.06 and 09.04.06 – Minutes 16700-18400

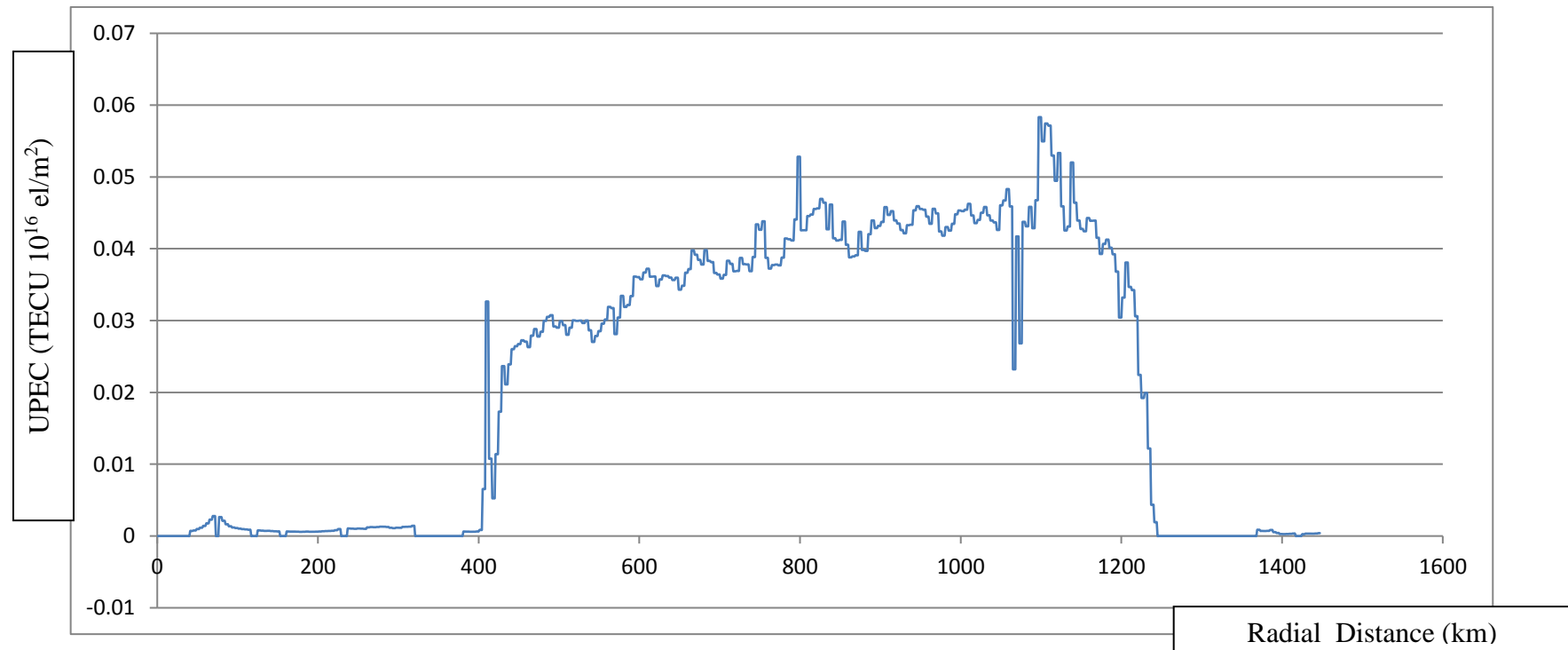


Figure 8.19 Upper Plasmaspheric Electron Content (UPEC) generated for twenty day between 21.03.06 and 09.04.06 for minutes 16700-18400. The X axis is calibrated with the Radial Distance in km.. Straight lines connect gaps between the series. Y axis denotes UPEC in TECU(10^{16} el/m²).

8.2.10 Upper Plasmaspheric Electron Content (UPEC) generated between 21.03.06 and 09.04.06 – Minutes 18600-20100

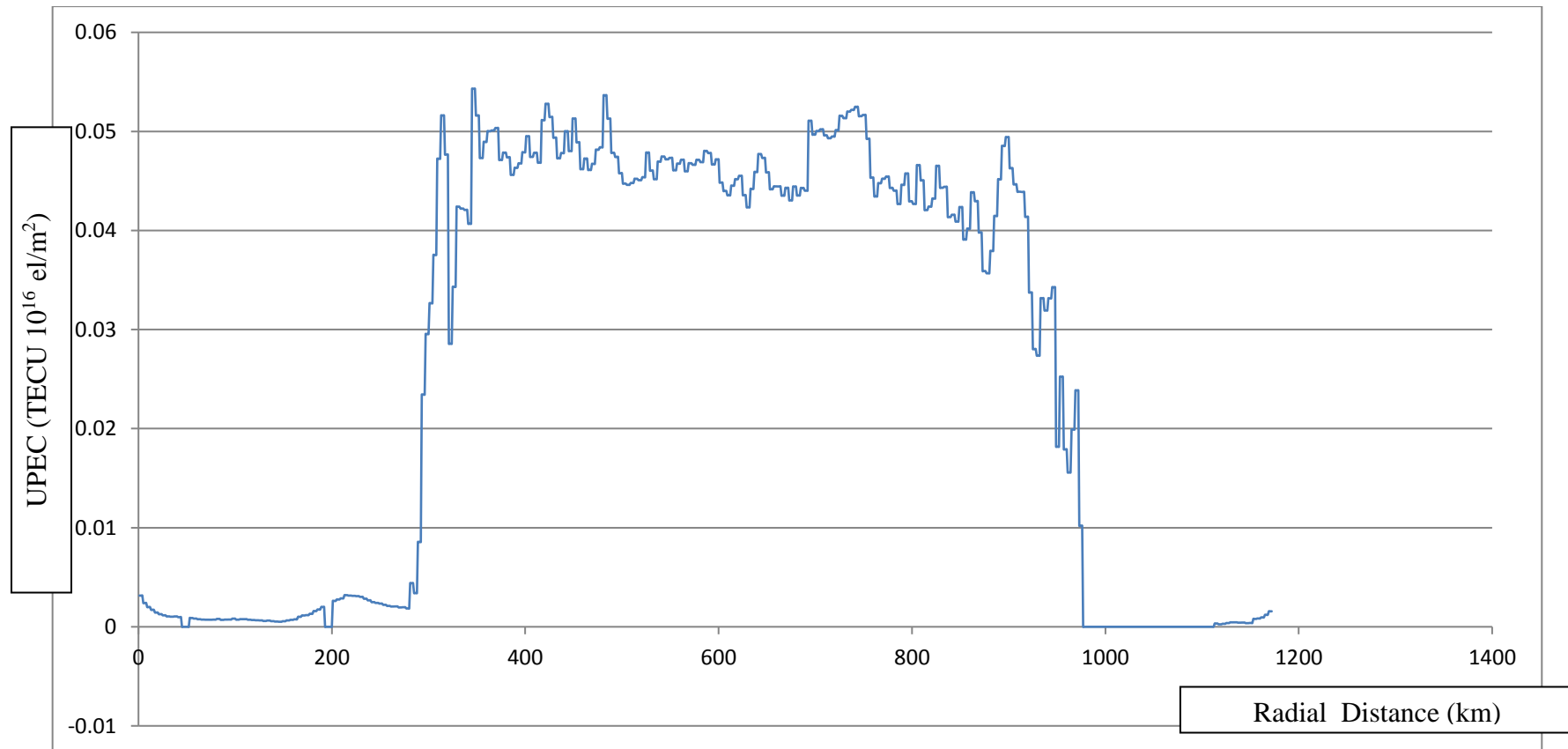


Figure 8.20 Upper Plasmaspheric Electron Content (UPEC) generated for twenty day between 21.03.06 and 09.04.06 for minutes 18600-20100. The X axis is calibrated with the Radial Distance in km.. Straight lines connect gaps between the series. Y axis denotes UPEC in TECU(10^{16} el/m²).

8.2.11 Upper Plasmaspheric Electron Content (UPEC) generated between 21.03.06 and 09.04.06 – Minutes 20250-21900

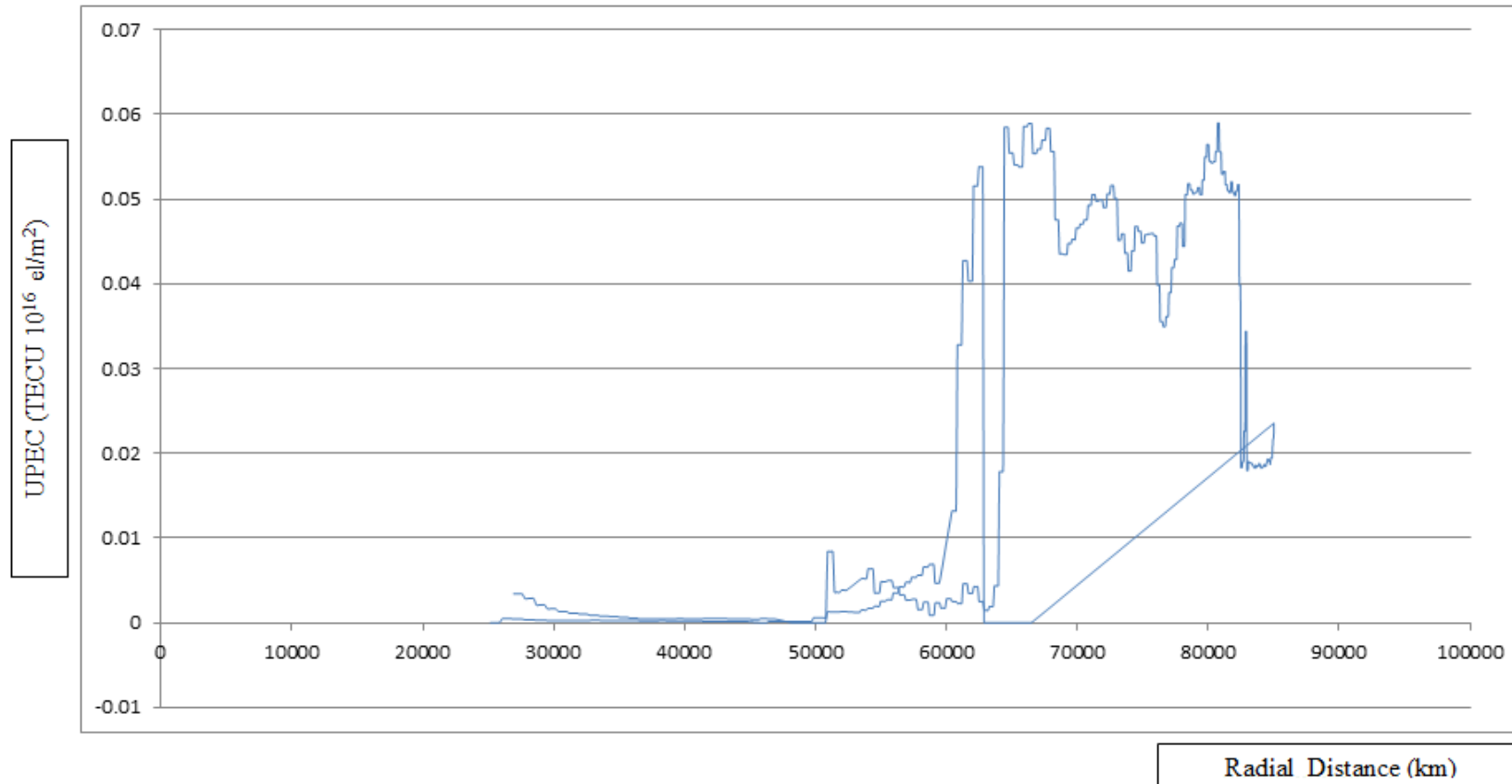


Figure 8.21 Upper Plasmaspheric Electron Content (UPEC) generated for twenty day between 21.03.06 and 09.04.06 for minutes 20250-21900. The X axis is calibrated with the Radial Distance in km.. Straight lines connect gaps between the series. Y axis denotes UPEC in TECU(10^{16} el/m 2).

8.2.12 Upper Plasmaspheric Electron Content (UPEC) generated between 21.03.06 and 09.04.06 – Minutes 21900-23600

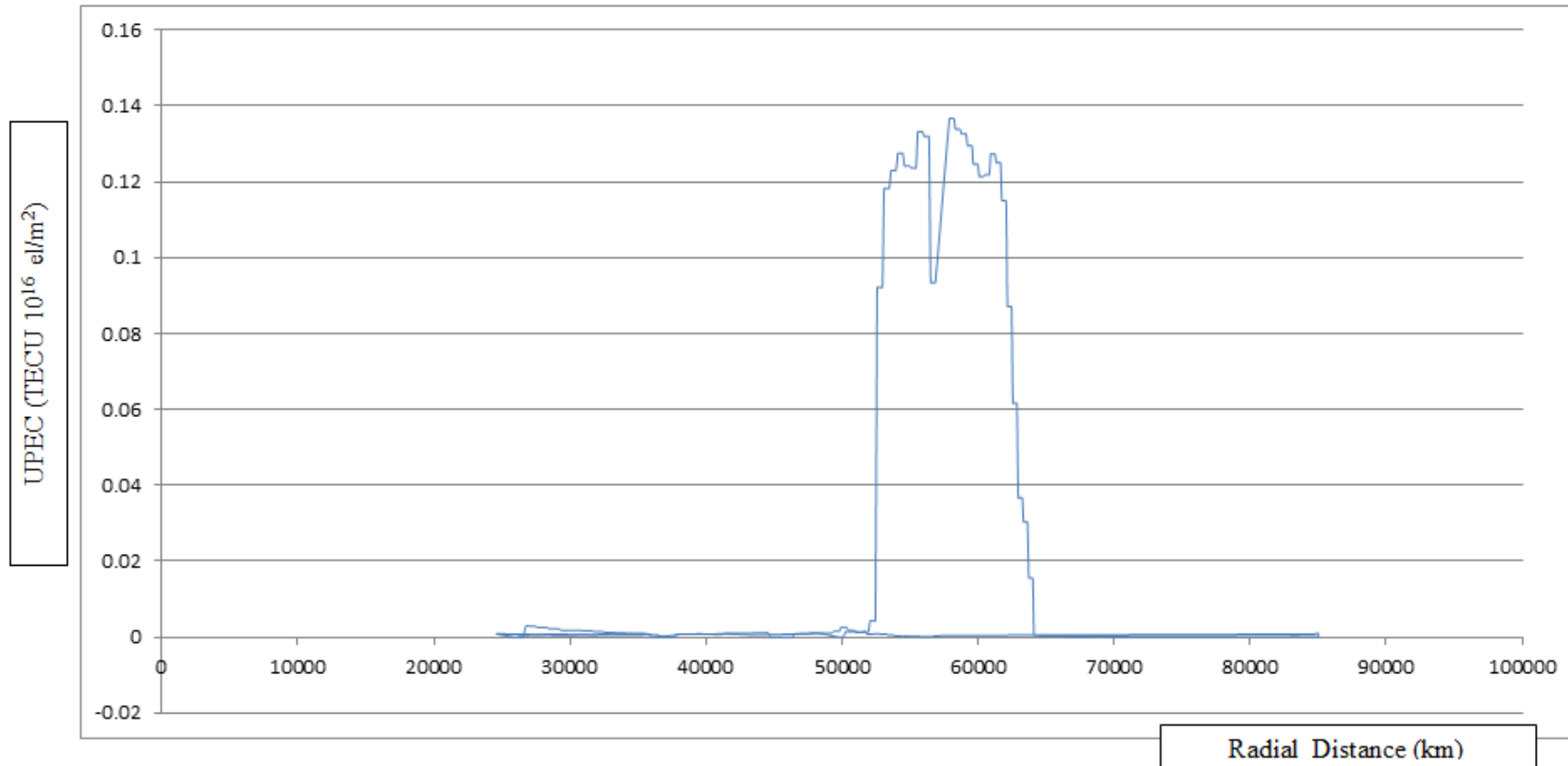


Figure 8.22 Upper Plasmaspheric Electron Content (UPEC) generated for twenty day between 21.03.06 and 09.04.06 for minutes 21900-23600. The X axis is calibrated with the Radial Distance in km.. Straight lines connect gaps between the series. Y axis denotes UPEC in TECU(10^{16} el/m²).

8.2.13 Upper Plasmaspheric Electron Content (UPEC) generated between 21.03.06 and 09.04.06 – Minutes 23600-25300

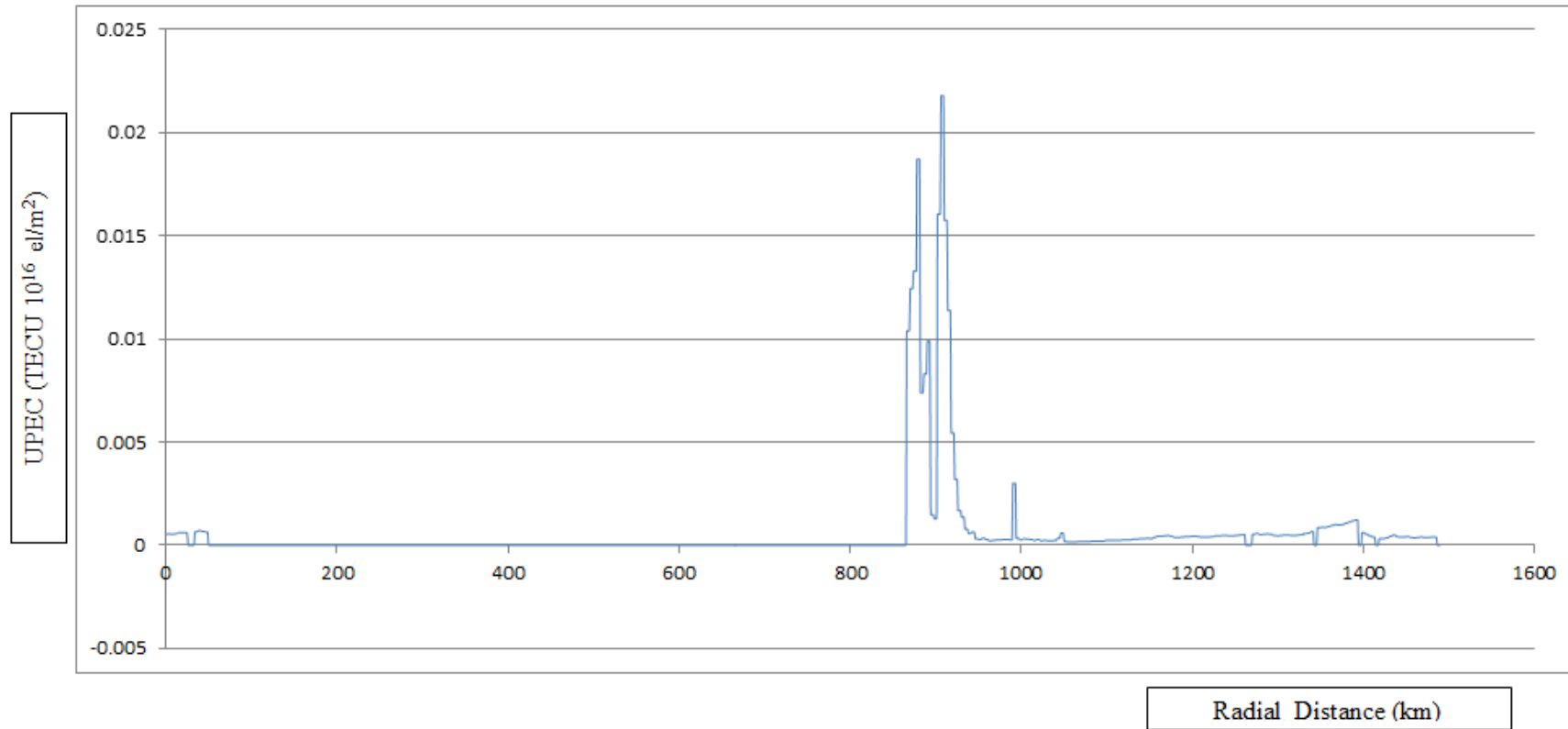


Figure 8.23 Upper Plasmaspheric Electron Content (UPEC) generated for twenty day between 21.03.06 and 09.04.06 for minutes 23600-25300. The X axis is calibrated with the Radial Distance in km.. Straight lines connect gaps between the series. Y axis denotes UPEC in TECU(10^{16} el/m²).

8.2.14 Upper Plasmaspheric Electron Content (UPEC) generated between 21.03.06 and 09.04.06 – Minutes 25300-26950

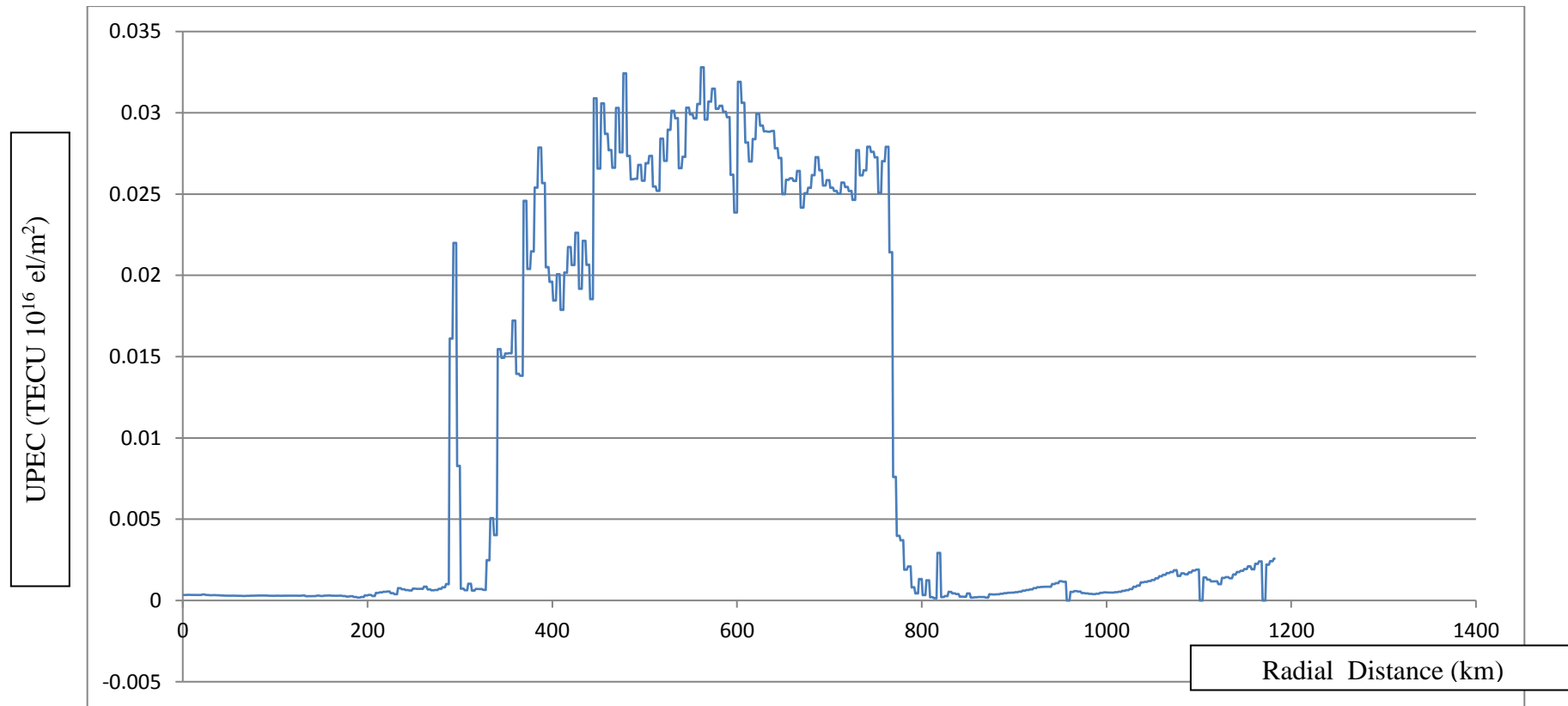


Figure 8.24 Upper Plasmaspheric Electron Content (UPEC) generated for twenty day between 21.03.06 and 09.04.06 for minutes 25300-26950. The X axis is calibrated with the Radial Distance in km.. Straight lines connect gaps between the series. Y axis denotes UPEC in TECU(10^{16} el/m²).

8.2.15 Upper Plasmaspheric Electron Content (UPEC) generated between 21.03.06 and 09.04.06 – Minutes 26950-28600

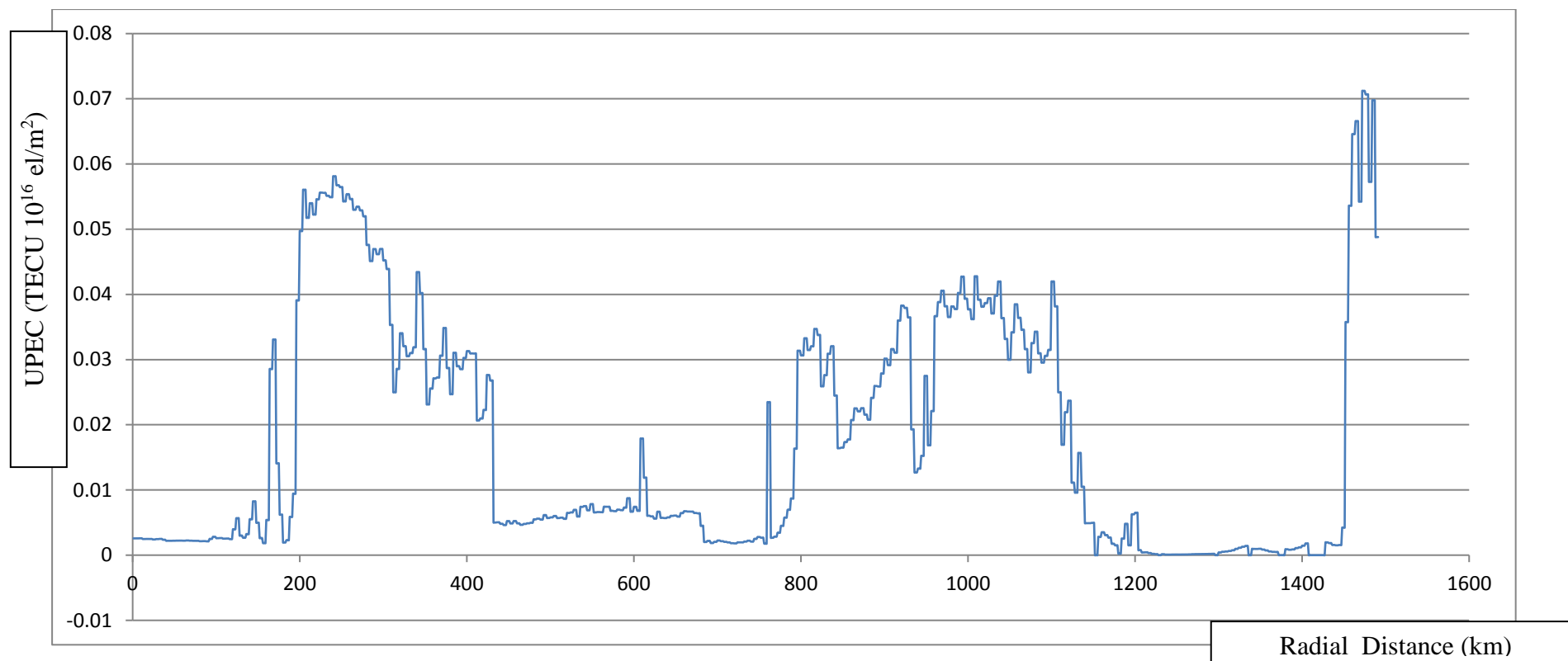


Figure 8.25 Upper Plasmaspheric Electron Content (UPEC) generated for twenty day between 21.03.06 and 09.04.06 for minutes 26950-28600. The X axis is calibrated with the Radial Distance in km.. Straight lines connect gaps between the series. Y axis denotes UPEC in TECU(10^{16} el/m²).

8.3 Variation of Upper Plasmaspheric Electron Content (UPEC) as a function of longitude

8.3.1 Upper Plasmaspheric Electron Content (UPEC) generated between 21.03.06 and 09.04.06 – Minutes 0001 to 1650

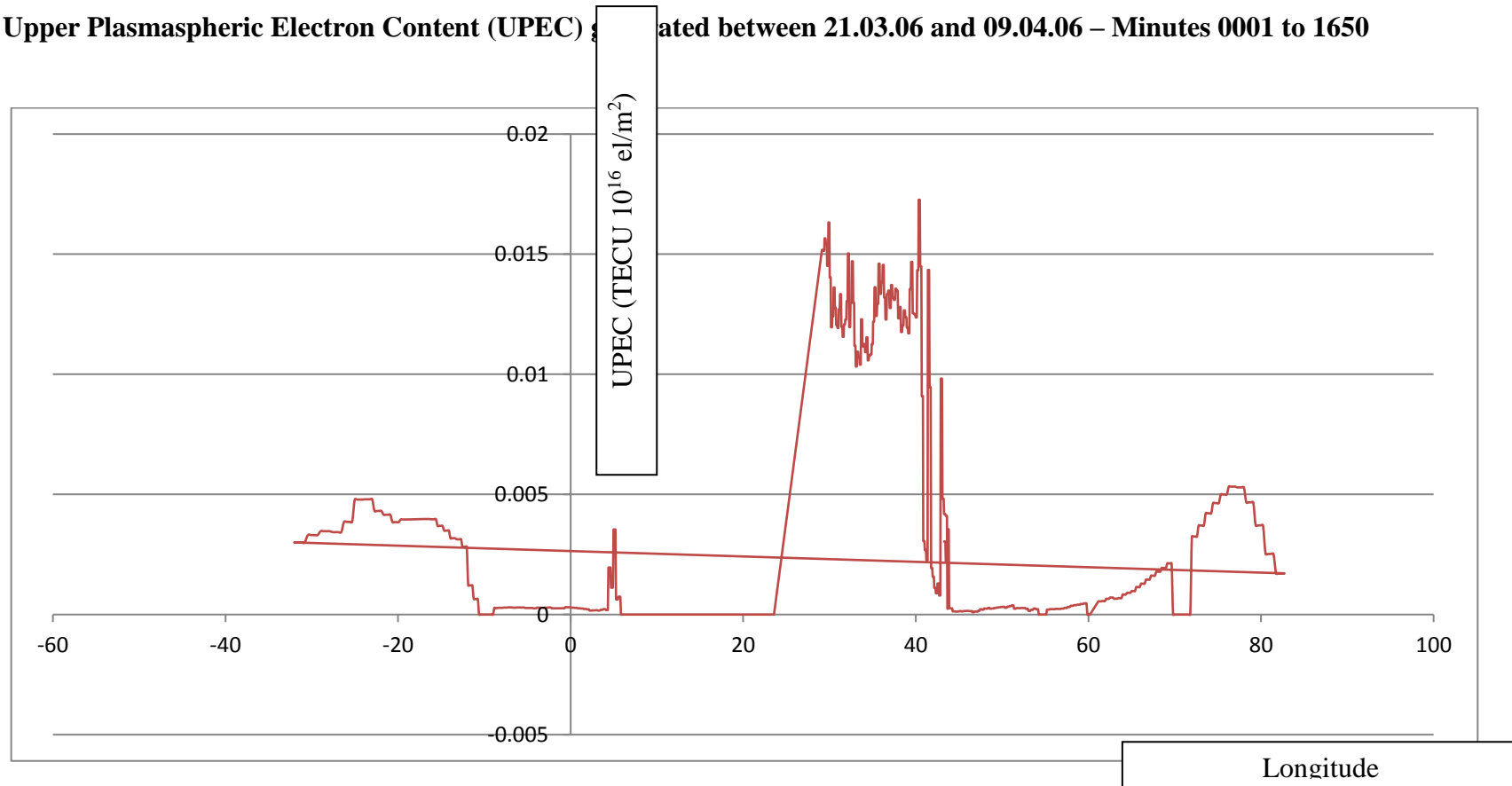


Figure 8.26 The Variation of Upper Plasmaspheric Electron Content (UPEC) generated between 21.03.06 and 09.04.06 for minutes 0001 to 1650. The X axis is calibrated with the longitude. Straight lines connect gaps between the series. Y axis denotes UPEC in TECU(10^{16} el/m²).

8.3.2 Upper Plasmaspheric Electron Content (UPEC) generated between 21.03.06 and 09.04.06 – Minutes 1600-3200

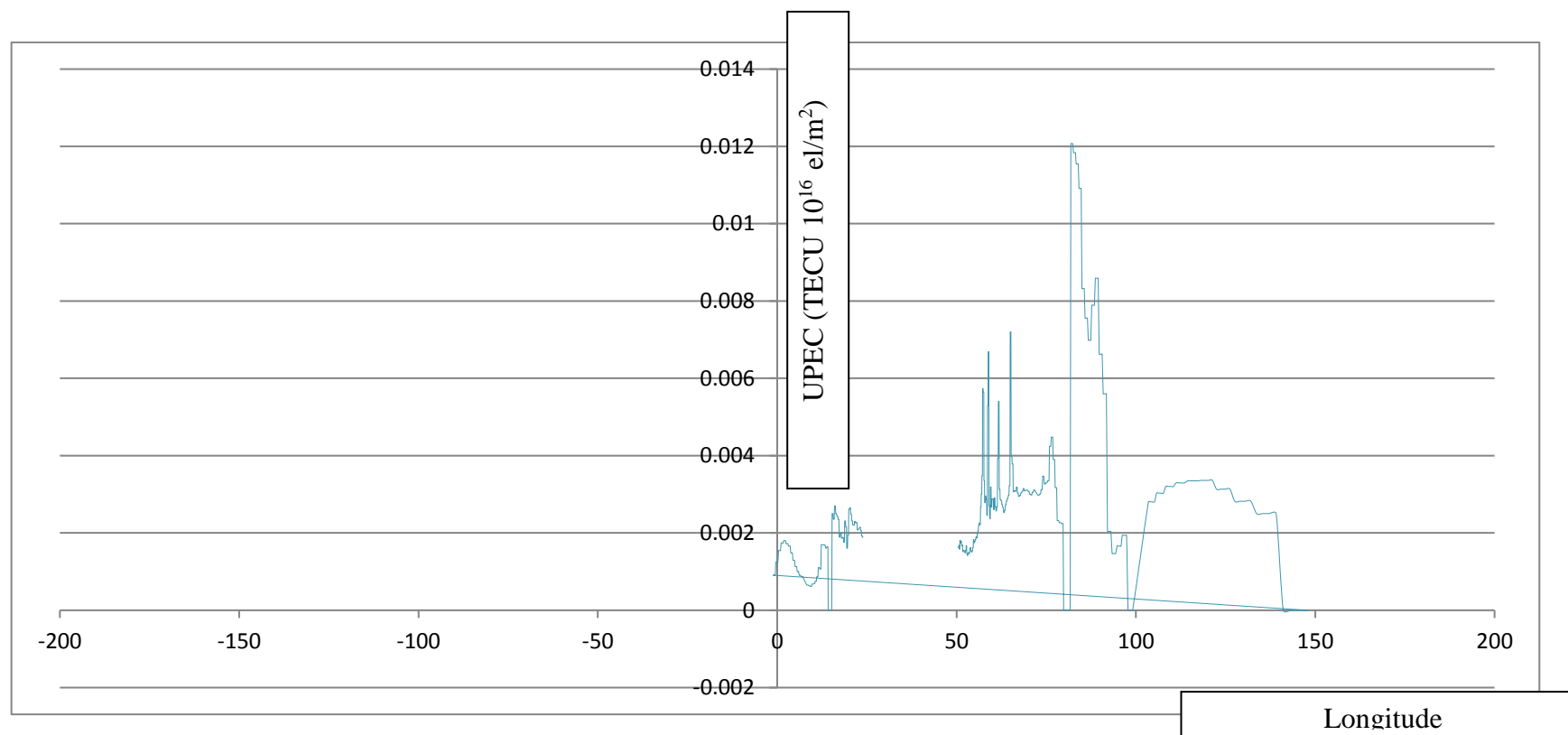


Figure 8.27 The Variation of Upper Plasmaspheric Electron Content (UPEC) generated between 21.03.06 and 09.04.06 for minutes 1600-3200. The X axis is calibrated with the longitude. Straight lines connect gaps between the series. Y axis denotes UPEC in TECU(10^{16} el/m²).

8.3.3 Upper Plasmaspheric Electron Content (UPEC) generated between 21.03.06 and 09.04.06 – Minutes 3400-5100

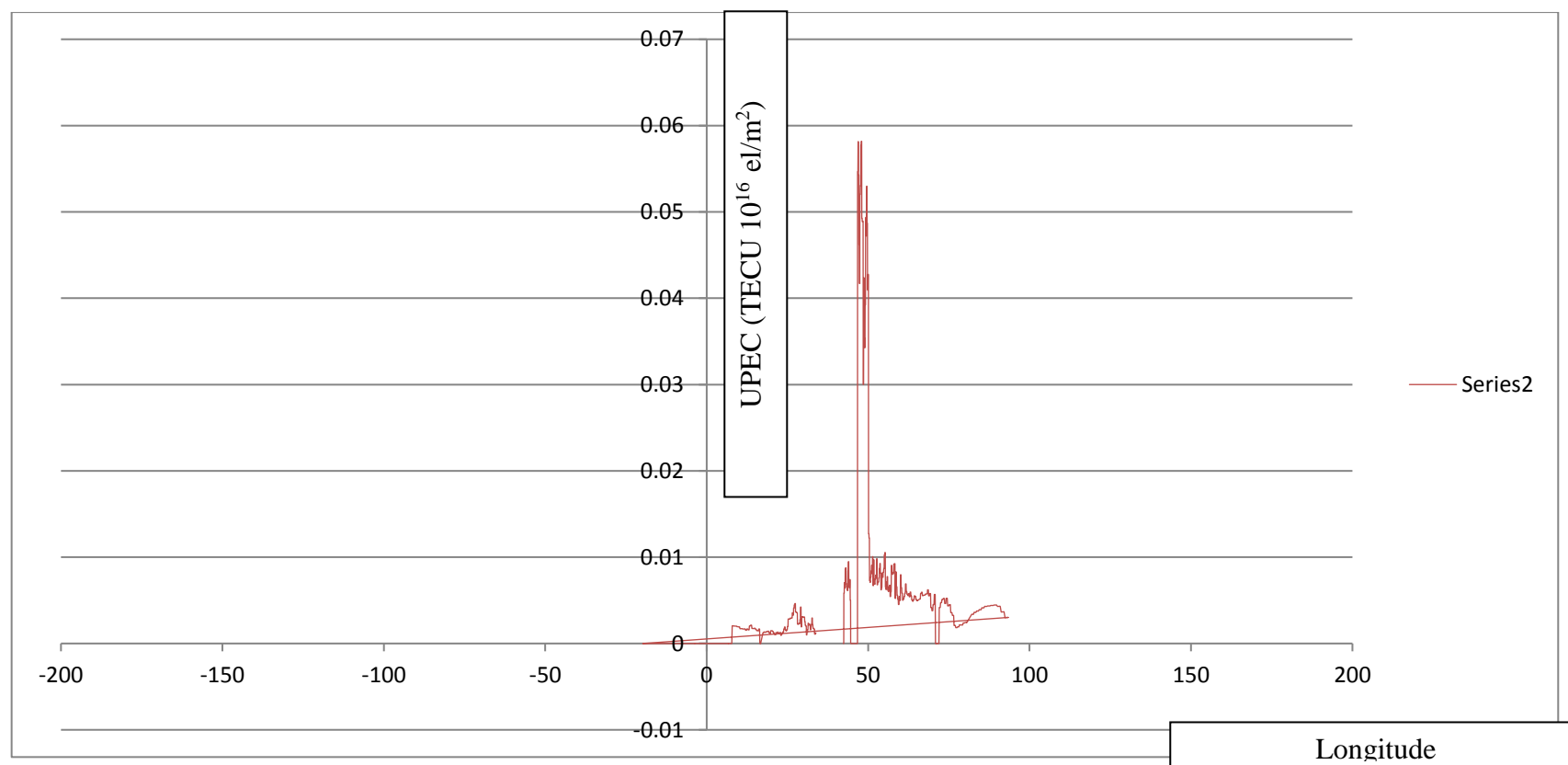


Figure 8.28 The Variation of Upper Plasmaspheric Electron Content (UPEC) generated between 21.03.06 and 09.04.06 for minutes 3400-5100. The X axis is calibrated with the longitude. Straight lines connect gaps between the series. Y axis denotes UPEC in TECU(10^{16} el/m²).

8.3.4 Upper Plasmaspheric Electron Content (UPEC) generated between 21.03.06 and 09.04.06 – Minutes 5100-6700

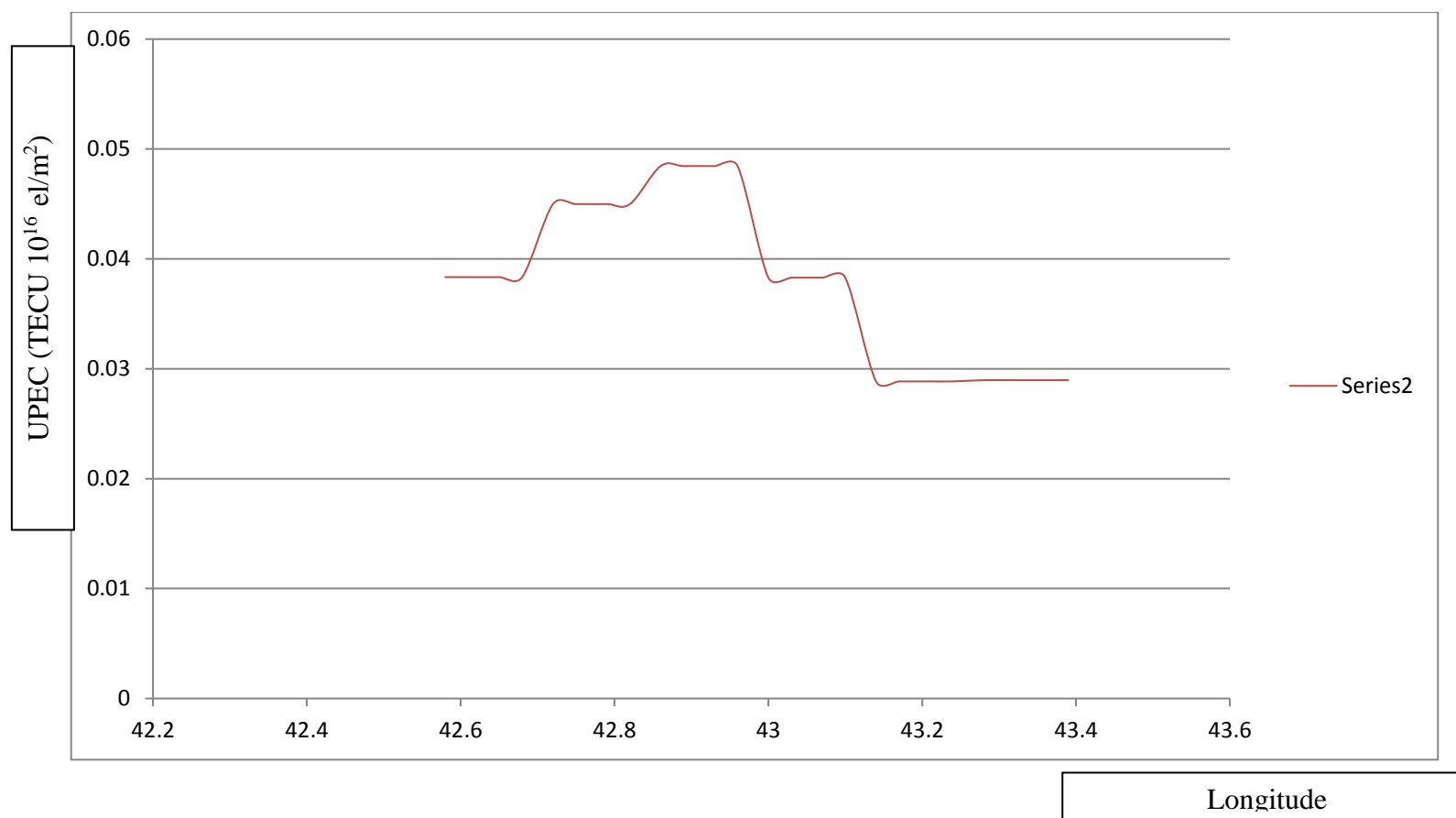


Figure 8.29 The Variation of Upper Plasmaspheric Electron Content (UPEC) generated between 21.03.06 and 09.04.06 for minutes 5100-6700. The X axis is calibrated with the longitude. Straight lines connect gaps between the series. Y axis denotes UPEC in TECU(10^{16} el/m²).

8.3.5 Upper Plasmaspheric Electron Content (UPEC) generated between 21.03.06 and 09.04.06 – Minutes 6700-8400

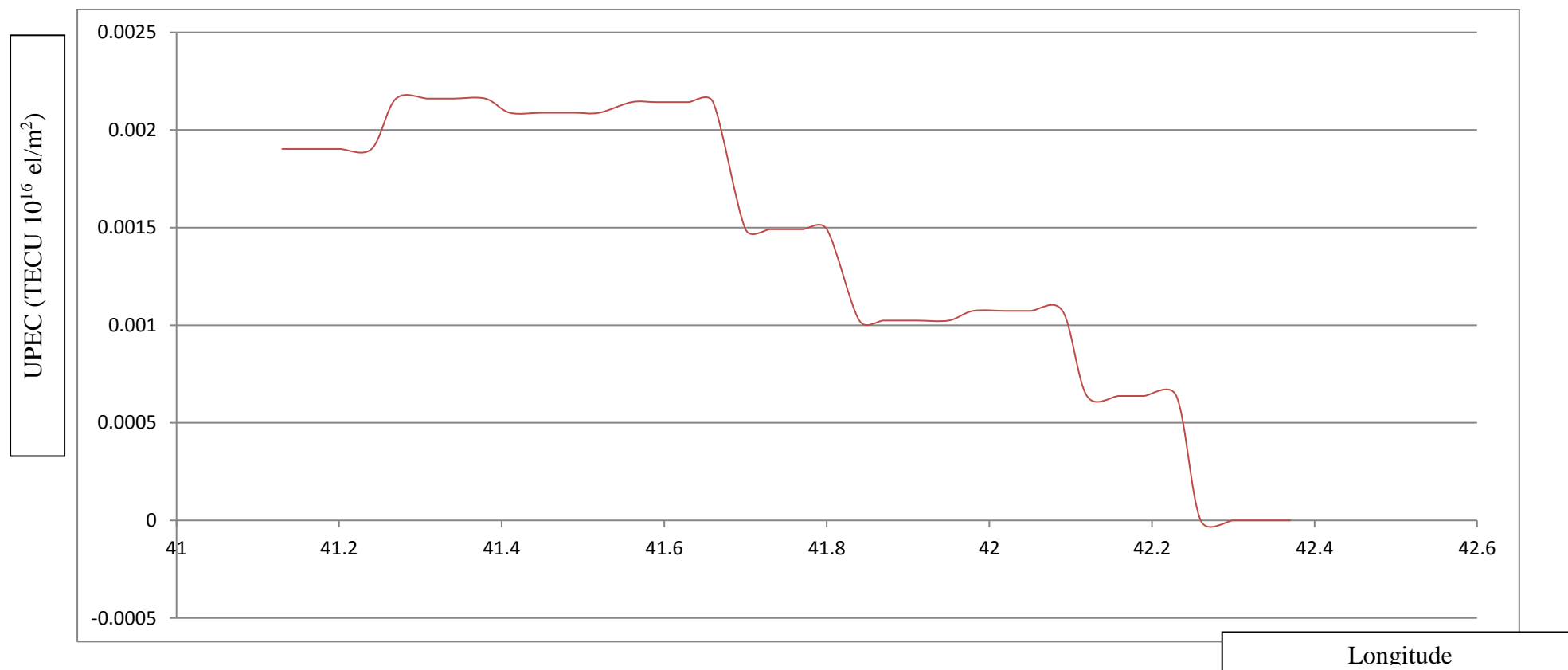


Figure 8.30 The Variation of Upper Plasmaspheric Electron Content (UPEC) generated between 21.03.06 and 09.04.06 for minutes 6700-8400. The X axis is calibrated with the longitude. Straight lines connect gaps between the series. Y axis denotes UPEC in TECU(10^{16} el/m²).

8.3.6 Upper Plasmaspheric Electron Content (UPEC) generated between 21.03.06 and 09.04.06 – Minutes 11000-11800

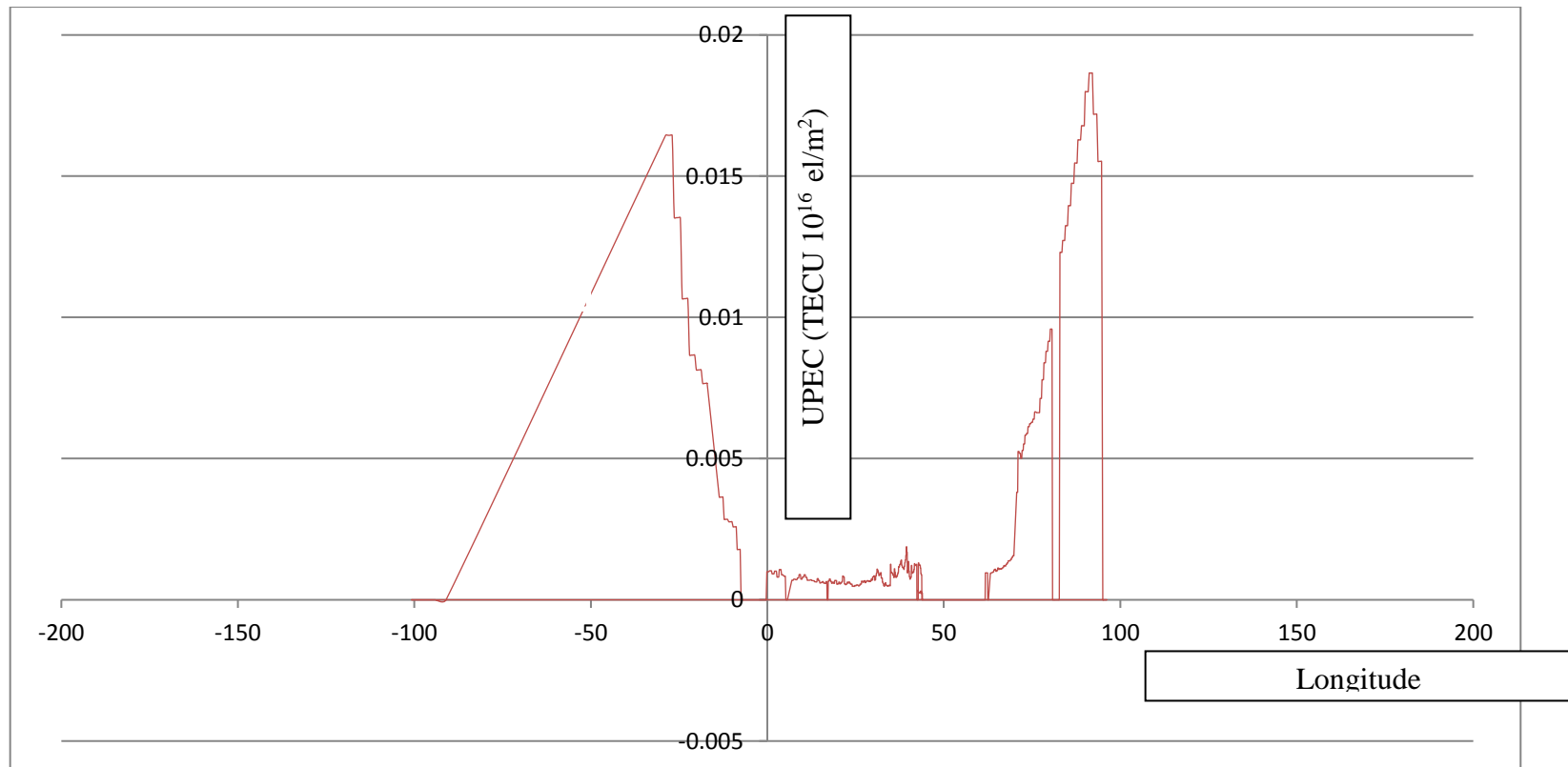


Figure 8.31 The Variation of Upper Plasmaspheric Electron Content (UPEC) generated between 21.03.06 and 09.04.06 for minutes 11000-11800. The X axis is calibrated with the longitude. Straight lines connect gaps between the series. Y axis denotes UPEC in TECU(10^{16} el/m²).

8.3.7 Upper Plasmaspheric Electron Content (UPEC) generated between 21.03.06 and 09.04.06 – Minutes 15850 -17500

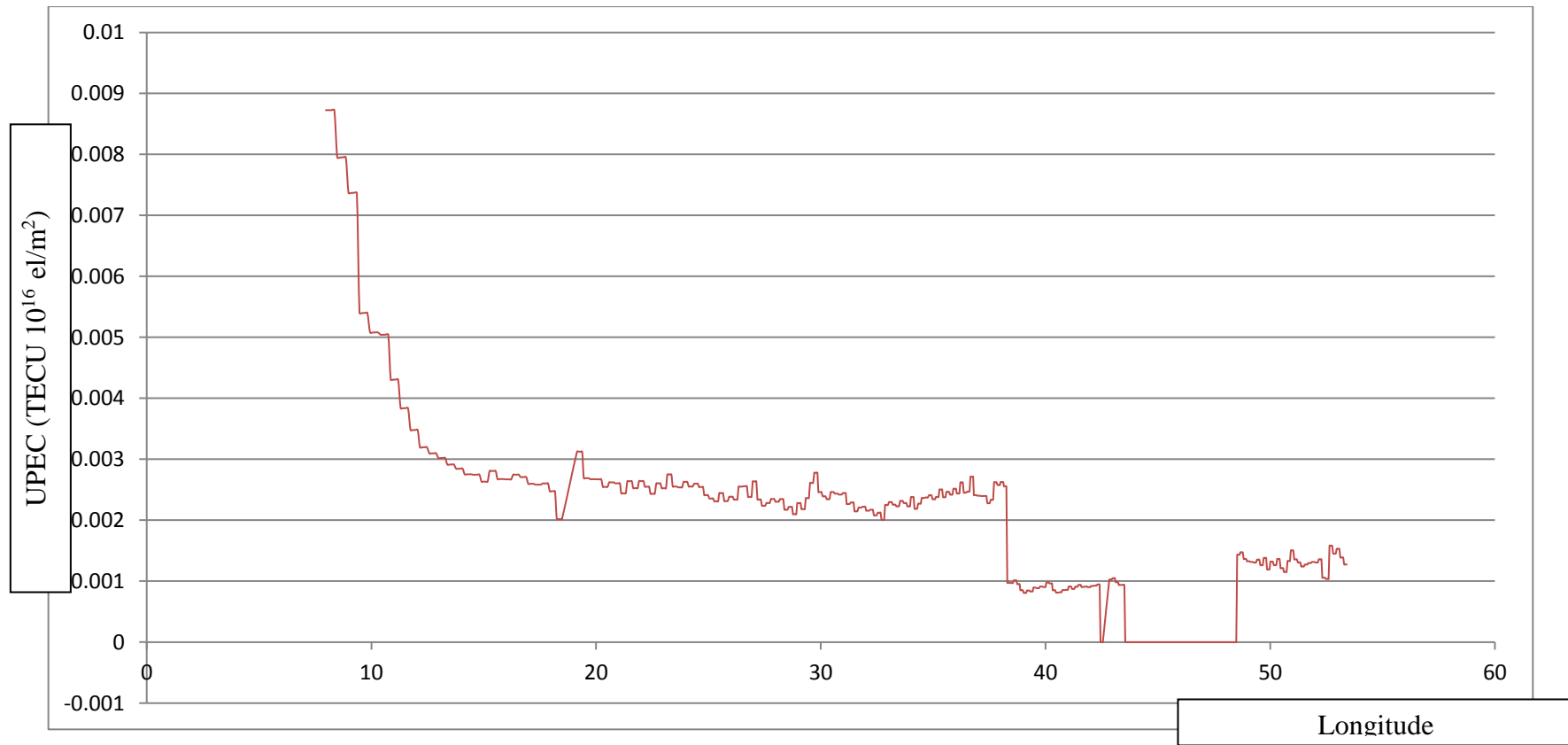


Figure 8.32 The Variation of Upper Plasmaspheric Electron Content (UPEC) generated between 21.03.06 and 09.04.06 for minutes 15850 - 17500

. The X axis is calibrated with the longitude. Straight lines connect gaps between the series. Y axis denotes UPEC in TECU(10^{16} el/m²).

8.3.8 Upper Plasmaspheric Electron Content (UPEC) generated between 21.03.06 and 09.04.06 – Minutes 22700-24300

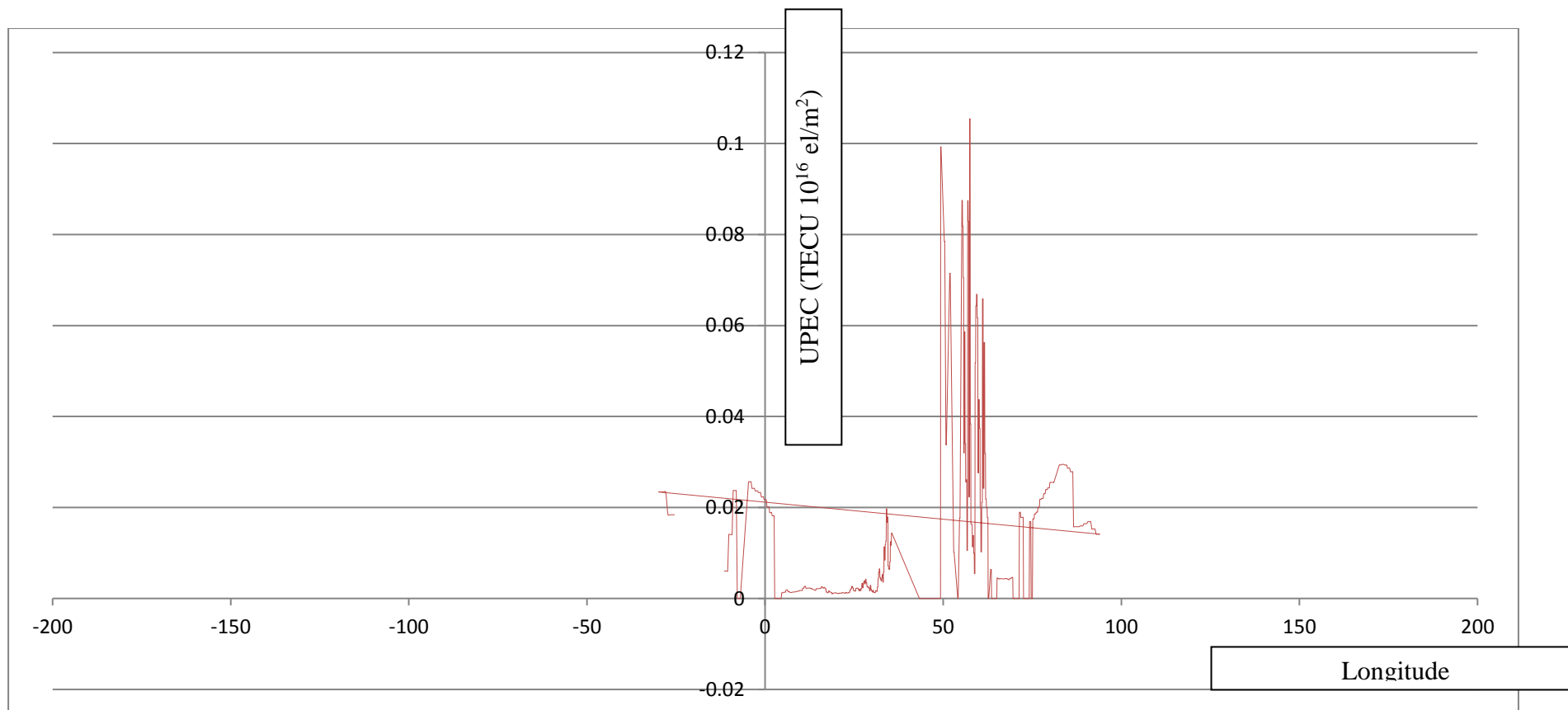


Figure 8.33 The Variation of Upper Plasmaspheric Electron Content (UPEC) generated between 21.03.06 and 09.04.06 for minutes 22700-24300. The X axis is calibrated with the longitude. Straight lines connect gaps between the series. Y axis denotes UPEC in TECU(10^{16} el/m²).

8.3.9 Upper Plasmaspheric Electron Content (UPEC) generated between 21.03.06 and 09.04.06 – Minutes 32200 -34500

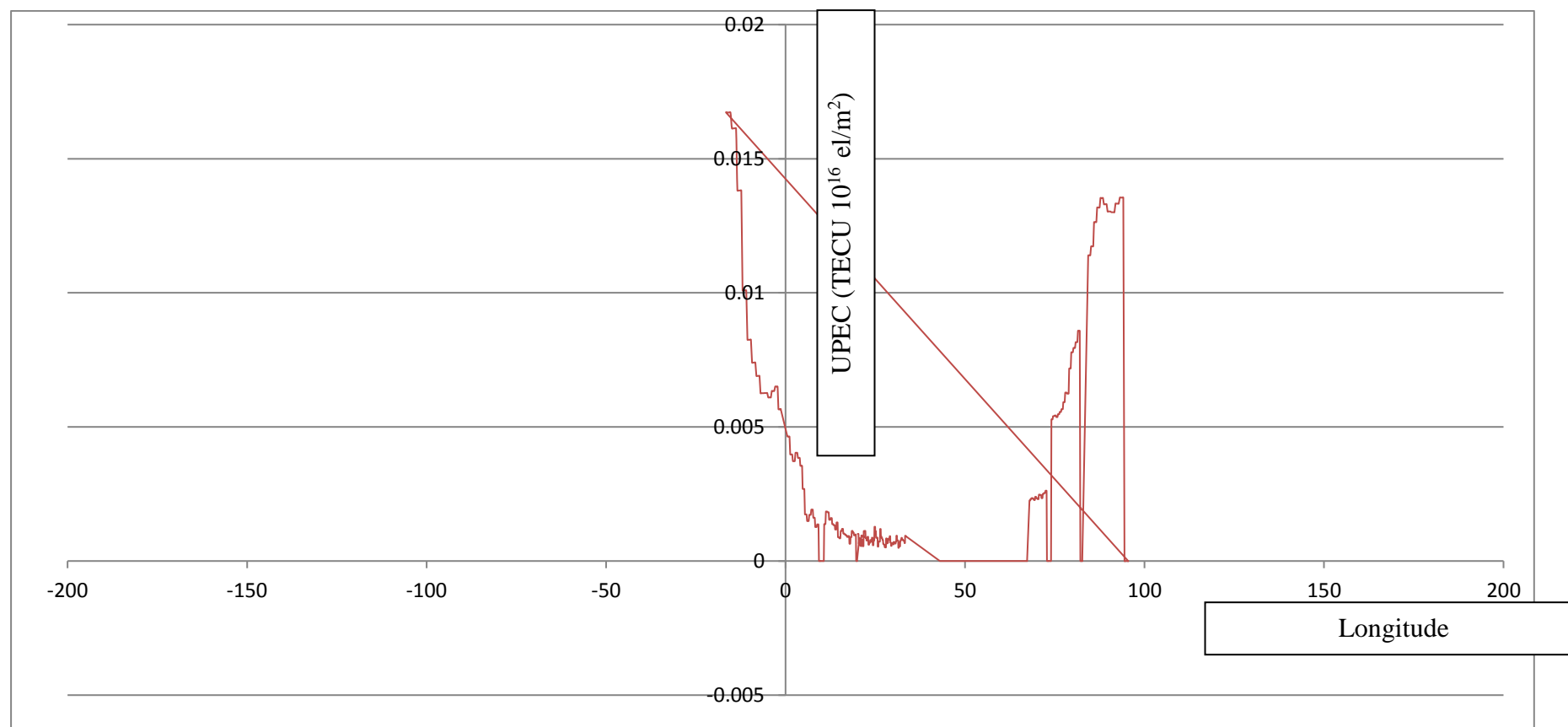


Figure 8.34 The Variation of Upper Plasmaspheric Electron Content (UPEC) generated between 21.03.06 and 09.04.06 for minutes 32200 - 34500. The X axis is calibrated with the longitude. Straight lines connect gaps between the series. Y axis denotes UPEC in TECU(10^{16} el/m²).

8.3.10 Upper Plasmaspheric Electron Content (UPEC) generated between 21.03.06 and 09.04.06 – Minutes 32200 -34500

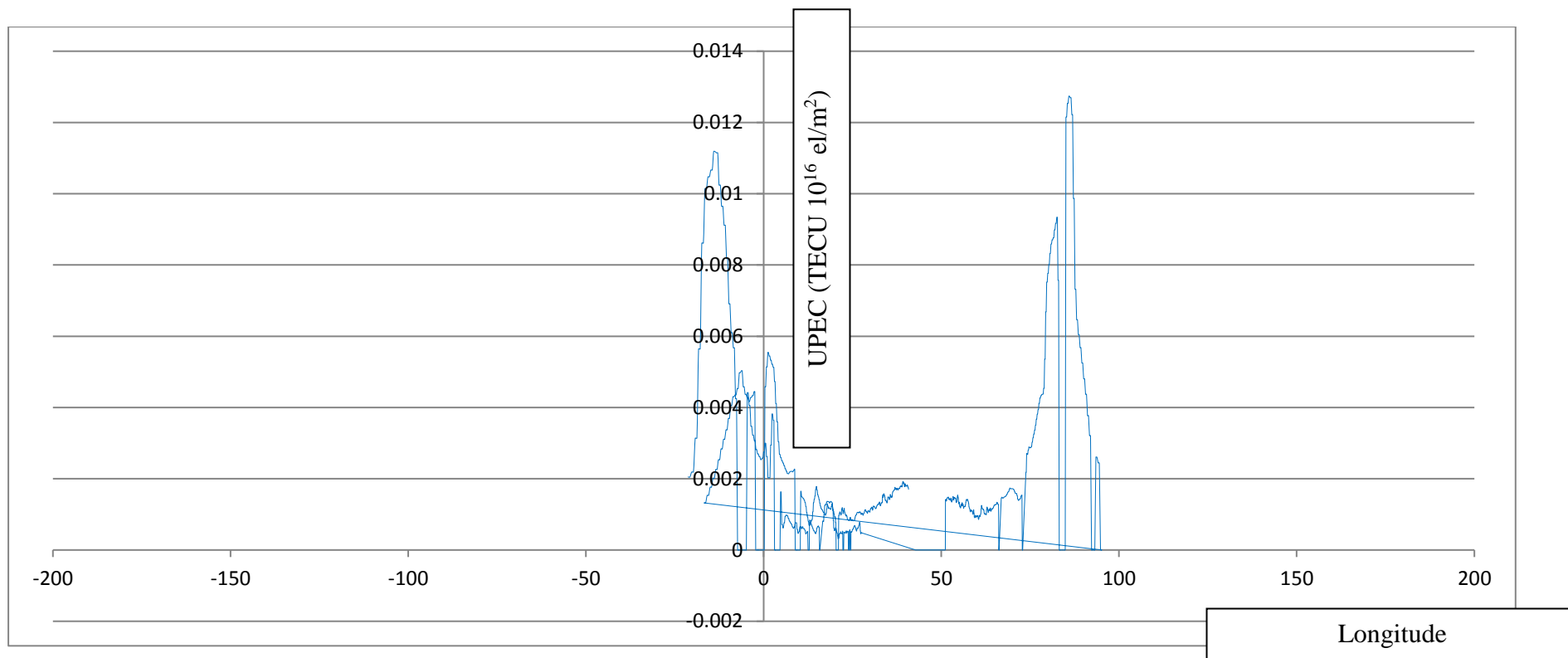


Figure 8.35 The Variation of Upper Plasmaspheric Electron Content (UPEC) generated between 21.03.06 and 09.04.06 for minutes 32200 - 34500. The X axis is calibrated with the longitude. Straight lines connect gaps between the series. Y axis denotes UPEC in $\text{TECU}(10^{16} \text{ e/m}^2)$.

8.4 Observations from the results of Upper Plasmaspheric Electron Content (UPEC) generated by the TEC Builder methodology from TC1 data

- 1 The electron density instrument has been turned off at around 25000 km radial distance during descend to protect instrument from saturating and getting damaged. Therefore, the sub 25000 km component of the UPEC cannot be derived due to lack of data.
- 2 Nevertheless, the exponential growth pattern of UPEC can clearly be observed close to the 30000-25000 km radial distance range.
- 3 The possible sub 25000 km component of the UPEC can be derived by extrapolating the exponential growth pattern of Plasmaspheric in the 30000-25000 km radial distance range.
- 4 The instrument has been turning off whenever there is a hike in electron density. Therefore it has not been possible to derive the UPEC data in such instances.
- 5 The Plasmapause is able to be clearly identifiable around 60000-80000 km radial distance range after which a sudden increase in electron density occurs.

- 6 The correlation between the electron density above the Plasmapause and the TEC figure below that altitude is clearly established. A higher electron density in the altitudes above the Plasmapause always results in a higher UPEC.
- 7 A lower electron density in the altitudes above the Plasmapause always results in a lower UPEC.
- 8 A higher electron density in the altitudes above the Plasmapause always results in a sharper exponential growth UPEC close to the 30000-25000 km radial distance range.
- 9 A lower electron density in the altitudes above the Plasmapause always results in a shallower exponential growth UPEC close to the 30000-25000 km radial distance range.
- 10 The observed Upper UPEC generated by the TEC Builder methodology with the available data set is less than 1% of a TECU (10^{16} el/m²).

8.5 Further Research and Developments

At the start of this research it was stated:

“The contribution of the Upper Plasmasphere (the altitudes above semi-synchronous orbit height up to the Plasmapause height) to the Total Electron Content at any given location has been and continues to be an un-quantified component (Basu et al. 1985). So far, as TEC could not be measured directly and needs to be derived from other parameters, it has not been possible to derive this component from traditional methods such as incoherent scattering radars, ground based ionosondes, satellite sounders and GPS. GPS dual frequency measurements cannot be employed as the Upper Plasmaspheric altitudes are above the GPS satellite orbit altitudes.... ..This research aims to develop this methodology as such that the UPEC component can be determined by applying it on the in situ measurements of electron density measured by any satellite having an eccentric elongated orbit.”

This TEC Builder methodology developed for and describe in this research can be utilised on any mission that has in situ measurements of electron density measured by any satellite having an eccentric elongated orbit.”

This research foresees the following future developments as possible endeavours in that regard.

- a) A dedicated mission to generate a comprehensive equatorial TEC database based on this methodology
- b) Development of an International GNSS System for tracking, communications, ranging, search and rescue and disaster management applications
- c) Development of a comprehensive TEC model and Scintillation model

8.5.1 A dedicated mission to generate a comprehensive equatorial TEC research based on this methodology

A dedicated mission can be launched with a highly eccentric orbit to generate a comprehensive equatorial TEC database based on this methodology. Such a future mission could be preferably launched in the equatorial belt, thus providing the opportunity to develop a an archive of data as well as a real time source for better understanding of the Appleton anomaly Effects on Plasmaspheric Electron Content.

That mission will be ideally have six satellites, with one pair sharing the same line of apsides, and the three pairs equally spaced around the globe (with 120° in between their line of line of apsides) . The two satellites with the same Line of Apsides will ideally Inclination angles of $+10^\circ$ and -10° , thus covering the Appleton Anomaly region, comprehensively.

The three Lines of Apsides can be strategically arranged to cover the three equatorial regions of interest namely, Southeast Asia/South Asia, Africa/ Middle East and Caribbean/South America.

The Figures 8.1 and 8.2 details the structure of such a mission.

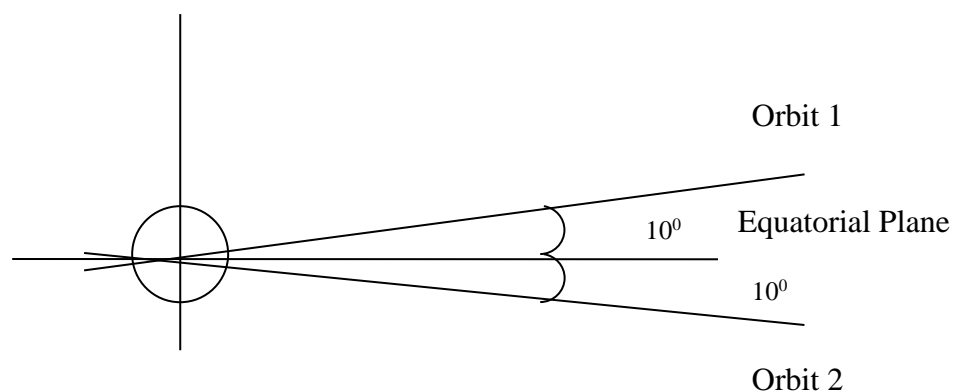


Figure 8.36 The orbit arrangement for a dedicated mission to generate a comprehensive equatorial TEC research based on this methodology. The two orbits for a pair of satellites with the same Line of Apsides

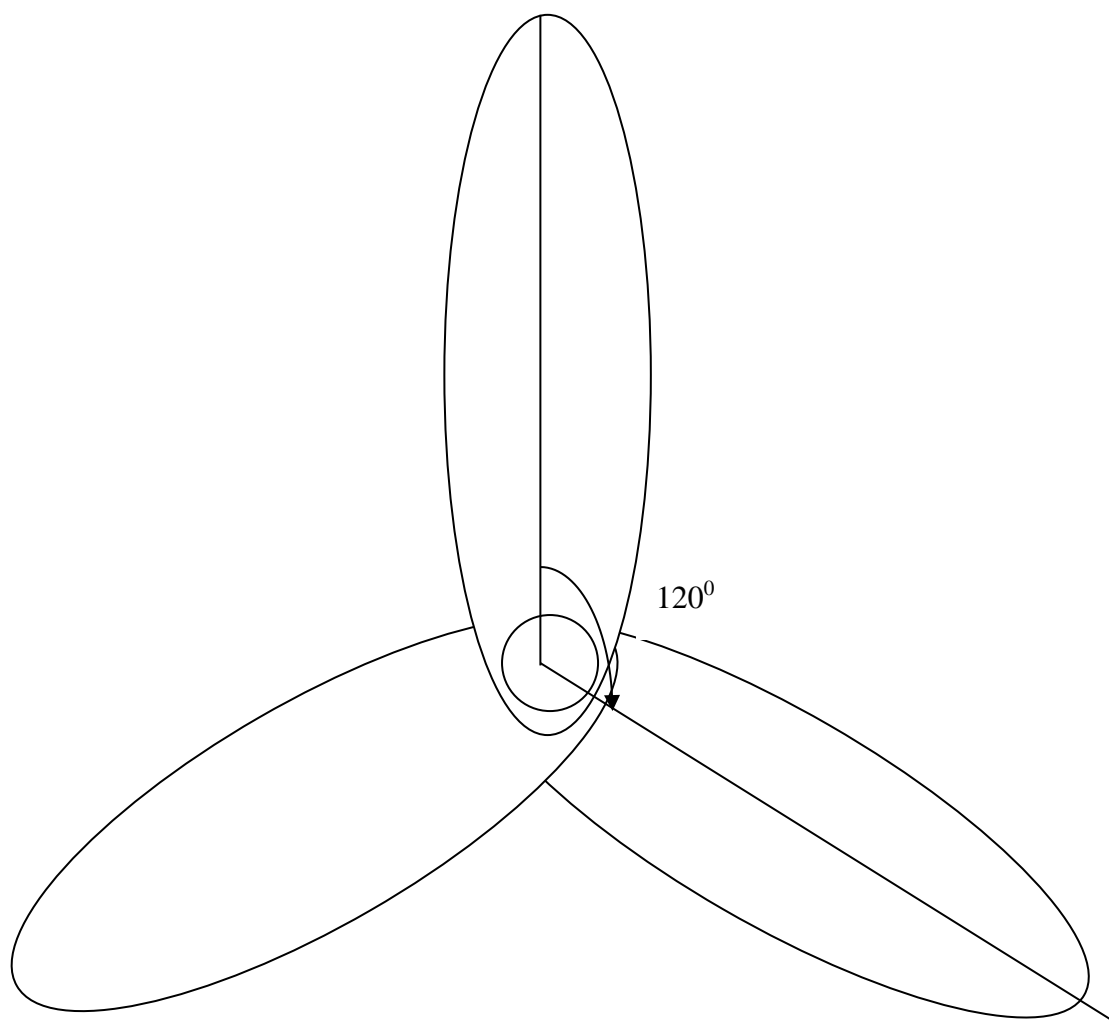


Figure 8.37 The orbit arrangement for a dedicated mission to generate a comprehensive equatorial TEC research based on this methodology. Plane view from the North pole.

8.5.2 Development of an International GNSS System for tracking, communications, ranging, search and rescue and disaster management applications

The need for a global GNSS System for tracking, communications, ranging, search and rescue and disaster management applications has been felt for a long time. The prevailing GNSS systems lack all the capabilities required of such a system, as elaborated in Section 1.6.

Such a system will require a very high level of precision, taking into consideration the very advanced ranging applications envisioned such as Drones.

The methodology developed in this research will be able to provide precise TEC measurements needed for such operations.

8.5.3 Development of a comprehensive TEC model and Scintillation model

The existing TEC and Scintillation models have their own limitations. Therefore, the need for a comprehensive model for TEC and Scintillation prediction has ever been felt, but more so at these times for the same reasons elaborated above.

Like in the case of an advanced GNSS system, the methodology developed in this research will be able to provide precise TEC measurements needed for such a model development exercise.

Appendices

Appendix 1 – ACFTIMESBUILD.C

```
# include <stdio.h>

main(int argc, char *argv[]) {

FILE *fplv1;
unsigned short p[84];
unsigned short q[84];
unsigned int timems=0;
unsigned int p321; /* Fixed ACF Count */
unsigned int p322;
unsigned int p323;
unsigned int p331;
unsigned int p332;
unsigned int p333;

/* Declaring variables for the first Time Series*/

unsigned int offset1;
unsigned int scale1;
unsigned int s101;
unsigned int s102;
unsigned int s103;
unsigned int s104;
unsigned int s105;
unsigned int s106;
unsigned int s107;
unsigned int s108;
unsigned int s109;
unsigned int s110;
unsigned int s111;
unsigned int s112;
unsigned int s113;
unsigned int s114;
unsigned int s115;
unsigned int s116;
unsigned int s117;
unsigned int s118;
unsigned int s119;
unsigned int s120;
unsigned int s121;
unsigned int s122;
```



```
unsigned int s123;  
unsigned int s124;  
unsigned int s125;  
unsigned int s126;  
unsigned int s127;  
unsigned int s128;  
unsigned int s129;  
unsigned int s130;  
unsigned int s131;  
unsigned int s132;  
unsigned int s133;  
unsigned int s134;  
unsigned int s135;  
unsigned int s136;  
unsigned int s137;  
unsigned int s138;  
unsigned int s139;  
unsigned int s140;  
unsigned int s141;  
unsigned int s142;  
unsigned int s143;  
unsigned int s144;  
unsigned int s145;  
unsigned int s146;  
unsigned int s147;  
unsigned int s148;  
unsigned int s149;  
unsigned int s150;  
unsigned int s151;  
unsigned int s152;  
unsigned int s153;  
unsigned int s154;  
unsigned int s155;  
unsigned int s156;  
unsigned int s157;  
unsigned int s158;  
unsigned int s159;  
unsigned int s160;  
unsigned int s161;  
unsigned int s162;
```

```
/* Declaring variables for the second Time Series*/
```

```
unsigned int offset2;  
unsigned int scale2;  
unsigned int s201;  
unsigned int s202;  
unsigned int s203;  
unsigned int s204;  
unsigned int s205;
```

unsigned int s206;
unsigned int s207;
unsigned int s208;
unsigned int s209;
unsigned int s210;
unsigned int s211;
unsigned int s212;
unsigned int s213;
unsigned int s214;
unsigned int s215;
unsigned int s216;
unsigned int s217;
unsigned int s218;
unsigned int s219;
unsigned int s220;
unsigned int s221;
unsigned int s222;
unsigned int s223;
unsigned int s224;
unsigned int s225;
unsigned int s226;
unsigned int s227;
unsigned int s228;
unsigned int s229;
unsigned int s230;
unsigned int s231;
unsigned int s232;
unsigned int s233;
unsigned int s234;
unsigned int s235;
unsigned int s236;
unsigned int s237;
unsigned int s238;
unsigned int s239;
unsigned int s240;
unsigned int s241;
unsigned int s242;
unsigned int s243;
unsigned int s244;
unsigned int s245;
unsigned int s246;
unsigned int s247;
unsigned int s248;
unsigned int s249;
unsigned int s250;
unsigned int s251;
unsigned int s252;
unsigned int s253;
unsigned int s254;
unsigned int s255;

```

unsigned int s256;
unsigned int s257;
unsigned int s258;
unsigned int s259;
unsigned int s260;
unsigned int s261;
unsigned int s262;

/* Declaring variables for the Fixed Energy ACFs*/
unsigned int facflag0;
unsigned int facffoffset;
unsigned int facfscale;

unsigned int facflag1;
unsigned int facflag2;
unsigned int facflag3;
unsigned int facflag4;
unsigned int facflag5;
unsigned int facflag6;
unsigned int facflag7;
unsigned int facflag8;
unsigned int facflag9;
unsigned int facflag10;
unsigned int facflag11;
unsigned int facflag12;
unsigned int facflag13;
unsigned int facflag14;
unsigned int facflag15;
unsigned int facflag16;
unsigned int facflag17;
unsigned int facflag18;
unsigned int facflag19;
unsigned int facflag20;
unsigned int facflag21;
unsigned int facflag22;
unsigned int facflag23;
unsigned int facflag24;
unsigned int facflag25;
unsigned int facflag26;
unsigned int facflag27;
unsigned int facflag28;
unsigned int facflag29;
unsigned int facflag30;
unsigned int facflag31;

/* Declaring variables for the Stepped Energy ACFs*/
unsigned int sacflag0;
unsigned int sacffoffset;
unsigned int sacfscale;

```

```

unsigned int sacflag1;
unsigned int sacflag2;
unsigned int sacflag3;
unsigned int sacflag4;
unsigned int sacflag5;
unsigned int sacflag6;
unsigned int sacflag7;
unsigned int sacflag8;
unsigned int sacflag9;
unsigned int sacflag10;
unsigned int sacflag11;
unsigned int sacflag12;
unsigned int sacflag13;
unsigned int sacflag14;
unsigned int sacflag15;
unsigned int sacflag16;
unsigned int sacflag17;
unsigned int sacflag18;
unsigned int sacflag19;
unsigned int sacflag20;
unsigned int sacflag21;
unsigned int sacflag22;
unsigned int sacflag23;
unsigned int sacflag24;
unsigned int sacflag25;
unsigned int sacflag26;
unsigned int sacflag27;
unsigned int sacflag28;
unsigned int sacflag29;
unsigned int sacflag30;
unsigned int sacflag31;

```

```

int i=0;

```

```

/* initializing array q*/

```

```

for(i=0;i<84;i++){
    q[i]=0;
}

```

```

/* Opening input file */

```

```

if ((fplv1=fopen(argv[1],"r")) == NULL) {
    printf("Cannot open lv1 input file %s \n",argv[1]);
    return(-1);
}

```

```

/* Reading in a level1 packet in TED format */

```

```

while (fread(&q[0],2,84,fplv1)==84) {

int m=0;

for(m=0;m<84;m++){
p[m]=(((q[m] & 0xFF) << 8) + ((q[m] & 0xFFFFF00) >> 8));

}

/*Calculating time in milli seconds*/
timems=(p[10]*3600000) + (p[11]*60000) + (p[12]*1000) + p[13];

p321=((p[32] & 0xFF00) >> 8);
p322=(p[32] & 0xF0);
p323=(p[32] & 0xF);

p331=((p[33] & 0xFF00) >> 8);
p332=((p[33] & 0x30) >> 4);
p333=(p[33] & 0xF);

/* Building the first Time Series */

offset1=((p[74] & 0xF0) >> 4);
scale1=((p[75] & 0xC000) >> 14);

s101=(((p[67] & 0x300) >> 8) + offset1) << scale1);
s102=(((p[67] & 0xC00) >> 10) + offset1) << scale1);
s103=(((p[67] & 0x3000) >> 12) + offset1) << scale1);
s104=(((p[67] & 0xC000) >> 14) + offset1) << scale1);
s105=(((p[67] & 0x3) + offset1) << scale1);
s106=(((p[67] & 0xC) >> 2) + offset1) << scale1);
s107=(((p[67] & 0x30) >> 4) + offset1) << scale1);
s108=(((p[67] & 0xC0) >> 6) + offset1) << scale1);

s109=(((p[68] & 0x300) >> 8) + offset1) << scale1);
s110=(((p[68] & 0xC00) >> 10) + offset1) << scale1);
s111=(((p[68] & 0x3000) >> 12) + offset1) << scale1);
s112=(((p[68] & 0xC000) >> 14) + offset1) << scale1);
s113=(((p[68] & 0x3) + offset1) << scale1);
s114=(((p[68] & 0xC) >> 2) + offset1) << scale1);
s115=(((p[68] & 0x30) >> 4) + offset1) << scale1);
s116=(((p[68] & 0xC0) >> 6) + offset1) << scale1);

s117=(((p[69] & 0x300) >> 8) + offset1) << scale1);
s118=(((p[69] & 0xC00) >> 10) + offset1) << scale1);
s119=(((p[69] & 0x3000) >> 12) + offset1) << scale1);
s120=(((p[69] & 0xC000) >> 14) + offset1) << scale1);
s121=(((p[69] & 0x3) + offset1) << scale1);

```

```

s122=(((p[69] & 0xC) >> 2) + offset1) << scale1);
s123=(((p[69] & 0x30) >> 4) + offset1) << scale1);
s124=(((p[69] & 0xC0) >> 6) + offset1) << scale1);

s125=(((p[70] & 0x300) >> 8) + offset1) << scale1);
s126=(((p[70] & 0xC00) >> 10) + offset1) << scale1);
s127=(((p[70] & 0x3000) >> 12) + offset1) << scale1);
s128=(((p[70] & 0xC000) >> 14) + offset1) << scale1);
s129=(((p[70] & 0x3) + offset1) << scale1);
s130=(((p[70] & 0xC) >> 2) + offset1) << scale1);
s131=(((p[70] & 0x30) >> 4) + offset1) << scale1);
s132=(((p[70] & 0xC0) >> 6) + offset1) << scale1);

s133=(((p[71] & 0x300) >> 8) + offset1) << scale1);
s134=(((p[71] & 0xC00) >> 10) + offset1) << scale1);
s135=(((p[71] & 0x3000) >> 12) + offset1) << scale1);
s136=(((p[71] & 0xC000) >> 14) + offset1) << scale1);
s137=(((p[71] & 0x3) + offset1) << scale1);
s138=(((p[71] & 0xC) >> 2) + offset1) << scale1);
s139=(((p[71] & 0x30) >> 4) + offset1) << scale1);
s140=(((p[71] & 0xC0) >> 6) + offset1) << scale1);

s141=(((p[72] & 0x300) >> 8) + offset1) << scale1);
s142=(((p[72] & 0xC00) >> 10) + offset1) << scale1);
s143=(((p[72] & 0x3000) >> 12) + offset1) << scale1);
s144=(((p[72] & 0xC000) >> 14) + offset1) << scale1);
s145=(((p[72] & 0x3) + offset1) << scale1);
s146=(((p[72] & 0xC) >> 2) + offset1) << scale1);
s147=(((p[72] & 0x30) >> 4) + offset1) << scale1);
s148=(((p[72] & 0xC0) >> 6) + offset1) << scale1);

s149=(((p[73] & 0x300) >> 8) + offset1) << scale1);
s150=(((p[73] & 0xC00) >> 10) + offset1) << scale1);
s151=(((p[73] & 0x3000) >> 12) + offset1) << scale1);
s152=(((p[73] & 0xC000) >> 14) + offset1) << scale1);
s153=(((p[73] & 0x3) + offset1) << scale1);
s154=(((p[73] & 0xC) >> 2) + offset1) << scale1);
s155=(((p[73] & 0x30) >> 4) + offset1) << scale1);
s156=(((p[73] & 0xC0) >> 6) + offset1) << scale1);

s157=(((p[74] & 0x300) >> 8) + offset1) << scale1);
s158=(((p[74] & 0xC00) >> 10) + offset1) << scale1);
s159=(((p[74] & 0x3000) >> 12) + offset1) << scale1);
s160=(((p[74] & 0xC000) >> 14) + offset1) << scale1);
s161=(((p[74] & 0x3) + offset1) << scale1);
s162=(((p[74] & 0xC) >> 2) + offset1) << scale1);

```

```

/* Building the second Time Series */

```

```

offset2=((p[83] & 0xF000) >> 12);
scale2=((p[83] & 0xC0) >> 6);

s201=(((p[75] & 0x3) + offset2) << scale2);
s202=(((p[75] & 0xC) >> 2) + offset2) << scale2);
s203=(((p[75] & 0x30) >> 4) + offset2) << scale2);
s204=(((p[75] & 0xC0) >> 6) + offset2) << scale2);

s205=(((p[76] & 0x300) >> 8) + offset2) << scale2);
s206=(((p[76] & 0xC00) >> 10) + offset2) << scale2);
s207=(((p[76] & 0x3000) >> 12) + offset2) << scale2);
s208=(((p[76] & 0xC000) >> 14) + offset2) << scale2);
s209=(((p[76] & 0x3) + offset2) << scale2);
s210=(((p[76] & 0xC) >> 2) + offset2) << scale2);
s211=(((p[76] & 0x30) >> 4) + offset2) << scale2);
s212=(((p[76] & 0xC0) >> 6) + offset2) << scale2);

s213=(((p[77] & 0x300) >> 8) + offset2) << scale2);
s214=(((p[77] & 0xC00) >> 10) + offset2) << scale2);
s215=(((p[77] & 0x3000) >> 12) + offset2) << scale2);
s216=(((p[77] & 0xC000) >> 14) + offset2) << scale2);
s217=(((p[77] & 0x3) + offset2) << scale2);
s218=(((p[77] & 0xC) >> 2) + offset2) << scale2);
s219=(((p[77] & 0x30) >> 4) + offset2) << scale2);
s220=(((p[77] & 0xC0) >> 6) + offset2) << scale2);

s221=(((p[78] & 0x300) >> 8) + offset2) << scale2);
s222=(((p[78] & 0xC00) >> 10) + offset2) << scale2);
s223=(((p[78] & 0x3000) >> 12) + offset2) << scale2);
s224=(((p[78] & 0xC000) >> 14) + offset2) << scale2);
s225=(((p[78] & 0x3) + offset2) << scale2);
s226=(((p[78] & 0xC) >> 2) + offset2) << scale2);
s227=(((p[78] & 0x30) >> 4) + offset2) << scale2);
s228=(((p[78] & 0xC0) >> 6) + offset2) << scale2);

s229=(((p[79] & 0x300) >> 8) + offset2) << scale2);
s230=(((p[79] & 0xC00) >> 10) + offset2) << scale2);
s231=(((p[79] & 0x3000) >> 12) + offset2) << scale2);
s232=(((p[79] & 0xC000) >> 14) + offset2) << scale2);
s233=(((p[79] & 0x3) + offset2) << scale2);
s234=(((p[79] & 0xC) >> 2) + offset2) << scale2);
s235=(((p[79] & 0x30) >> 4) + offset2) << scale2);
s236=(((p[79] & 0xC0) >> 6) + offset2) << scale2);

s237=(((p[80] & 0x300) >> 8) + offset2) << scale2);
s238=(((p[80] & 0xC00) >> 10) + offset2) << scale2);
s239=(((p[80] & 0x3000) >> 12) + offset2) << scale2);
s240=(((p[80] & 0xC000) >> 14) + offset2) << scale2);
s241=(((p[80] & 0x3) + offset2) << scale2);
s242=(((p[80] & 0xC) >> 2) + offset2) << scale2);

```

```
s243=(((p[80] & 0x30) >> 4) + offset2) << scale2);
s244=(((p[80] & 0xC0) >> 6) + offset2) << scale2);
```

```
s245=(((p[81] & 0x300) >> 8) + offset2) << scale2);
s246=(((p[81] & 0xC00) >> 10) + offset2) << scale2);
s247=(((p[81] & 0x3000) >> 12) + offset2) << scale2);
s248=(((p[81] & 0xC000) >> 14) + offset2) << scale2);
s249=(((p[81] & 0x3) + offset2) << scale2);
s250=(((p[81] & 0xC) >> 2) + offset2) << scale2);
s251=(((p[81] & 0x30) >> 4) + offset2) << scale2);
s252=(((p[81] & 0xC0) >> 6) + offset2) << scale2);
```

```
s253=(((p[82] & 0x300) >> 8) + offset2) << scale2);
s254=(((p[82] & 0xC00) >> 10) + offset2) << scale2);
s255=(((p[82] & 0x3000) >> 12) + offset2) << scale2);
s256=(((p[82] & 0xC000) >> 14) + offset2) << scale2);
s257=(((p[82] & 0x3) + offset2) << scale2);
s258=(((p[82] & 0xC) >> 2) + offset2) << scale2);
s259=(((p[82] & 0x30) >> 4) + offset2) << scale2);
s260=(((p[82] & 0xC0) >> 6) + offset2) << scale2);
```

```
s261=(((p[83] & 0x300) >> 8) + offset2) << scale2);
s262=(((p[83] & 0xC00) >> 10) + offset2) << scale2);
```

```
/* Building the Fixed Energy ACFs */
```

```
facflag0=((p[34] << 8) + ((p[35] & 0xFF00) >> 8));
facoffset=(((p[35] & 0xFF) << 16) + p[36]);
facfscale=((p[37] & 0xFC00) >> 10);
```

```
facflag1=(((p[37] & 0x3F0) >> 4) + facoffset) << facfscale);
facflag2=((((p[37] & 0xF) << 2) + ((p[38] & 0xC000) >> 14)) + facoffset) <<
facfscale);
facflag3=(((p[38] & 0x3F00) >> 8) + facoffset) << facfscale);
facflag4=(((p[38] & 0xFC) >> 2) + facoffset) << facfscale);
facflag5=((((p[38] & 0x3) << 4) + ((p[39] & 0xF000) >> 12)) + facoffset) <<
facfscale);
facflag6=(((p[39] & 0xFC0) >> 6) + facoffset) << facfscale);
facflag7=(((p[39] & 0x3F) + facoffset) << facfscale);
```

```
facflag8=(((p[40] & 0xFC00) >> 10) + facoffset) << facfscale);
facflag9=(((p[40] & 0x3F0) >> 4) + facoffset) << facfscale);
facflag10=((((p[40] & 0xF) << 2) + ((p[41] & 0xC000) >> 14)) + facoffset) <<
facfscale);
facflag11=(((p[41] & 0x3F00) >> 8) + facoffset) << facfscale);
facflag12=(((p[41] & 0xFC) >> 2) + facoffset) << facfscale);
facflag13=((((p[41] & 0x3) << 4) + ((p[42] & 0xF000) >> 12)) + facoffset) <<
facfscale);
facflag14=(((p[42] & 0xFC0) >> 6) + facoffset) << facfscale);
```



```

facflag15=(((p[42] & 0x3F) + facffoffset) << facfscale);

facflag16=(((p[43] & 0xFC00) >> 10) + facffoffset) << facfscale);
facflag17=(((p[43] & 0x3F0) >> 4) + facffoffset) << facfscale);
facflag18=(((p[43] & 0xF) << 2) + ((p[44] & 0xC000) >> 14)) + facffoffset) <<
facfscale);
facflag19=(((p[44] & 0x3F00) >> 8) + facffoffset) << facfscale);
facflag20=(((p[44] & 0xFC) >> 2) + facffoffset) << facfscale);
facflag21=(((p[44] & 0x3) << 4) + ((p[45] & 0xF000) >> 12)) + facffoffset) <<
facfscale);
facflag22=(((p[45] & 0xFC0) >> 6) + facffoffset) << facfscale);
facflag23=(((p[45] & 0x3F) + facffoffset) << facfscale);

facflag24=(((p[46] & 0xFC00) >> 10) + facffoffset) << facfscale);
facflag25=(((p[46] & 0x3F0) >> 4) + facffoffset) << facfscale);
facflag26=(((p[46] & 0xF) << 2) + ((p[47] & 0xC000) >> 14)) + facffoffset) <<
facfscale);
facflag27=(((p[47] & 0x3F00) >> 8) + facffoffset) << facfscale);
facflag28=(((p[47] & 0xFC) >> 2) + facffoffset) << facfscale);
facflag29=(((p[47] & 0x3) << 4) + ((p[48] & 0xF000) >> 12)) + facffoffset) <<
facfscale);
facflag30=(((p[48] & 0xFC0) >> 6) + facffoffset) << facfscale);
facflag31=(((p[48] & 0x3F) + facffoffset) << facfscale);

/* Building the Stepped Energy ACFs */

sacflag0=((p[49] << 8) + ((p[50] & 0xFF00) >> 8));
sacffoffset=(((p[50] & 0xFF) << 16) + p[51]);
sacfscale=((p[52] & 0xFC00) >> 10);

sacflag1=(((p[52] & 0x3F0) >> 4) + facffoffset) << facfscale);
sacflag2=(((p[52] & 0xF) << 2) + ((p[53] & 0xC000) >> 14)) + facffoffset) <<
facfscale);
sacflag3=(((p[53] & 0x3F00) >> 8) + facffoffset) << facfscale);
sacflag4=(((p[53] & 0xFC) >> 2) + facffoffset) << facfscale);
sacflag5=(((p[53] & 0x3) << 4) + ((p[54] & 0xF000) >> 12)) + facffoffset) <<
facfscale);
sacflag6=(((p[54] & 0xFC0) >> 6) + facffoffset) << facfscale);
sacflag7=(((p[54] & 0x3F) + facffoffset) << facfscale);

sacflag8=(((p[55] & 0xFC00) >> 10) + facffoffset) << facfscale);
sacflag9=(((p[55] & 0x3F0) >> 4) + facffoffset) << facfscale);
sacflag10=(((p[55] & 0xF) << 2) + ((p[56] & 0xC000) >> 14)) + facffoffset) <<
facfscale);
sacflag11=(((p[56] & 0x3F00) >> 8) + facffoffset) << facfscale);
sacflag12=(((p[56] & 0xFC) >> 2) + facffoffset) << facfscale);
sacflag13=(((p[56] & 0x3) << 4) + ((p[57] & 0xF000) >> 12)) + facffoffset) <<
facfscale);
sacflag14=(((p[57] & 0xFC0) >> 6) + facffoffset) << facfscale);

```

```
sacflag16=(((p[58] & 0xFC00) >> 10) + facoffset) << facfscale);
sacflag17=(((p[58] & 0x3F0) >> 4) + facoffset) << facfscale);
sacflag18=((((p[58] & 0xF) << 2) + ((p[59] & 0xC000) >> 14)) + facoffset) <<
facfscale);
sacflag19=(((p[59] & 0x3F00) >> 8) + facoffset) << facfscale);
sacflag20=(((p[59] & 0xFC) >> 2) + facoffset) << facfscale);
sacflag21=((((p[59] & 0x3) << 4) + ((p[60] & 0xF000) >> 12)) + facoffset) <<
facfscale);
sacflag22=(((p[60] & 0xFC0) >> 6) + facoffset) << facfscale);
sacflag23=(((p[60] & 0x3F) + facoffset) << facfscale);
```

```
sacflag24=(((p[61] & 0xFC00) >> 10) + facfoffset) << facfscale);
sacflag25=(((p[61] & 0x3F0) >> 4) + facfoffset) << facfscale);
sacflag26=((((p[61] & 0xF) << 2) + ((p[62] & 0xC000) >> 14)) + facfoffset) <<
facfscale);
sacflag27=(((p[62] & 0x3F00) >> 8) + facfoffset) << facfscale);
sacflag28=(((p[62] & 0xFC) >> 2) + facfoffset) << facfscale);
sacflag29=((((p[62] & 0x3) << 4) + ((p[63] & 0xF000) >> 12)) + facfoffset) <<
facfscale);
sacflag30=(((p[63] & 0xFC0) >> 6) + facfoffset) << facfscale);
sacflag31=(((p[63] & 0x3F) + facfoffset) << facfscale);
```

225

```

facflag9, facflag10, facflag11, facflag12, facflag13, facflag14, facflag15, facflag16,
facflag17, facflag18, facflag19, facflag20, facflag21, facflag22, facflag23, facflag24,
facflag25, facflag26, facflag27, facflag28, facflag29, facflag30, facflag31, sacffoffset,
sacfscale, sacflag0, sacflag1, sacflag2, sacflag3, sacflag4, sacflag5, sacflag6, sacflag7,
sacflag8, sacflag9, sacflag10, sacflag11, sacflag12, sacflag13, sacflag14, sacflag15,
sacflag16, sacflag17, sacflag18, sacflag19, sacflag20, sacflag21, sacflag22, sacflag23,
sacflag24, sacflag25, sacflag26, sacflag27, sacflag28, sacflag29, sacflag30, sacflag31);

}

fclose(fplv1);

}

```

Appendix 2

The executable file is generated by

```
gcc -lm -o <executable file> tlmdecom.c tlmproc.c
```

See TLMDECOM.txt for run instructions. To generate correlator data use

```
<executable file> hk_file sci_file output_file /f=4 /h=1 /i=5
```

Where `hk_file` is of form `YYMMDDwh.na1`

and `sci_file` is of form `YYMMDDwn.na1`

where `YYMMDD` refers to Year Month Day

The output file is binary and has a header followed by science data as described in the format document.

Appendix 3 Tlmdecom.c

```
/*{{{ include files*/
#include <stdio.h>
#include <stdlib.h>
#include <ctype.h>
#include <time.h>
#include <string.h>
#include <math.h>

#include "tlmproc.h"
/*}}} */
/*{{{ defines*/

/*}}} */
/*{{{ global variables*/
unsigned char *HKptr;
FILE *LogFile, *OutFile;
int SourceInst = -1;
int HeaderType = 0; /* 0 = 'decom' format, 1 = 'DSD' format */
double HKtime, FirstTime;
long HKcount = 0;
long TelemCount[8] = { 0, 0, 0, 0, 0, 0, 0, 0 };

extern int SOffset_mode;

int EW5MOTAG, EW5RSCNT, EW2SCFRQ, EW5MCSRC, EW2CALST;
int EW2VMON2, EW2VMON3, EW5VMON, EW2TMON;
/*}}} */

/*{{{ int proc_hk (hk_ptr, pkt_size, ob_time)*/
int proc_hk (hk_ptr, pkt_size, ob_time)
unsigned char *hk_ptr;
int pkt_size;
double ob_time;
{
if (!valid_hk (hk_ptr)) return (0);
HKptr = hk_ptr;
HKtime = ob_time;
if (HKcount == 0) FirstTime = ob_time;
HKcount++;
EW5MOTAG = (hk_ptr[0] << 8) + hk_ptr[1];
EW5RSCNT = (hk_ptr[2] << 8) + hk_ptr[3];
EW5MCSRC = (hk_ptr[14] & 0x40) >> 6;
EW2CALST = hk_ptr[21] & 0x3f;
EW2VMON2 = hk_ptr[52];
EW2VMON3 = hk_ptr[53];
EW5VMON = hk_ptr[56];
EW2TMON = hk_ptr[58];
return (1);
}
/*}}} */
/*{{{ int proc_raw (hk_ptr, pkt_size, ob_time)*/
int proc_raw (hk_ptr, pkt_size, ob_time)
unsigned char *hk_ptr;
int pkt_size;
double ob_time;
{
TelemCount[7] += pkt_size;
```

```

return (1);
}
/*}}}} */
/*{{{ int proc_unused (hk_ptr, pkt_size)*/
int proc_unused (hk_ptr, pkt_size, ob_time)
unsigned char *hk_ptr;
int pkt_size;
double ob_time;
{
TelemCount[6] += pkt_size;
return (1);
}
/*}}}} */
/*{{{ int ifwrite (buffer, size, filep)*/
int ifwrite (buffer, size, filep)
int *buffer, size;
FILE *filep;
/* Writes array of ints to file, MSB first */
{
int i;

for (i = 0; i < size; i++) {
    fputc (buffer[i] >> 8, filep);
    fputc (buffer[i] & 0xff, filep);
    if (ferror (filep)) return (EOF);
}
return (size);
}
/*}}}} */
/*{{{ void MakeDecomHeader (int *header, unsigned char *tlm_ptr,*/
void MakeDecomHeader (int *header, unsigned char *tlm_ptr,
                      int pkt_size, double pkt_time)
{
struct tm *inttime;
long ltime;
int i;

/* Zero all words of header to start */
for (i = 0; i < 23; i++) header[i] = 0;

header[0] = 0x81;
header[1] = EW5MOTAG;

/* Put in the timestamp */
ltime = (long)pkt_time;
inttime = gmtime (&ltime);
if (inttime != NULL) {
    header[2] = inttime->tm_year;
    header[3] = inttime->tm_mon+1;
    header[4] = inttime->tm_mday;
    header[5] = inttime->tm_hour;
    header[6] = inttime->tm_min;
    header[7] = inttime->tm_sec;
    header[8] = (int)((pkt_time - floor (pkt_time)) * 1000.0);
}

header[9] = pkt_size / 2 - 2;
header[10] = samp_clks (tlm_ptr);
header[11] = source (tlm_ptr) == 3; /* 0 for normal mode, 1 for burst
mode */

```

```

/* Put in the UDEF bits, UDEF0 = bits 0 and 3, UDEF = bits 1 and 4 */
header[12] = blkcount (tlm_ptr) * 9;

header[21] = EW2CALST;
}
/*}}} */
/*{{{ void MakeDSDHeader (int *header, unsigned char *tlm_ptr,*/
void MakeDSDHeader (int *header, unsigned char *tlm_ptr,
                    int pkt_size, double pkt_time)
{
    struct tm *inttime;
    long ltime;
    int i;

    /* Zero all words of header to start */
    for (i = 0; i < 32; i++) header[i] = 0;

    header[4] = source (tlm_ptr);
    header[6] = pkt_size / 2 - 2;

    /* Put in the timestamp */
    ltime = (long)pkt_time;
    inttime = gmtime (&ltime);
    if (inttime != NULL) {
        header[7] = inttime->tm_year;
        header[8] = inttime->tm_mon+1;
        header[9] = inttime->tm_mday;
        header[10] = inttime->tm_hour;
        header[11] = inttime->tm_min;
        header[12] = inttime->tm_sec;
        header[13] = (int)((pkt_time - floor (pkt_time)) * 1000.0);
    }
    header[15] = samp_clks (tlm_ptr);

    /* Put in the UDEF bits */
    header[16] = blkcount (tlm_ptr);

    /* Put in the STAFF specific bits */
    header[17] = EW5MOTAG;
    header[18] = EW5MCSRC;
    header[21] = EW2VMON2;
    header[22] = EW2VMON3;
    header[23] = EW5VMON;
    header[24] = EW5RSCNT;
    header[25] = EW2TMON;
    header[26] = EW2TMON;
    header[27] = EW2CALST;
    header[28] = EW2SCFRQ;
}
/*}}} */
/*{{{ int proc_sci (tlm_ptr, pkt_size, ob_time, ss_offset)*/
int proc_sci (tlm_ptr, pkt_size, ob_time, ss_offset)
unsigned char *tlm_ptr;
int pkt_size;
double ob_time, ss_offset;
{
    double pkt_time;
    int src;
    static int header[32];

    src = source(tlm_ptr);

```

```

if (src > 5) return (0);
TelemCount[src] += pkt_size;
if (src != SourceInst) return (1);

pkt_time = ob_time + ss_offset + samp_clks (tlm_ptr) / 900.0;

if ((HeaderType & 2) && src == 5) { /* Convert correlator to Cluster
format */
    pkt_size = 68;          /* Set packet size to 68 */
    tlm_ptr[5] &= 0x0f;     /* Clear stepped energy limit bits */
}

if (HeaderType & 1) {
    MakeDSDHeader (header, tlm_ptr, pkt_size, pkt_time);
    ifwrite (header, 32, OutFile);
}
else {
    MakeDecomHeader (header, tlm_ptr, pkt_size, pkt_time);
    ifwrite (header, 23, OutFile);
}

fwrite (tlm_ptr + 4, pkt_size - 4, 1, OutFile);
return (1);
}
/*}}} */
/*{{{ void write_err (pkt_time, message)*/
void write_err (pkt_time, message)
double pkt_time;
char *message;
{
    fprintf (LogFile, "Error: (%s) %s\n", doubletime (pkt_time), message);
}
/*}}} */
/*{{{ void telem_usage ()*/
void telem_usage ()
{
    int i;

    static char *InstNames[] = { "EFW:", "STAFF SA:", "STAFF SC:",
                                "WHISPER:",
                                "WBD:", "Correlator:", "Unused:", "Raw:"
};

    printf ("\nTelemetry usage summary from %s", doubletime (FirstTime));
    printf (" to %s (%d formats).\n\n", doubletime (HKtime), HKcount);
    if (HKcount > 0) for (i = 0; i < 8; i++) {
        printf ("%16s %8ld bytes, %8ld bps\n", InstNames[i], TelemCount[i],
                TelemCount[i] / HKcount * 65536 / 42207);
    }
    for (i = 0; i < 7; i++) TelemCount[7] -= TelemCount[i];
    printf ("Overheads etc.: %8ld bytes, %8ld bps.\n", TelemCount[7],
            TelemCount[7] / HKcount * 65536 / 42207);
}
/*}}} */

/*{{{ main*/
main (argc, argv)
int argc;
char **argv;
{
    int format, arg;

```



```

long start, finish;
FILE *HKfile, *SCIfile;

format = 2;
start = 0;
finish = 864001;
LogFile = stdout;
SSoffset_mode = 0;

if (argc < 3) {
    fprintf (stderr, "TLMDECOM version 2.0 (Double Star)\n");
    fprintf (stderr, "usage: TLMDECOM hk_file sci_file output_file
[options]\n"
        "[options] may be /f=format /h=header /i=instr /s=start_time
/e=end_time\n");
    exit (1);
}
/*{{{ process arguments*/
HKfile = fopen (argv[1], "rb");
if (HKfile == NULL) {
    fprintf (stderr, "Can't open HK data file '%s'\n", argv[1]);
    exit (1);
}
SCIfile = fopen (argv[2], "rb");
if (SCIfile == NULL) {
    fprintf (stderr, "Can't open SCI data file '%s'\n", argv[2]);
    exit (1);
}
OutFile = fopen (argv[3], "wb");
if (OutFile == NULL) {
    fprintf (stderr, "Can't open output file '%s'\n", argv[3]);
    exit (1);
}
for (arg = 4; arg < argc; arg++) {
    if (strncmp (argv[arg], "/f=", 3) == 0) format = atoi (argv[arg] +
3);
    else if (strncmp (argv[arg], "/i=", 3) == 0) SourceInst = atoi
(argv[arg] + 3);
    else if (strncmp (argv[arg], "/h=", 3) == 0) HeaderType = atoi
(argv[arg] + 3);
    else if (strncmp (argv[arg], "/s=", 3) == 0) start = encode_time
(argv[arg] + 3);
    else if (strncmp (argv[arg], "/e=", 3) == 0) finish = encode_time
(argv[arg] + 3);
    else {
        fprintf (stderr, "Don't understand option '%s'\n", argv[arg]);
        exit (1);
    }
}
/*}}}} */

if (proc_file (HKfile, SCIfile, start, finish, format)) {
    telem_usage ();
    exit (0);
}
fprintf (stderr, "Aborting due to fatal error.\n");
exit (2);
}
/*}}}} */

```

Appendix 4 tlmproc.c

```
/*{{{ include files*/
#include <stdio.h>
#include <stdlib.h>
#include <ctype.h>
#include <time.h>
#include <string.h>
#include <math.h>

#include "tlmproc.h"
/*{{{F tlmproc.h*/
/*:::F TLMPROC.H*/
/*}}} */
/*}}} */
/*{{{ structures*/
/* ROW telemetry data file logical record header */
struct row_file_header {
    unsigned char tag, chan;          /* Always 0, 1 */
    long time, size;
};
/*}}} */
/*{{{ global variables*/
static unsigned char HKblock[HK_SIZE], SCIBlock[SCI_SIZE];
double OnBoardTimes[8], SnapshotOffsets[8];

int SOffset_mode = 1;
/*}}} */
/*{{{ struct tm *decodetime (timep)*/
struct tm *decodetime (timep)
long *timep;
{
    static struct tm timebuf;
    struct tm *gmptr;

    if ((gmptr = gmtime (timep)) != NULL) return (gmptr);

    timebuf.tm_year = 0;
    timebuf.tm_mon = 0;
    timebuf.tm_mday = 0;
    timebuf.tm_hour = (int)((*timep / 3600) % 24);
    timebuf.tm_min = (int)((*timep / 60) % 60);
    timebuf.tm_sec = (int)(*timep % 60);
    return (&timebuf);
}

/*}}} */
/*{{{ char *doubledate (dtime)*/
char *doubledate (dtime)
double dtime;
{
    struct tm *inttime;
    static char strtime[64];
    long ltime;

    ltime = (long)dtime;
    inttime = decodetime (&ltime);
    if (inttime == NULL) return ("****/**/** **.*.*.*****");
    sprintf (strtime, "%4d/%02d/%02d %02d:%02d:%02d.%06.0f",
            inttime->tm_year+1900, inttime->tm_mon+1, inttime->tm_mday,
```

```

        inttime->tm_hour, inttime->tm_min, inttime->tm_sec,
        (dtype - floor (dtype)) * 1000000.0);
return (strtime);
}
/*}}} */
/*{{{ char *doubletime (dtype)*/
char *doubletime (dtype)
double dtype;
{
    struct tm *inttime;
    static char strtime[16];
    long ltime;

    ltime = (long)dtype;
    inttime = decodetime (&ltime);
    if (inttime == NULL) return ("**:**:");
    sprintf (strtime, "%02d:%02d:%02d",
        inttime->tm_hour, inttime->tm_min, inttime->tm_sec);
    return (strtime);
}
/*}}} */
/*{{{ long encode_time (string)*/
long encode_time (string)
char *string;
{
    int hour, min, sec;

    sscanf (string, "%d:%d:%d", &hour, &min, &sec);
    return ((long)hour * 3600 + (long)min * 60 + sec);
}
/*}}} */
/*{{{ long read_lrec (filep, bufsize, format, bufptr, timeptr)*/
long read_lrec (filep, bufsize, format, bufptr, timeptr)
FILE *filep;
long bufsize;
int format;
unsigned char *bufptr;
double *timeptr;
/* Reads one logical record from binary telemetry file. Returns size
of
    record found (bytes) or -1 for end of file, -2 for error. */
{
    long tlm_blk_size;
    struct row_file_header head;
    unsigned char SIShead[SIS_HEADSIZE];
    unsigned char DDShead[DDS_HEADSIZE];

    switch (format) {
        case fmROW_TLM:
            /*{{{ read ROW format file*/
            if (fread (&head, 10, 1, filep) < 1) return ((long)-1);
            /* printf ("read_lrec: size = %d\n", (int)(head.size / 2)); */
            if (head.tag != 0 || head.chan != 1 ||
                head.size < 0 || head.size > bufsize) return ((long)-2);
            if (timeptr != NULL) *timeptr = head.time * 0.001;
            if (fread (bufptr, (size_t)(head.size), 1, filep) < 1) return (-2);
            tlm_blk_size = head.size;
            break;
            /*}}} */
        case fmCCS_TLM:
        case fmSIS_TLM:

```

```

    case fmFDG_TLM:
        /*{{{ read SIS/CCS format file*/
        if (fread (SIShead, SIS_HEADSIZE, 1, filep) < 1) return ((long)-1);
        tlm_blk_size = (long) (SIShead[4]) * 256 + SIShead[5] - 7;
        if (tlm_blk_size > bufsize) return ((long)-2);
        if (fread (bufptr, (size_t)tlm_blk_size, 1, filep) < 1) return
        ((long)-2);
        *timeptr = SIShead[7] * 256.0*65536.0 + SIShead[8] * 65536.0 +
                    SIShead[9] * 256.0 + SIShead[10] * 1.0 + SIShead[11] /
256.0 +
                    SIShead[12] / 65536.0 + SIShead[13] / (256.0*65536.0);
        /*}}} */
        break;
    case fmDDS_TLM:
        /*{{{ read DDS format file*/
        if (fread (DDShead, DDS_HEADSIZE, 1, filep) < 1) return ((long)-1);
        tlm_blk_size = (long) (DDShead[10]) * 256 + DDShead[11];
        if (tlm_blk_size > bufsize) return ((long)-2);
        if (fread (bufptr, (int)tlm_blk_size, 1, filep) < 1) return ((long)-
2);
        *timeptr = (DDShead[0] * 256.0 + DDShead[1] - 4383) * 86400.0 +
                    DDShead[2] * 16777.216 + DDShead[3] * 65.536 +
                    DDShead[4] * 0.256 + DDShead[5] * 0.001 +
                    DDShead[6] * 0.000256 + DDShead[7] * 0.000001;
        /*}}} */
        break;
    default:
        return ((long)-2);
}
/*
fprintf (stderr, "Read block of %ld bytes at %16.6f\n", tlm_blk_size,
*timeptr);
*/
return (tlm_blk_size);
}

/*}}} */
/*{{{ static int proc_sci_pkt (tlm_ptr, pkt_size)*/
static int proc_sci_pkt (tlm_ptr, pkt_size)
unsigned char *tlm_ptr;
int pkt_size;
{
return (proc_sci (tlm_ptr, pkt_size,
    OnBoardTimes[reset_cnt (tlm_ptr)],
    SnapshotOffsets[reset_cnt (tlm_ptr)]));
}
/*}}} */
/*{{{ static void asmb_sci_pkt (tlm_ptr, pkt_size, sci_time)*/
static void asmb_sci_pkt (tlm_ptr, pkt_size, sci_time)
unsigned char *tlm_ptr;
int pkt_size;
double sci_time;
{
/*{{{ local variables and tables*/
int i;
static unsigned char AsmbBuffer[MAXASMBSIZE];
static int AsmbSize = 0, BlockCount = 0, AsmbFlag = 0;
/*}}} */

/*{{{ check for partially assembled block at EOF*/
if (pkt_size == 0) { /* Special call to handle EOF */

```

```

        if (AsmbFlag) {
            write_err (sci_time, "EOF found or error reading file during re-
assembly");
        }
        return;
    }
}
/*}}}} */

/*{{{ check for invalid block for re-assembly*/
if (AsmbFlag &&
    (blkpos(tlm_ptr) == SINGLE_BLK || blkpos(tlm_ptr) == FIRST_BLK ||
    source(tlm_ptr) != source(AsmbBuffer) || pkt_size + AsmbSize >
MAXASMBSIZE+1)) {
    proc_sci_pkt (AsmbBuffer, AsmbSize);
    write_err (sci_time, "Incorrect block found during re-assembly");
    printf ("... blkpos = %d, source = %d, size = %d+%d\n",
        blkpos(tlm_ptr), source(tlm_ptr), pkt_size, AsmbSize);
    AsmbFlag = FALSE;
    AsmbSize = 0;
}
/*}}}} */

/*{{{ assemble subsequent blocks and return*/
if (AsmbFlag) {
    if (blkcount(tlm_ptr) != BlockCount)
        write_err (sci_time, "One or more sub-blocks appear to be
missing");
    BlockCount = (blkcount(tlm_ptr) + 1) % 4;
    for (i = PKT_HEADSIZE; i < pkt_size; i++) AsmbBuffer[AsmbSize + i -
PKT_HEADSIZE] = tlm_ptr[i];
    AsmbSize += pkt_size - PKT_HEADSIZE;
    if (blkpos(tlm_ptr) == LAST_BLK) {
        proc_sci_pkt (AsmbBuffer, AsmbSize);
        AsmbFlag = FALSE;
        AsmbSize = 0;
    }
    return;
}
/*}}}} */

/*{{{ check for invalid block not during re-assembly*/
if (!AsmbFlag && (blkpos(tlm_ptr) == MIDDLE_BLK || blkpos(tlm_ptr) ==
LAST_BLK))
{
    write_err (sci_time, "Middle or last block when single or first
expected");
    printf ("... blkpos = %d, source = %d, size = %d+%d\n",
        blkpos(tlm_ptr), source(tlm_ptr), pkt_size, AsmbSize);
}
/*}}}} */

/*{{{ start a re-assembly sequence and return*/
if (blkpos(tlm_ptr) == FIRST_BLK && pkt_size <= MAXASMBSIZE) {
    BlockCount = 0;
    for (i = 0; i < pkt_size; i++) AsmbBuffer[i] = tlm_ptr[i];
    AsmbFlag = TRUE;
    AsmbSize = pkt_size;
    return;
}
/*}}}} */

```

```

/*{{{ handle individual blocks*/
proc_sci_pkt (tlm_ptr, pkt_size);
/*}}} */
}
/*}}} */
/*{{{ double CalcSSoffset (hk_ptr)*/
double CalcSSoffset (hk_ptr)
unsigned char *hk_ptr;
{
int offset_delta, count_delta, offset_now, count_now, invalid;
double offset_error;
static int offset1, offset2, count1, count2, count_last, average_valid
= 0;
static double final_offset, average_offset_delta;

/*{{{ initialise things needed for more than one mode*/
/* Extract params from HK frame */
count_now = hk_rst_cnt (hk_ptr);
offset_now = hk_ss_off (hk_ptr);
invalid = (hk_ss_inval (hk_ptr) && offset_now > 220) || offset_now >
950;

/* If missing HK frame must flag averages and previous counts as
invalid */
if (count_now - count_last != 1) {
    average_valid = 0;
    count1 = 0;
    count2 = 0;
}

/* Compute deltas */
offset_delta = offset2 - offset1;
if (offset_delta > 555) offset_delta -= 1111;
if (offset_delta < -555) offset_delta += 1111;
count_delta = count2 - count1;
/*}}} */

switch (SSoffset_mode) {
    case 0: /* Assume always zero */
        final_offset = 0.0;
        break;

    case 1: /* Assume SSoffset always valid */
        final_offset = offset_now;
        break;

    case 2: { /* If invalid replace by extrapolation */
        /*{{{ */
        if (invalid && count_delta > 0 && count_delta <= 4) {
            final_offset = offset2 +
                offset_delta * (count_now - count2) / count_delta;
            /* This offset should always be > 220; measured offset would be
            valid
                otherwise. If less than zero should be wrapped upwards. Make
            decision
                point halfway between; ie. wrap upwards if less than 110.
            Only wrap
                down if this produces a value > 110; ie. if calculated offset
            > 1236. */
            if (final_offset < 110.0) final_offset += 1111.0;
            if (final_offset > 1221.0) final_offset -= 1111.0;
        }
    }
}

```

```

    }
    else final_offset = offset_now;
    /*}}} */
}
break;

case 3: { /* Do running average offset using valid input */
    /*{{{ */

    /* Averages become valid, or may be updated, following two
       consecutive HK frames with valid EW5SSOFF parameters */
    if (count_delta == 1) {
        if (average_valid)
            average_offset_delta += 0.1 * (offset_delta -
average_offset_delta);
        else {
            average_offset_delta = offset_delta;
            average_valid = 1;
        }
    }
    if (average_valid) {
        final_offset += average_offset_delta;
        if (!invalid) {
            offset_error = offset_now - final_offset;
            while (offset_error > 555.5) offset_error -= 1111.0;
            while (offset_error < -555.5) offset_error += 1111.0;
            final_offset += 0.1 * offset_error;
        }
        if (offset_now > 250) {
            if (final_offset < 125.0) final_offset += 1111.0;
            if (final_offset > 1236.0) final_offset -= 1111.0;
        }
        else {
            if (final_offset < -125.0) final_offset += 1111.0;
            if (final_offset > 986.0) final_offset -= 1111.0;
        }
    }
    else final_offset = offset_now;

    /*
    printf ("'CalcSSoffset' now: %d (%d), delta: %6.1f (%d), final:
%6.1f\n",
            offset_now, !invalid, average_offset_delta,
average_valid, final_offset);
    */
    /*}}} */
}

}

if (!invalid) {
    count1 = count2; count2 = count_now;
    offset1 = offset2; offset2 = offset_now;
}
count_last = count_now;

if (final_offset > 1111.0) final_offset = 1111.0;
if (final_offset < 0.0) final_offset = 0.0;
return (final_offset * 0.000001);
}
/*}}} */
/*{{{ int proc_file_def (hk_file, sci_file, start, finish, format)*/

```

```

int proc_file_def (hk_file, sci_file, start, finish, format)
FILE *hk_file, *sci_file;
long start, finish;
int format;
{
    /*{{{ local variables*/
    unsigned char *tlm_data_ptr;
    long HK_blk_size, SCI_blk_size, time_of_day;
    int ResetCount, inst_blk_size, inst_blk_pos;
    int tlm_blk_size, SCI_num_blks, blk, dif_blk_cnt;
    static double HKtime, SCItime;
    /*}}} */

    SCItime = HKtime = 0.0;
    dif_blk_cnt = 0;
    while ((HK_blk_size = read_lrec (hk_file, (long)HK_SIZE, format,
    HKblock, &HKtime)) >= 0) {
        dif_blk_cnt--;
        while (HKtime - 6.152 > SCItime) {
            if ((SCI_blk_size = read_lrec (sci_file, (long)SCI_SIZE,
            format, SCIblock, &SCItime)) < 0) {
                printf ("proc_file_def: status %ld on science file.\n",
                SCI_blk_size);
                return (SCI_blk_size == -1);
            }
            dif_blk_cnt++;
        }
        /*{{{ record time info*/
        ResetCount = hk_rst_cnt (HKblock);
        OnBoardTimes[(ResetCount+0) % 8] = HKtime;
        SnapshotOffsets[(ResetCount+7) % 8] = CalcSSoffset (HKblock);
        time_of_day = (long) HKtime % 86400;
        /*}}} */
        if (HKtime - 4.152 > SCItime) {
            if (time_of_day >= start && proc_hk (HKblock, HK_SIZE, HKtime)) {
                /*{{{ check if resync has occurred*/
                if (dif_blk_cnt != 0) {
                    printf ("Resync: (%s) %d excess science blocks read.\n",
                    doubletime (HKtime), dif_blk_cnt);

                    dif_blk_cnt = 0;
                }
                /*}}} */
                if (SCI_blk_size >= 306*62) SCI_num_blks = 62;
                else if (SCI_blk_size >= 1000) SCI_num_blks = 10;
                else SCI_num_blks = 1;
                for (blk = 0; blk < SCI_num_blks; blk++) {
                    /*{{{ process each spacecraft block*/
                    tlm_blk_size = (unsigned)(SCI_blk_size / SCI_num_blks);
                    tlm_data_ptr = SCIblock + tlm_blk_size * blk;
                    proc_raw (tlm_data_ptr, tlm_blk_size, SCItime);
                    inst_blk_size = blksize (tlm_data_ptr);
                    inst_blk_pos = blkpos (tlm_data_ptr);
                    while (inst_blk_size > PKT_HEADSIZE || inst_blk_pos ==
                    FIRST_BLK) {
                        if (headword (tlm_data_ptr) == 0xffff) break;
                        if (inst_blk_size <= tlm_blk_size) {
                            asmb_sci_pkt (tlm_data_ptr, inst_blk_size, SCItime);
                        }
                        else write_err (SCItime, "Instrument block overruns
                        telemetry block");
                        tlm_blk_size -= inst_blk_size;
                    }
                }
            }
        }
    }
}

```



```

        if (tlm_blk_size > 0) {
            tlm_data_ptr += inst_blk_size;
            inst_blk_size = blksize (tlm_data_ptr);
            inst_blk_pos = blkpos (tlm_data_ptr);
        }
        else {
            inst_blk_size = 0;
            inst_blk_pos = SINGLE_BLK;
        }
    }
    if (tlm_blk_size > 0) proc_unused (tlm_data_ptr, tlm_blk_size,
SCItime);
    /*}}} */
}
}
if (time_of_day > finish) return (1);
}
}
printf ("proc_file_def: status %ld on HK file.\n", HK_blk_size);
return (HK_blk_size == -1); /* TRUE if eof, FALSE if other error */
}
/*}}} */
/*{{{ int FudgeTime (timeptr)*/
void FudgeTime (timeptr)
double *timeptr;
{
    static double lastHKtime = 0.0;
    double deltat;

    deltat = *timeptr - lastHKtime;
    printf ("SIS fudge time delta: %8.4f\n", deltat);

    if (fabs (*timeptr - lastHKtime) > 60.0) {
        printf ("SIS time resync: %s", doubledate (lastHKtime));
        printf (" to: %s\n", doubledate (*timeptr));
        lastHKtime = *timeptr;
    }
    else {
        *timeptr = lastHKtime;
    }
    lastHKtime += 84414.0 / 16384.0;
}
/*}}} */
/*{{{ int proc_file_sis (hk_file, sci_file, start, finish, format)*/
int proc_file_sis (hk_file, sci_file, start, finish, format)
FILE *hk_file, *sci_file;
long start, finish;
int format;
{
    /*{{{ local variables*/
    unsigned char *tlm_data_ptr;
    long HK_blk_size, SCI_blk_size, time_of_day;
    int ResetCount, inst_blk_size, inst_blk_pos;
    int tlm_blk_size, SCI_num_blks, blk, hk_ok;
    static double HKtime, SCItime;
    /*}}} */

    SCItime = HKtime = 0.0;
    while ((HK_blk_size = read_lrec (hk_file, (long)HK_SIZE, format,
HKblock, &HKtime)) >= 0) {

```

```

    /* printf ("HKblock: %s, %d bytes\n", doubletime(HKtime),
HK_blk_size); */
    /*{{{ record time info*/
    ResetCount = hk_rst_cnt (HKblock);
    if (format == fmFDG_TLM) FudgeTime (&HKtime);
    OnBoardTimes[(ResetCount+0) % 8] = HKtime;
    SnapshotOffsets[(ResetCount+7) % 8] = CalcSSoffset (HKblock);
    time_of_day = (long) HKtime % 86400;
    if (time_of_day >= start) hk_ok = proc_hk (HKblock, HK_SIZE,
HKtime);
    /*}}} */
    do {
        SCI_blk_size = read_lrec (sci_file, (long)SCI_SIZE,
                                format, SCIblock, &SCItime);
        if (SCI_blk_size < 0) return (SCI_blk_size == -1);
        /* printf ("SCIblock: %s, %d bytes\n", doubletime(SCItime),
SCI_blk_size); */
        if (time_of_day > start && hk_ok) {
            SCI_num_blks = 1;
            blk = 0;
            /*{{{ process each spacecraft block*/
            tlm_blk_size = (unsigned)(SCI_blk_size / SCI_num_blks);
            tlm_data_ptr = SCIblock + tlm_blk_size * blk;
            proc_raw (tlm_data_ptr, tlm_blk_size, SCItime);
            inst_blk_size = blksize (tlm_data_ptr);
            inst_blk_pos = blkpos (tlm_data_ptr);
            while (inst_blk_size > PKT_HEADSIZE || inst_blk_pos ==
FIRST_BLK) {
                if (headword (tlm_data_ptr) == 0xffff) break;
                if (inst_blk_size <= tlm_blk_size) {
                    asmb_sci_pkt (tlm_data_ptr, inst_blk_size, SCItime);
                }
                else write_err (SCItime, "Instrument block overruns telemetry
block");
                tlm_blk_size -= inst_blk_size;
                if (tlm_blk_size > 0) {
                    tlm_data_ptr += inst_blk_size;
                    inst_blk_size = blksize (tlm_data_ptr);
                    inst_blk_pos = blkpos (tlm_data_ptr);
                }
                else {
                    inst_blk_size = 0;
                    inst_blk_pos = SINGLE_BLK;
                }
            }
            if (tlm_blk_size > 0) proc_unused (tlm_data_ptr, tlm_blk_size,
SCItime);
            /*}}} */
        }
        while (SCItime < HKtime + 4.0);
        if (time_of_day > finish) return (1);
    }
    return (HK_blk_size == -1); /* TRUE if eof, FALSE if other error */
}
/*}}} */
/*{{{ int proc_file_row (hk_file, sci_file, start, finish, format)*/
int proc_file_row (tlm_file, dummy_file, start, finish, format)
FILE *tlm_file, *dummy_file;
long start, finish;
int format;
{

```

```

/*{{{ local variables*/
unsigned char *tlm_data_ptr;
long tlm_blk_size, time_of_day;
int ResetCount, inst_blk_size, inst_blk_pos;
static double HKtime, tlm_blk_time;
int hk_ok;
/*}}} */

tlm_blk_time = 0.0;
time_of_day = -1; /* Make sure science not processed before first HK
*/
hk_ok = 0;
while ((tlm_blk_size = read_lrec (tlm_file, (long)SCI_SIZE,
                                format, SCIBlock, &tlm_blk_time)) >= 0) {
    if (tlm_blk_size == HK_ACT_SIZE) {
        memcpy (HKblock, SCIBlock, HK_SIZE);
        HKtime = tlm_blk_time;
        hk_ok = proc_hk (HKblock, HK_SIZE, HKtime);
        /*{{{ record time info*/
        ResetCount = hk_rst_cnt (HKblock);
        OnBoardTimes[(ResetCount+0) % 8] = HKtime;
        SnapshotOffsets[(ResetCount+7) % 8] = CalcSSoffset (HKblock);
        time_of_day = (long) HKtime % 86400;
        /*}}} */
    }
    else {
        if (time_of_day >= start && hk_ok) {
            /*{{{ process each spacecraft block*/
            tlm_data_ptr = SCIBlock;
            proc_raw (tlm_data_ptr, (int)tlm_blk_size, tlm_blk_time);
            inst_blk_size = blksize (tlm_data_ptr);
            inst_blk_pos = blkpos (tlm_data_ptr);
            while (inst_blk_size > PKT_HEADSIZE || inst_blk_pos ==
FIRST_BLK) {
                if (headword (tlm_data_ptr) == 0xffff) break;
                if (inst_blk_size <= (int)tlm_blk_size) {
                    asmb_sci_pkt (tlm_data_ptr, inst_blk_size, tlm_blk_time);
                }
                else write_err (tlm_blk_time, "Instrument block overruns
telemetry block");
                tlm_blk_size -= inst_blk_size;
                if (tlm_blk_size > 0) {
                    tlm_data_ptr += inst_blk_size;
                    inst_blk_size = blksize (tlm_data_ptr);
                    inst_blk_pos = blkpos (tlm_data_ptr);
                }
                else {
                    inst_blk_size = 0;
                    inst_blk_pos = SINGLE_BLK;
                }
            }
            if (tlm_blk_size > 0) proc_unused (tlm_data_ptr,
(int)tlm_blk_size, tlm_blk_time);
            /*}}} */
        }
        if (time_of_day > finish) return (1);
    }
}
return (tlm_blk_size == -1); /* TRUE if eof, FALSE if other error */
/*}}} */
/*{{{ int proc_file (hk_file, sci_file, start, finish,
format)*/

```

```

int proc_file (hk_file, sci_file, start, finish, format)
FILE *hk_file, *sci_file;
long start, finish;
int format;
{
switch (format) {
case 0:
return proc_file_row (hk_file, sci_file, start, finish, format);
case 5:
case 6:
return proc_file_sis (hk_file, sci_file, start, finish, format);
default:
return proc_file_def (hk_file, sci_file, start, finish, format);
}
}
/*}}}} */

```

Appendix 5 Tlmproc.h

```
/*{{{ constants*/
#define SCI_SIZE 65536          /* Bytes */
#define HK_SIZE 256            /* Bytes */
#define HK_ACT_SIZE 192        /* Bytes */
#define MAXASMBSIZE 4096       /* Bytes */

#define SIS_HEADSIZE 14        /* Bytes */
#define DDS_HEADSIZE 15        /* Bytes */
#define PKT_HEADSIZE 2

#define TRUE 1
#define FALSE 0

#define SINGLE_BLK 0
#define FIRST_BLK 1
#define LAST_BLK 2
#define MIDDLE_BLK 3

#define COR_INST_NUM 5

#define fmROW_TLM 0            /* Cluster DWP ROW telemetry file */
#define fmROW_CMD 1            /* Cluster DWP ROW command log file */
#define fmCCS_TLM 2            /* Cluster CCS telemetry file */
#define fmM94_TLM 3            /* ELISMA DWP telemetry file ROW or
GSE-C */
#define fmDDS_TLM 4            /* Cluster Data Delivery System file
*/
#define fmSIS_TLM 5            /* Cluster WEC EGSE telemetry file */
#define fmFDG_TLM 6            /* Cluster WEC EGSE telemetry file,
time stamps to be fudged */

/*}}} */

/*{{{ sci packet macros*/
#define blksize(p) ((p[0]&1) << 9) + (p[1] << 1) + 2
#define blkpos(p) ((p[0]&0xc0) >> 6)
#define source(p) ((p[0]&0x38) >> 3)
#define blkcount(p) ((p[0]&0x06) >> 1)
#define headword(p) ((p[0] << 8) + p[1])
#define samp_clks(p) (((p[2]&0x1f) << 8) + p[3])
#define reset_cnt(p) ((p[2]&0xe0) >> 5)

#define cor_stp_lev(p) (p[5] & 0x0f)
#define cor_shft_1(p) ((p[5] & 0xf0) >> 4)
#define cor_shft_2(p) (p[4] & 0x0f)
#define cor_shft_stp(p) ((p[4] & 0xf0) >> 4)
#define cor_zl_1(p) ((p[6] << 8) + p[7])
#define cor_zl_2(p) ((p[22] << 8) + p[23])
#define cor_zl_stp(p) ((p[38] << 8) + p[39])
/*}}} */

/*{{{ hk block macros*/
#define valid_hk(p) (p[0] == 0xcd)
#define hk_rst_cnt(p) ((p[2] << 8) + p[3])
#define hk_ss_off(p) (((p[4] & 0x07) << 8) + p[5])
#define hk_ss_inval(p) ((p[4] & 0x08) != 0)
#define cor_lvl_1(p) (p[41] & 0x0f)
#define cor_lvl_2(p) ((p[41] & 0xf0) >> 4)
```

```

#define cor_hbr(p)    ((p[40] & 0x80) >> 7)
#define peace_fps(p) ((p[46] & 0xc0) >> 6)
#define peace_srp(p) (((p[46] & 0x0f) << 8) + p[47])

#define mac_exec(p)   ((p[10] & 0x80) >> 7)
#define mac_slot(p)   (p[11] & 0x3f)

#define mlc_echo_cnt(p) (p[55])
#define mlc_echo_1_f(p) (p[56])
#define mlc_echo_1_p(p) (p[57])
/*}}} */

/*{{{ tlmproc.fun*/
struct tm *decodetime(long *timep);
char *doubledate(double dtime);
char *doubletime(double dtime);
long encode_time(char *string);
long read_lrec(FILE *filep, long bufsize, int format, unsigned char
*bufptr, double *timeptr);
static int proc_sci_pkt(unsigned char *tlm_ptr, int pkt_size);
static void asmb_sci_pkt(unsigned char *tlm_ptr, int pkt_size, double
sci_time);
double CalcSSoffset(unsigned char *hk_ptr);
int proc_file_def (FILE *hk_file, FILE *sci_file, long start, long
finish, int format);
void FudgeTime(double *timeptr);
int proc_file_sis (FILE *hk_file, FILE *sci_file, long start, long
finish, int format);
int proc_file_row (FILE *tlm_file, FILE *dummy_file, long start, long
finish, int format);
int proc_file (FILE *hk_file, FILE *sci_file, long start, long
finish, int format);
/*}}} */
/*{{{ timcheck.fun*/
int proc_hk(unsigned char *hk_ptr, int pkt_size, double ob_time);
int proc_raw(unsigned char *hk_ptr, int pkt_size, double ob_time);
int proc_unused(unsigned char *hk_ptr, int pkt_size, double
ob_time);
int proc_sci(unsigned char *tlm_ptr, int pkt_size, double
ob_time, double ss_offset);
void write_err(double pkt_time, char *message);
/*}}} */

```

Appendix 6 Least Square Fit

Considering a common plane equation of the format: $ax + by + cz + d = 0$

Substituting: $-\frac{d}{c} = c_1$; $\frac{a}{c} = a_1$ and $\frac{b}{c} = b_1$

$$c_1 = a_1x + b_1y + z \quad \text{A.6.1}$$

If this plane, passes through the origin (0,0,0), then c_1 should be equal to zero. For the plane equation to be derived from a finite points of x, y, z coordinates, the values of a and b should be found such that c_1 is minimal. Thence, using the Sum of Squared Errors of prediction (SSE) method;

$$SSE(a, b, c) = \sum_{i=1}^n (ax_i + by_i + z_i + c_i)^2 \quad \text{A.6.2}$$

Appendix 7 Deriving solution to $ax + by + z + c = 0$ format

Consider $(ax + by + z + c)^2$;

$$(ax + by + z + c)^2 = [(ax + by) + (z + c)]^2$$

$$(ax + by + z + c)^2 = [(ax + by)^2 + 2(ax + by)(z + c) + (z + c)^2]$$

$$(ax + by + z + c)^2 = [(a^2x^2 + 2abxy + b^2y^2) + (2axz + 2acx + 2byz + 2bcy) + (z^2 + 2cz + c^2)]$$

$$(ax + by + z + c)^2 = [a^2x^2 + b^2y^2 + z^2 + c^2 + 2abxy + 2axz + 2acx + 2byz + 2bcy + 2cz] \quad \text{A.7.1}$$

Setting the partial derivatives with respect to a, b & c and equating to zero:

$$\text{If } f(a, b, c) = [a^2x^2 + b^2y^2 + z^2 + c^2 + 2abxy + 2axz + 2acx + 2byz + 2bcy + 2cz] \quad \text{A.7.2}$$

Taking partial derivatives respect to a :

$$\frac{\partial f(a, b, c)}{\partial a} = \frac{\partial}{\partial a} [a^2x^2 + b^2y^2 + z^2 + c^2 + 2abxy + 2axz + 2acx + 2byz + 2bcy + 2cz] \quad \text{A.7.3}$$

$$\frac{\partial f(a, b, c)}{\partial a} = 2x^2a + 2xyb + 2xc + 2xz \quad \text{A.7.4}$$

Equating it to zero gives:

$$2x^2a + 2xyb + 2xc + 2xz = 0 \quad \text{A.7.5}$$

Taking partial derivatives respect to b :

$$\frac{\partial f(a, b, c)}{\partial b} = \frac{\partial}{\partial b} [a^2x^2 + b^2y^2 + z^2 + c^2 + 2abxy + 2axz + 2acx + 2byz + 2bcy + 2cz] \quad \text{A.7.6}$$

$$\frac{\partial f(a,b,c)}{\partial b} = 2xya + 2y^2b + 2yc + 2yz \quad \mathbf{A.7.7}$$

Equating it to zero gives:

$$2xya + 2y^2b + 2yc + 2yz = 0 \quad \mathbf{A.7.8}$$

Taking partial derivatives respect to c :

$$\frac{\partial f(a,b,c)}{\partial c} = \frac{\partial}{\partial c} \left[(a^2x^2 + b^2y^2 + z^2 + c^2 + 2abxy + 2axz + 2acx + 2byz + 2bcy + 2cz) \right] \quad \mathbf{A.7.9}$$

$$\frac{\partial f(a,b,c)}{\partial c} = 2xa + 2yb + 2c + 2z \quad \mathbf{A.7.10}$$

Equating it to zero gives:

$$2xa + 2yb + 2c + 2z = 0 \quad \mathbf{A.7.11}$$

The three simultaneous equations (A.7.5, A.7.8 and A.7.11) need to be solved to deduce a, b & c .

Appendix 8 Solving simultaneous equations with 3 unknowns

Consider the three simultaneous equations with 3 unknowns a, b & c :

$$m_1a + n_1b + o_1c + d_1 = 0 \quad \text{A.8.0}$$

$$m_2a + n_2b + o_2c + d_2 = 0 \quad \text{A.8.1}$$

$$m_3a + n_3b + o_3c + d_3 = 0 \quad \text{A.8.2}$$

$$(A.8.0) \times m_2 \quad \Rightarrow \quad m_1m_2a + n_1m_2b + o_1m_2c + d_1m_2 = 0 \quad \text{A.8.3}$$

$$(A.8.1) \times m_1 \quad \Rightarrow \quad m_1m_2a + n_2m_1b + o_2m_1c + d_2m_1 = 0 \quad \text{A.8.4}$$

$$(A.8.3) - (A.8.4) \Rightarrow$$

$$(n_1m_2 - n_2m_1)b + (o_1m_2 - o_2m_1)c + (d_1m_2 - d_2m_1) = 0 \quad \text{A.8.5}$$

Similarly,

$$(A.8.0) \times m_3 \quad \Rightarrow \quad m_1m_3a + n_1m_3b + o_1m_3c + d_1m_3 = 0 \quad \text{A.8.6}$$

$$(A.8.2) \times m_1 \quad \Rightarrow \quad m_1m_3a + n_3m_1b + o_3m_1c + d_3m_1 = 0 \quad \text{A.8.7}$$

$$(A.8.6) - (A.8.7) \Rightarrow$$

$$(n_1m_3 - n_3m_1)b + (o_1m_3 - o_3m_1)c + (d_1m_3 - d_3m_1) = 0 \quad \text{A.8.8}$$

$$(A.8.8) \times (n_1m_2 - n_2m_1) \Rightarrow$$

$$(n_1m_2 - n_2m_1)(n_1m_3 - n_3m_1)b + (o_1m_2 - o_2m_1)(n_1m_3 - n_3m_1)c + (d_1m_2 - d_2m_1)(n_1m_3 - n_3m_1) = 0$$

$$\text{A.8.9}$$

$$(A.8.5) \times (n_1m_2 - n_2m_1) \Rightarrow$$

$$(n_1m_2 - n_2m_1)(n_1m_3 - n_3m_1)b + (o_1m_3 - o_3m_1)(n_1m_2 - n_2m_1)c + (d_1m_3 - d_3m_1)(n_1m_2 - n_2m_1) = 0$$

$$\text{A.8.10}$$

$$(A.8.9) - (A.8.10) \quad \Rightarrow$$

$$\begin{aligned} & \left[(o_1 m_2 - o_2 m_1)(n_1 m_3 - n_3 m_1) - (o_1 m_3 - o_3 m_1)(n_1 m_2 - n_2 m_1) \right] c \\ & + \\ & (d_1 m_2 - d_2 m_1)(n_1 m_3 - n_3 m_1) - (d_1 m_3 - d_3 m_1)(n_1 m_2 - n_2 m_1) = 0 \end{aligned}$$

$$A.8.11$$

$$\therefore \quad c = (-1) \frac{\left[(d_1 m_2 - d_2 m_1)(n_1 m_3 - n_3 m_1) - (d_1 m_3 - d_3 m_1)(n_1 m_2 - n_2 m_1) \right]}{\left[(o_1 m_2 - o_2 m_1)(n_1 m_3 - n_3 m_1) - (o_1 m_3 - o_3 m_1)(n_1 m_2 - n_2 m_1) \right]} \quad A.8.12$$

$$A.8.5 \quad \Rightarrow \quad (n_1 m_2 - n_2 m_1)b + (o_1 m_2 - o_2 m_1)c + (d_1 m_2 - d_2 m_1) = 0$$

$$\therefore \quad b = \left[\frac{(o_1 m_2 - o_2 m_1)c + (d_1 m_2 - d_2 m_1)}{(n_2 m_1 - n_1 m_2)} \right] \quad A.8.13$$

$$A.8.0 \quad \Rightarrow \quad m_1 a + n_1 b + o_1 c + d_1 = 0$$

$$\therefore \quad a = \left[\frac{-1}{m_1} \right] (n_1 b + o_1 c + d_1) \quad A.8.14$$

Appendix 9 Angle between two planes

The orbital plane equation is determined in the form:

$$ax + by + z + c = 0 \quad \text{A.9.0}$$

The equation of the equatorial plane is:

$$z = 0 \quad \text{A.9.1}$$

If a plane is defined by the equation

$$px + qy + rz + s = 0 \quad \text{A.9.2}$$

With x, y, z being the Cartesian coordinates, then the equation of the Normal vector to that plane is given by:

$$\vec{n} = p\vec{i} + q\vec{j} + r\vec{k} \quad \text{A.9.3}$$

If the Normal vector of the orbital plane is called n_o and the Normal vector of the equatorial plane is called n_e , then from A.9.0, A.9.1, A.9.2 and A.9.3, they can be derived as follows:

From A.9.1, A.9.2 and A.9.3;

$$p = a, q = b, r = 1 \Rightarrow \vec{n}_o = a\vec{i} + b\vec{j} + \vec{k} \quad \text{A.9.4}$$

From A.9.2 and A.9.3;

$$p = 0, q = 0, r = 1 \Rightarrow \vec{n}_e = \underline{k} \quad \text{A.9.5}$$

The angle between these two Normal vectors is same as the angle between the orbital plane and the equatorial plane, as demonstrated in Figure 7.1 below.

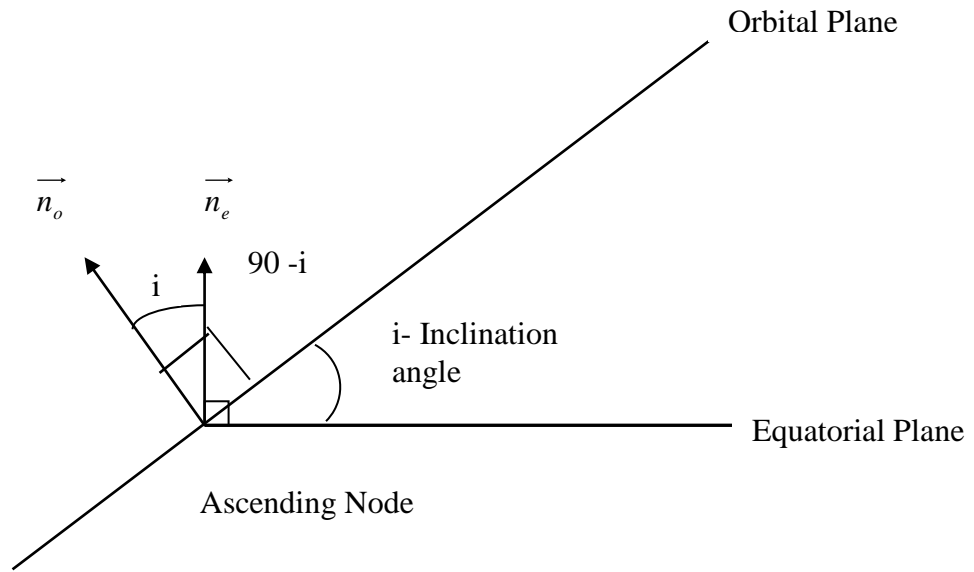


Figure A.9.1 Angle between the Orbital plane and the Equatorial plane being equal to the angle between their Normal vectors n_o and n_e , which equals Inclination angle

A.9.1 Angle between two vectors

If two vectors are given by;

$$\vec{n}_1 = p_1 \underline{i} + q_1 \underline{j} + r_1 \underline{k} \quad \text{and} \quad \vec{n}_2 = p_2 \underline{i} + q_2 \underline{j} + r_2 \underline{k}$$

Then the angle between them is given by:

$$\alpha(\vec{n}_1, \vec{n}_2) = \cos^{-1} \left\{ \frac{|p_1 p_2 + q_1 q_2 + r_1 r_2|}{\left(\sqrt{p_1^2 + q_1^2 + r_1^2} \right) \left(\sqrt{p_2^2 + q_2^2 + r_2^2} \right)} \right\} \quad \text{A.9.6}$$

Appendix 10 Coordinate transformation of a two axes Cartesian plane by an angle of θ

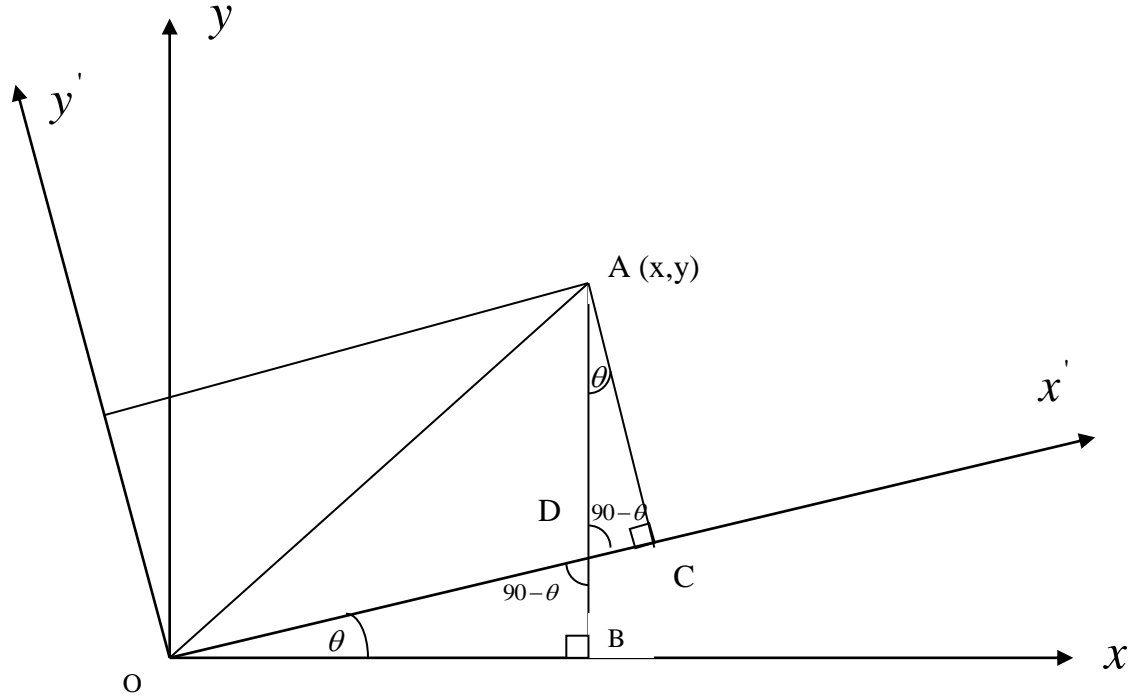


Figure A.10.1 Coordinate transformation of a two axes Cartesian plane by an angle of θ

Let x, y be the original Cartesian axes and x', y' be the transformed Cartesian axes.

If the axes are rotated by θ^0 , then;

$$\angle BOD = \theta^0 \quad \text{A.10.1}$$

$$\therefore \angle ODB = (90 - \theta)^0$$

$$\therefore \angle ADC = (90 - \theta)^0$$

$$\therefore \angle DAC = \theta^0 \quad \text{A.10.2}$$

$$A(x, y) \Rightarrow OB = x \quad \text{A.10.3}$$

$$AB = y \quad \text{A.10.4}$$

If the new transformed coordinates are x', y' for A, then:

$$A(x', y') \Rightarrow OC = x' \quad \text{A.10.5}$$

$$AC = y' \quad \text{A.10.6}$$

In $\triangle OBD$

$$\tan \theta = \frac{BD}{OB}$$

$$BD = OB \times \tan \theta$$

$$\text{A.10.2} \Rightarrow$$

$$BD = x \times \tan \theta \quad \text{A.10.7}$$

$$\cos \theta = \frac{OB}{OD}$$

$$OD = \frac{OB}{\cos \theta}$$

$$OD = \frac{x}{\cos \theta} \quad \text{A.10.8}$$

But

$$AB = AD + BD$$

$$\text{A.10.3, A.10.6} \Rightarrow$$

$$y = AD + x \tan \theta$$

\therefore

$$AD = y - x \tan \theta \quad \text{A.10.9}$$

In $\triangle ADC$

$$\cos \theta = \frac{AC}{AD}$$

$$AC = AD \times \cos \theta \quad \text{A.10.10}$$

$$\text{A.10.5, A.10.7} \Rightarrow$$

$$y' = (y - x \tan \theta) \cos \theta$$

$$y' = (y \cos \theta - x \tan \theta \cdot \cos \theta)$$

$$y' = (y \cos \theta - x \sin \theta) \quad \text{A.10.11}$$

In $\triangle ADC$

$$\sin \theta = \frac{DC}{AD}$$

$$DC = AD \times \sin \theta \quad \text{A.10.12}$$

A.10.5, A.10.11 \Rightarrow

$$x' = OD + DC$$

$$x' = \frac{x}{\cos \theta} + AD \times \sin \theta$$

$$x' = \frac{x}{\cos \theta} + (y - x \tan \theta) \sin \theta$$

$$x' = \frac{x}{\cos \theta} + y \sin \theta - x \tan \theta \times \sin \theta$$

$$x' = \frac{x}{\cos \theta} + y \sin \theta - x \frac{\sin \theta}{\cos \theta} \times \sin \theta$$

$$x' = \frac{x}{\cos \theta} - x \frac{\sin^2 \theta}{\cos \theta} + y \sin \theta$$

$$x' = \frac{x}{\cos \theta} [1 - \sin^2 \theta] + y \sin \theta$$

$$x' = \frac{x}{\cos \theta} [\cos^2 \theta] + y \sin \theta$$

$$x' = \frac{x}{\cos \theta} [\cos^2 \theta] + y \sin \theta$$

$$x' = x \cos \theta + y \sin \theta \quad \text{A.10.13}$$

Therefore, the new coordinates of a two dimensional coordinate system, after a rotation by θ^0 are given by:

$$x' = (x \cos \theta + y \sin \theta)$$

$$y' = (y \cos \theta - x \sin \theta)$$

Appendix 11 PEACE energy range (eV) and Correlator levels

PEACE energy range (eV)	Correlator level	Correlator level
0.000, 0.832, 1.443, 2.041,	15	
2.636, 3.229, 3.821, 4.413,	14	
5.005, 5.598, 6.190, 6.782,	13	
7.375, 7.967, 8.560, 9.153,	12	
9.746, 10.625, 11.815, 13.286,	11	
14.791, 16.548, 18.658, 20.737,	10	
23.135, 25.821, 28.831, 32.133,	9	
36.049, 40.297, 44.846, 50.024,	8	15
55.836, 62.582, 70.017, 78.085,	7	14
87.458, 97.863, 109.290, 122.102,	6	13
136.336, 152.349, 170.231, 190.019,	5	12
212.148, 237.055, 264.910, 296.187,	4	11
331.156, 369.991, 413.407, 461.726,	3	10
515.794, 576.134, 643.802, 719.616,	2	9
803.999, 897.987, 1002.989, 1120.755,	1	8
1252.556, 1399.612, 1564.128, 1747.450,		7
1951.860, 2181.087, 2437.590, 2724.052,		6
3043.314, 3399.809, 3798.656, 4243.776,		5
4741.099, 5299.795, 5921.832, 6613.463,		4
7392.532, 8264.201, 9230.086, 10313.096,		3
11528.010, 12871.997, 14375.944, 16068.883,		2
17956.100, 20070.984, 22428.947, 25042.089		1

Table A11 PEACE energy range (eV) and Correlator levels

Reference List

Basu S. et al. (1985) 'Chapter 10 – Ionospheric Radio wave Propagation' in Jursa, A. S. (ed.) 'Handbook of Geophysics and the Space Environment', Air Force Geophysics Laboratory Air Force Systems Command United States Air Force.

Basu, S. (2003) 'Ionospheric Scintillation: A Tutorial', CEDAR Workshop, Longmont, Colorado.US.

Beloff, N. et al., (2004) 'Storm time changes in total electron content in ionosphere measured by low orbiting topside sounder', *Annales Geophysicae*, pp.2741- 2746.

Beniguel, Y. and Hamel, P. (2011) 'A global ionosphere scintillation propagation model for equatorial regions', *Space Weather Space Climate Journal*, DOI: 10.1051/swsc/2011004.

Béniguel, Y. (2011) 'GISM Global Ionospheric Scintillation Model', GISM Technical Manual, pp.1-21.

Biktash, L. (2005) 'Role of the Magnetospheric and Ionospheric Current in Generation of the Equatorial Scintillations During Geomagnetic Storms', Izmiran, Troitsk, Mosco Region, Russia. Proceedings of ISSS-7, pp 26-31.

Biktash, L. (2009) 'The Solar Wind and Geomagnetic Indices for Study of Probability Appearance of the Equatorial Scintillations During Geomagnetic Storms', Presentation

at the International Association of Geomagnetism and Aeronomy IAG- 2Symposium,
Cairo 7th of December,2009

Bockstiegel K., Benko M. and Hobe S. (eds.) (2005) ‘Space Law- Basic Legal Documents’, Volume 1, Institute of Air and Space Law at the Cologne University, Eleven International Publishing, B.V.5.4, pp10-15

Bodner, M. (2014) ‘Russia Eager to Set Up Glonass Monitoring Stations in 36 Countries’. The Moscow Times. Available at:
<https://themoscowtimes.com/articles/russia-eager-to-set-up-glonass-monitoring-stations-in-36-countries-34572>, Accessed on 23/04/2014

Breed, A. M. and Goodwin, G. L. (2017) ‘Ionospheric Slab Thickness and Total Electron Content Determined in Australia’, STSP Meetings- Ionospheric Slab Thickness and Total Electron Content Determined in Australia, pp. 1-10.

Buckley et al., (2000) ‘Multipoint Plasma Measurement’, Proceedings of the Cluster II workshop on Multiscale, pp 303-306.

Buckley et al., (2001) Multipoint Measurements versus Theory’, Proceedings of the Les Woolliscroft Memorial Conference / Sheffield Space Plasma Meeting; pp19-26.

Cornilleau-Wehrlin N. et al., (1997) ‘The Cluster Spatio-Temporal Analysis of Field Fluctuations (STAFF) Experiment’ Space Science Reviews, Volume 79, Issue 1–2, pp 107–136

ESA , (2011) ‘GNSS Applications’, European Space Agency Navipedia, Available at http://www.navipedia.net/index.php/GNSS_Applications (Accessed : 15.02.2018).

ESA, (2013) ‘Cluster – Instruments’ , European Space Agency, Available at <http://sci.esa.int/cluster/33024-instruments/> (Accessed : 11.12.2013).

Garner, T. W., et al., (2008) ‘Total electron content measurements in ionospheric physics’, *Advances in Space Research* 42, pp. 720- 726

Gorman, F. J. Jr. and Soicher, H. (1973) ‘Plasmaspheric Effects on One-Way Satellite Timing Signals’, *Communications/Automatic Data Processing Laboratory*, pp. 441-452.

Hapgood, M. A. (1992) ‘Space Physics Coordinate Transformations: A User Guide’, *Planer. Space Sci.* Vol. 40, No. 5. pp. 711-717.

IEEE, (2011) ‘Global Ionospheric Propagation Model’, Paris, *GISM_user_manual*, v6.53, pp. 1- 33.

Johnstone et al., (1997) ‘PEACE – A Plasma Electron And Current Experiment’ *Space Science review*. Kluwer Academic Publishers, Issue 79 pp.351-398

Kenpankho, P. et al. (2011) 'Comparison of GPS TEC measurements with IRI TEC prediction at the equatorial latitude station, Chumphon, Thailand', *Earth Planets Space*, 63, 365–370, pp. 365- 370.

Klobuchar J. et al., (1973) 'Total Electron Content Studies of the Ionosphere' Air Force Cambridge Research Laboratories L.G. Hanscom Field, Massachusetts.

Li, G. , Baiqi Ning, B. and Yuan, H. (2007) 'Analysis of ionospheric scintillation spectra and TEC in the Chinese low latitude region', *Earth Planets Space*, 59, pp. 279–285.

Maral G and Bousquet M (1993) 'Satellite Communication Systems', John Wiley and Sons 2nd Edition.

Mazzella, A. J., Jr. (2012), Determinations of plasmasphere electron content from a latitudinal chain of GPS stations, *Radio Sci.*, 47 , RS1013, doi:10.1029/2011RS004769

MSSL, (2000), 'MSSL Space Plasma Physics Group', Available at http://www.mssl.ucl.ac.uk/www_plasma/missions/cluster/about_peace/peace_images.php (Accessed : 11.05.2009),

Nasa Earth Observatory (2011) 'Catalog of Earth Satellite Orbits : Feature Articles' Available from <http://earthobservatory.nasa.gov/Features/OrbitsCatalog/page2.php>

Pisacane V. L. (ed.) (2005) 'Fundamentals of Space Systems', Oxford University Press

Polischuk, G. M. et al. (2002) 'The Global Navigation Satellite System Glonass: Development and Usage in the 21st Century', 34th Annual Precise Time and Time Interval (PTTI) Meeting, pp. 151- 160.

Rich F.J. and Basu Su. (1985) 'Chapter 9 – Ionospheric Physics' in Jursa, A. S. (ed.) (1985) 'Handbook of Geophysics and the Space Environment', Air Force Geophysics Laboratory Air Force Systems Command United States Air Force.

Rosbach, U. (2001) 'Positioning and Navigation Using the Russian Satellite System GLONASS', Studiengang Geodäsie Und Geoinformation Universität Der Bundeswehr München.

Torkar K. (2007) 'Users Guide to the Double Star Science Data System', European Space Agency, Issue 1, Revision 3

Woolliscroft et al.,(1997) 'The Digitalwave-Processing Experiment on Cluster', Space Science review, Issue 79 pp.212-230.

Ya'acob, N. , Abdullah, M. and Ismail, M. (2010) 'GPS Total Electron Content (TEC) Prediction at Ionosphere Layer over the Equatorial Region', Intech Open Science/Open Minds, pp. 487-508.

Bibliography

Angelopoulos, V. (2005) 'Themis in Relation to Cluster and Double Star', Space Sciences Laboratory, University of California, Berkeley, pp. 1- 5.

Bagiya, M. S. et al (2009) 'TEC variations during low solar activity period (2005–2007) near the Equatorial Ionospheric Anomaly Crest region in India', *Annales Geophysicae*, pp. 1047- 1057.

Beach, T. L. and Kintner, P. M. (2001) 'Development and Use of a GPS Ionospheric Scintillation Monitor', *IEEE Transactions on Geoscience and Remote Sensing*, Vol. 39, NO. 5, pp. 918- 928.

Bekkeng, T. A. (2010) 'Miniaturized Langmuir probe systems for in-situ space plasma measurements', Tore Andr'e Bekkeng Miniaturized Langmuir probe systems.

Bhattacharya, S., KPurohit, P. and KGwal, A. (2011) 'Influence of Magnetospheric and Ionospheric currents on radio wave scintillation during storm time condition', *International Journal of Environmental Sciences, India*, Volume 1, No 5, pp. 924- 937.

Bhavnani, K. H. and Vancour, R. P. (1991) 'Coordinate Systems for Space and Geophysical Applications', Phillips Laboratory Air Force Systems Command, Massachusetts, Scientific Report No. 9.

Bianchi, C., Ciraolo, L. and Scotto, C. (1994) 'Low Ionospheric Observations by means of the Software receiver for Omega signal', *Annali Di Geofisica*, Vol. 37, N.1, pp. 93 – 99.

Biktash, L. (2009) 'The Solar Wind and Geomagnetic Indices for Study of Probability Appearance of the Equatorial Scintillations During Geomagnetic Storms', Presentation at the International Association of Geomagnetism and Aeronomy IAGA-2 Symposium, Cairo 7th of December, 2009

Bo, X. , et al. (2007) 'Seasonal Variation of the Ionospheric Total Electron Content, Maximum Electron Density and Slab Thickness over Wuhan', Institute of Geology and Geophysics, Chinese Academy of Science, pp. 125- 131.

Booker, H.G. (1975) 'The Role of the Magnetosphere in Satellite and Radio-Star Scintillation', Defense Nuclear Agency, California, USA.

Carpenter, D. L. and Anderson, R. R. (1992) 'An ISEE/ Whistler Model of Equatorial Density in the Magnetosphere', *Journal of Geophysical Research*, Vol. 97, No. A2, pp. 1097- 1108.

Coker C. et al., (2011) 'Global Assimilative Ionospheric Modeling and COSMIC-2'.

Dandouras, I., Cao, J. and Vallat, C. (2009) 'Energetic ion dynamics of the inner magnetosphere revealed in coordinated Cluster-Double Star observations', *Journal of Geophysical Research*, Vol. 114, A01S90, doi:10.1029/2007JA012757, pp1-14.

Datta-Barua, S. , Doherty, P.H. , Delay, S.H. , Dehel, T. and Klobuchar, J.A. (2008) 'Ionospheric Scintillation Effects on Single and Dual Frequency GPS Positioning', FAA WAAS program.

Dierendonck, A. J. V. , Klobuchar, J. and Hua, Q. 'Ionospheric Scintillation Monitoring Using Commercial Single Frequency C/A Code Receivers', US Air Force Contract No. F19628-92-C-0139.

Dyrud, L. et al. (2007) 'Ionospheric Measurement With GPS', Center for Remote Sensing, Inc, pp. 1-19.

F. W. Menk, F. W. et al. (2004) 'Monitoring the plasmapause using geomagnetic field line resonances', Journal of Geophysical Research, Vol. 109, A04216, doi:10.1029/2003JA010097.

Fazakerley, A. N. et al. (2005) 'The Double Star Plasma Electron and Current Experiment', Annales Geophysicae, UK, pp. 1-47.

Fremouw, E.J and Lansinger, J.M. (1981) 'A Computer Model For High-Latitude Phase Scintillation Based On Wideband Satellite Data From Poker Flat'. Defense Nuclear Agency, Washington D.C.

Frernouw, E. J. , and Secan, J. A. (1984) 'Modeling and scientific application of scintillation result', Radio Science, Volume 19, Number 3, pp. 687-694.

Garner, T. W. et al. (2008) 'Total electron content measurements in ionospheric physics', Science Direct, Advances in Space Research 42, pp. 720- 726.

Giordano, S. et al. (2013) 'UVCS/SoHO Catalog of Coronal Mass Ejections from 1996 to 2005: Spectroscopic Properties', Journal of Geophysical Research, DOI:10.1029.

Groves, K. , (2004) 'Monitoring Ionospheric Scintillation with GPS', Air Force Research Laboratory. Massachusetts

Hajkowicz, L. A. and Minakoshim H. (2003) 'Mid-latitude ionospheric scintillation anomaly in the Far East', Annales Geophysicae (2003) 21: 577–581 European Geosciences Union, pp. 577-581.

Heck, B. (2004) 'Error Sources in Highly Precise GPS Positioning -Modelling and Mitigation', Lecture Series UFPR, Curitiba/Brasil.

Heise, S. et al (2001) 'Initial Results on Ionosphere/Plasmasphere Sounding Based on GPS Data Obtained on Board CHAM', Institut für Kommunikation und Navigation ESA Space Weather Workshop, ESTEC, Noordwijk, Netherlands, pp. 1-8.

Huba, J. D. (2011) 'NRL Plasma Formulary', The Office of Naval Research, Washington D C, pp. 1-71.

Jehle, M., Small, D. and Meier, E. (2009) 'Comparison of Different Tec Map Estimation Methods', Remote Sensing Laboratories (RSL), Department of Geography University of Zurich.

Kantor, I. J., de Paula, E. R. and Rezende, L. F. C. (2000) 'Tec Measurements with GPS data', Instituto Nacional De Pesquisas Espaciais, Brazil.

Kintner, P. M. Jr, Humphreys, T. and Hinks, J. (2011) 'GNSS and Ionospheric Scintillation How to Survive the next Solar Maximum', Inside GNSS, Texas pp. 22- 30.

Klimov, S. I., (2002) ' "Obstanovka" Experiment Onboard International Space Station for Space Weather Research', Space Research Institute, Mosco, Russia, pp. 1- 13.

Leitinger, R. ,et al. (2004) 'Relations between electron content and peak density: regular and extreme behaviour', Annals of Geophysics, Supplement to Vol. 47, N. 2/3, pp. 1093- 1107.

Mansilla, G. A., Mosert, M. and Ezquer, R. G. (2005) 'Seasonal variation of the total electron content, maximum electron density and equivalent slab thickness at a South-American station'.

NASA (2012) 'CDF User's Guide', Space Physics Data Facility NASA / Goddard Space Flight Center, Version 3.5.

Obrou, O. K., Ackah, J. B and Zaka, K. (2011) 'Study of a geomagnetic storm effect on the ionospheric scintillation and Total Electron Content (TEC) over the SCINDA station in Abidjan', UN/UAE/USA Workshop on the Applications of Global Navigation Satellite Systems Dubai.

Paula, E. R. D. , et al (2007) 'Characteristics of the Ionospheric F-region plasma irregularities over Brazilian longitudinal sector', Indian Journal of Radio & Space Physics , Vol. 36, pp. 268- 277

Peredo, M., Wong, M., and Hills, H. K. (1992) 'Data and Software resources at the Satellite Situation Center', Geofisica International, Vol. 31, Num. 2, pp. 135-144.

Purohit, P. K. et al. (2011) 'GPS Derived Total Electron Content (TEC) Variations over Indian Antarctica Station, Maitri', World Academy of Science, Engineering and Technology Vol:59, pp. 1984- 1986.

Robert, P. (2003) 'Rocotlib: a Coordinate Transformation Library for Solar-Terrestrial studies', Rocotlib Coordinate Transformations Library V 1.8 - P. Robert, pp. 2- 111.

Sardon, E., Jakowski, N. and Rius, A. (1993) 'Comparison of Ionospheric Tec Obtained from Faraday Rotation of Geostationary Satellite Signals and from GPS Data', Instituto de Astronomía y Geodesia (CSIC-UCM), Madrid (Spain), Satellite Ground Station Neustrelitz (DLR), Neustrelitz (Germany), LAEFF (INTA-CSIC), Madrid (Spain).

Skone, S. and Jong, M. D. (2000) ‘ The impact of geomagnetic substorms on GPS receiver performance’, *Earth Planets Space*, 52, pp. 1067- 1071.

Sreeja, V. V. et al (2011) ‘Tackling ionospheric scintillation threat to GNSS in Latin America’, *J Space Weather Space Clim*, DOI: 10.1051/swsc/2011005.

Stalvey, J. D. (2001) ‘Inversion of Nighttime Electron Densities Using Satellite Observations’, *New Mexico Institute of Mining and Technology, Mexico*, pp. 1-79.

Vasyliunas, V.M. (1967) ‘Low Energy E3xtros in Tke Magretos as Observed by OGO-1 and OGO-3’, *Laboratory for Nuclear Science and Physics Department, Massachusetts Institute of Technology Cambridge, Massachusetts*, pp. 1-22.

Wang, X. at el (2008) ‘Short-term relationship of total electron content with geomagnetic activity in equatorial regions’, *Journal of Geophysical Research*, Vol. 113, A11308, doi:10.1029/2007JA012960.

Washeleski, R. L. (2013) ‘Laser Thomson scattering measurements of electron temperature and density in a Hall-effect plasma’, *Michigan Technological University*.

Wernik, A. W. et al. (2004) ‘Ionospheric Irregularities, Scintillation and Its Effect on Systems’, *ACTA Geophysica Polonica*, Vol. 52, No. 2, pp. 237- 249.

Yermolaev, Y. I. , et al (2005) ‘A Year Later: Solar, Heliospheric, and Magnetospheric Disturbances in November 2004’, *Geomagnetism and Aeronomy*, Translated from *Geomagnetizm i Aeronomiya*, Vol. 45, No. 6, pp. 681–719.